



3D Printing of Microcontainers for Oral Delivery of Drugs and Probiotics

Chang, Tien-Jen

Publication date:
2021

Document Version
Publisher's PDF, also known as Version of record

[Link back to DTU Orbit](#)

Citation (APA):
Chang, T.-J. (2021). *3D Printing of Microcontainers for Oral Delivery of Drugs and Probiotics*. DTU Health Technology.

General rights

Copyright and moral rights for the publications made accessible in the public portal are retained by the authors and/or other copyright owners and it is a condition of accessing publications that users recognise and abide by the legal requirements associated with these rights.

- Users may download and print one copy of any publication from the public portal for the purpose of private study or research.
- You may not further distribute the material or use it for any profit-making activity or commercial gain
- You may freely distribute the URL identifying the publication in the public portal

If you believe that this document breaches copyright please contact us providing details, and we will remove access to the work immediately and investigate your claim.

The background of the cover is a close-up photograph of a 3D printer's nozzle. The nozzle is positioned at the top, and a bright blue laser or light source is focused on the tip, creating a glowing blue spot. The printer's body is dark, and the overall scene is dimly lit, emphasizing the precision and technology of the printing process.

3D Printing of Microcontainers for Oral Delivery of Drugs and Probiotics

Tien-Jen Chang

PhD Thesis

August 2021

Department of Health Technology, Technical University of Denmark (DTU)

Supervisor: Anja Boisen

Co-supervisors: En-Te Hwu and Line Hagner Nielsen

Preface

This PhD thesis is submitted as partial fulfillment of the requirements for obtaining a Ph.D. degree from the Technical University of Denmark. This project was carried out at the Department of Health Technology from the 1st of September 2018 to the 31st of August 2021, in the center for Intelligent Drug delivery and sensing Using microcontainers and Nanomechanics (IDUN), funded by the Danish National Research Foundation (grant no. DNRF122) and by the Villum Fonden (grant no. 9301). Furthermore, the study was supported by the Novo Nordisk Foundation (NNF17OC0026910) as a part of the project Microstructures, Microbiota and Oral Delivery (MIMIO). The main supervisor of this PhD project is Professor Anja Boisen. Associate Professor Line Hagner Nielsen and Associate Professor En-Te Hwu are the co-supervisors. All are associated with the Department of Health Technology at the Technical University of Denmark.

Tien-Jen Chang

Department of Health Technology, Technical University of Denmark (DTU)

Kongens Lyngby, August 2021



Acknowledgments

First of all, I would like to acknowledge my supervisor Prof. Anja Boisen. Thanks of you make this project possible. You are an excellent leader with wisdom and passion. You really encourage me a lot, especially in some difficult times. I would also like to express my gratitude to my co-supervisor, Associate Prof. Line Hagner Nielsen, for generously introducing much knowledge of the pharmaceutical field and always providing helpful suggestions. You are a nice mentor. I really learned a lot from you. My co-supervisor, Associate Prof. En-Te Hwu played a significant role throughout my PhD project. Many thanks to you for sharing plenty of technical know-how. Most importantly, your innovative and crazy idea always inspire me. Besides, thank you for always being so nice to provide many supports in lab, and in life. Moreover, thank you for introducing this fantastic project to me.

I would like to thank my master student Eduard co-supervised with Juliane and Rolf. With all of your great effort, this brilliant result can be achieved. Thanks to Martin for the nice support of the parameter testing of the 3D printer in the beginning. Thanks to Lukas for the initial system setup, shorting the time for developing the 3D printer. A major thank you to everyone in the IDUN group for creating this friendly working and learning environment. I am really proud to be part of this group. Special thanks to Mette, Oleksii, Nikolaj, Sriram, and Lasse for always spending time sharing your knowledge and experience. Thanks to Tracy for the great help in remote controlling CryoSEM in the lockdown period. I would also like to acknowledge our brilliant lab technicians and administrative staff, Lars, Tine, Louise, Dorthe, Per, Jesper, and Sanne, for always being nice for immediate support. Thanks to Lasse, Fatemeh, Rolf, Philip, Roman, and Sriram for proofreading this thesis. I get much help in this most challenging period. Rolf, thank you for always bringing motivation for a nice workout when I am stuck in the lab. This helps me a lot for recharging. Thanks to my office mate, Juliane. With your amazing idea and collaboration for Xmas decoration, we can enjoy the accompany of Nissil for two years. Besides, I appreciate being part of the Friday bar group. Thanks to all the crews in these three years, Amirali, Philip, Elizabeth, Line, Khorshid, Juliane, Sarvesh, Varadarajan, and Arianna, for making so many fantastic Friday nights.

Finally, I would like to thank my family and friends in Taiwan. Due to Covid, we have not met for almost two years, but you still support and encourage me a lot from far away, especially when I receive the exclusive snack and products from my hometown. I also enjoy video charting with all of you for every important or simple, pleasure or grieved moment. Thanks to my friends of CCIC for always providing immediate help and joyful moments of the cocktail club for easing pressure. Thanks to all my friends in Denmark. It is not easy to be used to a new culture and study a PhD program at the same time, but your nice accompany and encouragement support me till the end.

Abstract

Microcontainers (MCs), as innovative oral delivery microdevices, have already been validated to successfully deliver drugs through the gastrointestinal (GI) tract. The MCs protect the delivered content against the harsh environment in the stomach and provide a unidirectional drug release in the intestine, resulting in an overall increase in drug absorption. At the same time, the MCs have the potential to successfully deliver probiotics to the intestinal mucosa in a more efficient way than the current technologies today. However, the MCs do not achieve optimal delivery since the MCs have limited retention time during the transit process through the GI tract. Besides, the release orientation of MCs is uncontrollable, limiting the delivery rate. One potential strategy to extend retention and control orientation is via manipulating mucoadhesion of the MCs. This thesis focuses on improving the geometry structure of MCs to enhance mucoadhesion, resulting in controlled orientation and overall extended intestinal retention.

To realize innovative geometry design, we custom-built a 3D printer with micro/nanoscale printing resolution and centimeter-scale printing volume. This printer allows more design and fabrication freedom for microscale features embedded in the design of the MCs. The 3D printer integrates an HD-DVD optical pickup unit (originally designed for Xbox game console) as a core optical module to solidify photopolymer. The 3D printer achieves the highest printing resolution of 385 nm along the lateral direction. Hence, MCs with overhanging structures and additive features can be realized.

Investigation of the mucoadhesive forces of the MCs provides a preliminary understanding for proofing the concept of geometry design. Nevertheless, the current technique lacks an experienced and suitable instrument to quantify mucoadhesive forces under the micro-newton scale (the range in which MCs normally behave). Therefore, the mucoadhesive force of a single MC is difficult to detect. To overcome the force measuring gap, we repurposed a DVD optical pickup unit for constructing a broad range force analyzer. Within a novel design of a cantilever force transducer, the force analyzer implements high sensitive force measurement of force range from 1.1 N to 40 nN, while the force resolution is 0.99 nN.

With the proposed high-resolution 3D printer and broad range force analyzer, we realized MCs with novel geometry followed by mucoadhesive forces measurement of a single MC. Three design strategies were implemented to enhance intestinal mucoadhesion. First, we designed an

asymmetrical structure of MCs to increase the probability of facing the drug release side to the mucus layer. Then, additive micro-pillars were printed on the MCs to enhance mucoadhesion. Besides, we designed a multiple arrows structure on the side of MCs to provide a hook for deeper entanglement into the mucus layer. An *ex vivo* tensile strength experiment provided a preliminary investigation of MCs mucoadhesive forces, verifying the designed geometry structure. To trace the MCs along the GI tract in an *in vivo* study in rats, we fabricated radiopaque MCs with embedded BaSO₄ nanoparticles using the 3D printer. Planar X-ray scanning showed the distribution of MCs through the GI tract of the rats at various time points, 0.5, 1, 2, and 3 h. The results indicated that while most MCs passed the small intestine after 3 h, approximately 40 % of MCs equipped with micro-pillars stayed in the distal intestine. Besides, the spatial dynamics of MCs during the transit process were captured by CT scans. CryoSEM observed the mucosa interaction of MC, showing the mucus layer embedment of MC with specific orientation, sideways and facing release-side to the mucosa. Lastly, the 3D printed MCs were loaded with the model drug, furosemide, and the cavity was coated with a pH-sensitive polymer of Eudragit[®] L100. An *in vitro* drug release study proved the concept of controlling the drug release.

Finally, the *in vivo* result implied that the micro-pillars might have a slight trend of improved mucoadhesion, but no statistically significant enhancement was found through all of these three designs. However, in this project, we demonstrated that the proposed micro and nanoscale 3D printer is the most suitable tool to realize the innovative geometry of MCs, especially from the aspect of printing resolution, printing volume, and economic benefit. Simultaneously, the broad range force analyzer provides reliable *ex vivo* measurement of MCs mucoadhesive forces. The procedure of 3D printed microdevices incorporated with BaSO₄ particle allows obtaining comprehensive mucoadhesive information via *in vivo* study. Within all these complete and powerful tools, other designs of MCs with “crazy” geometry shapes can be realized to improve the retention time in the intestine in the future.

Resume

Mikrocontainere (MCere) er allerede bekræftet som værende fungerende innovative orale leveringsenheder, der succesfuldt kan levere medikamenter til tarmsystemet. MCer yder beskyttelse imod det barske miljø i maven, samt sørger for en ensrettet medikamentlevering i tarmen, hvilket resulterer i en forøget absorption. Derudover har MCer potentialet til at levere probiotika til tarmens slimlag, mere effektivt sammenlignet med eksisterende teknologier. Dog kan MCer ikke opnå en optimal levering, da gennemløbstiden i tarmen er begrænset. Derudover er frigivelsesorienteringen ukontrollerbar, hvilket mindsker leveringsraten. En potentiel strategi til forlængelse af gennemløbstiden og kontrol af orienteringen, er ved manipulation af MCernes mucoadhæsive egenskaber. Denne afhandling fokuserer på forbedring af mucoadhæsionen via MCernes geometriske strukturer, for dermed at sikre en kontrolleret orientering og en langsommere gennemløbstid gennem mave- tarmkanalen.

For at realisere innovative geometriske designs, har vi specialbygget en 3D printer med mikro- og nanoskala opløsning. Denne printer tillader flere designs og giver mulighed for at inkorporere mikroskala funktioner direkte i MC designet. Denne 3D printer integrerer en HD-DVD optisk pickup enhed (originalt designet til en x-boks spillekonsol), som et optisk kernemodul, til at størkne fotopolymerer. 3D printeren opnår den højeste printeopløsning, på 385nm, ved print i den vandrette retning. Hvilket muliggør massefremstilling af MCer med innovative strukturer og additive funktioner.

Den indledende forståelse for konceptet bag MCers geometriske designs, fås ved undersøgelser af MCers mucoadhæsive kræfter. Dog manglede den nuværende teknik et erfarent og passende instrument til kvantificeringen af mucoadhæsive kræfter under mikro-newton skalaen (det område MCer befinder sig). Derfor var mucoadhesion af en enkelt MC svær at detektere. For at løse dette problem, genanvendte vi en optisk pickup enhed, fra en DVD, til fremstillingen af en måleenhed til et bredt kraftudviklingsområde. Med et nyt design, indeholdende en cantilever kraftudviklings transducer, kunne måleenheden detektere høj-sensitivitets målinger i et kraftudviklingsområde på 1.1 N til 40 nN, med en kraftudviklingsopløsning på 0.99 nN.

Med denne højopløsnings 3D printer og bredt spændende kraftudviklingsmåleenhed, har vi realiseret MCer med innovativ geometri og en efterfølgende måling af den mucoadhæsive kraftudvikling. Tre designstrategier blev implementeret for at øge mucoadhæsionen på tarmens slimhinde. Først designede vi MCer med en asymmetrisk struktur, for at øge sandsynligheden

for at frigivelsessiden blev orienteret mod tarmens slimlag. Derefter printede vi additive mikrosøjler på MCerne for at forøge mucoadhæsionen. Desuden designede vi adskillige pilelignede strukturer på siden af MCeren som, ligesom en krog, kan gribe dybere ind i slimlaget. Et indledende *ex vivo* trækstyrke eksperiment undersøgte mucoadhæsions kræfterne, og bekræftede dermed de designede geometriske figurer. Vha. 3D printeren fabrikerede vi radioaktive MCer med indbygget BaSO₄ nanopartikler, for derefter, i et dertil designet *in vivo* studie, at kunne spore MCerne gennem rotters tarmsystem. Fordelingen af MCer igennem tarmsystemet, kunne identificeres, via plane røntgen skanninger, efter 0.5, 1, 2, og 3 timer. Resultatet indikerede, at selvom de fleste MCer forlod tarmen inden 3 timer, opholdte ca. 50% af MCer med mikrosøjler sig stadig i tarmen på dette tidspunkt. Derudover dokumenterede vi bevægelsesmønsteret af MCer på vej gennem tarmen ved brug af CT skanninger. MCens interaktion med tarmens slimlag kunne identificeres med CryoSEM og illustrerede dermed MCens specifikke orientering i slimlaget; sidelæns og med åbningen vendt mod slimlaget. Derudover blev de 3D printede MCer fyldt med modelmedikamentet Furosemid og åbningen blev forseglet med den pH sensitive polymer Eudragit[®] L100. Et *in vitro* forsøg cementerede evnen til at kontrollere medikamentfrigivelsen.

Endelig viste *in vivo* studiet også, at mikrosøjlerne muligvis har en tendens til forøget mucoadhæsion, dog var der ingen statistisk signifikans ved de tre designs. Dette projekt har dog bevist, at vores mikro- og nanoprinter er det mest anvendelige værktøj til realisering af disse innovative geometriske strukturer på MCerne, særligt i forhold til opløseligheden, op- og nedskalering og det økonomiske incitament. Samtidig giver den bredt spændende kraftudviklingsmåleenhed pålidelige *in vivo* målinger af MCernes mucoadhæsive kræfter. Information om mucoadhæsionen, kan opnås via et *in vivo* forsøg med 3D printede mikroenheder, inkorporeret med BaSO₄ partikler. Med disse komplette og kraftfulde værktøjer, kan også andre MC designs med vanvittige geometriske former realiseres, for at i fremtiden at forøge MCernes opholdstid i tarmen.

Table of Contents

Preface	ii
Acknowledgments.....	iii
Abstract.....	iv
Resume.....	vi
List of abbreviations	ix
List of publications and other contributions	x
1. Introduction.....	1
1.1 Hypothesis and aim.....	2
1.2 Outline of the thesis	3
2. Background.....	4
2.1 Oral delivery system for administration of probiotics and drugs.....	4
2.1.1 Intestinal anatomy	5
2.1.2 Mucus.....	6
2.1.3 Mucoadhesion.....	8
2.2 Microdevices for oral delivery system.....	9
2.2.1 Microcontainers (MCs).....	10
2.2.2 Geometric strategies for enhancing mucoadhesion of microcontainers.....	12
2.3 Mucoadhesion characterization method for microcontainers	14
2.3.1 <i>Ex vivo</i> tensile strength measurement	15
2.3.2 Evaluation of mucoadhesion after animal studies using advanced visualization method....	17
2.4 3D printing in the pharmaceutical field	19
2.4.1 Fused deposition modeling	20
2.4.2 Vat photopolymerization.....	21
2.5 Optical pickup unit (OPU).....	24
2.5.1 Sensing application of optical pickup unit.....	26
2.5.2 Manufacturing application of optical pickup unit.....	27
3. Results and discussion	28
3.1 Micro and nanoscale 3D printing using optical pickup unit from a gaming console.....	28
3.2 Microscale mucoadhesion force analyzer using DVD optical pickup unit.....	33
3.3 3D printed radiopaque microdevices with enhanced mucoadhesion geometry for oral drug delivery	42
4. Conclusion	53
5. Future perspectives	54
6. References.....	55
Appendix.....	68

List of abbreviations

2D	Two dimensional
3D	Three dimensional
AFM	Atomic force microscopy
API	Active pharmaceutical ingredients
CD	Compact disc
CT	X-ray computed tomography
DLP	Digital light processing
EDX	Energy dispersive X-ray
FDA	Food and drug administration
FDM	Fused disposition modeling
FES	Focus error signal
GI	Gastrointestinal
DVD	Digital versatile disc
HD-DVD	High-definition digital versatile disc
MCs	Microcontainers
NA	Numerical aperture
OPU	Optical pickup unit
PBS	Phosphate-buffered saline
PCB	Printed circuit board
PDIC	Photodiodes-intergraded-circuit
PMMA	Poly methyl methacrylate
RMS	Root mean squared
SEM	Scanning electron microscopy
Si	Silicon
SLA	Stereolithography
UV	Ultraviolet
VCM	Voice coil motor

List of publications and other contributions

Publications

Paper 1

Micro and nanoscale 3D printing using optical pickup unit from a gaming console

Tien-Jen Chang, Lukas Vaut, Martin Voss, Oleksii Ilchenko, Line Hagner Nielsen, Anja Boisen and En-Te Hwu

Published on Communications Physics, volume 4, issue 23, 2021

DOI: 10.1038/s42005-021-00532-4

Paper 2

Microscale mucoadhesion force analyzer using DVD optical pickup unit (temporary)

Tien-Jen Chang, Line Hagner Nielsen, Anja Boisen, En-Te Hwu

In preparation – to be submitted to HardwareX

Paper 3

3D printed radiopaque microdevices with enhanced mucoadhesion geometry for oral drug delivery (preliminary)

Tien-Jen Chang, Rolf Bech Kjeldsen, Juliane Fjelrad Christfort, Eduard Marzo I Vila, Tommy Sonne Alstrøm, Kinga Zòr, En-Te Hwu, Line Hagner Nielsen, Anja Boisen (temporary order)

In preparation – to be submitted to Science Advances

Other contributions

3D printed anaerobic and temperature-controlled *in vitro* model enabling real-time release studies with live bacteria

Juliane Fjelrad Christfort, Chrysillis Judy Magaard Polhaus, Pi Westi Bondegaard, Tien-Jen Chang, En Te Hwu, Line Hagner Nielsen, Kinga Zòr, and Anja Boisen

Submitted to HardwareX

HD-DVD Based Microscale 3D Printer

Tien-Jen Chang, Lukas Vaut, Martin Voss, Line Hagner Nielsen, En-Te Hwu, Anja Boisen

Poster at 45th Micro and Nano Engineering Conference (MNE)

September 23 - 26, 2019, Rhode island, Greece

Submicron scale stereolithography using HD-DVD optical pickup unit

Tien-Jen Chang, Lukas Vaut, Martin Voss, Oleksii Ilchenko, Line Hagner Nielsen, Anja Boisen and En-Te Hwu

Poster at SPIE Photonic West 2021

March 6 - 11, 2021, Virtual version

Hacking blu-ray drives for high-throughput 3D printing

Edwin En-Te Hwu, Martin Voss, Tien-Jen Chang, Hsien-Shun Liao, Anja Boisen

Poster at SPIE Photonic West 2021

March 6 - 11, 2021, Virtual version

3D Printed Microdevices for Oral Drug Delivery

Tien-Jen Chang, Martin Voss, Lukas Vaut, Juliane Fjelrad Christfort, En-Te Hwu, Line Hagner Nielsen, Anja Boisen

Poster at 12th World Meeting on Pharmaceutics, Biopharmaceutics and Pharmaceutical Technology

May 11 - 14, 2021, Virtual version

1. Introduction

In the pharmaceutical field, oral delivery is the preferred and most patient-compliant route to deliver both drugs and probiotics [1,2]. When the drugs and probiotics pass through the stomach during the delivery process, some of them will be damaged by the acidic and enzymatic environment [3,4]. Therefore, it can be necessary with oral delivery systems that protect the drugs and probiotics through the stomach and deliver to the intestine where absorption occurs. In the past years, the concept of microcontainers (MCs) has been proposed as an oral delivery vehicle for, e.g., drugs and/or probiotics [5,6]. The MCs are polymeric devices, which protect the delivery content from low gastric pH values and enzymatic degradation. A pH-sensitive polymer can be coated on the cavity of the loaded MCs to isolate the drugs or probiotics and provide a fast release at target site in the intestine [7]. Also, the MCs offer a unidirectional release of the drugs or probiotics directly to the intestinal epithelium, and can therefore, potentially deliver the drugs and probiotics into the mucus layer of the gastrointestinal (GI) tract.

When the drugs and probiotics reach the target site of the intestine, the treatment effect depends on the amount seeded in the intestinal mucus layer [8]. The MCs are the delivery vehicle, so the transit dynamics of MCs are critical. However, the release orientation of MCs is uncontrollable due to their symmetrical structure [9,10]. As a result, only a fraction of the MCs directly faces the release side towards the intestinal epithelium. Besides, the MCs have a fast retention time in the intestine, compromising the delivery rate [11]. A possible way to extend retention and control orientation is by increasing the mucoadhesion of the MCs [10,12]. Mucoadhesive properties of MCs are related to the geometry of MCs, as the structure directly contacts the mucus layer to cause attractive interfacial force. Large contact area of MCs and delicate spike-like additive structure can provide stronger interfacial force and deeper entanglement with mucus, resulting in enhanced mucoadhesion of MCs. However, the present fabrication methods, photolithography [13], hot embossing [14], and hot punching [15], lack the flexibility to form true 3D geometries with overhanging structures.

3D printing technology can realize innovative complex structures [16]. However, current 3D printing techniques are still challenging to realize MCs since no suitable printer possesses high printing resolution and large printing volume at the same time. Advanced two-photon technique reaches a nanoscale resolution to construct a delicate microscale structure, but it comprises a limited printing volume of a few hundred microns and lacks the ability to reach high throughput

[17–20]. On the contrary, stereolithography (SLA) and digital light processing (DLP) have the potential to realize mass production, but they have a commonly smallest printing resolution of approximately tens-of-microns, which is not precise enough to print microscale structures with nanoscale features. As a result, the concept of 3D printed MCs can only be demonstrated in the millimeter scale [10].

1.1 Hypothesis and aim

Hypothesis

For this thesis, I hypothesize that by utilizing an HD-DVD optical pickup unit (OPU) as a core optical component to cure photopolymer layer-by-layer, the nanoscale focal spot of the OPU will achieve micro- and nanoscale 3D printing resolution. Therefore, the 3D printed MCs with microscale overhanging structures will be realized with a large printing volume.

Besides, it is also hypothesized that the innovative microscale structures and resulting enlarged contact area will enhance the mucoadhesion of MCs. Hence, the interaction of the MCs with the intestinal mucus layer will be increased by optimizing the geometry and shape to achieve controlled release orientation and extended intestinal residence time.

Aim

This PhD thesis aims to fabricate MCs with complex structures by a high-precision custom-built micro and nanoscale 3D printer. With the innovative and complex structures, the 3D printed MCs are expected to increase mucoadhesion through optimizing the geometry and shape. To achieve these goals, the project is divided into four parts with the following study objectives:

- Integrate an HD-DVD OPU, a nanoscale resolution positioning system, and a suitable photopolymer to build a micro and nanoscale resolution 3D printer.
- Develop a force analyzer for measuring mucoadhesive forces on a single MC.
- Characterize the mucoadhesive properties of MCs by implementing *ex vivo* and *in vivo* studies.

1.2 Outline of the thesis

This thesis initially introduces the background of oral delivery systems and the role of mucus and mucoadhesion in oral delivery. Then, the microdevices concept is introduced to assist the oral delivery system, including the concept and current development of MCs. Geometric strategies are introduced to enhance mucoadhesion of MCs for optimal delivery. To characterize mucoadhesion of MCs, the related *ex vivo* and *in vivo* study methods are introduced. The 3D printing technique is described as the most suitable way to realize the innovative designs of oral delivery microdevices. Simultaneously, the current bottleneck of high-resolution 3D printing applications in the pharmaceutical field is summarized. Lastly, the development and application of OPU are elaborated.

The result and discussion part will correspond to one published journal article and two manuscripts in preparation. The first article (Paper I) introduces the development of the HD-DVD 3D printer with micro and nanoscale printing resolution for fabricating microscale structures. The second manuscript (Paper II) mentions the development of an OPU force analyzer to achieve a broad range of force measurements from newton to nano-newton. The force analyzer was used for characterizing the mucoadhesion of a single MC in order to evaluate the feasibility of different designs. Finally, the third manuscript (Paper III) describes the MC design and fabrication, followed by *ex vivo* and *in vivo* studies for investigating mucoadhesion of designed MCs. *In vitro* study proves the concept of controlled drug release from 3D printed MCs.

2. Background

2.1 Oral delivery system for administration of probiotics and drugs

Probiotics, live microorganisms, are food supplements that can benefit the host by inhibiting harmful bacteria and improving microbial balance in the GI tract [21–23]. The treatment mechanism and theory of probiotics are still not fully understood [24]. However, through clinical studies, probiotics presented the ability to maintain health and prevent diseases [25]. Probiotics, such as *lactobacillus* and *bifidobacterium*, appeared to be efficient in the treatment of irritable bowel syndrome [26,27]. Patients with allergic rhinitis obtained an improved live quality by ingesting *lactobacillus paracasei* probiotics [28–30]. The GI tract is the largest site for microbiota symbiosis, and most probiotics aim to colonize on the intestinal surface. Hence, an oral delivery system is believed to be the most suitable route to deliver probiotics [2].

Unlike probiotics, which mainly seed on the interior epithelial surface in the GI tract, drugs need to be absorbed into the blood circulation system for obtaining therapeutic effects [31]. Oral delivery of drugs is a preferred way since it is non-invasive compared to other drug delivery routes, e.g., intravenous and subcutaneous injection and the rectal route [1,32,33]. Patients usually have higher compliance to select oral drug delivery route due to no feeling of pain, convenience, and relatively low price [34–36]. Besides, the patients can easily self-administer pharmaceutical compounds via the oral route without professional support from medical personnel [37]. In an oral delivery system, the drug compound is administered from the oral cavity and transited along the GI tract for absorption [38].

The oral delivery route has many advantages, but there are still many challenges that lead to lower bioavailability of drugs and lower delivery rate of probiotics [2,3,33]. The first challenge is the harsh gastric environment. The acidic gastric juice decomposes the food content but also destroys the functionality of drugs and probiotics, when the drugs and probiotics reach the stomach [4,39]. Thus, most drugs and probiotics lose the functionality of therapy before reaching the target site. Even after reaching the target site, the delivery content is immediately released in the lumen in all directions [8]. As a result, less delivery content successfully reaches the surface of the intestine for absorption or colonization. For drugs, the intricate mucus and tight epithelium might be another obstacle for absorption [40,41]. Besides, enzymes might degrade proteins or peptides drugs [42,43]. Therefore, the oral delivery route is unpredictable

for drug absorption rate and probiotics delivery rate. It is a challenge to estimate the effect of treatment [3,44].

2.1.1 Intestinal anatomy

The oral delivery route along the GI tract reaches from the oral cavity and ends in the rectum, and can be divided into esophagus, stomach, small intestine, and colon (**Figure 1**) [45,46]. Usually, the small intestine is the target site for drug absorption. The functionality of the small intestine is to digest food content and absorb nutrition [46]. The human small intestine can be divided into three parts, duodenum, jejunum, and ileum, with a total length of approximately 3 m [47]. The intestinal wall consists of four layers: serosa, muscularis, submucosa, and mucosa [39]. The mucosa is the interface for drug transport into the human body and the site for probiotics to colonize. Hence, drugs and probiotics need to arrive in the lumen of the small intestine for absorption and colonization, respectively. The mucosa comprises tissue (including epithelium, basement membrane, connective tissue), mucus, and mucus hosting microorganisms. A thick mucus layer covers the intestinal mucosa. The epithelial surface of the small intestine consists of numerous villi, which appear as microscale finger-like structures. On each villus, countless micro-villi covers the surface to increase the area [39]. The contact area of a human small intestine can reach 30 - 40 m² [48]. The tremendous contact area significantly enhances the absorption of food nutrition and also drugs. Furthermore, the intestinal muscles provide GI motility to transport the food content in the lumen via peristalsis [39,49].

The colon is usually the target site for delivering probiotics. The colon has a length of approximately 150 cm [50] for absorbing water, electrolytes, and short-chain fatty acids [51–53]. There is no villi structure on the surface of the colon. The surface only contains numerous colonic crypt cells, which secrete mucus and renew the intestine lining.

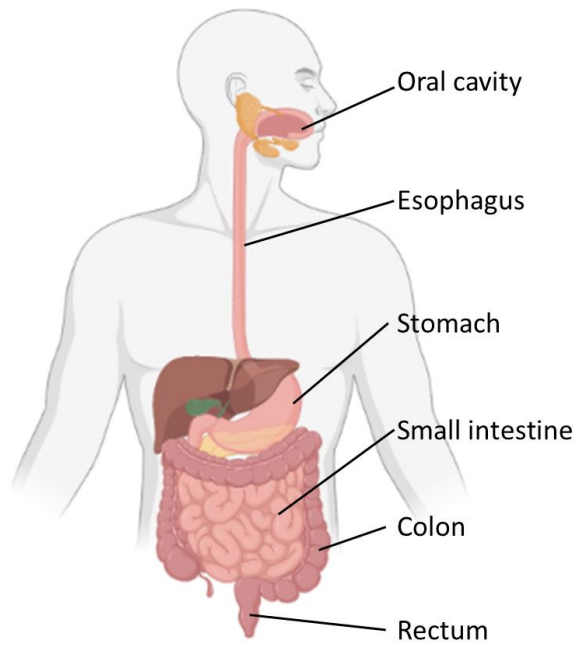


Figure 1. Illustration of anatomy of human gastrointestinal (GI) tract with the oral delivery path orderly from oral cavity, esophagus, stomach, small intestine, colon to rectum. Created with BioRender.com.

2.1.2 Mucus

Mucus is a viscoelastic layer that covers the surface of the stomach, small intestine, and colon, protecting epithelial cells against harmful substances [54,55]. Simultaneously, it provides lubricants for smoothly passing the food ingredient in the lumen. As microorganisms mainly colonize in mucus layer [56], mucus also provides a physical barrier as host defense towards microorganisms. Mucus is secreted from goblet cells of the intestinal epithelium, with approximately 10 liters per day in the human GI tract [55]. The overall composition of mucus includes water (95%), mucin, lipids, proteins, enzymes, salts, electrolytes, and immunoglobulins [57,58]. The mucus layer consists of two parts: loosely adherent and firmly adherent (**Figure 2**) [59]. These two layers vary in thickness in different parts of the intestine. Hence, the thickness of the mucus layer varies along the GI tract [60]. The thickness measurement studies of human intestine are still few since the challenge in measuring *in vivo* [60]. However, thickness data in rats might be close to humans with micrometer scale deviations, revealing a trend of thickness along with the different intestine sites [61,62]. In the duodenum and jejunum of rats, the mucus layer thickness is estimated to be approximately 120-200 μm [59]. The ileum and colon have a relatively thicker mucus layer, reaching approximately 450-950 μm .

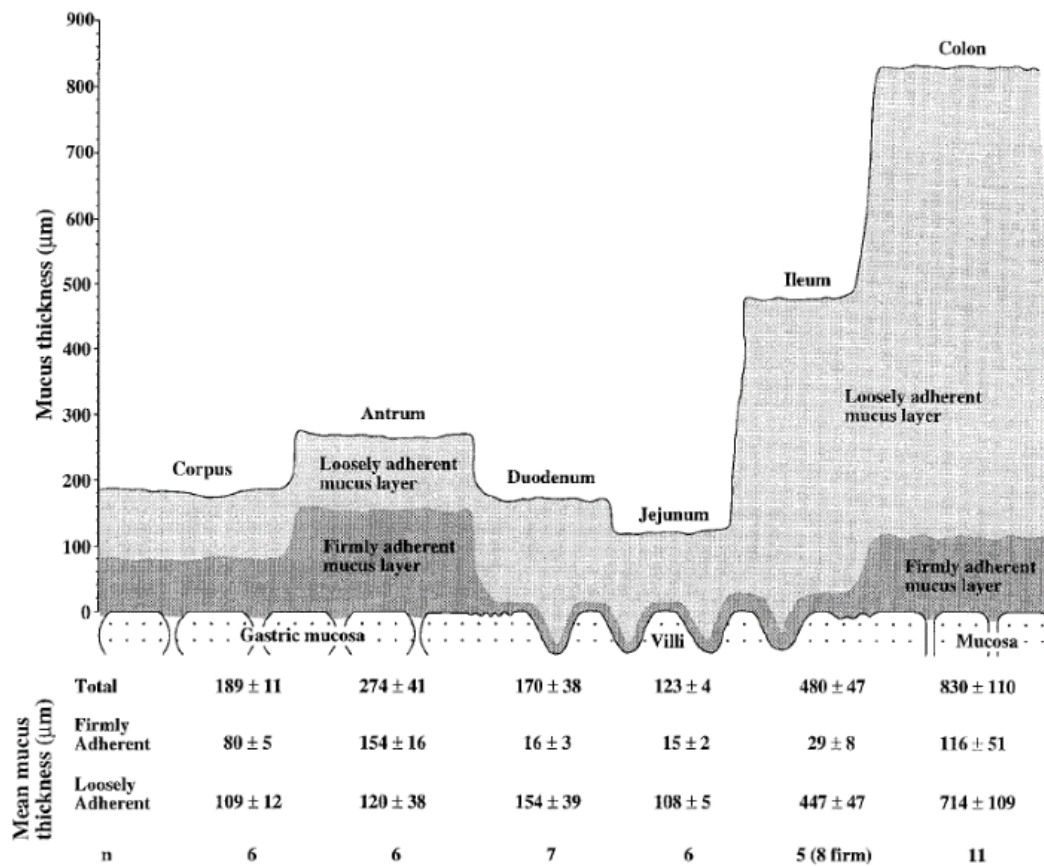


Figure 2. Schematic presenting the thicknesses of the loosely adherent and firmly adherent mucus layers *in vivo* in different sites of the rat gastrointestinal (GI) tract from corpus to colon [59]. The duodenum and jejunum comprise a total mucus layer thickness in the range of approximately 120 to 200 μm , while the ileum and colon have a relatively thick mucus layer of approximately 450 to 950 μm . Reprinted with permission from publisher.

The mucus is constructed by the mesh structure of mucin fiber (**Figure 3A**) [55,63]. Mucin is a glycoprotein that consists of an O-linked glycosylated polypeptide backbone (**Figure 3B**) [58,64]. The O-linked glycosylated polypeptide consists of a peptide core and O-glycosylated oligosaccharide. The polypeptide core is connected to link monomers of mucin together in a folded structure. On the oligosaccharide chains, the monosaccharides residuals contain negatively charged sulphate or carboxyl end groups, resulting in a negatively charged mucin mesh structure [54,57].

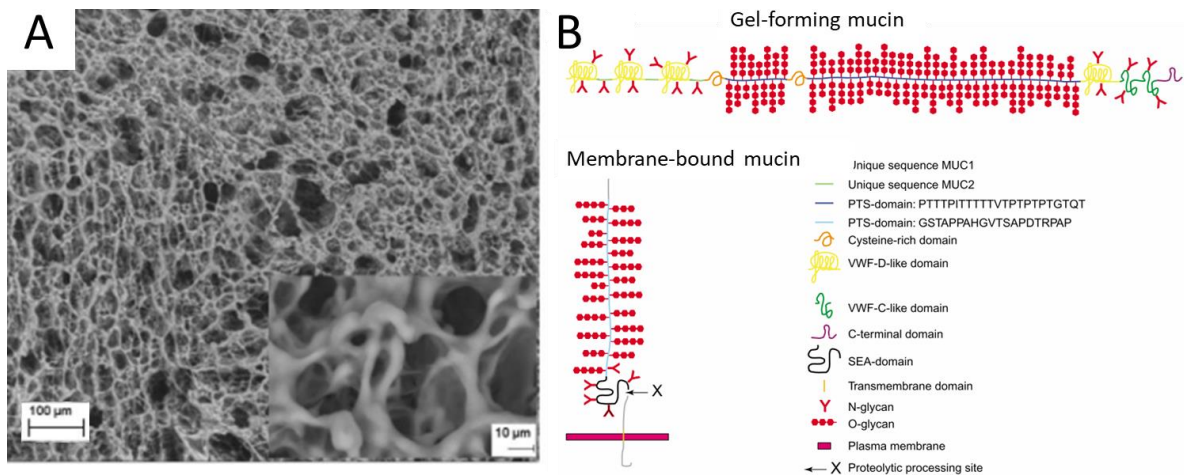


Figure 3. A) SEM image of pig ileum mucosa shows mucus mesh structure with tens of microns size holes [65]. B) Illustration of mucin structure [66]. A) Shared under a Creative Commons Attribution 4.0 International License, and B) reprinted/adapted with permission from publisher.

2.1.3 Mucoadhesion

Mucoadhesion is a term for representing the tendency of two materials, at least one of which is biological mucus, to cling together by interfacial forces [12,67]. The mucoadhesion consists of two major stages: the contact stage and the consolidation stage [57,64]. In the contact stage, the contact of the mucosal surface induces mucoadhesive interaction. During the consolidation stage, the adhesive bond is consolidated to entangle the surface with the mucus mesh structure. However, the mechanism of mucoadhesion is not fully understood. Various complex processes might attribute to the mechanism. Currently, mucoadhesion is explained by six theories [12,68].

The electronic theory: While a contact of the mucosal surface occurs, an exchange of electrons between two contact surfaces forms an electrical double layer with opposite charges. The attracting force of opposite charges contributes to the adhesive effect [57,68].

The wetting theory: The surface energies of components influence their ability to spread over the mucosal surface. Therefore, a higher mucoadhesion can be reached by the ability of components themselves. This theory is more applicable for the liquid mucoadhesive system with low viscosity [57,68].

The diffusion theory: The interpenetration between mucoadhesive polymer chains and mucus cause the adhesion. This occurs along a concentration gradient affected by the length and mobility of the molecular chains [57,68].

The mechanical theory: Adhesion is caused by a mechanical interlocking, which occurs while the mucoadhesive components penetrate into irregularities of the rough surface. The adhesion

can be further improved by increased surface roughness and enhanced viscoelastic and plastic properties [57,68,69].

The absorption theory: Adhesion of mucus is mainly contributed by chemical interaction, such as hydrogen bond, Van Der Waals forces, and covalent bonds [57,68].

The fracture theory: This theory is usually for the study of the mechanical measurement of mucoadhesion. It evaluates the mucoadhesive forces needed to detach the sample from the mucus after adhesion occurs. This theory is suitable for analyzing a single and uniform material with known dimensions [57,68].

2.2 Microdevices for oral delivery system

Benefited from advanced microfabrication techniques, microdevices were realized and proposed to aid the oral delivery of drugs in the past decades [13,70,71]. The microdevices each carry a small portion of active pharmaceutical ingredients (API). Through the administration of a number of microdevices, equal efficacious of a centimeter-scale tablet can be reached. Unlike the conventional tablets where drug is released in all directions, microdevices are usually designed to sustainably release with a unidirectional release, hopefully towards the surface of epithelium (**Figure 4A**) [13,72]. Microdevices can engulf themselves into the mucus layer and efficiently release drugs to the epithelium. Therefore, microdevices may improve the drugs absorption rate and oral bioavailability, especially for poorly water-soluble and poorly permeable drugs [13]. For example, flat disk-like microdevices with multiple cavities were fabricated by photolithographic processes to achieve a unidirectional release of drug and enhanced bioavailability (**Figure 4B**) [73,74]. Rectangular single-reservoir microstructures were fabricated by soft-lithographic processes for drug delivery (**Figure 4C**) [75]. Hot embossing fabricated microwells were demonstrated oral drug delivery of furosemide (**Figure 4D**) [7]. Finally, the microscale dimension of devices will not obstruct the GI passage and can be excreted by mucus turnover and GI motility after delivery.

In addition to purely carrying drugs, microdevices can also be designed with some innovative multi-function to overcome delivery barriers, e.g., protection of drugs, control of release profile, target specific intestinal site release, and self-encapsulation [70,76]. Recently, a microstructure made of bilayered material can self-fold to encapsulate compounds for drug delivery [75].

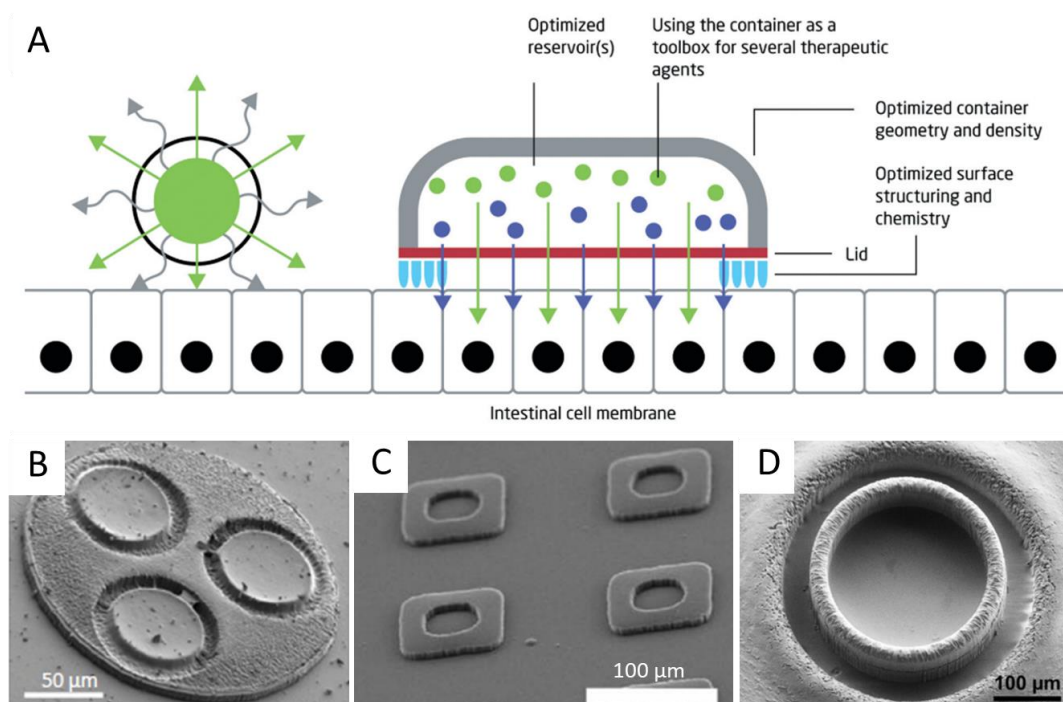


Figure 4. Microdevices for oral drug delivery. **A)** Diagram showing microdevices release drugs towards intestinal epithelium and conventional drugs are released in all directions in the GI tract. [13] **B)** Microscale disk-like structure with three cavities for unidirectional release of drugs [73,74]. **C)** Single-reservoir microstructures fabricated by soft-lithographic processes for drug delivery [75]. **D)** Hot embossing fabricated microwells were demonstrated oral drug delivery of furosemide [7]. Reprinted/adapted with permission from respective publishers.

2.2.1 Microcontainers (MCs)

MCs are polymeric microdevices for oral delivery (**Figure 5A**) [5,77]. MCs are originally designed as a cylinder structure of 320 μm in diameter and 250 μm in height, with a cavity on one side for loading and releasing drugs and probiotics. Hence, MCs can provide a unidirectional release of drugs through the GI tract, effectively increasing drug delivery rate and absorption. Besides, a pH-sensitive lid can be coated on the cavity to seal the drug, avoiding the harsh environment of stomach destroying the drug and probiotics, and release the delivery content to the specific site along the GI tract [7]. MCs have already shown the capability to increase oral bioavailability of the poorly water-soluble drug, e.g., furosemide and ketoprofen [5,78]. Additionally, they presented promising performance of delivery of probiotics [6], insulin [79,80], lysozyme [81], vaccines [82], and antibiotics [83].

MCs have been mainly fabricated by a photolithography method, which utilizes a UV mask for selectively exposing the negative epoxy-based photoresist SU-8, thereby building up hollow structures [13]. The photolithography process consists of one or more cycles, each consisting of spin coating, solvent bake out (soft bake), UV exposure for initiating cross-linking and post exposure bake (PEB). After the final PEB step, the structures are developed to obtain thousands

of highly monodisperse delivery devices (**Figure 5B**). To move towards the use of biodegradable materials, hot embossing [14] and hot punching methods [15,84] were utilized for mass-producing MCs. Poly lactic-co-glycolic acid (PLGA) and poly- ϵ -caprolactone (PCL) were hot punched by a nickel stamp to form the structure [85]. The result demonstrates that the structure could be degraded after several weeks. Both the photolithography and hot embossing method mass-produce MCs efficiently. However, as subtractive manufacture, these methods cannot achieve an arbitrary 3D structure design of MCs, such as overhanging structure.

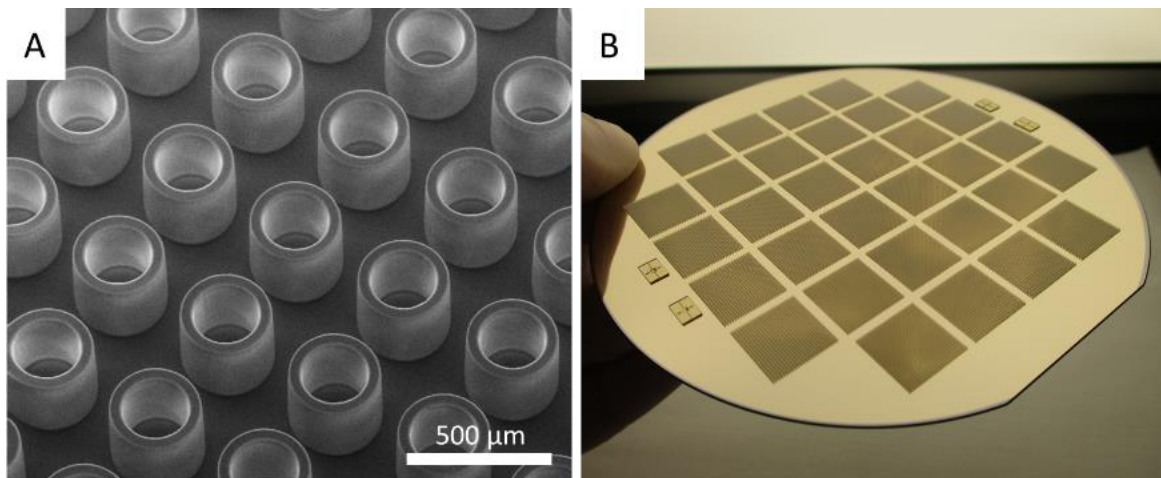


Figure 5. Microcontainers (MCs) **A)** SEM image of SU-8 MCs fabricated by a photolithography process, with a dimension of 320 μm in diameter and 250 μm in height. **B)** Photograph of a total of 20000 MCs on a 4-inch Si wafer. On each 12.8 \times 12.8 mm^2 square, 625 MCs were fabricated in a 25 \times 25 array.

The fabricated MCs undergo further processes, including loading content, coating lid, detaching from a substrate, and capsule filling (encapsulation), as shown in **Figure 6**. To fill the delivery content inside the MCs, many loading methods have been developed, such as manual powder filling [13,86], hot punching [87–89], supercritical impregnation [90,91], powder embossing [92], and inkjet printing [93]. These methods possess specific advantages, such as high throughput, reduced waste, efficiency, or simplicity. Meanwhile, they have specific process parameters and conditions, such as high temperature, high pressure, liquid form, limiting the type of loaded content. For filling with probiotics, because probiotics are usually prepared as powder form and sensitive to temperature, the manual powder filling method is more suitable.

While loading compounds into the MCs by manual powder filling, a metal or PDMS-based mask covers the MCs to expose only the cavity and shield the space between MCs [94]. The mask reduces the waste of delivered content since it prevents loading in between the MCs.

Then a brush is used to fill and compact the powder and an air gun for blowing the residual powder away. After the drug or probiotics have been loaded, the metal or PDMS shadow mask is removed.

An ultrasonic spray coater is used to uniformly spray a polymer to cover the cavity with a few microns of each layer [5,7]. By repeating the layer coating process, the thickness of the lid can be controlled to seal and protect the MCs. After the preparation steps, the MCs are detached from the substrate and loaded into a suitable capsule for oral delivery usage.

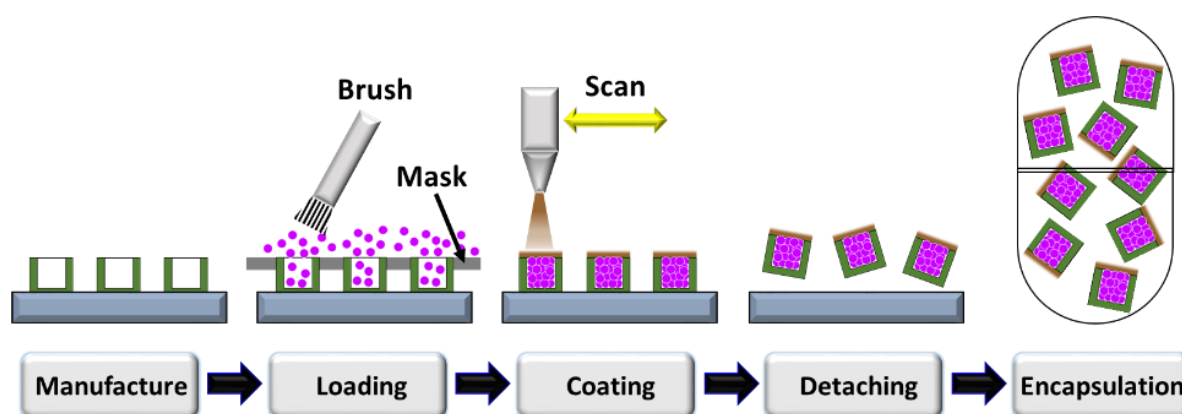


Figure 6. Schematic of microcontainers (MCs) preparation process, including manufacture, drug loading by manual powder filling, lid coating using spray coater, detaching MCs from the substrate, and encapsulating MCs into a capsule.

2.2.2 Geometric strategies for enhancing mucoadhesion of microcontainers

MCs provide a unidirectional release, however, they usually take a random orientation in the GI tract due to their symmetrical structure, making it difficult to ensure release towards the epithelium [9,10]. Furthermore, the retention time of MCs is also difficult to increase. To achieve a longer retention time and direction control for MCs, mucoadhesion enhancement is an option [95].

A strong mucoadhesion of the microdevices is crucial since more substantial mucoadhesion has the potential to assist microdevices to stay longer on the mucus layer [95,96]. Thus, the microdevices will not be lost in the lumen or blended into digest content. As a result, drug absorption rate and probiotics colonization could be improved [97]. There are many feasible strategies to increase mucoadhesion, including geometry, surface topography, biochemical surface modification, and mucoadhesive polymer coating [95,98]. Recently, microcontainers coated with mucoadhesive material, such as chitosan and polyethylene glycol (PEG), were presented three times enhancement of mucoadhesion via an *ex vivo* flow-through study [81].

However, this promising result did not significantly increase drug absorption via an *in vivo* study [99].

The geometry structure of MCs plays an essential role in the transit process since the structure directly interacts with the mucus layer. The larger the contact area the more is the interfacial force between the device and mucus increased, leading to enhanced mucoadhesive properties [95]. Besides, the structure sustains the force from the fluid flow in the intestine [95]. Some different geometry designs were recently proposed for enhancement of mucoadhesion, e.g., triangular and squared (**Figures 7A and B**) [100]. The squared MCs exhibited a more pronounced mucoadhesion compared to the other designs. Besides shape, the size of microdevices might also be matter. Different heights of MCs were investigated via an *ex vivo* study, demonstrating that the high and short MCs behave in significantly different postures on the mucosa [9]. Flat inkjet printed microdevices were fabricated with different sizes from 200 to 450 μm in diameter to compare transit mechanisms *in vivo* (**Figure 7C**) [101,102]. The 450- μm -diameter design showed a broader distribution and longer retention in the GI tract compared to other smaller devices.

Furthermore, delicate complex structures increase mucoadhesive properties of microdevices, as the fine structures can entangle with the mucin mesh structures for increasing contact area. For example, nanoscale structures, such as straw-like pillars and fibers, were utilized to cover the surface of microdevices for increasing adhesion (**Figures 7D and E**) [103,104]. Shape-changing microdevices used microscale hook structures to directly grip and firmly adhere on the mucus layer, leading over 24 h retention time in the colon (**Figure 7F**) [105].

To assist devices with the direction of drug release, anchor structures were proposed as additive features on the release side of devices (**Figure 7G-I**) [10,106]. The branch-like structures significantly enlarge the contact area to mucus. In addition, these delicate structures protrude in all directions, leading to deep entanglement with the mucus layer and even with the villi structure of the small intestine. These innovative designs of geometry were proved an enhanced mucoadhesion via *ex vivo* studies. These overhanging features were produced by 3D printing method. However, limited by 3D printing resolution, these ideas were realized in millimeter-scale, lacking the support evidence for validating the same effect in micrometer-scale devices. Simultaneously, the millimeter-scale dimension is a challenge for passing the devices through the rat GI tract. Hence, the concept is not validated by *in vivo* studies.

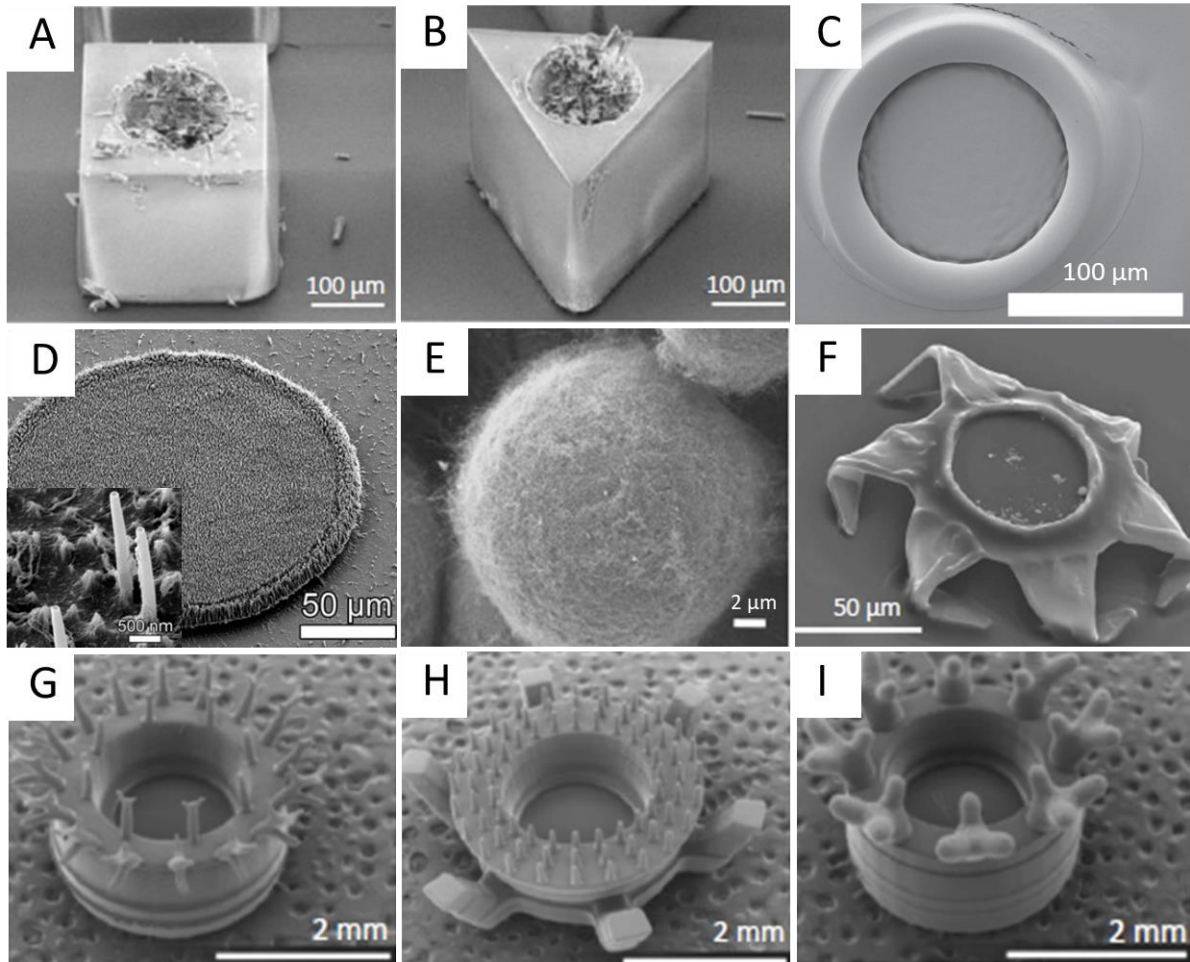


Figure 7. Geometric features modification of microdevices for the improvement of mucoadhesion. *In situ* rats study investigated the mucoadhesion of MCs with **A)** square and **B)** triangle design, showing more retained square MCs in the colon of rats [100]. **C)** Planar round microdevices with an optimal dimension of 450 μm in diameter to extend retention time in the rats GI tract [101,102]. **D)** Seal microdevices with nanoscale straw shape feature for enhancing adhesion to mucosa [103]. **E)** Nanoscale wire cover on silica microdevices for strengthening mucoadhesion [104]. **F)** Star-shape-like microdevices actively bend the hook structures to firmly adhere to colon mucosa for up to 24 h [105]. **G)-I)** Millimeter-scale cylinder-reservoir devices with complex anchor-like structures for concept demonstration of enhancement of mucoadhesion via *ex vivo* tensile strength measurement and *ex vivo* flow-through method [10]. Reprinted/adapted with permission from respective publishers. A), B) and D) shared under a Creative Commons Attribution 4.0 International License.

2.3 Mucoadhesion characterization method for microcontainers

To evaluate the mucoadhesion of oral delivery system, an *ex vivo* flow-through method and an *ex vivo* tensile strength method are the intuitive ways to investigate the interaction between the mucus layer and the device [97]. Both have already been used for illustrating the mucoadhesion of plenty of oral delivery devices [9,10,107]. These *ex vivo* methods rely on small segments of fresh intestinal tissue extracted from pigs. However, these small tissue segments cannot represent the whole intestine, as most crucial factors (temperature, pH value, moisture) and mucus properties are variant in the GI tract [60,108]. These models also lack the real GI tract

motility and the transit mechanism. Hence, *in vivo* animal studies play a vital role in comprehensive understanding and validation of mucoadhesion measurements.

2.3.1 *Ex vivo* tensile strength measurement

The *ex vivo* tensile strength method directly quantifies the mucoadhesive forces of a single device by mechanical force measurement [109]. This method usually relies on a tensile force analyzer consisting of a force detection module and a vertical moving module (**Figure 8A**) [110]. The force detection module measures the mucoadhesive forces along the vertical direction while the moving module moves the device to contact the mucus. The recorded force and displacement data are plotted to a force-displacement curve which shows the interaction between the mucus and the device (**Figure 8B**) [111]. The procedure usually consists of two parts, approaching and withdrawing. In the approaching process, the moving module approaches the device to attach the mucus layer at a constant speed. The attachment is held for a given contact time while reaching a given contact force as the resistance between the device and the mucus layer. Then the moving module withdraws the device from the mucus layer for detachment with a constant speed (usually the same as approaching speed). During the withdrawing process, the mucus layer continuously adheres to the sample, showing increasing mucoadhesive forces till reaching a maximum peak force, F_{max} (**Figure 8B**). After peak force, the mucus detaches from the sample, reducing the mucoadhesive forces. The peak force is usually utilized for the comparison of mucoadhesion. Simultaneously, the area between the force curve and the coordinate axis in the withdrawing process represents the working energy of adhesion, W_{ad} .

The tensile strength technique is simple, but many factors and parameters influence the experimental results. From the instruments aspect, contact time, contact force, and speed need to be considered for optimizing measurements [112]. In general, the mucus sample conditions, such as pH value, viscosity, and thickness, exist relatively large variations [113,114]. This variation usually affects the measurement of the mucoadhesive forces. Additionally, the environmental parameters, such as temperature and relative humidity, also influence tissue behavior. Sometimes, the environment directly influences tissue hydration or dehydration, affecting the measured mucoadhesive force outcome. Therefore, experiment design and parameters control are critical.

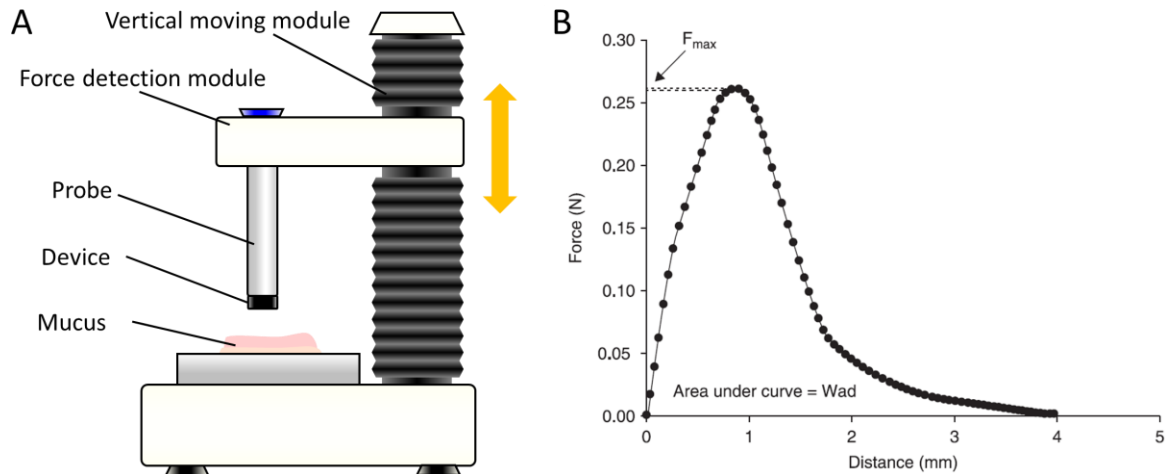


Figure 8. *Ex vivo* mucoadhesive force by tensile strength measurements. **A)** Schematic of tensile strength measuring instrument consisted of force detection module and vertical moving module. **B)** Mucoadhesive force-distance curve while withdrawing a sample from the mucosa, showing a maximum peak of mucoadhesive forces, F_{max} , and working energy of mucoadhesion, W_{ad} (area between force curve and axis) [111]. B) Reprinted/adapted with permission from publisher.

The force detection module is the major component during tensile force measurement, as it defines the force measuring range and resolution. Within the pharmaceutical field, texture analyzer is the most widely used instrument for detecting mucoadhesive forces required to detach samples from intestinal tissue [109,115]. This instrument provides measurements in the force range from few newtons to few milli-newtons. However, the mucoadhesive force of the MCs is generally at the micro-newton scale. To measure the mucoadhesive force of MCs, an instrument with increasing force measurement sensitivity and resolution is needed. Upgrading the force detection module of the texture analyzer could potentially increase force resolution. However, the moving module of the texture analyzer causes a relatively large degree of vibration to micro-newton scale force measurement, leading to significant signal noise, which seriously interferes with the force resolution [115].

To increase the measuring sensitivity of mucoadhesive force, atomic force microscopy (AFM) was modified to investigate the interaction of mucus and microparticles (**Figure 9A**) [65]. The AFM achieved nano-newton scale force measurement through a highly sensitive optical module and a micro-cantilever with high stiffness (**Figure 9B**). Nevertheless, limited by the fragile microscale cantilever, the AFM only carried a sample size with a maximum of tens of micrometer particles.

Apparently, the current mucoadhesive forces measuring method cannot provide a reliable measurement of mucoadhesive forces at the micro-newton scale. Other commercial microscale

tensile force instruments might potentially be repurposed for this request. However, most of these costly equipments are not open source, resulting in difficulty modifying to customized function [116].

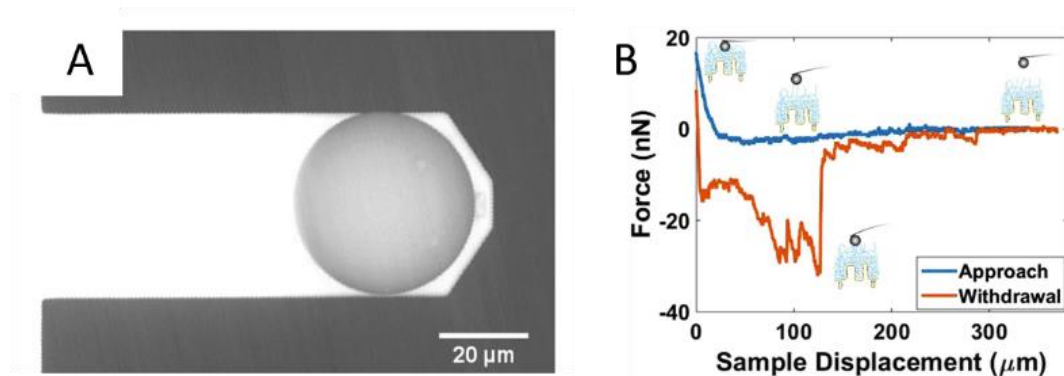


Figure 9. Modified atomic force microscopy (AFM) system for measuring mucoadhesion of microparticles at nano-newton scale *ex vivo*. **A)** A micro-cantilever carried a single spherical silica particle with a diameter of 40 μm on its free end using an epoxy adhesive [65]. **B)** The force-sample displacement curve was obtained by approaching and withdrawing the microparticles on pig ileum mucosa [65]. Shared under a Creative Commons Attribution 4.0 International License.

2.3.2 Evaluation of mucoadhesion after animal studies using advanced visualization method

In vivo animal studies directly validate the performance of microdevices of drugs absorption and bioavailability through blood sampling, but can also provide comprehensive information on the retention time of microdevices [97]. The mucoadhesive properties can be evaluated by analyzing the retention and transit time of the microdevices along the GI tract. To obtain precise data, visualization methods play a crucial role in investigating the retention and quantifying the distribution of microdevices along the GI tract at various time points.

With the help of advanced microscopy, the local intestinal retention of microdevices can be observed after *in vivo* studies. Recently, shape-changing microdevices were validated enhance mucoadhesion to the colon mucus for over 24 h retention using SEM (**Figure 10A**) [105]. An *in situ* closed-loop perfusion technique was used to investigate the mucoadhesion of MCs. The *in situ* way utilized a rat colon section to observe the retention of MCs [100]. After sacrificing the animal, the remaining MCs on intestinal tissue were manually counted using optical microscopy, demonstrating the more mucoadhesive property of cubic MCs (**Figure 10B**).

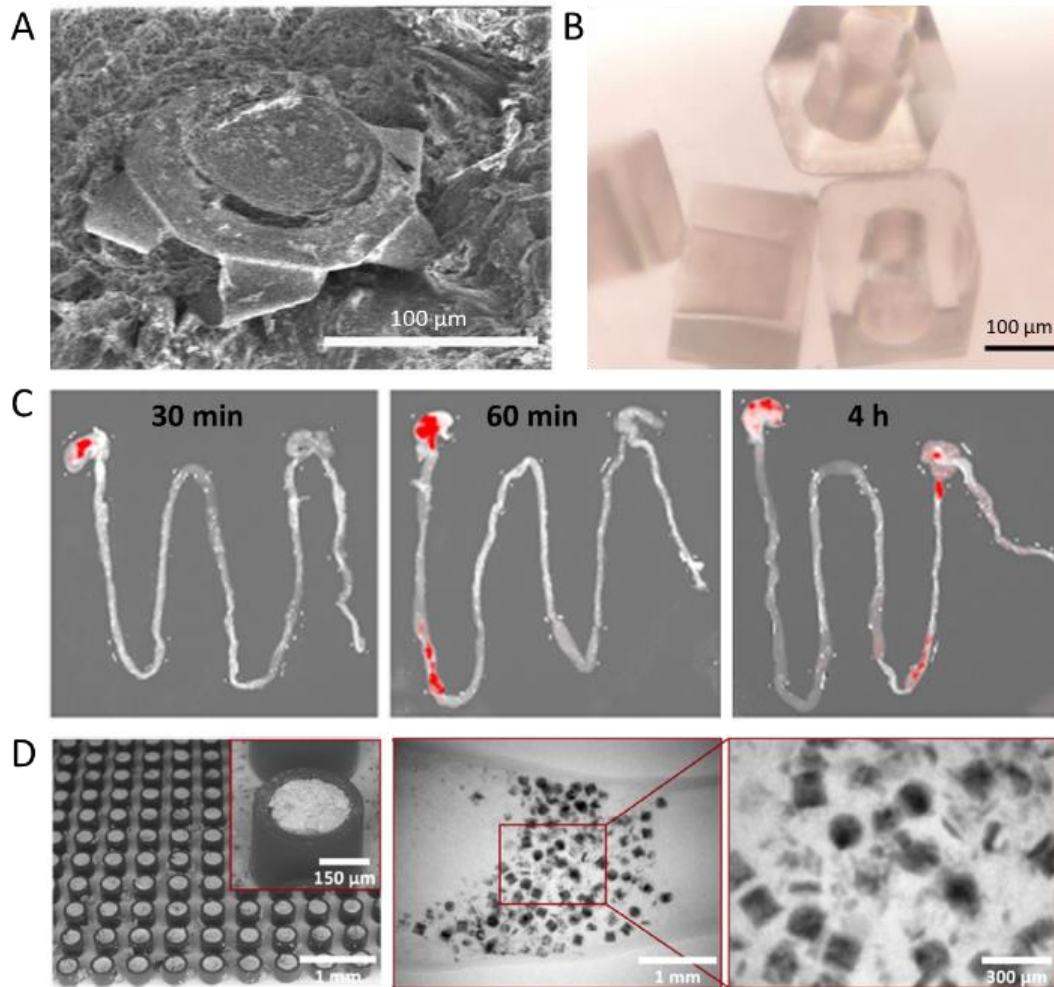


Figure 10. *In vivo* study for investigating mucoadhesion of microdevices. **A)** SEM image shows gripper microdevices adhere to the colon mucosa for up to 24 h [105]. **B)** The result of *in situ* closed-loop perfusion technique shows that the cubic microcontainers (MCs) (with square shape) present significantly stronger mucoadhesion [100]. **C)** Distribution of microdevices with fluorescent polymer conjugate along rat gastrointestinal (GI) tract at different time points shows the transit mechanism and retention of microdevices [101]. **D)** SU-8 MCs filled contrast agent, BaSO₄, presents high contrast visual effect in the intestine [11]. Reprinted/adapted with permission from respective publishers, and A) and B) shared under a Creative Commons Attribution 4.0 International License.

Nevertheless, microscopy is challenging to quantify the distribution of microdevices through the entire GI tract. While the GI tract is long, and the microdevices are often embedded inside the mucus layer or shielded by food content, manual counting with microscopy is time-consuming and hard to distinguish microdevices from the tissue. Furthermore, opening the intestine with scissors or knife usually destroys the microdevices.

To observe the distribution of microdevices through the entire GI tract, techniques for strengthening the visual effect, such as imaging contrast of microdevices, can facilitate the investigation process [97]. The fluorescent polymer conjugate could provide a photo signal

through the GI tract (**Figure 10C**). This method overviewed transit movement and distribution of microdevices at different time points [101]. A contrast agent, BaSO₄, was manually filled inside the MCs for X-ray images (**Figure 10D**). The MCs were distinguished with high contrast images in the GI tract [11]. An overview of the distribution of MCs was obtained by planar X-ray image. Although filling the BaSO₄ powder compromises the loading capacity of drugs, it provides a preliminary study of mucoadhesion of microdevices itself.

2.4 3D printing in the pharmaceutical field

3D printing is a term for a series of additive manufacturing techniques, constructed stereoscopic structure by the sequential additive deposition or combination of material, mainly with a layer-by-layer form [16]. As a revolutionary manufacturing technique, 3D printing has had an obvious growth in research and application of oral drug delivery in recent years [117]. Especially in 2015, the first FDA-approved 3D printed tablet, Spritam® (Aprecia Pharmaceuticals), revealed a new possibility for drug manufacturing [118]. This trend attributes to several advantages of the 3D printing technique. The primary benefit is that 3D printing allows more flexibility of geometric design than conventional drug manufacturing processes, e.g., granulation, coating, and extrusion. [119]. The layer-by-layer forming process can realize arbitrary 3D printing structures of drugs [120]. These structures achieve various functionality for improving treatment, e.g., tunable release profiles, extended GI retention, and target site release, rather than immediately release at an unspecific site [119]. For example, Kyobula *et al.* 3D printed complex honeycomb-like tablets with various mesh sizes for controlling drug release [121]. Besides, the 3D printing technique can fabricate a prototype in one process in a short period of time. The rapid prototyping significantly shortens the cycle time of drug formulation development [122]. In addition, without the need for expensive mold or other accessorial components, the 3D printing technique saves the cost and material, reaching the economic effect for the pharmaceutical market [122]. However, the printing speed might hinder manufacturing capacity for mass production. Nevertheless, 3D printing can produce small batches of drugs at a practical cost. Thus, 3D printing has a great potential to customize or personalize drugs for individual demands, e.g., multiple drugs with customized ratios, rather than the outdated concept of "one-size-fits-all" [119]. Recently, a single tablet consisted of five drugs was printed to demonstrate the potential for personalized tablets [123]. Finally, 3D printing can achieve novel delivery mechanisms by innovative structures and novel dosage concepts of personalized drugs within an acceptable cycle time and competitive cost.

For the application of oral drug delivery, plenty of 3D printing methods were proposed. In general, these methods can be classified into four main types of processes: material extrusion process [124,125], powder bed fusion process [126–128], material or binder jetting process [129], and vat photopolymerization-based process [16,119]. Each method is based on different manufacturing theories and techniques. Hence, the material property, printing resolution, surface topography, and material selection might lead to huge variations. The selection of a suitable technique is usually done according to the need of the application.

2.4.1 Fused deposition modeling

Fused deposition modeling (FDM) is the preferred 3D printing technique in the pharmaceutical field due to its simplicity, and low cost, ease of use. FDM is classified as the material extrusion process, as the FDM printer extrudes a polymeric filament through a nozzle and follows a series of 2D patterns to deposit the material layer-by-layer [130]. The API can be load into 3D printed devices for functional release. Recently, a tablet with a hollow mesh structure for carrying drug particles was 3D printed with a Eudragit lid to delay the release of drugs at target sites (**Figure 11A**) [131]. A dual compartment dosage tablet was printed to physically isolate drugs and modulate release profile (**Figure 11B**) [132]. In addition, the API can also be mixed into the filament by a hot-melt extrusion process [133]. For example, a dual nozzle FDM printed two materials into a shell-core tablet embedded with API (**Figure 11C**) [134]. Furthermore, FDM printed electronic devices with drug-carrying modules for controlling gastric residents, and remote diagnosis and treatment (**Figure 11D**) [135]. However, the drawback of FDM might be the low printing speed and low printing resolution (minimum feature size is 0.3 mm). Also, as its filament heating process might destroy the functionality of API, the temperature usually needs to be considered and optimized for compatible polymer or drugs.

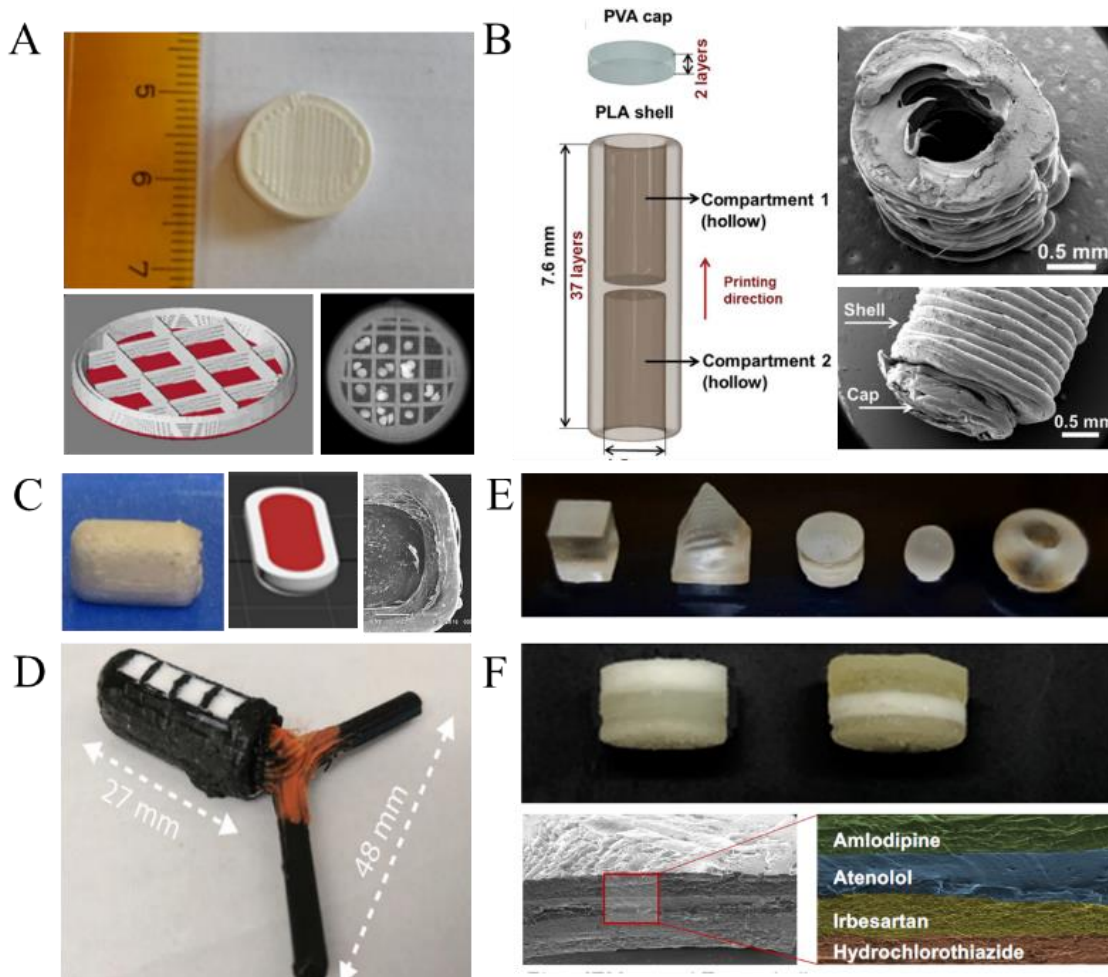


Figure 11. 3D printing for pharmaceutical application. **A)** Fused disposition modeling (FDM) 3D printed tablet with mesh structure for carrying active pharmaceutical ingredients (API), and a Eudragit lid for delayed releasing at a specific target site [131]. **B)** Dual compartments tablet for carrying multiple drugs with physical isolation and controlling release profile using FDM [132]. **C)** Multiple material 3D printed shell-core delayed-release tablet by dual nozzles FDM [134]. **D)** FDM printed gastric resident electronic with drug delivery module for prolonged stomach retention and remote diagnosis and treatment [135]. **E)** Stereolithography (SLA) printed tablets with different geometry shapes for investigating the release profile [136]. **F)** SLA printed multiple drugs tablet in layer form for co-delivery [137]. Reprinted/adapted with permission from respective publishers. D) and F) shared under a Creative Commons Attribution 4.0 International License.

2.4.2 Vat photopolymerization

Vat photopolymerization can further solidify sophisticated structures of drugs by its high printing resolution from tens of microns to hundreds of nanometers [119]. Hence, it has the potential to fabricate complex structures of microdevices. The first vat photopolymerization type 3D printer was proposed in the 1980s [138,139]. The vat photopolymerization can solidify liquid-form photo-sensitive polymers (also called photopolymer) [16]. The photopolymer mainly consists of monomers, initiators, and obligators. While exposed to light with active wavelength, usually UV light, the initiator connects the material into the solid form [140]. The smallest printing volume, voxel, is utilized to describe the printing resolution in the XYZ

directions. The voxel size is influenced by the light energy distribution [141–143]. The width of voxel V_w and the depth of voxel V_d are theoretically defined as

$$V_w = W_0 \cdot \sqrt{2 \cdot \frac{V_d}{D_p}} \quad (1)$$

$$V_d = D_p \cdot \ln(E_0/E_c) \quad (2)$$

where W_0 is the light beam radius; D_p is the laser penetration depth in the photopolymer; E_0 is the laser energy on the photopolymer surface; E_c is the threshold energy for photopolymerization.

Exposing the light spot on each assigned location along the lateral direction on a plane, a layer of 2D pattern can be realized. Through printing layer-by-layer, a 3D structure can be constructed. After the printing procedure, the residual photopolymer must be washed with solvent, usually ethanol or isopropanol. Then the structure is placed into a light chamber (with active wavelength) for post-curing to solidify completely.

The vat photopolymerization mainly consists of SLA [144], DLP [145], and two-photon [19,20] methods. The SLA focuses a light spot in the photopolymer, and raster scans the spot by a scanner (**Figure 12A**) [146]. Typically, the SLA can reach a resolution of around 30 μm [147]. Recently, tablets designed with different geometry shapes were printed by an SLA 3D printer to investigate the release profile of drugs (**Figure 11E**) [136]. SLA printer can also fabricate a tablet with multiple drug dosages in layer form through a complex procedure (**Figure 11F**) [137]. To further increase the printing speed, DLP utilizes a digital micromirror device to project an image with a numinous of binary pixels rather than raster scanning a single light spot (**Figure 12B**) [146]. Hence, DLP can significantly increase printing throughput.

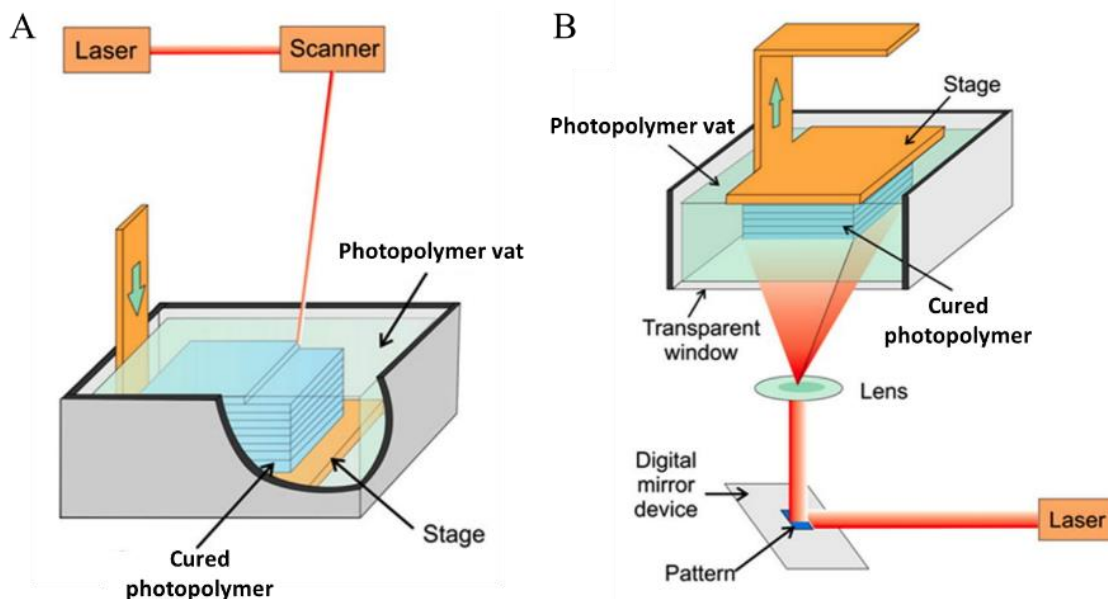


Figure 12. Illustration of vat photopolymerization-based 3D printing technique. **A)** Stereolithography (SLA) scans the laser beam along the lateral direction to cure photopolymer in vat layer-by-layer [148]. **B)** Digital light processing (DLP) utilizes a digital micromirror device to expose a 2D pattern upward to cure photopolymer in vat layer-by-layer, significantly shortening the printing cycle time [148]. Reprinted/adapted with permission from publisher.

A disadvantage of the vat photopolymerization-based drug formulation printing is the limited material selection, as most photopolymers might have health risk issues, e.g., high irritancy [149]. However, with the increasing development of biocompatible photopolymers, more applications of drugs formulation can be realized. Recently, Formlabs released a new biocompatible material, Biomed clear (certificated by the USP Class VI), and claimed this material is suitable for long-term mucosal membrane contact [150,151].

The SLA and DLP increase the printing resolution to fabricate fine structures and overcome the printing speed issue. However, their printing resolution is still not high enough to fabricate microdevices with intricate microscale features. In the case of MCs, only millimeter-scale size can be realized [10,152]. The emerging breakthrough technique, two-photon 3D printer, can realize complex and delicate features by its nanoscale (100~160 nm) printing resolution [20,153]. The two-photon 3D printer integrates a femtosecond laser to reach an extra small focal spot size, breaking the light diffraction limit. Also, the two-photon effect controls the depth of the focal spot in the nanometer scale along the axial direction. Hence, the two-photon printer can reach nanoscale voxel size in all directions. The two-photon 3D printer has already been utilized for some medical applications, such as hollow microneedles with thin needle walls and fine structures to reduce pain and damaged sites for patients [154]. However, limited by its small field of view (high magnification of objective lens) and stitching process [17], the

two-photon printer has a limited printing volume of a few hundred microns [18,19]. Besides, the printing speed is very slow, taking a long cycle time to manufacture a few hundred microns structure. In addition, the two-photon printer relies on an expensive laser and optics. Hence, all these drawbacks make it hard to be applied to fabricate a large number of microdevices. Apparently, there is a demand to develop a 3D printing process that possesses microscale printing resolution and large printing volume, with a competitive cost to achieve economic benefit.

2.5 Optical pickup unit (OPU)

In the 1980s, the OPU was invented as an optomechatronic component for reading and writing data on a disc [155]. Attributed by advanced manufacturing technology, the OPU integrated a complex optics, sensor, actuator, and electronic circuit in a match-box size. The OPU was initially designed for CD with a 780 nm laser. With a NA 0.5 objective lens, the focal laser spot size reached 800 nm in diameter [155]. The nanoscale focal spot minimized the data storage space needed, allowing a data capacity of hundreds of megabytes on a 120-mm-diameter disc. Due to the rising need for increased data capacity, a smaller focal spot size was needed. The OPU evolved and equipped laser diode from 650 (DVD) to 405 nm (HD-DVD, and Blu-ray) in wavelength. Simultaneously, higher NA objective lenses from 0.63 to 0.85 were used. Finally, the laser focal spot size of DVD, HD-DVD, and Blu-ray achieved from 530 to 250 nm in diameter, allowing gigabytes data storage capacity in the same diameter disc.

The OPU consists of an astigmatic optics and a photodiodes-intergraded-circuit (PDIC), as shown in **Figure 13A**. The optics design of each OPU is different; here, we utilized an HD-DVD OPU (PHR-803T, Toshiba, Tokyo, Japan) for illustrating the inner structure and optical path of OPU [156,157]. The OPU emits a laser from a laser diode. Then the laser orderly passes a series of optical elements and finally passes an objective lens and a transparent cover layer to focus a spot on a disc. The reflected laser from the disc returns along the original path to a beam splitter. The beam splitter reflects the laser onto the PDIC. The PDIC consists of four quadrants photodiodes, A, B, C, and D. The photodiodes A to D monitor the laser spots and generate signals S_A to S_D , respectively. When the laser is focused on the reflective surface, the laser spot appears a round shape on the PDIC (**Figure 13B**). When the focal point is off-center (while the reflective surface displaces along the axial direction), the laser spot appears an elliptical shape. Focus error signal (FES) presents this alteration by $FES = (S_A + S_C) - (S_B + S_D)$. The relation of FES to the displacement of reflective surface shows an S shape curve (S-

curve). The inner part of the S-curve is a highly sensitive linear region, which precisely detects the nanoscale distance change.

The OPU equips a voice coil motor (VCM) that drives the objective lens and aligns the focal spot on the disc. The VCM has a range in the Z-direction around $\pm 1000 \mu\text{m}$ and the X-direction around $\pm 350 \mu\text{m}$ [155].

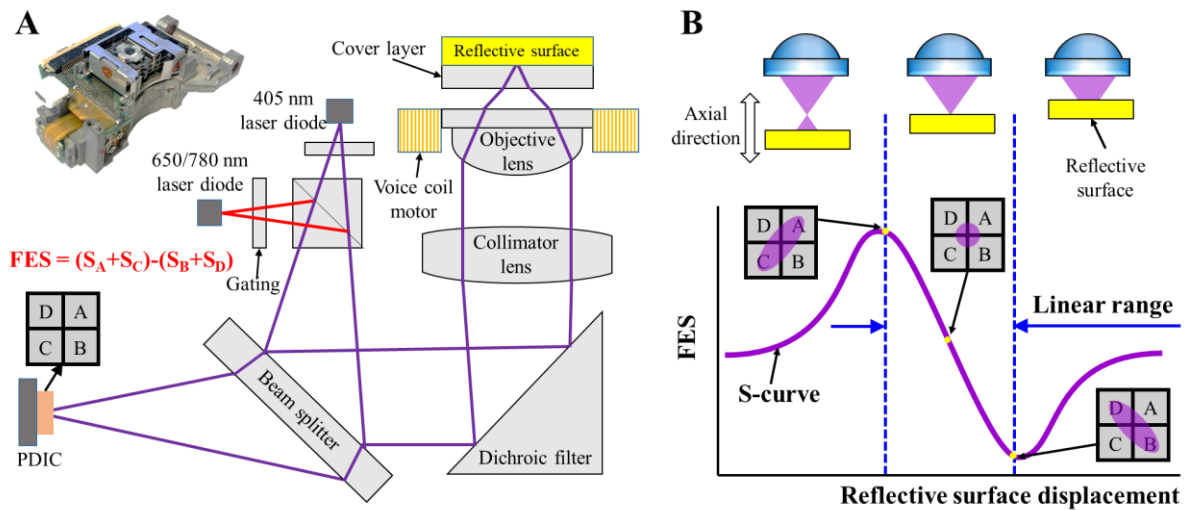


Figure 13. Illustration of the optical pickup unit (OPU) using a high-definition digital versatile disc (HD-DVD) OPU (PHR-803T). **A)** Photograph and schematic diagram of the inner optical module, sensor, and actuator. The OPU integrates three laser wavelengths (405/650/780 nm). The OPU emits a laser to focus on a reflective surface and receives the reflective laser on a four quadrants photodiodes-intergraded-circuit (PDIC). Focus error signal (FES) is obtained by calculating signals of photodiodes (S_A , S_B , S_C , and S_D), using an equation, $FES = (S_A + S_C) - (S_B + S_D)$. **B)** The relation of FES versus the displacement of the reflective surface. While shifting the reflective surface along the axial direction, the FES presents an S-curve with a high sensitive linear range.

The OPUs were repurposed for other promising applications in both sensing and manufacturing since the OPU comprises sensitive sensors and precise actuators. Besides, some OPUs, e.g., Blu-ray and HD-DVD, integrate multiple laser diodes to read/write various types of discs. Benefited from the mass market of personal data storage and transport, OPUs were mass-produced with a fully optimized industry manufacturing process. Therefore, most OPUs have an attractive cost, approximately under 10 USD. Nevertheless, in recent years, novel concepts emerged to improve data storage and transmission (e.g., solid-state disk or cloud data). Although the data storage request of OPU was gradually replaced, OPU brought plenty of wide-ranging applications [155].

2.5.1 Sensing application of optical pickup unit

The FES of DVD OPU has a high distance detection sensitivity of 4.209 and 4.040 mV/nm in air and aqueous environment, respectively [158]. In addition, the OPU has a high working bandwidth of 80 MHz [159]. Hence, the DVD OPU was utilized to sense an AFM probe (**Figure 14A**) [160,161]. The optics of OPU can replace a traditional optical lever module to sense a nanoscale deflection of a micro-cantilever. Furthermore, by calibrating the force constant of the micro-cantilever, the OPU can detect a pico-newton scale force. The OPU based AFM system demonstrated long-term stability for scanning images, successfully imaging DNA structure and highly ordered pyrolytic graphite (**Figure 14A**) [158]. The compact size of OPU simplified the mechanical design of the AFM and achieved a high system stiffness. Hence, a high-speed AFM scanning can also be achieved by the DVD OPU [162].

A compact fluorescence detection system utilized the HD-DVD OPU to detect beads on a chip (**Figure 14B**) [163,164]. The system provided a low-cost way to sense a two-dimensional fluorescent signal of microscale beads in the microchannel on the micro-fluid chip.

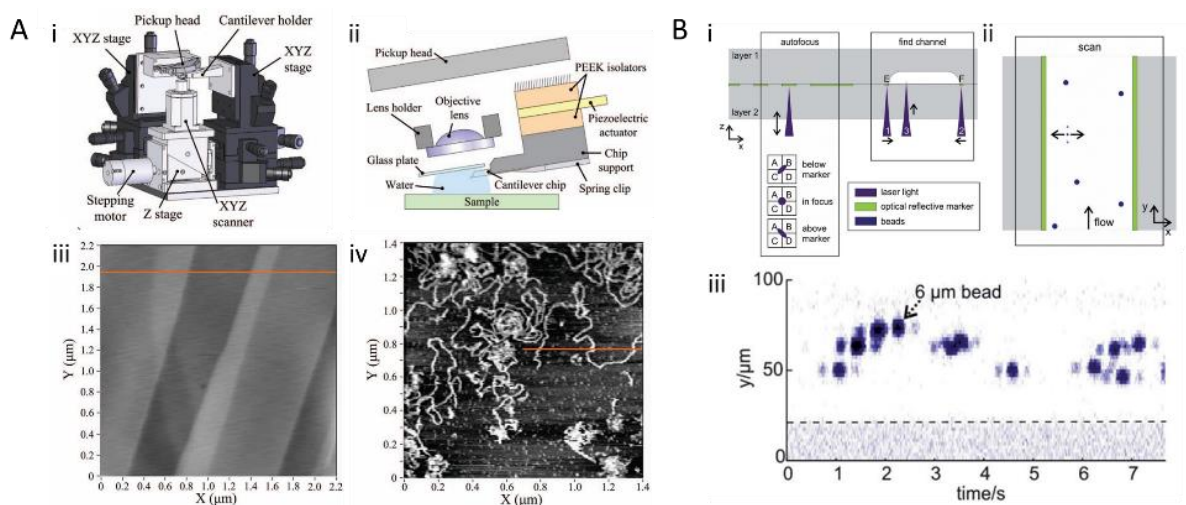


Figure 14. Sensing application of optical pickup unit (OPU). **A)** Development of AFM system using a DVD OPU. i) Diagram of system mechanism. ii) Illustration of integrating OPU optical path to sense micro-cantilever in water. AFM scanning images of iii) highly ordered pyrolytic graphite and iv) DNA in an aqueous environment [158]. **B)** Fluorescence detection system using an HD-DVD OPU to sense microscale fluorescence signal of beads in 2D direction. Schematic diagram of the microfluidic chip of the view from i) cross-section and ii) from above. iii) Multiple 6 μm fluorescent beads were detected in the microchannel [163]. Reprinted/adapted with permission from respective publishers.

2.5.2 Manufacturing application of optical pickup unit

The OPU has an excellent potential to provide nanoscale resolution for the 3D printing process of photopolymerization-based, as the OPU possesses a small focal spot of hundreds of nanometers in diameter, close to the light diffraction limit [155]. Recently, the Blu-ray OPU was applied to construct a 2D lithography system (**Figure 15A**) [165]. Following a 2D moving path, the system can cure a nanoscale wire of 450 nm in width (**Figure 15B**). The same theory of photopolymerization is applied in lithography, so the OPU laser could cure the photopolymer to reach nanoscale 3D printing resolution.

Furthermore, the HD-DVD OPU was installed on a three-dimensional positioning stage to build an open-source printed circuit board (PCB) printer [166]. The laser spot of OPU exposed a photo-resist dry-film on a copper board to print a circuit layout. After an etching process, the delicate circuit layout pattern was completed in a few square centimeters area.

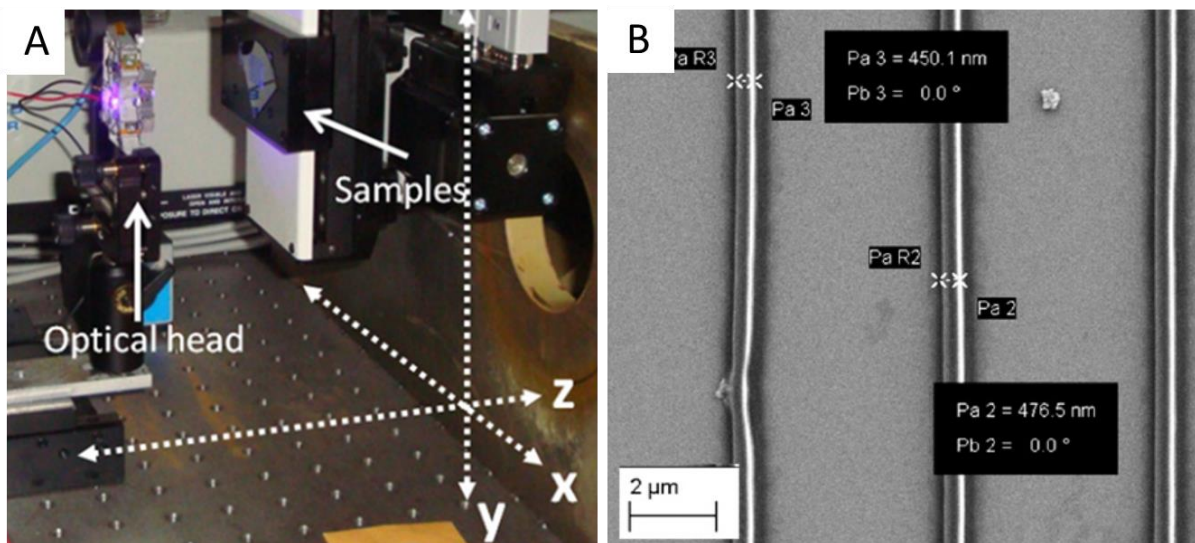


Figure 15. Manufacturing application of optical pickup unit (OPU). 2D lithography system using a Blu-ray OPU **A)** Photograph of system. **B)** Cured nanoscale wire of 450 nm in width along the lateral direction [165]. Reprinted/adapted with permission from publisher.

3. Results and discussion

The following section has been divided according to the papers presented in this PhD thesis (Paper I-III). Each subsection elaborates purpose and the selected result of the paper, while the related method description is mentioned. The discussion is based on the overall aim of this thesis. At the same time, the connection and relationship between each paper are mentioned.

3.1 Micro and nanoscale 3D printing using optical pickup unit from a gaming console

This subsection presents results obtained in Paper I "Micro and nanoscale 3D printing using optical pickup unit from a gaming console" (for the full paper, see Appendix I).

Purpose

This study aimed to utilize the HD-DVD OPU as a core optical module to develop a vat photopolymerization-based 3D printer. The nanoscale focal spot of the OPU is expected to realize micro and nanoscale printing resolution in a centimeter-scale printing volume. Thus, the 3D printer is able to produce the MCs with overhanging structure and delicate features.

Outcomes

This study was conducted to establish the foundation of this PhD project. The HD-DVD 3D printer was established to offer micro and nanoscale printing resolution, achieving the highest resolution of 385 nm along the lateral direction. Besides, the printer can 3D print multiple layers structures with a large printing volume (up to $50 \times 50 \times 25 \text{ mm}^3$).

Micro- and nanoscale 3D printer

We successfully utilized the HD-DVD OPU to custom-build a micro and nanoscale 3D printer (**Figure 16**). This OPU 3D printer consists of an XY-axis linear stage, a Z-axis linear stage, a 2-axis tilt stage, a Si substrate, a photopolymer vat, an HD-DVD OPU, and a control system. In the printing process, the XY-axis linear stage moves the OPU to realize the printing path along the lateral direction. Simultaneously, the OPU emits a 405 nm laser penetrating a 0.5-mm-thick transparent PMMA window to cure the photopolymer on the Si substrate in the photopolymer vat. The distance that the laser travels through the photopolymer is defined as photopolymer thickness, T_p . The Z-axis linear stage controls the vertical position of the substrate for layer-by-layer printing. The parallelism of the substrate and the printing path is adjusted by the two-axis tilt stage mounted on the Z-axis stage. The controlling system

integrates an embedded controller, a customized OPU driver, and a motor driver to operate the 3D printing procedure. The embedded controller connects to the OPU driver to tune the laser intensity, drive the VCM and receive the FES. The controller also connects to the motor driver for driving the XY- and Z-axis linear stages with the highest positioning resolutions of 312.5 and 62.5 nm, respectively. Through a graphical user interface, a computer communicates with the embedded controller for operating the printing procedure. The printing path is programmed by computer numerical control commands in G-code.

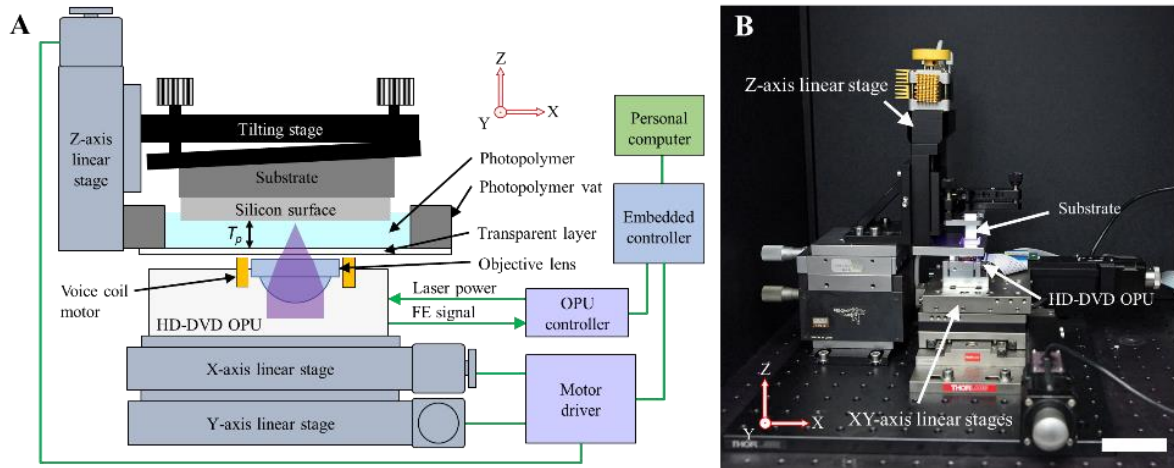


Figure 16. Development of custom-built 3D printer utilizing an HD-DVD optical pickup unit (OPU) as core optical module by focusing 405 nm laser beam to cure photopolymer in the vat. **A)** Mechanism of the printer, control system diagram, and optical path diagram with photopolymer thickness, T_p , indicated. **B)** Photograph of the system during the 3D printing process (scale bar represents 5 cm).

This custom-built printer has a theoretical 430-nm-diameter laser focal spot, which greatly increases the printing resolution to the nanoscale. Besides, as the linear stages have nanoscale positioning resolution, these stages can precisely implement printing paths to 3D print structure stably. In general, the vat photopolymerization-based printer with inverted design (exposure light upward) relies on an oxygen-preamble membrane to avoid the cured structure adhering to the transparent window [167,168]. The membrane allows a highly concentrated oxygen thin layer to spread on the transparent window to inhibit the photopolymerization effect. Here, the proposed printer relies on the surface energy difference between the transparent window (PMMA) and the substrate (Si). The surface energy of Si is larger than PMMA, so the cured structure adheres to the substrate stably. The easily accessible PMMA plate reduces the cost of the printer and simplifies system maintenance. As mentioned in the previous section 2.2.1, the SU-8 MCs produced by photolithography were manufactured in a 25×25 array on a $12.8 \times 12.8 \text{ mm}^2$ square Si chip [78]. To achieve a standardized preparation process of MCs (including follow-up loading, coating, and releasing), the printing substrate was also designed to be the

same square size. At the same time, the photopolymer vat was designed to fit the substrate with a size of $20 \times 30 \times 5 \text{ mm}^3$ (width \times length \times depth). The relatively small volume of vat can also prevent the waste of the expensive photopolymer.

Laser exposure dose experiment

To investigate the printing capability, we tuned the laser exposure dose to optimize printing resolution. In this printing system, the laser exposure dose can be modified by tuning both the printing speed and laser intensity. A commercially available white photopolymer (FLPGWH02; Formlabs, Somerville, MA, USA) was used. For a fixed photopolymer thickness (T_p) of $25 \mu\text{m}$, the printer cured lines in a rectangular frame at different laser exposure doses by tuning laser power from $2.97 \mu\text{W}$ to $2.15 \mu\text{W}$ and printing speed from 0.138 to 0.104 mm/s (**Figures 17A-D**). The result of cured line width exhibits a positive linear trend regarding laser exposure energy (**Figure 17E**). Increasing the printing speed or minimizing the laser intensity reduces laser exposure, and thereby decreasing the cured line width.

This test result reveals that the dimension of the printed structure is proportional to the laser exposure dose. **Figure 17E** provides a reference for the selection of suitable printing parameters. In this test, the operated laser intensity is only 2-3 % of the full power laser ($\sim 0.2 \text{ mW}$). Therefore, the printer has a great potential to further increase printing speed by raising the laser intensity.

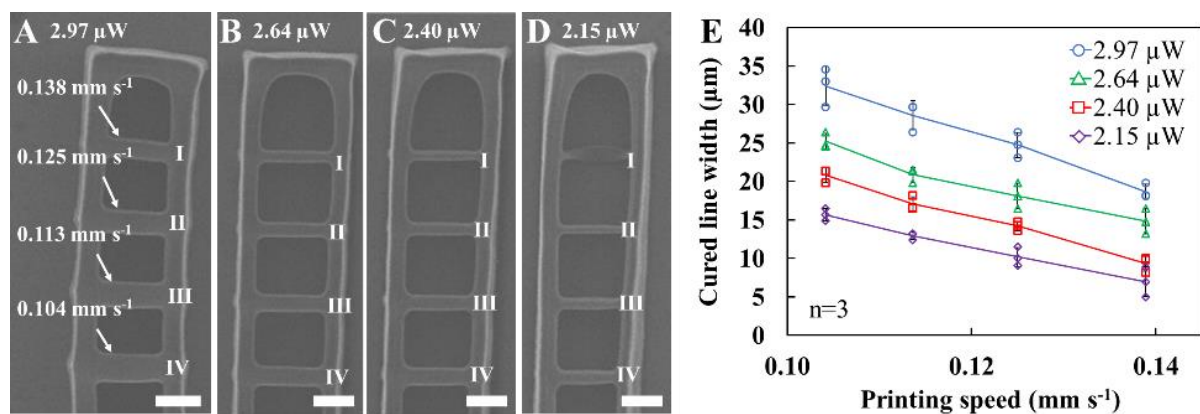


Figure 17. Verifying laser exposure dose by curing microscale lines in a rectangular frame with different parameter settings of printing speeds and laser intensity. SEM images of cured lines at laser powers of **A**) 2.97 , **B**) 2.64 , **C**) 2.40 , and **D**) $2.15 \mu\text{W}$. The printing speed of 0.104 , 0.113 , 0.125 , and 0.138 mm/s are labeled I, II, III, and IV, respectively (scale bar $50 \mu\text{m}$). **E**) Cured line width according to different parameter settings of printing speed and laser intensity (error bars represent one standard deviation, and n represents sample size).

Nanoscale printing resolution

According to an optical simulation result, the printing resolution of the proposed 3D printing mechanism is influenced by the photopolymer thickness, T_p . Hence, we reduced the photopolymer thickness to $6\ \mu\text{m}$ for investigating the highest printing resolution. For a fixed laser power of $2.40\ \mu\text{W}$, the printer cured nanoscale lines at different printing speeds of 0.25 to $0.16\ \text{mm/s}$ (**Figures 18A–D**). Two vertical features (with a $15\ \mu\text{m}$ separation) supported the cured nanoscale lines. The thinnest line of $385\ \text{nm}$ in width was printed with a printing speed of $0.25\ \text{mm/s}$ (**Figure 18D**). **Figure 18E** shows the cross-section contour of the 385-nm -wide line. The cured nanoscale line width presents a linear trend regarding the printing speed, as shown in **Figure 18F**.

Thinner photopolymer thickness achieves higher printing resolution. However, limited by the mechanical structure, the thinnest layer achieved is $6\ \mu\text{m}$. This optimization result presents that the printer can stably achieve a nanoscale printing resolution. Hence, the printer is able to fabricate delicate 3D structures.

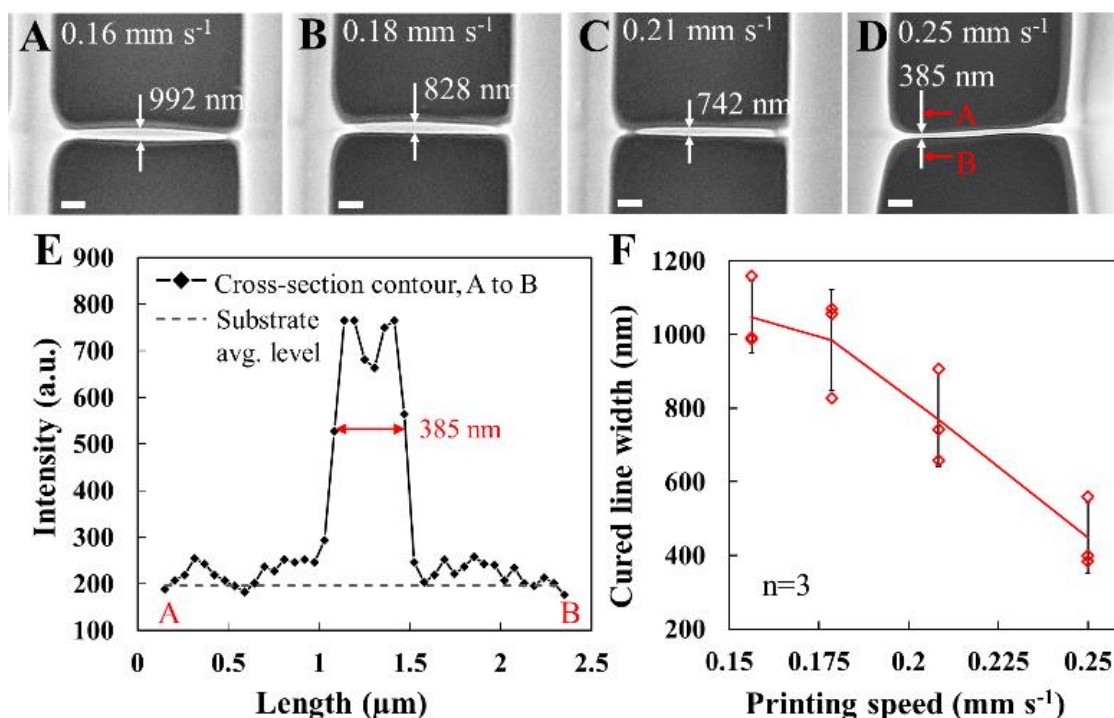


Figure 18. Nanoscale printing resolution experiment. SEM images of 3D printed nanoscale structures, as the printer cured the nanoscale lines at printing speeds of **A**) 0.16 , **B**) 0.18 , **C**) 0.21 , and **D**) $0.25\ \text{mm s}^{-1}$, resulting in line widths of 992, 879, 769, and $385\ \text{nm}$, respectively. To support nanoscale structures, two vertical lines (approximately $5\ \mu\text{m}$ in width) were printed with a distance of $15\ \mu\text{m}$ (scale bars $2\ \mu\text{m}$). **E**) Cross-section profile of cured line with $385\ \text{nm}$ in width in panel **D**. **F**) Cured line width according to printing speed at a fixed $2.40\ \mu\text{W}$ laser power and a $6\ \mu\text{m}$ photopolymer thickness (error bars represent one standard deviation, and n represents sample size).

3D printed microstructures and microcontainers

To validate the printing performance of the HD-DVD 3D printer, we 3D printed various microstructures (**Figure 19**). **Figures 19A** and **B** present a pyramid and a twisted tower, respectively. These microstructures were printed with layers of 25 μm in height. Besides, a cylinder MC was printed with 300 μm in diameter and 150 μm in height to demonstrate the concept of 3D printed MCs (**Figure 19C**). An 800- μm -wide and 400- μm -high gate structure was fabricated (**Figure 19D**).

This printing result proves the concept of the OPU based 3D printing mechanism. The printer can fabricate various microscale structures with dimensions close to the standard MCs (320 μm in diameter). Besides, the overhanging feature of the gate implies the manufacturing flexibility for realizing an undercut structure. In addition, while the G code divides the round path into sixty line segments, the cylinder MC presents a non-smooth surface of the side. The distinct surface texture also indicates the high printing resolution of this printer.

We successfully developed a micro and nanometre resolution 3D printer utilizing the HD-DVD OPU to cure the commercial photopolymer. The printer achieves the nanoscale printing resolution of 385 nm along the XY direction. Besides, the printer successfully manufactured microscale multiple-layers structures. Finally, the cylinder structure of 300 μm in diameter was printed to demonstrate the potential for the application of MCs 3D printing.

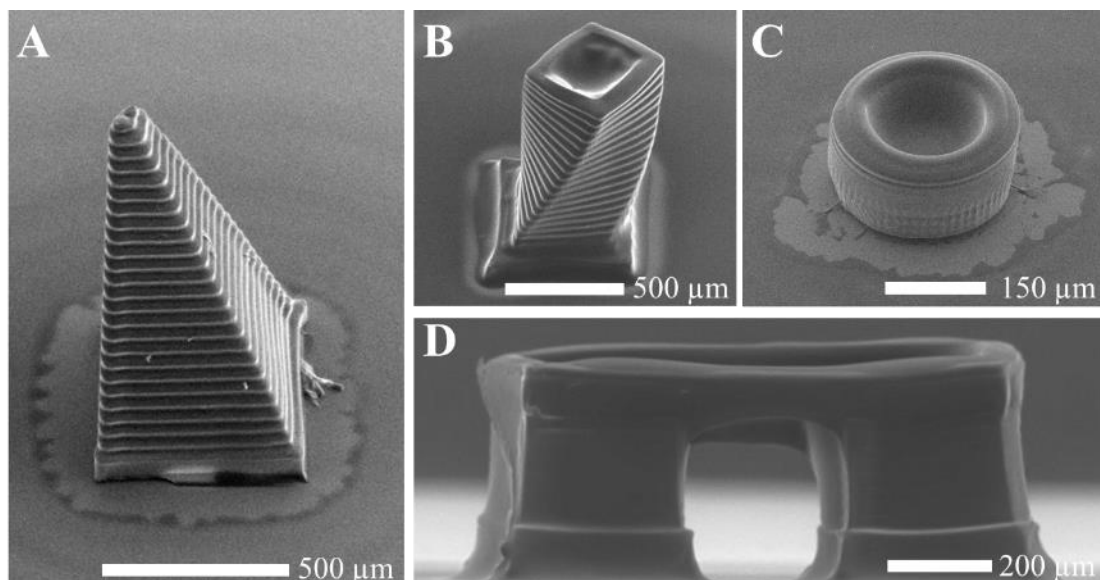


Figure 19. SEM images of 3D printed microscale structures. **A)** 850- μm -high pyramid structure constructed by multiple layers of 25 μm per layer height. **B)** Twisted tower. **C)** Microcontainer (MC) with cylinder structure. **D)** Gate structure with an overhang feature.

3.2 Microscale mucoadhesion force analyzer using DVD optical pickup unit

The following subsection presents results based on Paper II "Microscale mucoadhesion force analyzer using DVD optical pickup unit" (for the full paper, see Appendix II).

Motivation and purpose

In this project, mucoadhesive force is a key factor in evaluating the delivery mechanism of the designed MCs. However, the mucoadhesive force of MCs is in the range of micro-newton scale, and no suitable instrument can directly implement this measurement. This study aimed to develop an OPU based force analyzer with a reliable force sensing range of micro-newton scale. As a result, the force analyzer can characterize the mucoadhesive forces of a single MC.

Outcomes

The OPU force analyzer was developed with a broad range of force measurements from newton to nano-newton. A force calibration process was implemented to evaluate the instrument performance, overviewing the force measuring range, force sensitivity, and resolution. The force analyzer was demonstrated to reliably measure the mucoadhesive forces of a single MC.

OPU force analyzer

We designed and developed an OPU force analyzer with a force measurement range from newton to nano-newton by utilizing a DVD OPU (Top1300s, Sanyo Electric Co., Ltd., Osaka, Japan), as shown in **Figure 20**. In addition, a novel design of a cantilever force transducer can easily be modified to a suitable force-sensing range. This instrument is designed for the *ex vivo* tensile strength measurement mentioned in previous section 2.3.1 (**Figure 8A**) to obtain a mucoadhesive force-displacement curve (**Figure 8B**). Hence, this force analyzer consists of two core parts, a force detection module and a sample positioning module (**Figures 20A** and **C**). A control system connects to each module and builds a graphical user interface to operate the measurement process.

The sample positioning module carries the tissue along the vertical direction to implement the sample approaching or withdrawing process of tensile strength measurement. For high accuracy and stable movement, the sample positioning module equips an optical-level linear stepper motor (LTM 60-25, OWIS GmbH, Staufen, Germany). Assisted by an advanced motor driver for 128 divided sub-step, this linear stepper motor can reach 40 nm positioning resolution

along with the whole 25-mm-long travel distance. In addition, the tissue sample is placed on a manual linear stage which quickly moves the sample along the lateral direction.

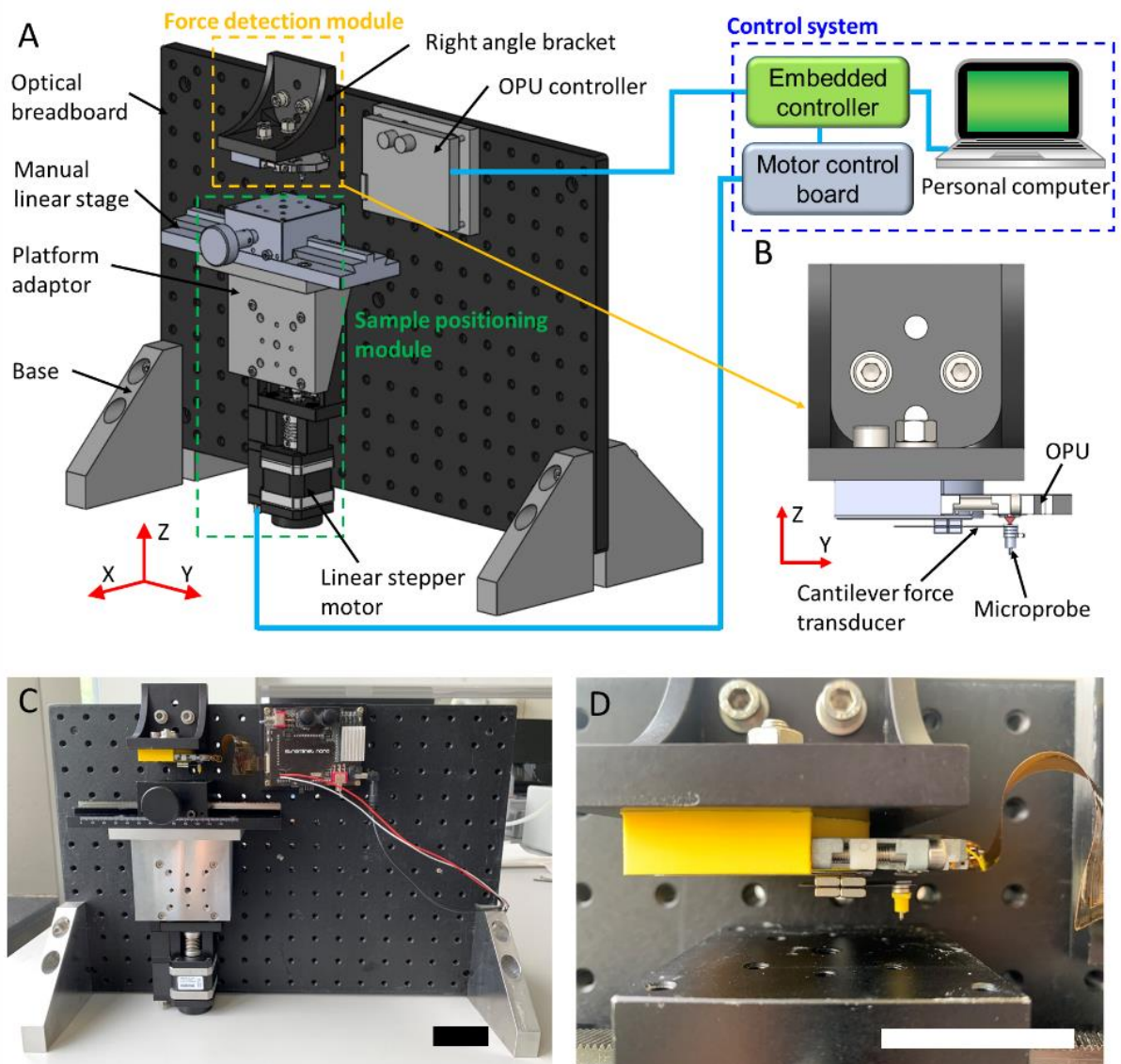


Figure 20. Development of broad range force analyzer using a DVD optical pickup unit (OPU) as a core measuring module to detect a cantilever deflection induced by applied force from newton to nano-newton. **A)** Schematic diagram of a control system and a mechanism, including force detection and sample positioning modules. **B)** Detailed diagram of force detection module assembled by OPU, cantilever force transducer, and microprobe. **C)** The whole system photograph (scale bar 5 cm). **D)** The force detection module photograph (scale bar 5 cm).

The force detection module was assembled by the DVD OPU and the cantilever force transducer (**Figures 20B** and **D**). The DVD OPU equips a 650 nm laser diode. The OPU feedbacks FES with the high sensitive linear region of the S-curve, as mention in section 2.5 (**Figure 13B**), to sense cantilever deflection induced by applied force (**Figure 21A**). The high

sensitive linear signal feedbacks cantilever deflection with the best distance resolution of 4.9 nm on this system.

The cantilever force transducer is assembled using a steel shim, a microprobe, and four rectangle magnets (**Figure 21B**). The microprobe directly contacts the intestinal mucus and transfers the adhesive force to the cantilever structure. The cantilever structure constructed by the steel shim converts the applied mucoadhesive force, F , to deflection, D , during the sample approaching and withdrawing process. This cantilever force transducer can be tuned to a suitable force range by selecting cantilever thickness (t_c) and length (l_c). The four rectangle magnets modify the cantilever length by shifting their position along the Y direction.

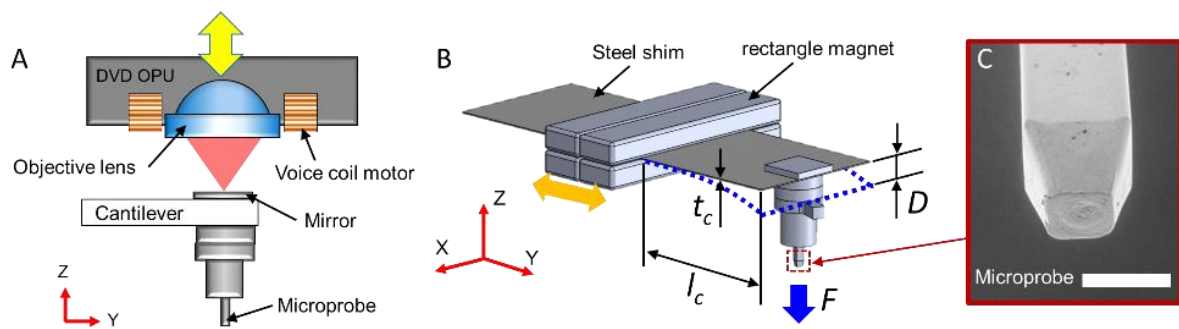


Figure 21. Illustration of the force detection module. **A)** The DVD optical pickup unit (OPU) focuses a 650-nm-wavelength laser beam on a mirror to sense the deflection of the cantilever force transducer. **B)** The cantilever deflection D is caused by the applied force F . The force detecting range of the cantilever force transducer is defined by the thickness (t_c) and length (l_c) of the cantilever, while t_c can be modified by shifting four rectangle magnets along the Y direction. **C)** SEM image of microprobe shows microscale contact area (scale bar 500 μm).

The control system integrates an embedded controller (myRIO-1900; National Instruments, Austin, TX, USA), a motor control board, and an OPU controller (**Figure 20A**). Users place commands to the embedded controller through a personal computer to drive the linear stepper motor and receive FES.

This OPU force analyzer comprises many merits. Unlike the texture analyzer moves probe and force detection module (**Figure 8A**), this force analyzer moves the sample. Hence, the force analyzer reduces interference of motor vibration to the force detection module, reaching higher sensing resolution. Besides, the cantilever force transducer equips a microprobe (**Figure 21C**). The microprobe has a microscale contact for carrying a single microdevice and increasing the reproducibility of micro-newton scale mucoadhesive forces measurement. Furthermore, the core components, OPU, steel shim, and microprobe, are cost-effective and accessible. As a result, this instrument is easily affordable. Finally, the broad range of force measurement can provide wide application in various areas.

Cantilever force transducer calibration of milli- and micro-newton scale force

Before implementing the tensile strength measurement, the system needs to be calibrated to a suitable force range and correct force sensitivity (S_F). The force sensitivity converts the FES voltage signal to corresponding force data. As the mucoadhesive force of a single MC is in the range of micro-newton, only the calibration of force range from milli- to micro-newton is shown in this thesis. Here, we directly loaded and unloaded the cantilever force transducer with a known applied force (**Figures 22A and B**). We observed the FES step for the corresponding applied force by repeating the loading and unloading processes (**Figure 22C**).

For the force range of milli-newton calibration, a 0.3 mm-thick cantilever force transducer was applied with a length from 8.26 to 18.4 mm. Then, we utilized a 0.1 mm-thick cantilever force transducer for the force range of micro-newton. A known weight from 2.74 to 60.98 mg was hanged on the cantilever, and then the sample positioning module lifted the weight to unload the cantilever. The force calibration curves and force sensitivity of milli- and micro-newton are shown in **Figures 22D and E**, respectively. All these calibration curves present a linear trend.

We further analyzed the S-curve linear range and RMS noise of 13.74 V and 64 mV, respectively. For parameter selection, we define the force range, sensitivity, and resolution of each cantilever force transducer setting in **Figures 22F and G**. **Figures 22F and G** provide a reference for easily selecting the cantilever parameters based on a suitable force measuring range.

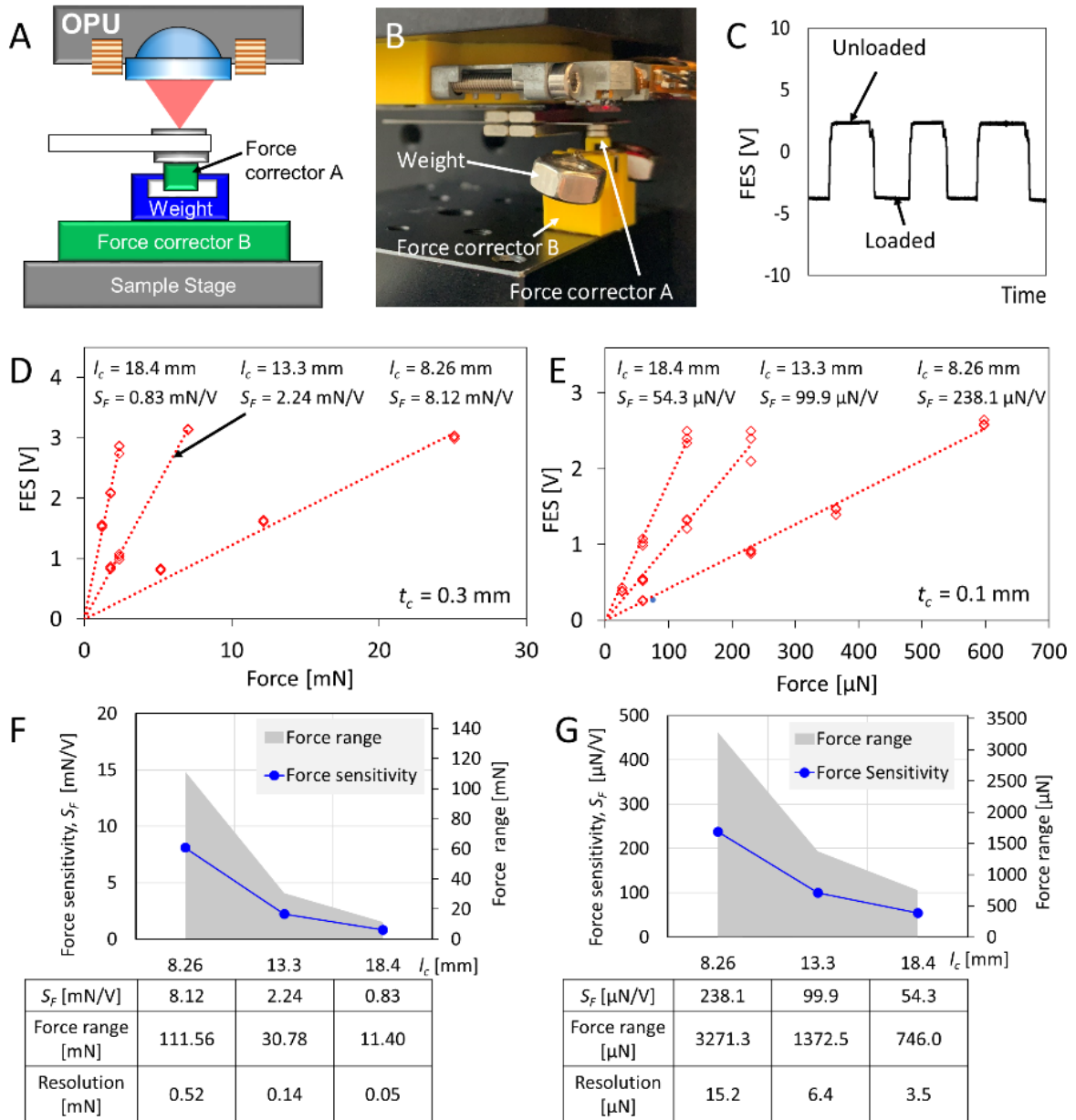


Figure 22. Force calibration of the range from milli-newton to micro-newton **A)** Schematic diagram of the calibration process by loading a known weight (from 2.74 to 60.98 mg) on the cantilever force transducer, and unloading cantilever by lifting the sample stage. **B)** Photograph of the force calibration process. **C)** Focus error signal (FES) step signal while loading/unloading the cantilever force transducer. **D)** Calibration curves of milli-newton scale force using 0.3 mm-thick cantilever present force sensitivity (S_F) of 0.83, 2.24, 8.12 mN/V, with adjusted cantilever length of 18.4, 13.3, and 8.26 mm, respectively, $n=3$. **E)** Calibration curves of milli-newton scale force using 0.1 mm-thick cantilever present force sensitivity (S_F) of 54.3, 99.9, 238.1 μ N/V, with adjusted cantilever length of 18.4, 13.3, and 8.26 mm, respectively, $n=3$. Force sensitivity (S_F), force range, and resolution of each cantilever parameter setting of **F)** milli-newton range **G)** micro-newton range.

Preliminary study of mucoadhesion alteration while time and moisture escape

While implementing the *ex vivo* tensile strength measurement to quantify the mucoadhesive forces of microdevices using intestinal tissue (as mention in subsection 2.3.1), various factors and effects might profoundly influence the outcome. However, some of these factors and effects are difficult to control, such as dehydration, tissue property, and sampling time. According to experience, dehydration normally turns severe as time passes, resulting in more viscosity and adhesion of intestinal mucus. Although the phenomenon might be a challenge to eliminate, a preliminary study can provide more understanding for facilitating a formal experiment design.

In this study, we set two experiment groups; dry and wet, to realize how time affected the adhesive behavior of the mucus layer. A piece of porcine small intestinal tissue was measured the mucoadhesive force using the microprobe for every 10 min of the interval. In the wet group, phosphate-buffered saline (PBS) with a pH of 6.5 was constantly sprayed on the surface of intestinal tissue to keep mucus moisture for each 20 min interval period. On the contrary, the tissue of the dry group was without any treatment. The parameter setting comprised a contact force of 80 μ N, a contact time of 1 s, and a constant approach/withdrawal speed of 0.156 mm/s. The measurement was implemented at room temperature of 20 °C and relative humidity 45 ± 5 %. A 100 Hz lowpass filter processed the force signal to increase the signal-noise ratio.

Figures 23A and B show the result of the dry and wet groups, respectively. The result indicates that the dehydration effect greatly influenced the mucoadhesive force in the dry group (**Figure 23C**). After 60 min, the mucoadhesive force increased approximately 130 % compared to the initial level. The sprayed PBS buffer inhibited this phenomenon in the wet group, with around 57 % increased mucoadhesive force within 60 min. Thus, the PBS buffer can stabilize the mucus property as time pass. Notably, both the dry and wet groups exhibited relatively stabilized mucoadhesion in 20 min. This observation might indicate that 20 min might be the threshold for implementing mucoadhesion measurement.

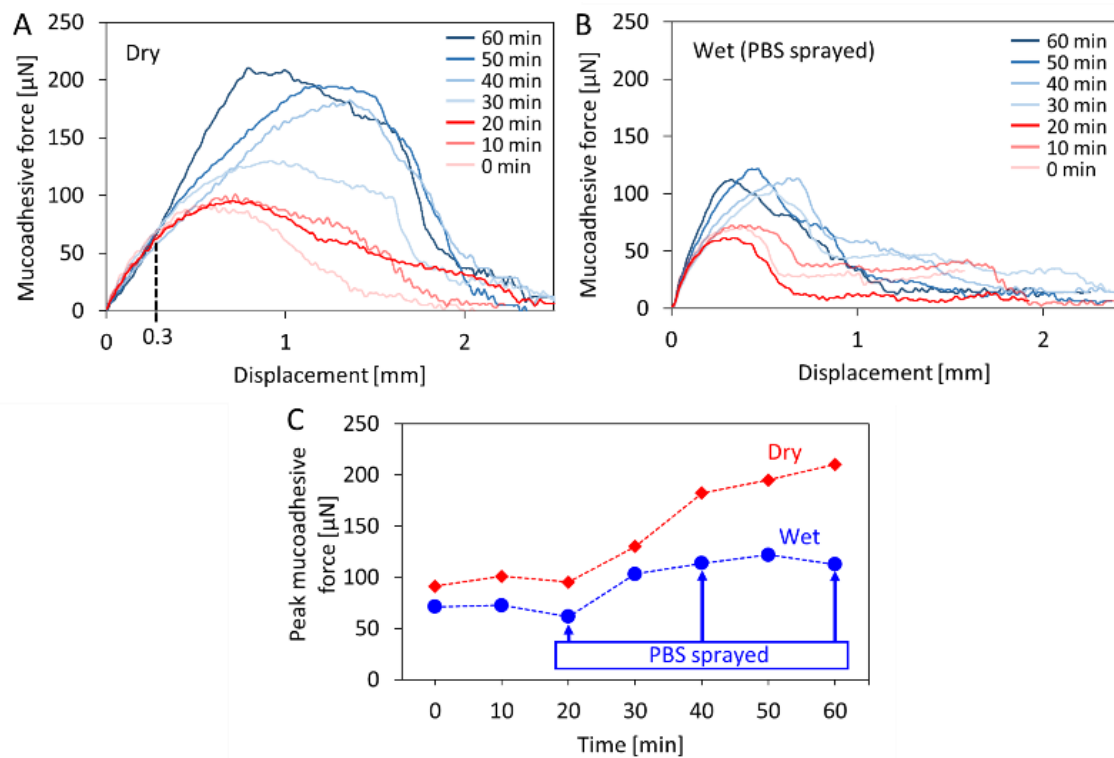


Figure 23. Investigation of mucoadhesive forces alteration while time and moisture escape. Mucoadhesive force to displacement curves were measured while withdrawing a microprobe from a porcine small intestinal mucosa of **A)** dry group (no treatment), and **B)** wet group (phosphate-buffered saline (PBS) sprayed on the tissue for every 20 min), for every 10 min of the interval. **C)** Peak mucoadhesive force of the dry and wet groups every 10 min in 1 h. The mucoadhesive force of the dry group increases 130 % after 1 h, while the wet group increases 57 %.

Mucoadhesive force measurement of microcontainers

To demonstrate the capability of force analyzer for measuring the mucoadhesive force of a single MC, the mucoadhesive force of the SU-8 MCs (320 μm in diameter) was investigated using the mucus layer from a porcine small intestinal tissue. For comparison, the adhesive property of PBS buffer to MCs was also investigated. First, a UV cross-linkable glue mounted a single MC on the microprobe for the contact of the sample (mucus and PBS) with the top and bottom side, respectively (**Figures 24A** and **B**). The fresh porcine small intestinal tissue was opened using scissors and placed on the sample stage with mucus layer upward (**Figure 24C**). In addition, a PMMA plate placed on the sample stage carried PBS buffer. The PBS buffer appeared a 30-mm-diameter round and a flat surface. While measuring adhesive force, the linear motor approached the PBS and mucus to MC, respectively, and then withdrawn MC until separation. The parameters were set to a constant speed of 0.078 mm/s and a contact time of 1 s. The test was repeated four times for each sample for both the top and bottom sides of MC.

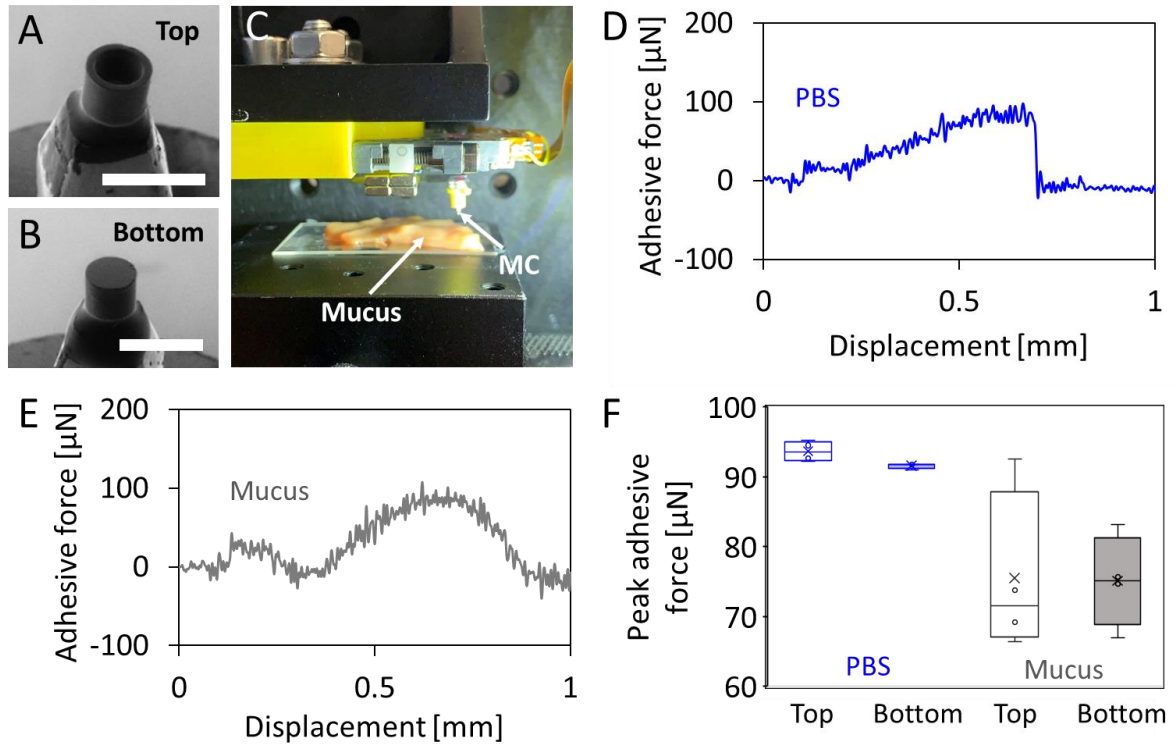


Figure 24. Investigation of adhesive force of phosphate-buffered saline (PBS) buffer and porcine small intestinal mucus to microcontainers (MCs). SEM image of mounting MC on the microprobe by UV cross-linkable glue with **A**) top and **B**) bottom side for measurement (scale bar 500 μm). **C**) Photograph of approaching and withdrawing MC to intestinal mucus with a constant speed of 0.078 mm/s and contact time of 1 s. While withdrawing the MC from the sample, the force detection module obtained the adhesive force to displacement curves of **D**) PBS buffer to MC, and **E**) porcine small intestinal mucus to MC, respectively. **F**) The peak adhesive force of PBS and mucus to both sides of MC, respectively. Both sides of MC present the same level of adhesion to PBS and mucus due to its symmetrical geometry. Mean \pm SD, $n = 4$.

The result shows the adhesive force-displacement curves of the PBS buffer and the mucus to MC in **Figures 24D** and **E**, respectively. The adhesion curve of PBS buffer to MC presents a right triangle profile. While withdrawing MC from PBS buffer, the adhesive force proportionally increased to an average peak force of 93.7 μN (top) and 91.6 μN (bottom). Then as the PBS buffer detached from the MC, the force curve slumped to the initial level. The intestinal mucus presents a symmetrical hill profile with an average peak force of 75.5 μN (top) and 75.1 μN (bottom) in the middle.

Figure 24F shows the comparison of peak adhesive force. The PBS buffer presents more adhesive to the MC than the mucus layer. As consideration of variation, the PBS buffer shows relatively small variation due to its homogenous material property. The larger deviation of mucus is probably attributed to the variation of the tissue sample itself. The property of tissue samples can vary a lot from the different sites of the GI tract. Besides, the MC has a symmetrical geometry structure, so both sides show a similar level of adhesion to PBS and

mucus, respectively. At the same time, the bottom side appears minor variation probably due to its more straightforward structure and less boundary edge of contact.

This OPU force analyzer successfully quantified the mucoadhesive force of a single MC with high signal-to-noise ratio data. Besides, the low variation of PBS buffer demonstrates the repeatability and reproducibility of the system. Therefore, this force analyzer is a reliable instrument for the characterization of microdevices mucoadhesion.

3.3 3D printed radiopaque microdevices with enhanced mucoadhesion geometry for oral drug delivery

The following subsection presents results based on Paper III, "3D printed radiopaque microdevices with enhanced mucoadhesion geometry for oral drug delivery" (for the full paper, see Appendix III).

Purpose

This study aims to 3D print MCs with innovative geometry designs for enhancing the mucoadhesion of MCs. The enhanced mucoadhesion can provide MCs a self-orientation control and a longer intestinal resident. These designs are validated by *ex vivo* and *in vivo* studies.

Outcomes

This project applied three design strategies, asymmetrical structure, micro-pillar, and arrow, to enhance mucoadhesion and thereby, retention time (**Figure 25**). The MCs are expected to achieve self-orientation and extended retention time while transiting along the GI tract through these designs. These designs are based on a square shape, as the cubic MCs (square design) showed stronger mucoadhesion via an *in situ* study in rats [100]. These novel designs of MCs were realized by the proposed high-resolution 3D printer (Paper I). Also, BaSO₄ nanoparticles were incorporated into a biocompatible photopolymer (Biomed, Formlabs, Somerville, MA, USA) to 3D print radiopaque MCs for tracking along the GI tract after an *in vivo* study. *Ex vivo* mucoadhesive force measurements (Paper II) provided a preliminary understanding of these three designs. Finally, an *in vivo* study was implemented to validate the mucoadhesion performance of each design. After the *in vivo* study, we extracted the GI tract to observe MCs distribution by planar X-ray imaging. CT scanning provided spatial dynamics of MCs in the small intestine. Then the detailed mucosa interaction of MCs was inspected by CryoSEM.

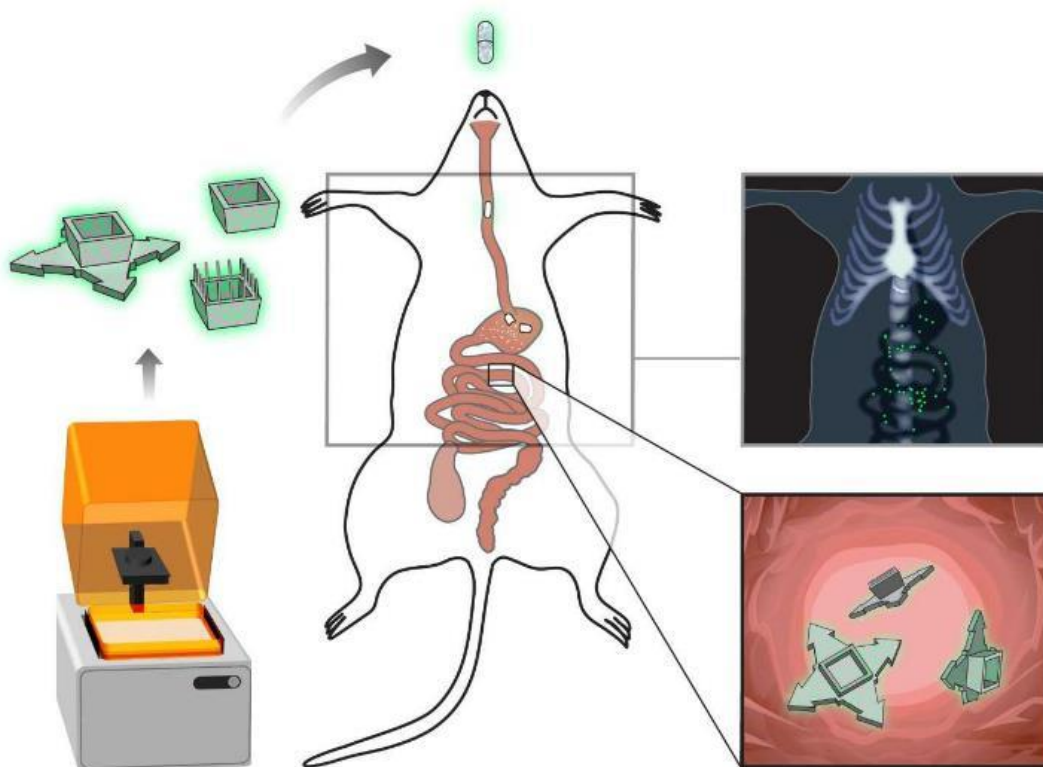


Figure 25. Schematic illustration of the experimental setup. Radiopaque microcontainers (MCs) were 3D printed in three designs (neutral, pillar, and arrow) and dosed to rats in gelatin capsules using oral gavage. Their location in the gastrointestinal (GI) tract was determined by planar X-ray imaging at four time-points (0.5, 1, 2, and 3 h) after dosing. Further observation of spatial dynamics and mucosal interactions of MCs in the small intestine was carried out using CT scanning and CryoSEM, respectively.

Design and fabrication of 3D printed microcontainers

To realize self-orientation, we designed the MCs with an asymmetrical structure (neutral design), with a larger area on the top side (with a cavity for the release), as shown in **Figure 26A**. The increased contact area might have larger mucoadhesion, increasing the chance of facing the top side directly to the mucosa. In addition, we designed micro-pillars as additive features on the MCs to assist stronger mucoadhesion (pillar design). The 10- μm -diameter micro-pillars can penetrate the mucus mesh structure for entanglement. Finally, four arrow structures were added on the side of the neutral MCs (arrow design). The large contact area might further enhance mucoadhesion, and the arrow structure can hook the mucus layer for deeper entanglement.

These three designs were successfully realized by utilizing the high-resolution HD-DVD 3D printer (Paper I). The biocompatible photopolymer was cured into the designed structure of MCs. The MCs were fabricated in a 10×10 array on the Si chip (**Figures 26B and C**). **Figures 26D and G** show the clear overhanging structure of the neutral design. The dimension of the neutral design were $400 \times 300 \times 200 \mu\text{m}^3$ (length \times width \times height). A total of 16 micro-pillars

were printed on the MCs (**Figures 26E and H**). The arrow structures printed on the side expand the MCs dimension to around 900 μm (**Figures 26F and I**).

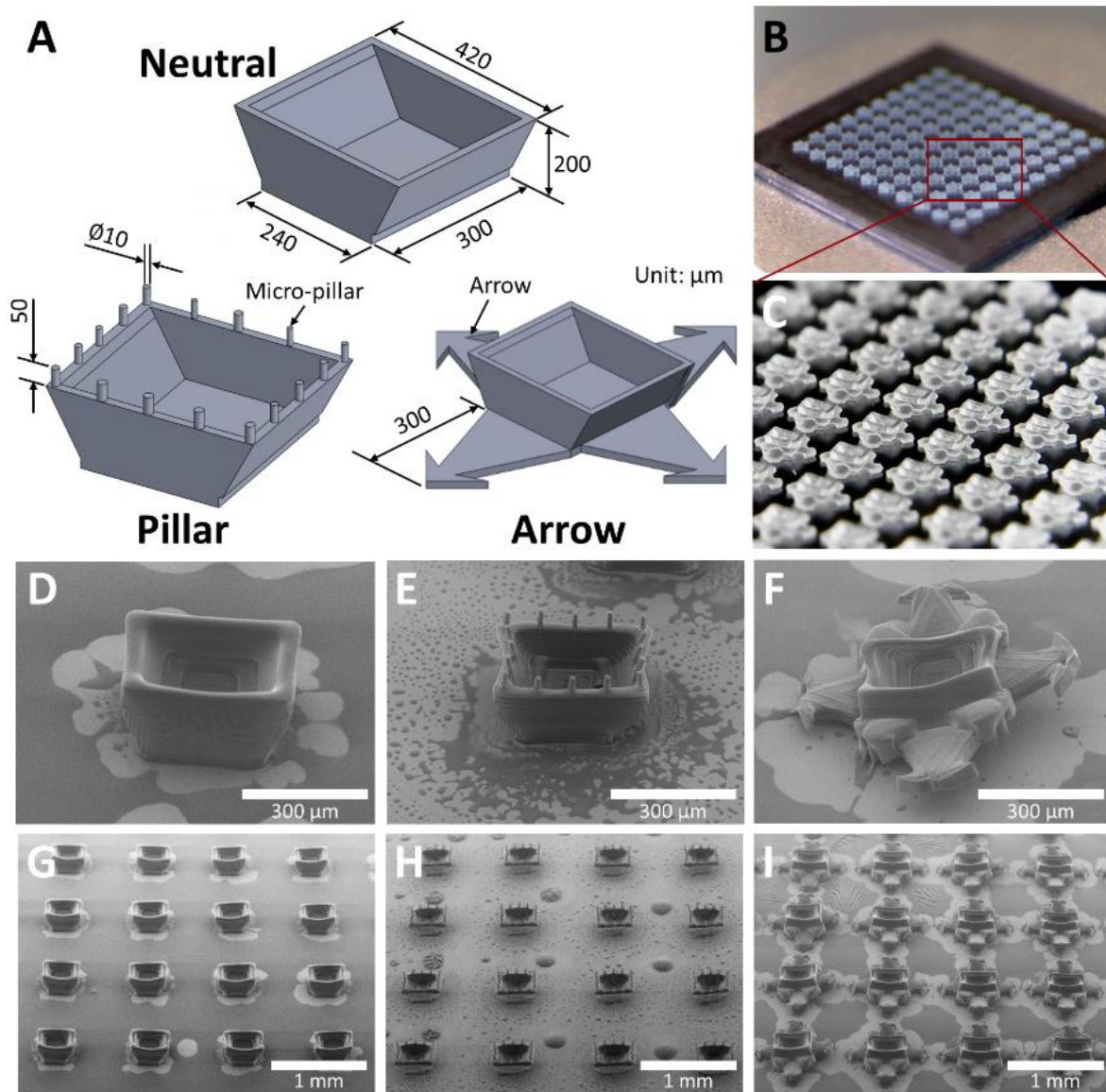


Figure 26. Design and fabrication of 3D printed microcontainers (MCs) with enhanced mucoadhesion geometry. **A)** Illustration and dimension of three designs, neutral, pillar, and arrow. **B)** Photograph of 3D printed 100 MCs in a 10×10 array on Si chip. **C)** Microscope image of detailed 3D printed MCs result. SEM images show MCs of **D)** neutral, **E)** pillar and **F)** arrow design. **G-I)** SEM images of the 3D printed large amount of MCs.

Ex vivo mucoadhesive forces measurement

To investigate the interaction between these three designs and mucus layer, we utilized the proposed OPU force analyzer (Paper II) to measure the mucoadhesive force of each designed MCs. Two *ex vivo* studies were operated to investigate the orientation, and mucoadhesion of additive features, respectively. In both studies, we utilized porcine small intestinal tissue.

In the study of orientation investigation, the force analyzer measured the mucoadhesive force of both sides of the MCs for comparison. In addition, symmetrical square MCs (dimension: $300 \times 200 \mu\text{m}^2$, width \times height) were 3D printed as control compared to asymmetrical neutral and arrow design. These designs were glued on the microprobe with the top and bottom sides upward, respectively (**Figure 27A**). The force analyzer recorded the mucoadhesive force while approaching and withdrawing the MCs during the measurement (**Figure 27C**). To eliminate the tissue variation, we used the microprobe as a standard to normalize the mucoadhesive force measured from different tissues. The result indicates that the square MCs have the same level of mucoadhesive force on both sides (**Figure 27D**). The top side of neutral MCs shows a larger mucoadhesion than the bottom side, proving the asymmetrical structure design. The arrow MCs show the significant enhancement of mucoadhesive forces on both sides. The result validates that the mucoadhesion has a direct relationship with the contact area at the microscale dimension. However, both the bottom side of neutral MC and square MC present a similar level of mucoadhesive forces, even if the bottom side of neutral MCs has a smaller area. The reason might be that the lateral slope on the bottom side of neutral MCs is still in contact with mucus for adhering.

In the study of additive features, we only measured the mucoadhesive forces on the top side of MCs for comparison of different additive features. The neutral was used as a control for representing no additive feature. Besides, the micro-pillars and forks were printed on MCs, respectively (**Figure 27B**). **Figure 27E** shows the normalized mucoadhesive force result. The micro-pillars show a slight enhancement of mucoadhesion compared to the other two types. However, none of these features presents a significant enhancement of mucoadhesive force.

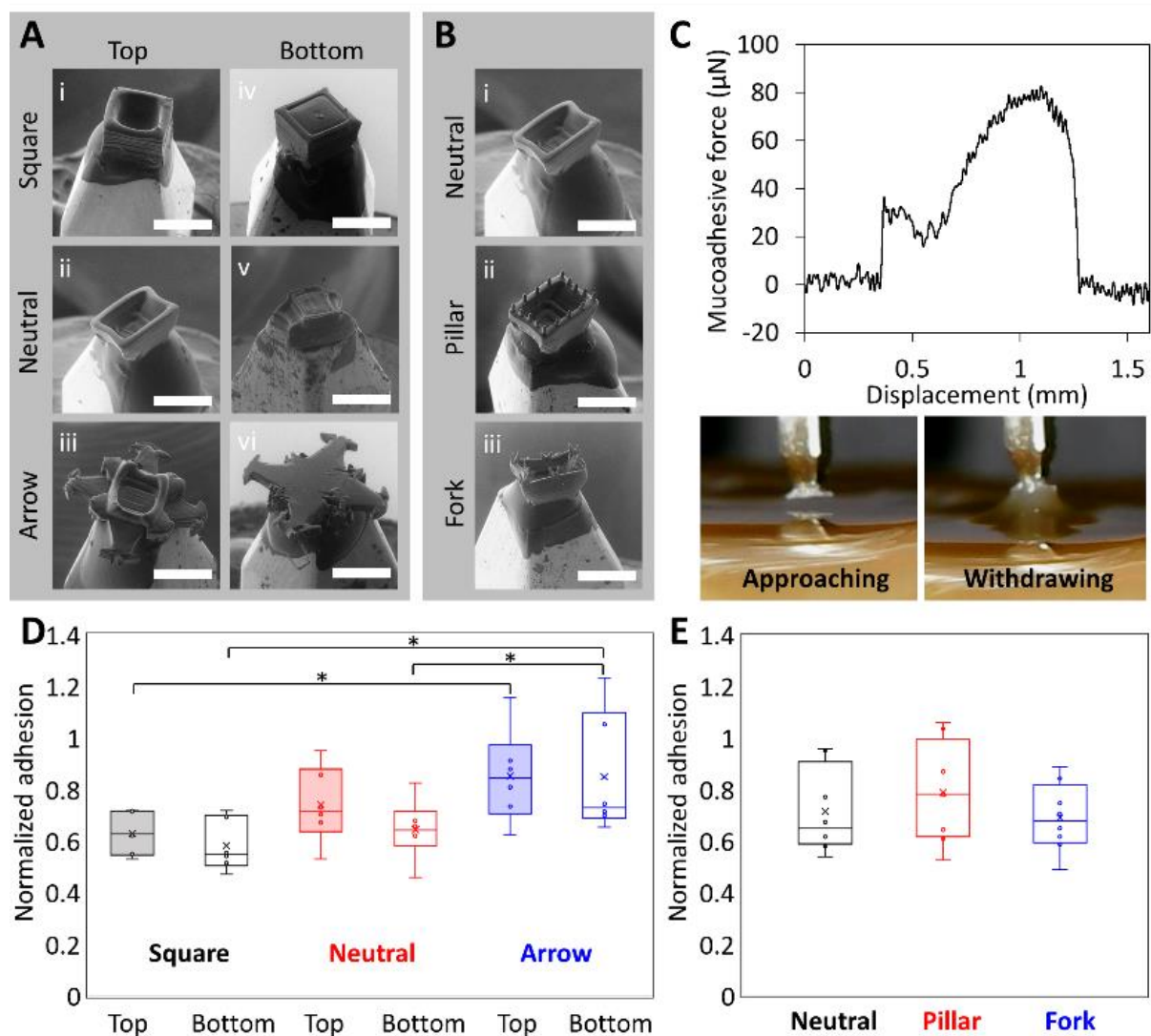


Figure 27. *Ex vivo* mucoadhesive force measurement of orientation and additive feature studies. **A)** SEM images of fixing a single (i) square, (ii) neutral, and (iii) arrow microcontainers (MCs) on microprobe with the top side upward; and (iv) square, (v) neutral, and (vi) arrow MC on the microprobe with the bottom side upward (scale bar: 300 μm). **B)** SEM image of fixing a single (i) neutral, (ii) pillar, and (iii) fork MC on the microprobe (scale bar: 300 μm). **C)** Mucoadhesive force versus displacement curve while approaching and withdrawing bottom side of arrow MC to porcine small intestinal tissue. **D)** Orientation study showing normalized mucoadhesion on both top and bottom sides of the square, neutral, and arrow MC. Mean \pm SD, $n = 6$, t-Test with two-sample variances. **E)** Additive feature study showing normalized mucoadhesion on the top side of neutral, pillar, and fork MC. Mean \pm SD, $n = 6$.

3D printed radiopaque microcontainers

As mentioned in subsection 2.3.2, the *in vivo* study can comprehensively understand the transition mechanism. In this study, the contrast agent BaSO_4 was used to track the MCs in the GI tract. The photopolymer manual mixed with BaSO_4 nanoparticles (37.9 w/v %) was cured into three designs of MCs (**Figures 28A-C**). **Figure 28D** shows a strong contrast of BaSO_4 nanoparticles embedded in the MCs.

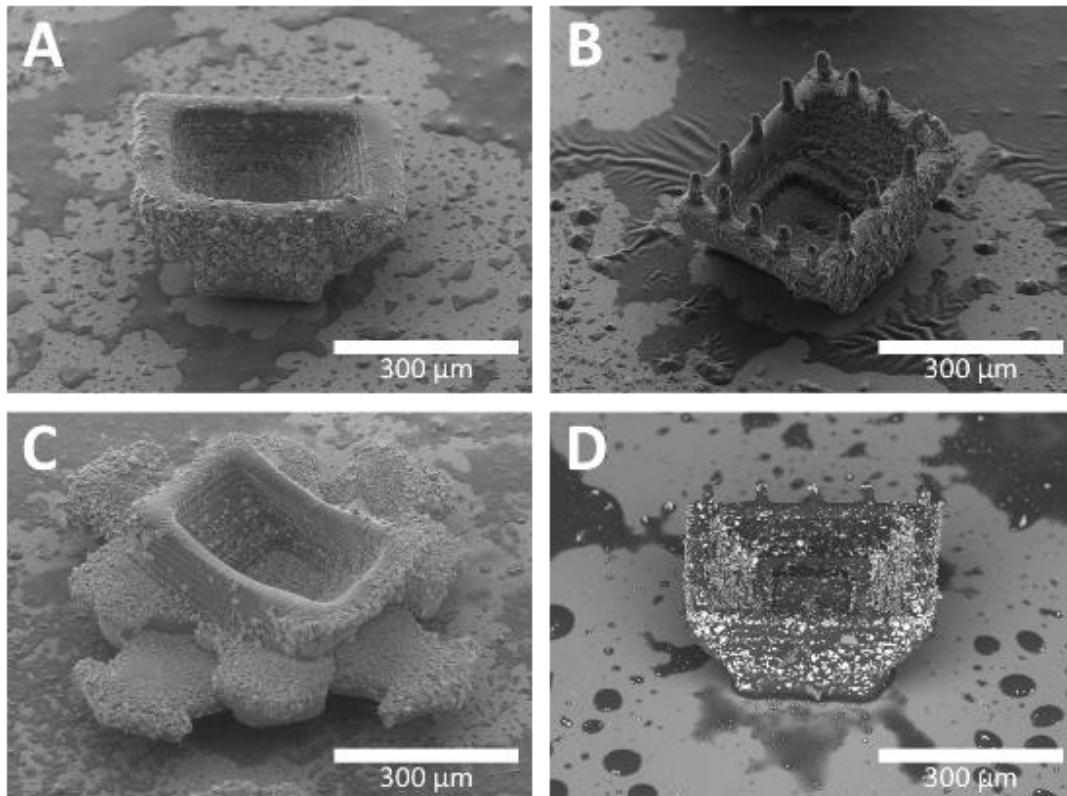


Figure 28. 3D printed radiopaque microcontainers (MCs) with embedded BaSO₄ nanoparticles. SEM image of **A)** neutral design, **B)** pillar design, **C)** arrow design, and **D)** high image contrast indicating BaSO₄ nanoparticles.

Besides, an energy dispersive x-ray analysis (EDX) method showed the surface distribution of the photopolymer and BaSO₄ by analyzing elements. Carbon, oxygen, barium, and sulfur were detected and mapped (**Figure 29A**), and the SEM image revealed a rough surface with numerous protruded microparticles. Although BaSO₄ nanoparticles were used, the aggregation effect led to microscale particle size. Besides this, the homogeneity of the BaSO₄ particles seemed weak (**Figure 29B**). The reason is the insolubility of BaSO₄ to the photopolymer. In the printing process, BaSO₄ was temporarily suspended in the photopolymer and gradually sedimented. The suspension effect of this material recipe is kept for over one day, allowing a complete 3D printing cycle.

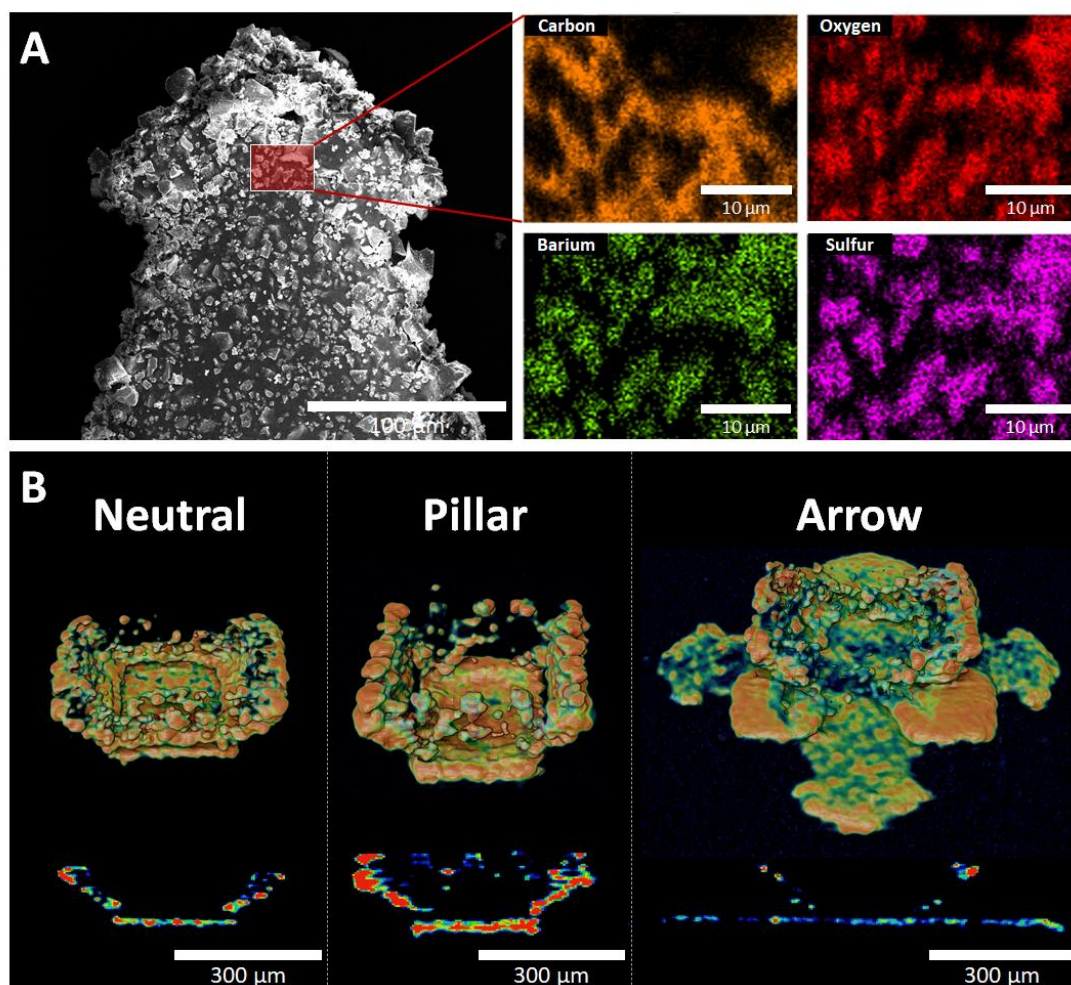


Figure 29. EDX analysis and μ CT scanning. **A)** SEM image of radiopaque microcontainers surface and EDX analysis mapping of detected elements, including carbon, oxygen, barium, and sulfur. **B)** μ CT scanning showing the homogeneity of BaSO₄ nanoparticles in the 3D printed radiopaque microcontainers.

Quantitative GI tract tracking for retention and transit time

To further confirm the mucoadhesive properties observed from the *ex vivo* study, we implemented an *in vivo* study in rats to analyze the transit time of these three MCs designs. Planar X-ray imaging was utilized for quantitative GI tracking. After oral administration of the 3D printed radiopaque MCs, the rats were euthanized at different time points of 0.5, 1, 2, and 3 h. Then the GI tracts were extracted for planar X-ray imaging. The X-ray images showed radiopaque MCs with a high contrast image for counting retained MCs at each time point (**Figure 30**).

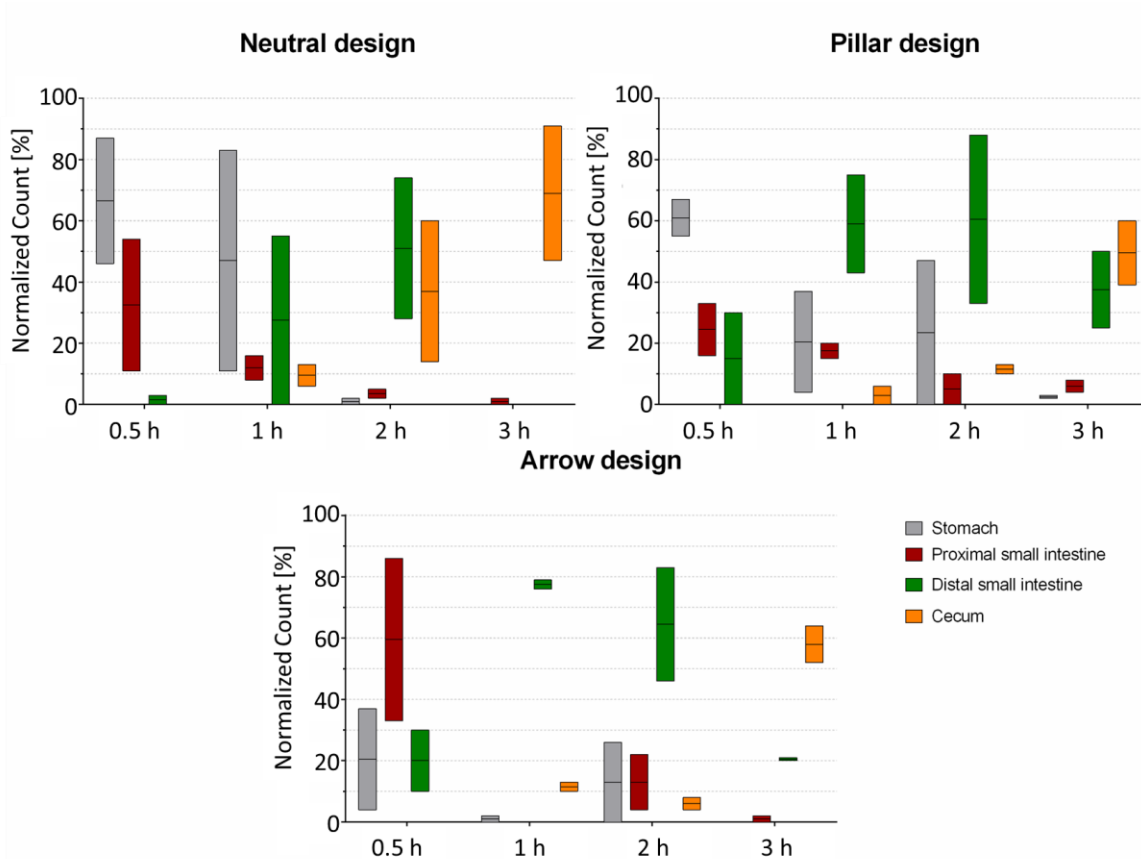


Figure 30. Gastrointestinal (GI) retention and transit time of neutral, pillar, and arrow microcontainers (MCs). Graphs showing the normalized count of each design of MCs at specific locations over time.

These results present that all three designed MCs entered the stomach after 0.5 h. For the neutral and pillar design of MCs, after 0.5 h, an average of around 60 % of MCs was found in the stomach. After 1 h, 10 % of the MCs appeared in the caecum. The amount of MCs which reached caecum increased to around 50-70 % after 3 h. After 0.5 h, only 20 % of the arrow design of MCs was found in the stomach, and around 60 % of the MCs reached the proximal small intestine. The overall result shows an apparent trend of entering and exiting the distal part of the small intestine. After 3 h, most of the three designs of MCs arrived in the caecum. However, around 40 % of the pillar design of MCs was distributed in the distal small intestine. The pillar design has a trend of longer retention time in the small intestine.

The result indicates that the pillar design of MCs slightly extends retention time in the small intestine. However, this *in vivo* rats study implies no significant mucoadhesion enhancement of all these three designs. Even though the arrow design of MCs presented a stronger mucoadhesion in the previous *ex vivo* study, the result did not translate into longer intestinal retention. The mucoadhesive force measured by *ex vivo* tensile strength measurement only

contains the force along the vertical direction. However, mucosal interaction of MCs also includes shear and detachment strength during the transit process [68]. Therefore, a complete mucoadhesive force measurement, including tensile, shear, and detachment strength, should be conducted to obtain a closer to actual condition outcome.

Although the micro-pillars structure shows longer retention than arrows structure is not a significant trend in this *in vivo* study, it might still reveal a possible development direction in the future. The 3D printed micro-pillars are average 10 – 15 μm in diameter, which is close to the hole of mucin mesh structure observed using SEM (**Figure 3A**) [65]. Hence, the micro-pillars might penetrate the mesh structure and increase interaction. Some microdevices also utilized similar strategies, such as straw-like pillar and wire, but nanoscale features to enhance mucoadhesion [103,104]. Recently, theragrippers utilized micro hooks (with tips of 3 μm in diameter) to actively grip the mucus of colon for over 24 h retention [105]. These studies indicate that the complex feature close to or smaller than mucus mesh structure can increase mucoadhesion. Other more complex microscale additive features might perform longer retention of MCs, like the microscale forks structure demonstrated in the previous *ex vivo* study (**Figure 27B**). While a complex design of anchor-like feature on a millimeter-scale 3D printed reservoir devices presented a promising enhancement of mucoadhesion in both *ex vivo* tensile strength and *ex vivo* flow-through study [10], this design can also be minimized to microscale dimension for extending intestinal retention.

Spatial dynamic and mucosal interaction

To further investigate the transit process of MCs inside the GI tract, we tried to observe spatial dynamics and mucosal interaction of MCs by CT scanning and CryoSEM, respectively. Spatial dynamics presents the 3D spatial posture of MCs in the small intestine (**Figure 31A**). Simultaneously, mucosal interactions describe the embedment of MCs in the mucosa and their specific orientation. Two pillar MCs were embedded in the mucosa with sideways release direction (**Figure 31B**). **Figure 31C** shows a pillar MC facing the release-side to the mucosa. The CryoSEM image observed the gesture and shape of MCs. As the MCs were embedded in the mucus, it is challenging to recognize their surface texture and micro-pillars feature. Despite the observation that the orientation presents a direct release to the mucosa, the random sampling data cannot provide solid evidence to support the designed self-orientation property. More data is needed for statistical analysis.

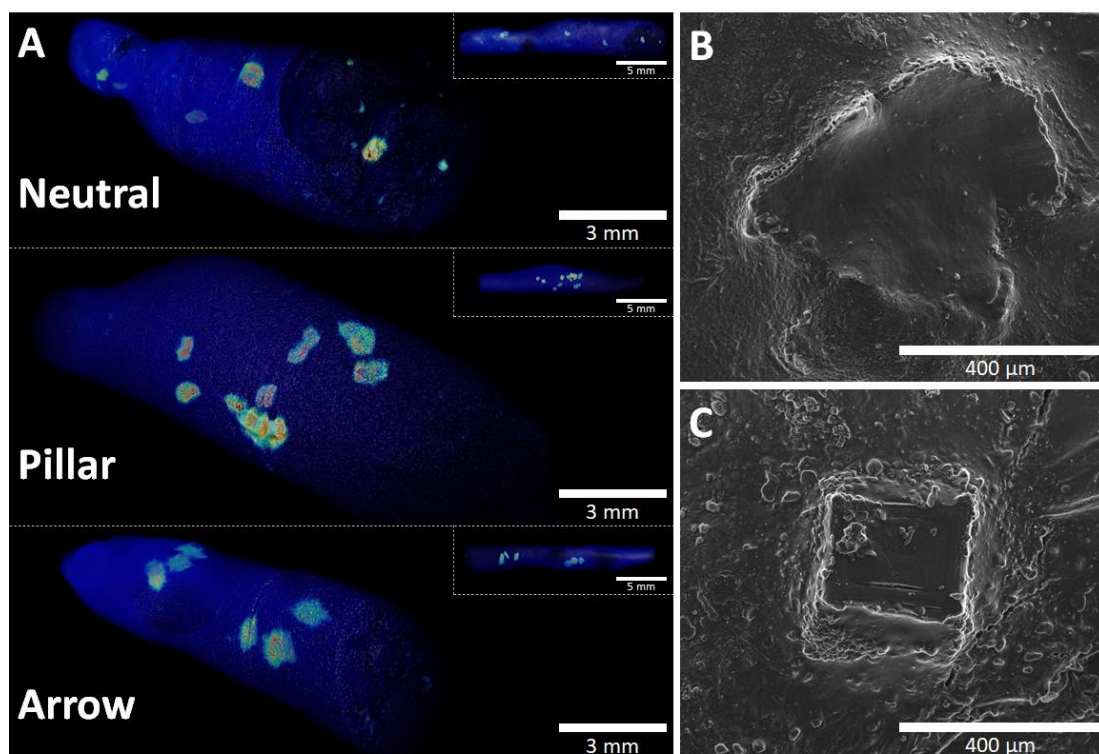


Figure 31. CT scan and CryoSEM image showing spatial dynamics and mucosal interactions of microcontainers (MCs). **A)** CT scan images of neutral, pillar, and arrow MCs inside small intestinal pieces, exhibiting their spatial dynamics. CryoSEM images of pillar MCs showing mucosal interactions such as embedment into the intestinal tissue and the MC orientation of **B)** side-way and **C)** facing the release side to the mucosa.

In vitro proof of concept of 3D printed MCs for controlled oral drug delivery

To evaluate that the 3D printed MCs perform the capability of carrying drug and controlled release, we loaded the 3D printed MCs with furosemide as a model drug (**Figure 32A**). Then the MCs were coated with a pH-sensitive polymer of Eudragit® L100 (**Figure 32B**). The release of furosemide was measured in media with gastric and intestinal pH values. Total 1.0 ± 0.2 mg furosemide powder was filled in 100 MCs. Each MC contented approximately 10 μ g of furosemide.

We studied the *in vitro* release profile of furosemide from MCs by a microDISS Profiler™ (**Figure 32C**). The release study consisted of two steps: a 30 min gastric step (4mM hydrochloric acid pH 2.4) and an intestinal step (PBS, pH 7.5). In the gastric step, 4.4 ± 1.0 % (mean \pm SD, n = 4) furosemide was released. When the study switched to the intestinal media, furosemide was continuously released until 90 min, with total released furosemide of 90.6 ± 5.0 % (mean \pm SD, n = 4). The 3D printed MCs presented a promising release profile. As a result, the 3D printed MCs can be used for target delivery of drugs to the small intestine through the oral delivery route.

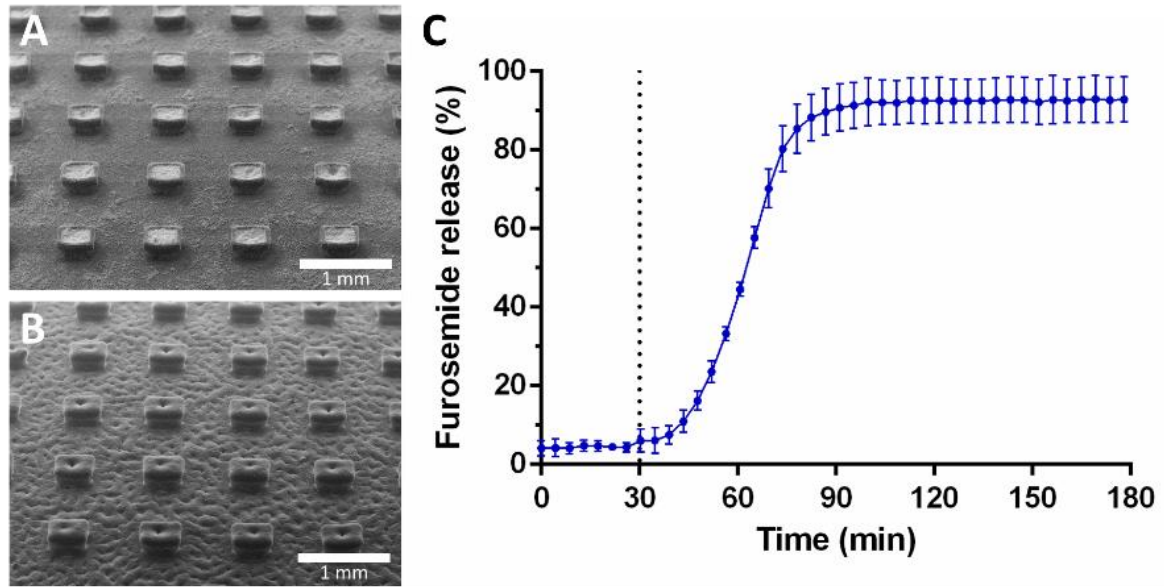


Figure 32. Proof-of-concept of the 3D printed microcontainers (MCs) for targeted drug delivery to the small intestine. SEM images of 3D printed neutral MCs **A**) loaded with furosemide powder, and **B**) coated with Eudragit® L100. **C**) Percentage release of furosemide from MCs. The release was measured in gastric pH (pH 2.4) in the first 30 min, followed by intestinal pH (pH 7.5). Mean \pm SD, n = 4.

4. Conclusion

In this project, we successfully developed a micro/nanoscale resolution large-volume 3D printer utilizing an HD-DVD OPU. This 3D printer is a suitable tool to manufacture the innovative geometry of MCs, especially from the aspect of printing resolution, scaling up, and effective cost. Besides, the OPU based force analyzer was developed for the measurement of force from newton to nano-newton. This force analyzer performs reliable characterization of mucoadhesion for a single MC via *ex vivo* study.

Three designs of MCs with overhanging structures and delicate additive features were produced with a large amount (approximately 2000 units in this thesis) by the 3D printing method. The 3D printed MCs were proofed the concept for controlled release drug, furosemide, by *in vitro* release study. The designed features, asymmetrical MCs, micro-pillar, and arrow, showed enhanced mucoadhesion in the *ex vivo* tensile strength measurement. However, the *ex vivo* study outcome did not translate into extended retention via *in vivo* study. Despite the fact that the *in vivo* result implies that the micro-pillars have a slight trend of enhanced mucoadhesion, no significant enhancement is found through all of these three designs. The overall result indicates that the mucoadhesive properties of the proposed MCs designs are not more vital enough to extend intestinal retention.

In addition, the procedure of 3D printed microdevices incorporated with BaSO₄ particles was developed to obtain mucoadhesive properties of MCs after *in vivo* study. Planar X-ray, CT scan, and CryoSEM were utilized to observe distribution, spatial dynamics, and mucosa interactions of MCs in the GI tract, respectively. With all these powerful tools proposed in this project, we established a complete process for studying the geometric design of MCs. This toolset can shorten the development cycle time of future design and assist with more helpful information for geometry optimization.

5. Future perspectives

In this project, we have already demonstrated a successful 3D printing technique to realize the innovative microscale structure of the MCs. Since the result implies that delicate small structure designs, micro-pillars, tend to increase mucoadhesion, sort of small complex structures (close to mucin mesh structure dimension) should be focused on enhancing the interaction of mucin mesh structure in the future. Besides, applying concept of active microdevices, e.g., microrobots, might have a breakthrough improvement of intestinal retention time [169]. The *ex vivo* tensile strength measurement characterized the mucoadhesion only along the vertical direction; hence the result is difficult to translate into *in vivo* outcome directly. The mucoadhesion along the shear direction should be taken into consideration. Besides, the *in vivo* study for evaluation of drug absorption can validate the delivery performance of designed MCs. More MCs should be delivered to reach an equivalent therapeutic effect or detectable dosage of the drug.

The proposed 3D printer produced sufficient MCs for *in vivo* study to observe MCs transit mechanism. However, the current throughput is still a challenge to implement a full *in vivo* drug release study. The manufacturing capacity of the printer can be further optimized by turning printing speed and laser power. Furthermore, as the core optical module, OPU, is compact, the printer is possible to integrate multiple OPUs in 2×2 or 3×3 matrices to achieve multiplying throughput.

Directly printing API inside the structure of MCs might further expand the functionality of MCs, such as co-delivery or multiple drugs [170]. By optimizing the recipe for mixing API into the photopolymer, the printer might directly cure formulation to solid structure [137]. The MCs reservoir can load other drugs for multiple drug release, a propellant for self-propelled movement [171], or a reaction component for sampling gut microbiota [172].

6. References

- [1] M.H. Becker, L.A. Maiman, Strategies for enhancing patient compliance, *J. Community Health*. 6 (1980) 113–135.
- [2] S. Asgari, A. Pourjavadi, T. Rask, A. Boisen, F. Ajalloueiian, Polymeric carriers for enhanced delivery of probiotics, *Adv. Drug Deliv. Rev.* 161–162 (2020) 1–21. <https://doi.org/10.1016/j.addr.2020.07.014>.
- [3] K.K. Jain, Drug Delivery Systems – An Overview, in: K.K. Jain (Ed.), *Drug Deliv. Syst.*, Humana Press, Totowa, USA, 2008: pp. 1–50.
- [4] D.F. Evans, G. Pye, R. Bramley, A.G. Clark, T.J. Dyson, J.D. Hardcastle, Measurement of gastrointestinal pH profiles in normal ambulant human subjects, *Gut*. 29 (1988) 1035–1041. <https://doi.org/10.1136/gut.29.8.1035>.
- [5] C. Mazzoni, F. Tentor, S.A. Strindberg, L.H. Nielsen, S.S. Keller, T.S. Alstrøm, C. Gundlach, A. Müllertz, P. Marizza, A. Boisen, From concept to in vivo testing: Microcontainers for oral drug delivery, *J. Control. Release*. 268 (2017) 343–351. <https://doi.org/10.1016/j.jconrel.2017.10.013>.
- [6] K. Kamguyan, A.M. Torp, J.F. Christfort, P.R. Guerra, T.R. Licht, L. Hagner Nielsen, K. Zor, A. Boisen, Colon-Specific Delivery of Bioactive Agents Using Genipin-Cross-Linked Chitosan Coated Microcontainers, *ACS Appl. Bio Mater.* 4 (2021) 752–762. <https://doi.org/10.1021/acsabm.0c01333>.
- [7] L.H. Nielsen, J. Nagstrup, S. Gordon, S.S. Keller, J. Østergaard, T. Rades, A. Müllertz, A. Boisen, pH-triggered drug release from biodegradable microwells for oral drug delivery, *Biomed. Microdevices*. 17 (2015) 55. <https://doi.org/10.1007/s10544-015-9958-5>.
- [8] S.L. Tao, M.W. Lubeley, T.A. Desai, Bioadhesive poly(methyl methacrylate) microdevices for controlled drug delivery, *J. Control. Release*. 88 (2003) 215–228. [https://doi.org/10.1016/S0168-3659\(03\)00005-1](https://doi.org/10.1016/S0168-3659(03)00005-1).
- [9] M. Dalskov Mosgaard, S. Strindberg, Z. Abid, R. Singh Petersen, L. Højlund Eklund Thamdrup, A. Joukainen Andersen, S. Sylvest Keller, A. Müllertz, L. Hagner Nielsen, A. Boisen, Ex vivo intestinal perfusion model for investigating mucoadhesion of microcontainers, *Int. J. Pharm.* 570 (2019) 118658. <https://doi.org/10.1016/j.ijpharm.2019.118658>.
- [10] L. Vaut, J.J. Juszczyk, K. Kamguyan, K.E. Jensen, G. Tosello, A. Boisen, 3D Printing of Reservoir Devices for Oral Drug Delivery: From Concept to Functionality through Design Improvement for Enhanced Mucoadhesion, *ACS Biomater. Sci. Eng.* 6 (2020) 2478–2486. <https://doi.org/10.1021/acsbiomaterials.9b01760>.
- [11] R.B. Kjeldsen, M.N. Kristensen, C. Gundlach, L.H.E. Thamdrup, A. Müllertz, T. Rades, L.H. Nielsen, K. Zór, A. Boisen, X-ray Imaging for Gastrointestinal Tracking of Microscale Oral Drug Delivery Devices, *ACS Biomater. Sci. Eng.* 7 (2021) 2538–2547. <https://doi.org/10.1021/acsbiomaterials.1c00225>.
- [12] S. Mansuri, P. Kesharwani, K. Jain, R.K. Tekade, N.K. Jain, Mucoadhesion: A promising approach in drug delivery system, *React. Funct. Polym.* 100 (2016) 151–172. <https://doi.org/10.1016/j.reactfunctpolym.2016.01.011>.
- [13] L.H. Nielsen, S.S. Keller, A. Boisen, Microfabricated devices for oral drug delivery.,

- Lab Chip. 18 (2018) 2348–2358. <https://doi.org/10.1039/c8lc00408k>.
- [14] R.S. Petersen, R. Mahshid, N.K. Andersen, S.S. Keller, H.N. Hansen, A. Boisen, Hot embossing and mechanical punching of biodegradable microcontainers for oral drug delivery, *Microelectron. Eng.* 133 (2015) 104–109. <https://doi.org/10.1016/j.mee.2014.11.009>.
- [15] R.S. Petersen, S.S. Keller, A. Boisen, Hot punching of high-aspect-ratio 3D polymeric microstructures for drug delivery, *Lab Chip*. 15 (2015) 2576–2579. <https://doi.org/10.1039/c5lc00372e>.
- [16] S.C. Ligon, R. Liska, J. Stampfl, M. Gurr, R. Mülhaupt, Polymers for 3D Printing and Customized Additive Manufacturing, *Chem. Rev.* 117 (2017) 10212–10290. <https://doi.org/10.1021/acs.chemrev.7b00074>.
- [17] R.R. Reiner, Y. Tanguy, J. Hoffmann, Process for producing a three-dimensional structure, 2016.
- [18] C. Schmidleithner, D.M. Kalaskar, Stereolithography, in: D. Cvetković (Ed.), *3D Print.*, IntechOpen, London, UK, 2018: pp. 3–22. <https://doi.org/10.5772/intechopen.78147>.
- [19] W. Xiong, L.J. Jiang, T. Baldacchini, Y.F. Lu, Laser additive manufacturing using nanofabrication by integrated two-photon polymerization and multiphoton ablation, in: M. Brandt (Ed.), *Laser Addit. Manuf.*, Elsevier, New York, 2017: pp. 237–256. <https://doi.org/10.1016/B978-0-08-100433-3.00009-9>.
- [20] S. Maruo, O. Nakamura, S. Kawata, Three-dimensional microfabrication with two-photon-absorbed photopolymerization, *Opt. Lett.* 22 (1997) 132. <https://doi.org/10.1364/OL.22.000132>.
- [21] T.S.B. Schmidt, J. Raes, P. Bork, The Human Gut Microbiome: From Association to Modulation, *Cell*. 172 (2018) 1198–1215. <https://doi.org/10.1016/j.cell.2018.02.044>.
- [22] L. Kopp-Hoolihan, Prophylactic and Therapeutic Uses of Probiotics, *J. Am. Diet. Assoc.* 101 (2001) 229–241. [https://doi.org/10.1016/S0002-8223\(01\)00060-8](https://doi.org/10.1016/S0002-8223(01)00060-8).
- [23] P. Begum, G. Madhavi, S. Rajagopal, B. Viswanath, M. Razak, V. Venkataratnamma, Probiotics as Functional Foods: Potential Effects on Human Health and its Impact on Neurological Diseases, *Int. J. Nutr. Pharmacol. Neurol. Dis.* 7 (2017) 23–33. https://doi.org/10.4103/ijnpnd.ijnpnd_90_16.
- [24] M.E. Sanders, I. Lenoir-Wijnkoop, S. Salminen, D.J. Merenstein, G.R. Gibson, B.W. Petschow, M. Nieuwdorp, D.J. Tancredi, C.J. Cifelli, P. Jacques, B. Pot, Probiotics and prebiotics: prospects for public health and nutritional recommendations, *Ann. N. Y. Acad. Sci.* 1309 (2014) 19–29. <https://doi.org/10.1111/nyas.12377>.
- [25] M.E. Sanders, Probiotics: Considerations for Human Health, *Nutr. Rev.* 61 (2003) 91–99. <https://doi.org/10.1301/nr.2003.marr.91-99>.
- [26] K. Whelan, Probiotics and prebiotics in the management of irritable bowel syndrome, *Curr. Opin. Clin. Nutr. Metab. Care.* 14 (2011) 581–587. <https://doi.org/10.1097/MCO.0b013e32834b8082>.
- [27] P. Moayyedi, A.C. Ford, N.J. Talley, F. Cremonini, A.E. Foxx-Orenstein, L.J. Brandt, E.M.M. Quigley, The efficacy of probiotics in the treatment of irritable bowel syndrome: A systematic review, *Gut*. 59 (2010) 325–332. <https://doi.org/10.1136/gut.2008.167270>.

- [28] D.J. Costa, P. Marteau, M. Amouyal, L.K. Poulsen, E. Hamelmann, M. Cazaubiel, B. Housez, S. Leuillet, M. Stavnsbjerg, P. Molimard, S. Courau, J. Bousquet, Efficacy and safety of the probiotic *Lactobacillus paracasei* LP-33 in allergic rhinitis: A double-blind, randomized, placebo-controlled trial (GA2LEN Study), *Eur. J. Clin. Nutr.* 68 (2014) 602–607. <https://doi.org/10.1038/ejcn.2014.13>.
- [29] M.F. Wang, H.C. Lin, Y.Y. Wang, C.H. Hsu, Treatment of perennial allergic rhinitis with lactic acid bacteria, *Pediatr. Allergy Immunol.* 15 (2004) 152–158. <https://doi.org/10.1111/j.1399-3038.2004.00156.x>.
- [30] K. Martens, B. Pugin, I. De Boeck, I. Spacova, B. Steelant, S.F. Seys, S. Lebeer, P.W. Hellings, Probiotics for the airways: Potential to improve epithelial and immune homeostasis, *Allergy.* 73 (2018) 1954–1963. <https://doi.org/10.1111/all.13495>.
- [31] U. Agrawal, R. Sharma, M. Gupta, S.P. Vyas, Is nanotechnology a boon for oral drug delivery ?, *Drug Discov. Today.* 19 (2014) 1530–1546. <https://doi.org/10.1016/j.drudis.2014.04.011>.
- [32] S. Maher, D.J. Brayden, Overcoming poor permeability: translating permeation enhancers for oral peptide delivery, *Drug Discov. Today Technol.* 9 (2012) e113–e119. <https://doi.org/10.1016/j.ddtec.2011.11.006>.
- [33] A.C. Anselmo, S. Mitragotri, An overview of clinical and commercial impact of drug delivery systems, *J. Control. Release.* 190 (2014) 15–28. <https://doi.org/10.1016/j.jconrel.2014.03.053>.
- [34] A.C. Anselmo, Y. Gokarn, S. Mitragotri, Non-invasive delivery strategies for biologics, *Nat. Rev. Drug Discov.* 18 (2018) 19–40. <https://doi.org/10.1038/nrd.2018.183>.
- [35] J. Jin, G.E. Sklar, V.M. Sen Oh, S.C. Li, Factors affecting therapeutic compliance: A review from the patient’s perspective, *Ther. Clin. Risk Manag.* 4 (2008) 269–286. <https://doi.org/10.2147/TCRM.S1458>.
- [36] J.M. Neutel, D.H.G. Smith, Improving Patient Compliance: A Major Goal in the Management of Hypertension, *J. Clin. Hypertens.* 5 (2003) 127–132. <https://doi.org/10.1111/j.1524-6175.2003.00495.x>.
- [37] C. Loh, A. MacRobert, J. Bedwell, J. Regula, N. Krasner, S. Bown, Oral versus intravenous administration of 5-aminolaevulinic acid for photodynamic therapy, *Br. J. Cancer.* 68 (1993) 41–51. <https://doi.org/10.1038/bjc.1993.284>.
- [38] L. Sultatos, Drug Absorption from the Gastrointestinal Tract, in: S.J. Enna, D.B. Bylund (Eds.), *XPharm Compr. Pharmacol. Ref.*, Elsevier, Berlin, Heidelberg, 2007: pp. 1–2. <https://doi.org/10.1016/B978-008055232-3.60021-2>.
- [39] D.U. Silverthorn, The digestive system, in: *Hum. Physiol. An Integr. Approach*, Pearson, London, 2016: pp. 654–692.
- [40] L.M. Ensign, R. Cone, J. Hanes, Oral drug delivery with polymeric nanoparticles: The gastrointestinal mucus barriers, *Adv. Drug Deliv. Rev.* 64 (2012) 557–570. <https://doi.org/10.1016/j.addr.2011.12.009>.
- [41] J.L. Madara, REGULATION OF THE MOVEMENT OF SOLUTES ACROSS TIGHT JUNCTIONS, *Annu. Rev. Physiol.* 60 (1998) 143–159. <https://doi.org/10.1146/annurev.physiol.60.1.143>.
- [42] J.E. Vela Ramirez, L.A. Sharpe, N.A. Peppas, Current state and challenges in

- developing oral vaccines, *Adv. Drug Deliv. Rev.* 114 (2017) 116–131.
<https://doi.org/10.1016/j.addr.2017.04.008>.
- [43] Xin Hua Zhou, Overcoming enzymatic and absorption barriers to non-parenterally administered protein and peptide drugs, *J. Control. Release.* 29 (1994) 239–252.
[https://doi.org/10.1016/0168-3659\(94\)90071-X](https://doi.org/10.1016/0168-3659(94)90071-X).
- [44] K. Thanki, R.P. Gangwal, A.T. Sangamwar, S. Jain, Oral delivery of anticancer drugs: Challenges and opportunities, *J. Control. Release.* 170 (2013) 15–40.
<https://doi.org/10.1016/j.jconrel.2013.04.020>.
- [45] Anatomy of the Digestive System, (n.d.). <https://www.saintlukeskc.org/health-library/anatomy-digestive-system>.
- [46] P.S. Leung, ed., *The gastrointestinal system*, Springer, New York, 2014.
- [47] A. Fanucci, P. Cerro, E. Fanucci, Normal Small-Bowel Measurements by Enteroclysis, *Scand. J. Gastroenterol.* 23 (1988) 574–576.
<https://doi.org/10.3109/00365528809093914>.
- [48] H.F. Helander, L. Fändriks, Surface area of the digestive tract-revisited, *Scand. J. Gastroenterol.* 49 (2014) 681–689. <https://doi.org/10.3109/00365521.2014.898326>.
- [49] M.G. Sarr, J.J. Cullen, M.F. Otterson, Gastrointestinal motility, in: W.W. Souba, D.W. Wilmore (Eds.), *Surg. Res.*, Academic Press, United States, 2001: pp. 507–532.
- [50] S. Sadahiro, T. Ohmura, Y. Yamada, T. Saito, Y. Taki, Analysis of length and surface area of each segment of the large intestine according to age, sex and physique, *Surg. Radiol. Anat.* 14 (1992) 251–257. <https://doi.org/10.1007/BF01794949>.
- [51] J. Debonnie, S. Phillips, Capacity of the human colon to absorb fluid, *Gastroenterology.* 74 (1978) 698–703.
- [52] S.F. Phillips, J. Giller, The contribution of the colon to electrolyte and water conservation in man, *J. Lab. Clin. Med.* 81 (1973) 733–746.
- [53] J.H. Cummings, E.W. Pomare, W.J. Branch, C.P. Naylor, G.T. Macfarlane, Short chain fatty acids in human large intestine, portal, hepatic and venous blood., *Gut.* 28 (1987) 1221–1227. <https://doi.org/10.1136/gut.28.10.1221>.
- [54] K. Khanvilkar, M.D. Donovan, D.R. Flanagan, Drug transfer through mucus, *Adv. Drug Deliv. Rev.* 48 (2001) 173–193. [https://doi.org/10.1016/S0169-409X\(01\)00115-6](https://doi.org/10.1016/S0169-409X(01)00115-6).
- [55] R.A. Cone, Barrier properties of mucus, *Adv. Drug Deliv. Rev.* 61 (2009) 75–85.
<https://doi.org/10.1016/j.addr.2008.09.008>.
- [56] D. Artis, Epithelial-cell recognition of commensal bacteria and maintenance of immune homeostasis in the gut, *Nat. Rev. Immunol.* 8 (2008) 411–420.
<https://doi.org/10.1038/nri2316>.
- [57] J. SMART, The basics and underlying mechanisms of mucoadhesion, *Adv. Drug Deliv. Rev.* 57 (2005) 1556–1568. <https://doi.org/10.1016/j.addr.2005.07.001>.
- [58] R. Bansil, B.S. Turner, Mucin structure, aggregation, physiological functions and biomedical applications, *Curr. Opin. Colloid Interface Sci.* 11 (2006) 164–170.
<https://doi.org/10.1016/j.cocis.2005.11.001>.
- [59] C. Atuma, V. Strugala, A. Allen, L. Holm, The adherent gastrointestinal mucus gel layer: Thickness and physical state in vivo, *Am. J. Physiol. - Gastrointest. Liver*

- Physiol. 280 (2001) 922–929. <https://doi.org/10.1152/ajpgi.2001.280.5.g922>.
- [60] P. Paone, P.D. Cani, Mucus barrier, mucins and gut microbiota: The expected slimy partners?, *Gut*. 69 (2020) 2232–2243. <https://doi.org/10.1136/gutjnl-2020-322260>.
- [61] A. ALLEN, W.J. CUNLIFFE, J.P. PEARSON, C.W. VENABLES, The adherent gastric mucus gel barrier in man and changes in peptic ulceration, *J. Intern. Med.* 228 (1990) 83–90. <https://doi.org/10.1111/j.1365-2796.1990.tb01477.x>.
- [62] R.D. Pullan, G.A. Thomas, M. Rhodes, R.G. Newcombe, G.T. Williams, A. Allen, J. Rhodes, Thickness of adherent mucus gel on colonic mucosa in humans and its relevance to colitis., *Gut*. 35 (1994) 353–359. <https://doi.org/10.1136/gut.35.3.353>.
- [63] A. Sarkar, F. Xu, S. Lee, Human saliva and model saliva at bulk to adsorbed phases – similarities and differences, *Adv. Colloid Interface Sci.* 273 (2019) 102034. <https://doi.org/10.1016/j.cis.2019.102034>.
- [64] V. V. Khutoryanskiy, Advances in Mucoadhesion and Mucoadhesive Polymers, *Macromol. Biosci.* 11 (2011) 748–764. <https://doi.org/10.1002/mabi.201000388>.
- [65] J. Sotres, S. Jankovskaja, K. Wannerberger, T. Arnebrant, Ex-Vivo Force Spectroscopy of Intestinal Mucosa Reveals the Mechanical Properties of Mucus Blankets, *Sci. Rep.* 7 (2017) 7270. <https://doi.org/10.1038/s41598-017-07552-7>.
- [66] J. Dekker, J.W.A. Rossen, H.A. Büller, A.W.C. Einerhand, The MUC family: an obituary, *Trends Biochem. Sci.* 27 (2002) 126–131. [https://doi.org/10.1016/S0968-0004\(01\)02052-7](https://doi.org/10.1016/S0968-0004(01)02052-7).
- [67] R. Shaikh, T.R.R. Singh, M.J. Garland, A.D. Woolfson, R.F. Donnelly, Mucoadhesive Drug Delivery Systems, *J. Pharm. BioAllied Sci.* 3 (2011) 89–100. <https://www.ncbi.nlm.nih.gov/pmc/articles/PMC3053525/>.
- [68] F.C. Carvalho, M.L. Bruschi, R.C. Evangelista, M.P.D. Gremião, Mucoadhesive drug delivery systems, *Brazilian J. Pharm. Sci.* 46 (2010) 1–17. <https://doi.org/10.1590/S1984-82502010000100002>.
- [69] N.A. Peppas, J.J. Sahlin, Hydrogels as mucoadhesive and bioadhesive materials: a review, *Biomaterials.* 17 (1996) 1553–1561. [https://doi.org/10.1016/0142-9612\(95\)00307-X](https://doi.org/10.1016/0142-9612(95)00307-X).
- [70] H.D. Chirra, T.A. Desai, Emerging microtechnologies for the development of oral drug delivery devices, *Adv. Drug Deliv. Rev.* 64 (2012) 1569–1578. <https://doi.org/10.1016/j.addr.2012.08.013>.
- [71] S. Sant, S.L. Tao, O.Z. Fisher, Q. Xu, N.A. Peppas, A. Khademhosseini, Microfabrication technologies for oral drug delivery, *Adv. Drug Deliv. Rev.* 64 (2012) 496–507. <https://doi.org/10.1016/j.addr.2011.11.013>.
- [72] S.L. Tao, T.A. Desai, Microdevices for Oral Drug Delivery, in: T. Desai, S. Bhatia (Eds.), *Ther. Micro/Nano Technol.*, Springer, New York, US, 2006: pp. 237–262.
- [73] H.D. Chirra, L. Shao, N. Ciaccio, C.B. Fox, J.M. Wade, A. Ma, T.A. Desai, Planar Microdevices for Enhanced In Vivo Retention and Oral Bioavailability of Poorly Permeable Drugs, *Adv. Healthc. Mater.* 3 (2014) 1648–1654. <https://doi.org/10.1002/adhm.201300676>.
- [74] H.D. Chirra, T.A. Desai, Multi-Reservoir Bioadhesive Microdevices for Independent Rate-Controlled Delivery of Multiple Drugs, *Small.* 8 (2012) 3839–3846. <https://doi.org/10.1002/smll.201201367>.

- [75] J. Guan, H. He, L.J. Lee, D.J. Hansford, Fabrication of Particulate Reservoir-Containing, Capsulelike, and Self-Folding Polymer Microstructures for Drug Delivery, *Small*. 3 (2007) 412–418. <https://doi.org/10.1002/sml.200600240>.
- [76] R. Fernandes, D.H. Gracias, Self-folding polymeric containers for encapsulation and delivery of drugs, *Adv. Drug Deliv. Rev.* 64 (2012) 1579–1589. <https://doi.org/10.1016/j.addr.2012.02.012>.
- [77] L.H. Nielsen, T. Rades, B. Boyd, A. Boisen, Microcontainers as an oral delivery system for spray dried cubosomes containing ovalbumin, *Eur. J. Pharm. Biopharm.* 118 (2017) 13–20. <https://doi.org/10.1016/j.ejpb.2016.12.008>.
- [78] L.H. Nielsen, A. Melero, S.S. Keller, J. Jacobsen, T. Garrigues, T. Rades, A. Müllertz, A. Boisen, Polymeric microcontainers improve oral bioavailability of furosemide, *Int. J. Pharm.* 504 (2016) 98–109. <https://doi.org/10.1016/j.ijpharm.2016.03.050>.
- [79] J.R. Jørgensen, M.L. Jepsen, L.H. Nielsen, M. Dufva, H.M. Nielsen, T. Rades, A. Boisen, A. Müllertz, Microcontainers for oral insulin delivery – In vitro studies of permeation enhancement, *Eur. J. Pharm. Biopharm.* 143 (2019) 98–105. <https://doi.org/10.1016/j.ejpb.2019.08.011>.
- [80] J.R. Jørgensen, F. Yu, R. Venkatasubramanian, L.H. Nielsen, H.M. Nielsen, A. Boisen, T. Rades, A. Müllertz, In Vitro, Ex Vivo and In Vivo Evaluation of Microcontainers for Oral Delivery of Insulin, *Pharmaceutics*. 12 (2020) 48. <https://doi.org/10.3390/pharmaceutics12010048>.
- [81] C. Mazzoni, R.D. Jacobsen, J. Mortensen, J.R. Jørgensen, L. Vaut, J. Jacobsen, C. Gundlach, A. Müllertz, L.H. Nielsen, A. Boisen, Polymeric Lids for Microcontainers for Oral Protein Delivery, *Macromol. Biosci.* 19 (2019) 1900004. <https://doi.org/10.1002/mabi.201900004>.
- [82] C. von Halling Laier, B. Gibson, J.A.S. Moreno, T. Rades, S. Hook, L.H. Nielsen, A. Boisen, Microcontainers for protection of oral vaccines, in vitro and in vivo evaluation, *J. Control. Release*. 294 (2019) 91–101. <https://doi.org/10.1016/j.jconrel.2018.11.030>.
- [83] S.E. Birk, J.A.J. Haagensen, H.K. Johansen, S. Molin, L.H. Nielsen, A. Boisen, Microcontainer Delivery of Antibiotic Improves Treatment of *Pseudomonas aeruginosa* Biofilms, *Adv. Healthc. Mater.* 9 (2020) 1901779. <https://doi.org/10.1002/adhm.201901779>.
- [84] Z. Abid, S. Strindberg, M.M. Javed, C. Mazzoni, L. Vaut, L.H. Nielsen, C. Gundlach, R.S. Petersen, A. Müllertz, A. Boisen, S.S. Keller, Biodegradable microcontainers – towards real life applications of microfabricated systems for oral drug delivery, *Lab Chip*. 19 (2019) 2905–2914. <https://doi.org/10.1039/c9lc00527g>.
- [85] Z. Abid, M. Dalskov Mosgaard, G. Manfroni, R. Singh Petersen, L. Hagner Nielsen, A. Müllertz, A. Boisen, S. Sylvest Keller, Investigation of Mucoadhesion and Degradation of PCL and PLGA Microcontainers for Oral Drug Delivery, *Polymers (Basel)*. 11 (2019) 1828. <https://doi.org/10.3390/polym11111828>.
- [86] L.H. Nielsen, S.S. Keller, K.C. Gordon, A. Boisen, T. Rades, A. Müllertz, Spatial confinement can lead to increased stability of amorphous indomethacin, *Eur. J. Pharm. Biopharm.* 81 (2012) 418–425. <https://doi.org/10.1016/j.ejpb.2012.03.017>.
- [87] R.S. Petersen, S.S. Keller, A. Boisen, Loading of Drug-Polymer Matrices in Microreservoirs for Oral Drug Delivery, *Macromol. Mater. Eng.* 302 (2017) 1600366.

<https://doi.org/10.1002/mame.201600366>.

- [88] Z. Abid, F. Andreoli, M.N. Kristensen, R.S. Petersen, A. Müllertz, A. Boisen, S.S. Keller, Hot punching for loading of biodegradable microcontainers with budesonide-Soluplus film, *Biomed. Microdevices*. 23 (2021) 37. <https://doi.org/10.1007/s10544-021-00572-1>.
- [89] R.S. Petersen, L.H. Nielsen, T. Rindzevicius, A. Boisen, S.S. Keller, Controlled Drug Release from Biodegradable Polymer Matrix Loaded in Microcontainers Using Hot Punching, *Pharmaceutics*. 12 (2020) 1050. <https://doi.org/10.3390/pharmaceutics12111050>.
- [90] P. Marizza, S.S. Keller, A. Müllertz, A. Boisen, Polymer-filled microcontainers for oral delivery loaded using supercritical impregnation, *J. Control. Release*. 173 (2014) 1–9. <https://doi.org/10.1016/j.jconrel.2013.09.022>.
- [91] P. Marizza, L. Pontoni, T. Rindzevicius, J.F. Alopaeus, K. Su, J.A. Zeitler, S.S. Keller, I. Kikic, M. Moneghini, N. De Zordi, D. Solinas, A. Cortesi, A. Boisen, Supercritical impregnation of polymer matrices spatially confined in microcontainers for oral drug delivery: Effect of temperature, pressure and time, *J. Supercrit. Fluids*. 107 (2016) 145–152. <https://doi.org/10.1016/j.supflu.2015.08.023>.
- [92] Z. Abid, C. Gundlach, O. Durucan, C. von Halling Laier, L.H. Nielsen, A. Boisen, S.S. Keller, Powder embossing method for selective loading of polymeric microcontainers with drug formulation, *Microelectron. Eng.* 171 (2017) 20–24. <https://doi.org/10.1016/j.mee.2017.01.018>.
- [93] N.K. Mandsberg, J. Højgaard, S.S. Joshi, L.H. Nielsen, A. Boisen, E. Te Hwu, Consumer-Grade Inkjet Printer for Versatile and Precise Chemical Deposition, *ACS Omega*. 6 (2021) 7786–7794. <https://doi.org/10.1021/acsomega.1c00282>.
- [94] K. Kamguyan, L.H.E. Thamdrup, L. Vaut, L.H. Nielsen, K. Zor, A. Boisen, Development and characterization of a PDMS-based masking method for microfabricated Oral drug delivery devices, *Biomed. Microdevices*. 22 (2020) 35. <https://doi.org/10.1007/s10544-020-00490-8>.
- [95] C.B. Fox, J. Kim, L. V. Le, C.L. Nemeth, H.D. Chirra, T.A. Desai, Micro/nanofabricated platforms for oral drug delivery, *J. Control. Release*. 219 (2015) 431–444. <https://doi.org/10.1016/j.jconrel.2015.07.033>.
- [96] M.A. Clark, B.H. Hirst, M.A. Jepson, Lectin-mediated mucosal delivery of drugs and microparticles, *Adv. Drug Deliv. Rev.* 43 (2000) 207–223. [https://doi.org/10.1016/S0169-409X\(00\)00070-3](https://doi.org/10.1016/S0169-409X(00)00070-3).
- [97] P.O. Okeyo, S.T. Rajendran, K. Zór, A. Boisen, Sensing technologies and experimental platforms for the characterization of advanced oral drug delivery systems, *Adv. Drug Deliv. Rev.* (2021) 113850. <https://doi.org/10.1016/j.addr.2021.113850>.
- [98] G.P. Andrews, T.P. Laverty, D.S. Jones, Mucoadhesive polymeric platforms for controlled drug delivery, *Eur. J. Pharm. Biopharm.* 71 (2009) 505–518. <https://doi.org/10.1016/j.ejpb.2008.09.028>.
- [99] J.F. Christfort, S. Strindberg, S. Al-khalili, D. Bar-Shalom, A. Boisen, L.H. Nielsen, A. Müllertz, In vitro and in vivo comparison of microcontainers and microspheres for oral drug delivery, *Int. J. Pharm.* 600 (2021) 120516. <https://doi.org/10.1016/j.ijpharm.2021.120516>.

- [100] J.F. Christfort, A.J. Guillot, A. Melero, L.H.E. Thamdrup, T.M. Garrigues, A. Boisen, K. Zór, L.H. Nielsen, Cubic Microcontainers Improve In Situ Colonic Mucoadhesion and Absorption of Amoxicillin in Rats, *Pharmaceutics*. 12 (2020) 355. <https://doi.org/10.3390/pharmaceutics12040355>.
- [101] W.R. Lykins, M.E. Hansen, X. Sun, R. Advincula, J.A. Finbloom, A.K. Jain, Y. Zala, A. Ma, T.A. Desai, Impact of Microdevice Geometry on Transit and Retention in the Murine Gastrointestinal Tract, *ACS Biomater. Sci. Eng.* (2021) acsbiomaterials.0c01606. <https://doi.org/10.1021/acsbiomaterials.0c01606>.
- [102] C.L. Nemeth, W.R. Lykins, H. Tran, M.E.H. ElSayed, T.A. Desai, Bottom-Up Fabrication of Multilayer Enteric Devices for the Oral Delivery of Peptides, *Pharm. Res.* 36 (2019) 89. <https://doi.org/10.1007/s11095-019-2618-3>.
- [103] C.B. Fox, Y. Cao, C.L. Nemeth, H.D. Chirra, R.W. Chevalier, A.M. Xu, N.A. Melosh, T.A. Desai, Fabrication of Sealed Nanostraw Microdevices for Oral Drug Delivery, *ACS Nano*. 10 (2016) 5873–5881. <https://doi.org/10.1021/acsnano.6b00809>.
- [104] K.E. Fischer, G. Nagaraj, R. Hugh Daniels, E. Li, V.E. Cowles, J.L. Miller, M.D. Bunker, T.A. Desai, Hierarchical nanoengineered surfaces for enhanced cytoadhesion and drug delivery, *Biomaterials*. 32 (2011) 3499–3506. <https://doi.org/10.1016/j.biomaterials.2011.01.022>.
- [105] A. Ghosh, L. Li, L. Xu, R.P. Dash, N. Gupta, J. Lam, Q. Jin, V. Akshintala, G. Pahapale, W. Liu, A. Sarkar, R. Rais, D.H. Gracias, F.M. Selaru, Gastrointestinal-resident, shape-changing microdevices extend drug release in vivo, *Sci. Adv.* 6 (2020) eabb4133. <https://doi.org/10.1126/sciadv.abb4133>.
- [106] F.J. Martin, C. Grove, Microfabricated drug delivery systems: Concepts to improve clinical benefit, *Biomed. Microdevices*. 3 (2001) 97–108. <https://doi.org/10.1023/A:1011442024658>.
- [107] L. Vaut, E. Scarano, G. Tosello, A. Boisen, Fully replicable and automated retention measurement setup for characterization of bio-adhesion, *The Authors*, 2019. <https://doi.org/10.1016/j.ohx.2019.e00071>.
- [108] E. Sjögren, B. Abrahamsson, P. Augustijns, D. Becker, M.B. Bolger, M. Brewster, J. Brouwers, T. Flanagan, M. Harwood, C. Heinen, R. Holm, H. Juretschke, M. Kubbinga, A. Lindahl, V. Lukacova, U. Münster, S. Neuhoff, M.A. Nguyen, A. Van Peer, C. Reppas, A.R. Hodjegan, C. Tannergren, W. Weitschies, C. Wilson, P. Zane, H. Lennernäs, P. Langguth, In vivo methods for drug absorption – Comparative physiologies, model selection, correlations with in vitro methods (IVIVC), and applications for formulation/API/excipient characterization including food effects, *Eur. J. Pharm. Sci.* 57 (2014) 99–151. <https://doi.org/10.1016/j.ejps.2014.02.010>.
- [109] T.A. Sonia, C.P. Sharma, Experimental techniques involved in the development of oral insulin carriers, in: *Oral Deliv. Insul.*, Woodhead Publishing, Sawston, UK, 2014: pp. 169–217. <https://doi.org/10.1533/9781908818683.169>.
- [110] R. Semwal, R.B. Semwal, D.K. Semwal, Mucoadhesive assessment – An encyclopedic review, *Curr. Med. Drug Res.* 2 (2018).
- [111] N. Thirawong, J. Nunthanid, S. Puttipipatkachorn, P. Sriamornsak, Mucoadhesive properties of various pectins on gastrointestinal mucosa: An in vitro evaluation using texture analyzer, *Eur. J. Pharm. Biopharm.* 67 (2007) 132–140. <https://doi.org/10.1016/j.ejpb.2007.01.010>.

- [112] J. das Neves, M.H. Amaral, M.F. Bahia, Performance of an in vitro mucoadhesion testing method for vaginal semisolids: Influence of different testing conditions and instrumental parameters, *Eur. J. Pharm. Biopharm.* 69 (2008) 622–632. <https://doi.org/10.1016/j.ejpb.2007.12.007>.
- [113] M. Koziolok, M. Grimm, D. Becker, V. Iordanov, H. Zou, J. Shimizu, C. Wanke, G. Garbacz, W. Weitschies, Investigation of pH and Temperature Profiles in the GI Tract of Fasted Human Subjects Using the Intellicap® System, *J. Pharm. Sci.* 104 (2015) 2855–2863. <https://doi.org/10.1002/jps.24274>.
- [114] N. Thirawong, J. Nunthanid, S. Puttipipatkachorn, P. Sriamornsak, Mucoadhesive properties of various pectins on gastrointestinal mucosa : An in vitro evaluation using texture analyzer, *Eur. J. Pharm. Biopharm.* 67 (2007) 132–140. <https://doi.org/10.1016/j.ejpb.2007.01.010>.
- [115] TA.XTplusC Texture Analyser, (2020). <https://www.stablemicrosystems.com/TAXTplus.html>.
- [116] MicroTester, (n.d.). https://www.cellscale.com/products/microtester/?gclid=Cj0KCQjw_8mHBhClARIsABfFgpgSOLSDS1Kgz_I fjosaM22S3SA0vDp4JQQncxxwWOyj2VZ3eH5qCrwaAiR6EALw_wcB.
- [117] J. Goole, K. Amighi, 3D printing in pharmaceuticals: A new tool for designing customized drug delivery systems, *Int. J. Pharm.* 499 (2016) 376–394. <https://doi.org/10.1016/j.ijpharm.2015.12.071>.
- [118] M. Pandey, H. Choudhury, J.L.C. Fern, A.T.K. Kee, J. Kou, J.L.J. Jing, H.C. Her, H.S. Yong, H.C. Ming, S.K. Bhattamisra, B. Gorain, 3D printing for oral drug delivery: a new tool to customize drug delivery, *Drug Deliv. Transl. Res.* 10 (2020) 986–1001. <https://doi.org/10.1007/s13346-020-00737-0>.
- [119] X. Xu, A. Awad, P. Robles-Martinez, S. Gaisford, A. Goyanes, A.W. Basit, Vat photopolymerization 3D printing for advanced drug delivery and medical device applications, *J. Control. Release.* 329 (2021) 743–757. <https://doi.org/10.1016/j.jconrel.2020.10.008>.
- [120] E. Mathew, G. Pitzanti, E. Larrañeta, D.A. Lamprou, 3D Printing of Pharmaceuticals and Drug Delivery Devices, *Pharmaceutics.* 12 (2020) 266. <https://doi.org/10.3390/pharmaceutics12030266>.
- [121] M. Kyobula, A. Adedeji, M.R. Alexander, E. Saleh, R. Wildman, I. Ashcroft, P.R. Gellert, C.J. Roberts, 3D inkjet printing of tablets exploiting bespoke complex geometries for controlled and tuneable drug release, *J. Control. Release.* 261 (2017) 207–215. <https://doi.org/10.1016/j.jconrel.2017.06.025>.
- [122] S.J. Trenfield, A. Awad, A. Goyanes, S. Gaisford, A.W. Basit, 3D Printing Pharmaceuticals: Drug Development to Frontline Care, *Trends Pharmacol. Sci.* 39 (2018) 440–451. <https://doi.org/10.1016/j.tips.2018.02.006>.
- [123] S.A. Khaled, J.C. Burley, M.R. Alexander, J. Yang, C.J. Roberts, 3D printing of five-in-one dose combination polypill with defined immediate and sustained release profiles, *J. Control. Release.* 217 (2015) 308–314. <https://doi.org/10.1016/j.jconrel.2015.09.028>.
- [124] J.V. Ecker, M. Kracalik, S. Hild, A. Haider, 3D - Material Extrusion - Printing with Biopolymers: A Review, *Chem. Mater. Eng.* 5 (2017) 83–96.

- <https://doi.org/10.13189/cme.2017.050402>.
- [125] M. Schouten, G. Wolterink, A. Dijkshoorn, D. Kosmas, S. Stramigioli, G. Krijnen, A Review of Extrusion-Based 3D Printing for the Fabrication of Electro- and Biomechanical Sensors, *IEEE Sens. J.* 21 (2021) 12900–12912. <https://doi.org/10.1109/JSEN.2020.3042436>.
- [126] D. Dev Singh, T. Mahender, A. Raji Reddy, Powder bed fusion process: A brief review, *Mater. Today Proc.* 46 (2021) 350–355. <https://doi.org/10.1016/j.matpr.2020.08.415>.
- [127] I. Gibson, D. Shi, Material properties and fabrication parameters in selective laser sintering process, *Rapid Prototyp. J.* 3 (1997) 129–136. <https://doi.org/10.1108/13552549710191836>.
- [128] K.. Tan, C.. Chua, K.. Leong, C.. Cheah, P. Cheang, M.. Abu Bakar, S.. Cha, Scaffold development using selective laser sintering of polyetheretherketone–hydroxyapatite biocomposite blends, *Biomaterials.* 24 (2003) 3115–3123. [https://doi.org/10.1016/S0142-9612\(03\)00131-5](https://doi.org/10.1016/S0142-9612(03)00131-5).
- [129] F. Dini, S.A. Ghaffari, J. Jafar, R. Hamidreza, S. Marjan, A review of binder jet process parameters; powder, binder, printing and sintering condition, *Met. Powder Rep.* 75 (2020) 95–100. <https://doi.org/10.1016/j.mprp.2019.05.001>.
- [130] O.A. Mohamed, S.H. Masood, J.L. Bhowmik, Optimization of fused deposition modeling process parameters: a review of current research and future prospects, *Adv. Manuf.* 3 (2015) 42–53. <https://doi.org/10.1007/s40436-014-0097-7>.
- [131] C.I. Gioumouxouzis, A.-T. Chatzitaki, C. Karavasili, O.L. Katsamenis, D. Tzetzis, E. Mystiridou, N. Bouropoulos, D.G. Fatouros, Controlled Release of 5-Fluorouracil from Alginate Beads Encapsulated in 3D Printed pH-Responsive Solid Dosage Forms, *AAPS PharmSciTech.* 19 (2018) 3362–3375. <https://doi.org/10.1208/s12249-018-1084-2>.
- [132] N. Genina, J.P. Boetker, S. Colombo, N. Harmankaya, J. Rantanen, A. Bohr, Anti-tuberculosis drug combination for controlled oral delivery using 3D printed compartmental dosage forms: From drug product design to in vivo testing, *J. Control. Release.* 268 (2017) 40–48. <https://doi.org/10.1016/j.jconrel.2017.10.003>.
- [133] A. Goyanes, A.B.M. Buanz, A.W. Basit, S. Gaisford, Fused-filament 3D printing (3DP) for fabrication of tablets, *Int. J. Pharm.* 476 (2014) 88–92. <https://doi.org/10.1016/j.ijpharm.2014.09.044>.
- [134] T.C. Okwuosa, B.C. Pereira, B. Arafat, M. Cieszynska, A. Isreb, M.A. Alhnan, Fabricating a Shell-Core Delayed Release Tablet Using Dual FDM 3D Printing for Patient-Centred Therapy, *Pharm. Res.* 34 (2017) 427–437. <https://doi.org/10.1007/s11095-016-2073-3>.
- [135] Y.L. Kong, X. Zou, C.A. McCandler, A.R. Kirtane, S. Ning, J. Zhou, A. Abid, M. Jafari, J. Rogner, D. Minahan, J.E. Collins, S. McDonnell, C. Cleveland, T. Bensel, S. Tamang, G. Arrick, A. Gimbel, T. Hua, U. Ghosh, V. Soares, N. Wang, A. Wahane, A. Hayward, S. Zhang, B.R. Smith, R. Langer, G. Traverso, 3D-Printed Gastric Resident Electronics, *Adv. Mater. Technol.* 4 (2019) 1800490. <https://doi.org/10.1002/admt.201800490>.
- [136] P.R. Martinez, A. Goyanes, A.W. Basit, S. Gaisford, Influence of Geometry on the Drug Release Profiles of Stereolithographic (SLA) 3D-Printed Tablets, *AAPS*

- PharmSciTech. 19 (2018) 3355–3361. <https://doi.org/10.1208/s12249-018-1075-3>.
- [137] P. Robles-Martinez, X. Xu, S.J. Trenfield, A. Awad, A. Goyanes, R. Telford, A.W. Basit, S. Gaisford, 3D Printing of a Multi-Layered Polypill Containing Six Drugs Using a Novel Stereolithographic Method, *Pharmaceutics*. 11 (2019) 274. <https://doi.org/10.3390/pharmaceutics11060274>.
- [138] H. Kodama, Automatic method for fabricating a three-dimensional plastic model with photo-hardening polymer, *Rev. Sci. Instrum.* 52 (1981) 1770–1773. <https://doi.org/10.1063/1.1136492>.
- [139] P.J. Bártolo, I. Gibson, *Stereolithography: Materials, Processes and Applications*, Springer, New York, US, 2011.
- [140] G. Taormina, C. Sciancalepore, M. Messori, F. Bondioli, 3D printing processes for photocurable polymeric materials: technologies, materials, and future trends, *J. Appl. Biomater. Funct. Mater.* 16 (2018) 151–160. <https://doi.org/10.1177/2280800018764770>.
- [141] P.F. Jacobs, *Rapid Prototyping & Manufacturing: Fundamentals of Stereolithography*, Society of Manufacturing Engineers, 1992.
- [142] J.H. Lee, R.K. Prud'homme, I.A. Aksay, Cure depth in photopolymerization: Experiments and theory, *J. Mater. Res.* 16 (2001) 3536–3544. <https://doi.org/10.1557/JMR.2001.0485>.
- [143] X. Zhang, X. Jiang, C. Sun, Micro-stereolithography of polymeric and ceramic microstructures, *Sensors Actuators A Phys.* 77 (1999) 149–156. [https://doi.org/10.1016/S0924-4247\(99\)00189-2](https://doi.org/10.1016/S0924-4247(99)00189-2).
- [144] S. Maruo, K. Ikuta, Submicron stereolithography for the production of freely movable mechanisms by using single-photon polymerization, *Sensors Actuators A Phys.* 100 (2002) 70–76. [https://doi.org/10.1016/S0924-4247\(02\)00043-2](https://doi.org/10.1016/S0924-4247(02)00043-2).
- [145] K. Kowsari, B. Zhang, S. Panjwani, Z. Chen, H. Hingorani, S. Akbari, N.X. Fang, Q. Ge, Photopolymer formulation to minimize feature size, surface roughness, and stair-stepping in digital light processing-based three-dimensional printing, *Addit. Manuf.* 24 (2018) 627–638. <https://doi.org/10.1016/j.addma.2018.10.037>.
- [146] T. Moritz, S. Maleksaeedi, *Additive manufacturing of ceramic components*, Elsevier Inc., 2018. <https://doi.org/10.1016/B978-0-12-812155-9/00004-9>.
- [147] D.-H. Ko, K.-W. Gyak, D.-P. Kim, Emerging microreaction systems based on 3D printing techniques and separation technologies, *J. Flow Chem.* 7 (2017) 72–81. <https://doi.org/10.1556/1846.2017.00013>.
- [148] B.C. Gross, J.L. Erkal, S.Y. Lockwood, C. Chen, D.M. Spence, Evaluation of 3D Printing and Its Potential Impact on Biotechnology and the Chemical Sciences, *Anal. Chem.* 86 (2014) 3240–3253. <https://doi.org/10.1021/ac403397r>.
- [149] A. Bagheri, J. Jin, Photopolymerization in 3D Printing, *ACS Appl. Polym. Mater.* 1 (2019) 593–611. <https://doi.org/10.1021/acsapm.8b00165>.
- [150] Chris Newmarker, Formlabs announces new biocompatible, medical-grade resins, (2020). <https://www.medicaldesignandoutsourcing.com/formlabs-announces-new-biocompatible-medical-grade-resins/>.
- [151] BioMed Clear Resin 1 L, (2021). <https://formlabs.com/store/biomed-clear-resin/>.

- [152] L. Vaut, K.E. Jensen, G. Tosello, A. Khosla, H. Furukawa, A. Boisen, Additive Manufacturing of Microreservoir Devices for Oral Drug Delivery Using an Acculas BA-30 Micro-Stereolithography Instrument: A Feasibility Study, *J. Electrochem. Soc.* 166 (2019) B3257–B3263. <https://doi.org/10.1149/2.0421909jes>.
- [153] J.F. Xing, M.L. Zheng, X.M. Duan, Two-photon polymerization microfabrication of hydrogels: an advanced 3D printing technology for tissue engineering and drug delivery, *Chem. Soc. Rev.* 44 (2015) 5031–5039. <https://doi.org/10.1039/c5cs00278h>.
- [154] A. Ovsianikov, B. Chichkov, P. Mente, N.A. Monteiro-Riviere, A. Doraiswamy, R.J. Narayan, Two Photon Polymerization of Polymer-Ceramic Hybrid Materials for Transdermal Drug Delivery, *Int. J. Appl. Ceram. Technol.* 4 (2007) 22–29. <https://doi.org/10.1111/j.1744-7402.2007.02115.x>.
- [155] E.E.-T. Hwu, A. Boisen, Hacking CD/DVD/Blu-ray for Biosensing, *ACS Sensors.* 3 (2018) 1222–1232. <https://doi.org/10.1021/acssensors.8b00340>.
- [156] Blu-ray Disc Association, White Paper Blu-Ray Disc™ Format, (2010) 1–48. http://www.blu-raydisc.com/Assets/Downloadablefile/White_Paper_General_4th_20150817_clean.pdf.
- [157] T. Chang, L. Vaut, M. Voss, O. Ilchenko, L.H. Nielsen, A. Boisen, E.-T. Hwu, Micro and nanoscale 3D printing using optical pickup unit from a gaming console, *Commun. Phys.* 4 (2021) 23. <https://doi.org/10.1038/s42005-021-00532-4>.
- [158] H.-S. Liao, K.-Y. Huang, I.-S. Hwang, T.-J. Chang, W.W. Hsiao, H.-H. Lin, E.-T. Hwu, C.-S. Chang, Operation of astigmatic-detection atomic force microscopy in liquid environments, *Rev. Sci. Instrum.* 84 (2013) 103709. <https://doi.org/10.1063/1.4826494>.
- [159] E. Hwu, S. Hung, C. Yang, K.-Y. Huang, I.-S. Hwang, Real-time detection of linear and angular displacements with a modified DVD optical head, *Nanotechnology.* 19 (2008) 115501. <https://doi.org/10.1088/0957-4484/19/11/115501>.
- [160] E.T. Hwu, H. Illers, W.M. Wang, I.S. Hwang, L. Jusko, H.U. Danzebrink, Anti-drift and auto-alignment mechanism for an astigmatic atomic force microscope system based on a digital versatile disk optical head, *Rev. Sci. Instrum.* 83 (2012) 013703. <https://doi.org/10.1063/1.3673001>.
- [161] E.-T. Hwu, H. Illers, L. Jusko, H.-U. Danzebrink, A hybrid scanning probe microscope (SPM) module based on a DVD optical head, *Meas. Sci. Technol.* 20 (2009) 084005. <https://doi.org/10.1088/0957-0233/20/8/084005>.
- [162] H.-S. Liao, Y.-H. Chen, R.-F. Ding, H.-F. Huang, W.-M. Wang, E.-T. Hwu, K.-Y. Huang, C.-S. Chang, I.-S. Hwang, High-speed atomic force microscope based on an astigmatic detection system, *Rev. Sci. Instrum.* 85 (2014) 103710. <https://doi.org/10.1063/1.4898019>.
- [163] L.I. Segerink, M.J. Koster, A.J. Sprenkels, A. van den Berg, A low-cost 2D fluorescence detection system for μm sized beads on-chip, *Lab Chip.* 12 (2012) 1780–1783. <https://doi.org/10.1039/c2lc21187d>.
- [164] M.J. Koster, A compact fluorescence detection system that uses a DVD pickup for the optical detection of beads, University of Twente, 2011.
- [165] C.A. Rothenbach, M.C. Gupta, High resolution, low cost laser lithography using a Blu-

- ray optical head assembly, *Opt. Lasers Eng.* 50 (2012) 900–904.
<https://doi.org/10.1016/j.optlaseng.2011.12.004>.
- [166] Hacking the PHR-803T, (2013). <http://www.diyoware.com/node/161>.
- [167] R. Janusiewicz, J.R. Tumbleston, A.L. Quintanilla, S.J. Mecham, J.M. DeSimone, Layerless fabrication with continuous liquid interface production, *Proc. Natl. Acad. Sci.* 113 (2016) 11703–11708. <https://doi.org/10.1073/pnas.1605271113>.
- [168] J.R. Tumbleston, D. Shirvanyants, N. Ermoshkin, R. Janusiewicz, A.R. Johnson, D. Kelly, K. Chen, R. Pinschmidt, J.P. Rolland, A. Ermoshkin, E.T. Samulski, J.M. DeSimone, Continuous liquid interface production of 3D objects, *Science* (80-.). 347 (2015) 1349–1352. <https://doi.org/10.1126/science.aaa2397>.
- [169] W. Gao, R. Dong, S. Thamphiwatana, J. Li, W. Gao, L. Zhang, J. Wang, Artificial Micromotors in the Mouse’s Stomach: A Step toward in Vivo Use of Synthetic Motors, *ACS Nano.* 9 (2015) 117–123. <https://doi.org/10.1021/nn507097k>.
- [170] S.E. Birk, C. Mazzoni, M. Mobasharah Javed, M. Borre Hansen, H. Krogh Johansen, J. Anders Juul Haagenen, S. Molin, L. Hagner Nielsen, A. Boisen, Co-delivery of ciprofloxacin and colistin using microcontainers for bacterial biofilm treatment, *Int. J. Pharm.* 599 (2021) 120420. <https://doi.org/10.1016/j.ijpharm.2021.120420>.
- [171] S.K. Srivastava, G. Clergeaud, T.L. Andresen, A. Boisen, Micromotors for drug delivery in vivo: The road ahead, *Adv. Drug Deliv. Rev.* 138 (2019) 41–55. <https://doi.org/10.1016/j.addr.2018.09.005>.
- [172] L. Chen, L. Gruzinskyte, S.L. Jørgensen, A. Boisen, S.K. Srivastava, An Ingestible Self-Polymerizing System for Targeted Sampling of Gut Microbiota and Biomarkers, *ACS Nano.* 14 (2020) 12072–12081. <https://doi.org/10.1021/acsnano.0c05426>.

Appendix I

Paper I




Micro and nanoscale 3D printing using optical pickup unit from a gaming console

Tien-Jen Chang, Lukas Vaut, Martin Voss, Oleksii Ilchenko, Line Hagner Nielsen, Anja Boisen and En-Te Hwu

Communications Physics, volume 4, issue 23, 2021

DOI: 10.1038/s42005-021-00532-4

Micro and nanoscale 3D printing using optical pickup unit from a gaming console

Tien-Jen Chang ¹✉, Lukas Vaut¹, Martin Voss¹, Oleksii Ilchenko ¹, Line Hagner Nielsen¹, Anja Boisen ¹ & En-Te Hwu¹

Conventional photopolymerization-based 3D printing still requires developing a concise and cost-effective method to improve the printing resolution at the nanoscale. Here, we propose the use of a gaming console optical drive pickup unit for 3D photopolymerization. This mass-produced optical pickup unit features a finely adjustable diode laser, allowing us to adjust the printing resolution from tens of micrometres down to hundreds of nanometres without requiring oxygen radical scavenging or costly femtosecond lasers. We evaluate the 3D printing performance using a commercial photopolymer under different laser exposure parameters. The proposed printing system achieves a resolution of 385 nm along the lateral direction and XYZ nano-resolution linear stages enable a printing volume of up to $50 \times 50 \times 25 \text{ mm}^3$. Finally, we demonstrate the fabrication of 3D stereoscopic microstructures. The substantially simplified optics proposed here paves the way for affordable high-resolution micro/nanoscale 3D fabrication.

¹The Danish National Research Foundation and Villum Foundation's Center for Intelligent Drug Delivery and Sensing Using Microcontainers and Nanomechanics (IDUN), Department of Health Technology, Technical University of Denmark, 2800 Kgs. Lyngby, Denmark. ✉email: tiech@dtu.dk

The 3D printing technology proposed in the 1980s has pioneered a new generation of manufacturing^{1–3}. By the additive building of structures layer-by-layer, 3D printing allows the creation of stereoscopic structures that cannot be obtained using traditional subtractive manufacturing methods, such as cutting, milling, lathing and grinding^{1,4}. Numerous ideas and materials have fostered the development of 3D printing techniques, including filament disposition modelling⁵, selective laser sintering^{6,7}, PolyJet⁸, aerosol jet printing⁹, digital light processing^{10,11}, continuous liquid interface production^{12,13}, and stereolithography (STL)¹⁴. These manufacturing techniques have enabled the fabrication of innovative geometries to obtain structures with new properties and applications. For instance, unlike traditional methods, 3D printing can enhance location-specific material properties in aircraft turbines and bind multiple materials, thus constituting a novel application in aerospace manufacturing¹⁵. Moreover, personalised production has recently increased research on pharmaceutical applications regarding customised drug dosage systems for individual treatment, with 3D printing playing an important role in its development¹⁶.

The resolution of a 3D printing system is described by the voxel size, which is the smallest 3D printed element that can be obtained while constructing a solid structure. Resolution varies according to the 3D printing technique. Macro 3D printers with millimetre-scale voxels are the most widely used and available on the market, whereas digital light processing and continuous liquid interface production provide voxel sizes down to tens of micrometres. Although it is difficult to obtain micro/nanoscale voxels, STL seems promising to achieve high-resolution 3D printing at such scales. STL applies a liquid photopolymer which mainly includes a photo-initiator, monomers, and oligomers. When the photopolymer is exposed to light at a specific wavelength, the photo-initiator absorbs the light energy and activates photopolymerization that cures the photopolymer into a solid structure¹. The light energy distribution affects the cured voxel size^{17–19}, with voxel depth V_d being theoretically defined as

$$V_d = D_p \ln\left(\frac{E_0}{E_c}\right), \quad (1)$$

where D_p is the penetration depth of the laser into the photopolymer, E_0 is the laser intensity on the photopolymer surface, and E_c is the critical exposure energy to start photopolymerization. In addition, voxel width V_w is defined as

$$V_w = W_0 \sqrt{2V_d/D_p}, \quad (2)$$

where W_0 is the radius of the light beam. As W_0 is proportional to V_w , directing the light beam to a small focal spot during photopolymerization can substantially increase the 3D printing resolution.

Limited by the focal spot size, conventional STL systems reach a spatial resolution of 5 μm . Femtosecond laser-based 3D printers can print nanoscale structures, but the printing area is limited by the field of view of the objective lens (140 \times 140 or 300 \times 300 μm^2). Moreover, the intricate stitching hinders printing at scales between micrometres and millimetres^{20–22}, and the complicated optics and expensive components prevent the widespread adoption of 3D printing based on femtosecond lasers.

There have been several attempts to achieve nanoscale photopolymerization in a cost effective fashion. A low-cost ultraviolet light emitting diode light source was proposed for a large area (over 1 \times 1 cm^2) nanoscale lithography system²³. This system requires a two-stage optical setup that cannot construct multiple layer 3D structures. A less expensive quasi-continuous-wave 405-nm diode pulse laser (repetition rate: 1 MHz, duty cycle: 5–10%) is adopted to realise high-resolution 3D printing²⁴. However, the

optical system is based on an expensive 3D printer (Photonics Professional GT, Nanoscribe, GmbH) and a Zeiss objective lens with a numerical aperture of 1.4. Both above mentioned systems share the common drawback that they require stitching process to achieve a millimetre or centimetre scale printing area.

The optical-pickup-unit (OPU) is a component for reading/writing data from optical storage discs such as Blu-rays, high-definition digital versatile discs (HD DVDs), DVDs, and compact discs (CDs)²⁵. The mass produced OPU (costs less than five USD) provides not only a light source but also diffraction-limited optics in a compact size, similar to a car key. Given its high-precision measurements and multiple wavelength laser modes, the OPU has been used for various other applications, such as atomic force microscopy^{26–28}, biosensing^{29,30}, and photolithography³¹. The HD-DVD OPU equips an aspherical objective lens with a numerical aperture of 0.65, aperture diameter of 3 mm, and assumed laser beam quality of 1. Therefore, the OPU achieves a theoretical laser spot size of 430 nm in diameter ($1/e^2$ width) with the 405 nm laser, as indicated by Eq. (3)^{25,32}.

$$\text{Laser spot radius} = \frac{4\lambda f M^2}{\pi D}, \quad (3)$$

where λ is the laser wavelength, f is the lens focal length, D is the input beam diameter at the lens, and M^2 is the laser beam quality. As the laser spot size is proportional to V_d in Eq. (2), the OPU laser spot delivers the required power for curing photopolymers at voxel sizes from tens of micrometres down to the nanoscale.

In this paper, we present the application of an OPU (Fig. 1a–c) as a compact and cost-effective solution to replace the conventional STL optical system and to eliminate the complexity of a STL system dramatically. An HD-DVD OPU extracted from a

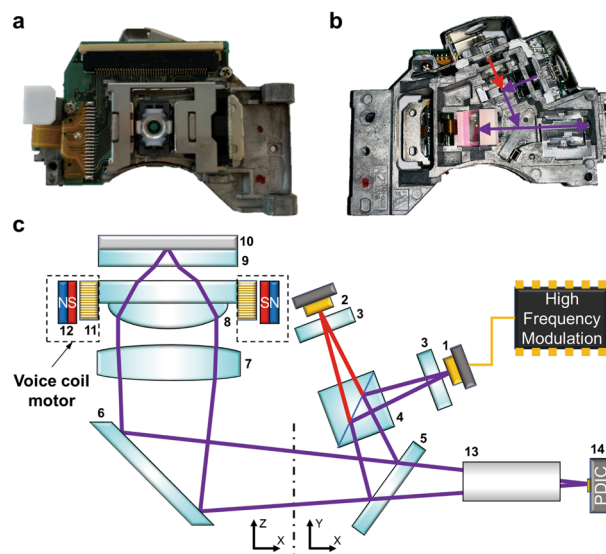


Fig. 1 High-definition digital versatile discs (HD DVDs) optical-pickup-unit (OPU) for 3D printing using photopolymerization. Photograph of HD DVDs OPU from **a** top view and **b** bottom view (the purple and red arrows indicate the optical path of 405 nm and 650/780 nm laser, respectively). **c** Intrinsic optical module, and actuators: 1: 405 nm laser diode, 2: 650/780 nm laser diode, 3: diffraction grating, 4: dichroic cube beam splitter, 5: beam splitter, 6: fold mirror, 7: collimating lens, 8: objective lens, 9: protective layer, 10: CD/DVD/HD-DVD disc data layer, 11: coil, 12: magnet, 13: expanding lens and 14: photodiode integrated circuit (PDIC). (The purple line represents 405 nm laser, while the red line represents 650/780 nm laser. Dot-dashed line indicates the transformation of view direction between XY panel and XZ panel).

gaming console (Xbox 360; Microsoft, Redmond, WA, USA) has an optical working distance of 1.25 mm, which is four times that of a Blu-ray OPU, thus being more flexible for STL 3D printing. In addition, the HD-DVD OPU equips multiple-wavelength (405/650/780 nm) continuous wave semiconductor laser diodes to read HD-DVD/DVD/CD data, expanding the compatibility to various types and curing wavelengths of photopolymers. Although conventional multimaterial STL printing and multiple-step printing using different exposure wavelengths are under development^{33–35}, the OPU may substantially simplify the optical system design. The OPU also integrates an astigmatic optical path and a photodiode integrated circuit to generate the focus error signal (FES)²⁵, which is fed back for closed-loop laser focusing during the reading of data pits on a disc. A voice coil motor actuates the objective lens vertically and horizontally to compensate the disc wobbling and follow data tracks, respectively²⁵. In the proposed OPU 3D printing system, the FES and voice coil motor are used for substrate parallelism correction (with non-photopolymer curing wavelength laser) and real-time fine-tuning of the printing level, respectively. This closed-loop printing mechanism further increases the performance of micro/nanoscale 3D printing compared to conventional open-loop STL systems. Finally, this 3D printing system realises multiple-layers 3D printed microstructure and achieves a nanoscale printing resolution along the lateral direction.

Results

OPU 3D printing system. Considering an inverted STL system³⁶, we designed a 3D printer with the laser spot directed upward. Figure 2a shows the developed OPU 3D printing system, which consists of XYZ linear stages, a tilt stage, a substrate holder, a photopolymer vat, an HD-DVD OPU, and a controlling system. The XY-axis linear stage positions the OPU for 2D printing, and the tilt stage mounted on the Z-axis stage adjusts the two-axis tilting angle of the substrate holder for optimal parallel positioning between the substrate and printing path. The OPU emits a 405 nm laser penetrating a transparent layer and focuses the laser inside the photopolymer vat (Fig. 2b, c). In the controlling system, an embedded controller connects to a customised OPU driver and a motor driver. The OPU driver adjusts the laser intensity, switches the laser wavelength, calculates the FES, and drives the voice coil motor. The motor driver controls the XY-axis and Z-axis linear stages with resolutions of 312.5 and 62.5 nm, respectively. The embedded controller communicates with a computer through a graphical user interface and implements the printing process via computer numerical control commands in G-code.

Conventional STL systems require external sensors for printing substrate levelling and achieving high-precision 3D printing. In contrast, the proposed OPU 3D printing system directly uses the embedded sensors to measure the distance between the focal spot and substrate surface at nanoscale resolution using the FES. The substrate surface and OPU focal plane can be precisely aligned in parallel by scanning the XY linear stage and adjusting the tilt stage (Fig. 2d). Levelling can also be performed with a non-curing laser wavelength (e.g., 650, 780 nm) when a 405 nm photopolymer is inside the vat. Before printing, the voice coil motor adjusts the objective lens along the Z direction for determining the photopolymer thickness. In addition, the FES determines whether the substrate surface reaches the focal spot (Fig. 2e). Thus, the OPU embedded sensing system can be used to optimise and increase the yield of micro/nanoscale 3D printing.

When levelling and calibration are complete, the G-code commands are executed for 3D printing, in which the Z-axis linear stage gradually lifts the substrate for realising layer-by-layer

printing (Fig. 2f). The 3D structures are completed by washing out the residual resin with ethanol. For delicate and complex structures, the substrates are immersed in ethanol for 10 min for thorough washing.

Photopolymer thickness and laser spot size. The OPU provides an optimal focal spot on an HD-DVD track when the laser passes through air and a protective layer²⁵. However, focusing the laser through the photopolymer distorts the focal condition given the higher refractive index (i.e., value defining the speed of light in a medium) of the photopolymer compared to air. According to the Snell's law, when the laser beam passes through the transparent layer into the next medium, its bending toward the normal line is higher in the photopolymer than in air. Consequently, laser divergence and an expanded focal spot with optical aberrations occur. To determine the optimal focus, we use the optical design software Zemax OpticStudio 20.1 (Zemax, Kirkland, WA, USA) to calculate the spot size at different photopolymer thicknesses, as this size represents the distance that the laser should travel through the photopolymer, as illustrated in Fig. 3a, b. This optical model is detailed in the optical path simulation section. As the objective lens concentrates the laser beam to pass through air and the protective layer, its simulated focal spot size is 454 nm ($1/e^2$ width). When the objective lens focuses the laser in a 25 μm thick photopolymer layer, the focal spot expands to 509 nm, and the maximum irradiance (energy per unit time) drops to 0.33. As the photopolymer layer thickness increases to 50, 75, and 100 μm , the focal spot further expands to 677, 720, and 816 nm, respectively, while the maximum irradiance drops to 0.18, 0.13, and 0.09, respectively. The simulation results show that increasing the photopolymer thickness reduces the laser energy concentration due to both the expanded focal spot size and reduced maximum irradiance.

Given the common focal spot divergence, a thick photopolymer layer reduces the printing resolution, as experimentally validated. The photopolymer thicknesses were set to 100, 75, 50, and 25 μm at fixed laser power of 2.40 μW . The system printed lines at speeds of 0.078–0.104 mm s^{-1} in a rectangular frame of 100 \times 900 μm (width \times length). The frame trapped the individual fragile line features. Figure 3c shows that the photopolymer thickness notably influences the printing performance, as the cured line width is smaller when decreasing the photopolymer thickness.

Laser exposure dose. In photopolymerization, the material dimension of the cured photopolymer exhibits a positive trend regarding laser exposure energy, as indicated by Eqs. (1) and (2). We controlled the laser exposure dose by adjusting both the printing speed and laser intensity to confirm this trend. For fixed laser power of 2.97 μW and photopolymer thickness of 25 μm , the developed system was used to print lines at different speeds from 0.104 to 0.138 mm s^{-1} in a rectangular frame of 100 \times 900 μm (width \times length), as shown in Fig. 4a. To determine the effect of laser intensity on the cured line width, this test was repeated at varying laser power of 2.64, 2.40, and 2.15 μW , obtaining the results shown in Fig. 4b–d, respectively. The trend of the cured width agreed with theory, as shown in Fig. 4e, as reducing the printing speed and increasing the laser intensity enhanced laser exposure, and thereby enlarging the cured line width.

Nanoscale printing resolution along the lateral direction. After system optimisation, we determined the highest achievable printing resolution by reducing the photopolymer thickness. Using the FES closed-loop feedback, the voice coil motor can precisely focus the laser spot on the silicon substrate. Figure 5a

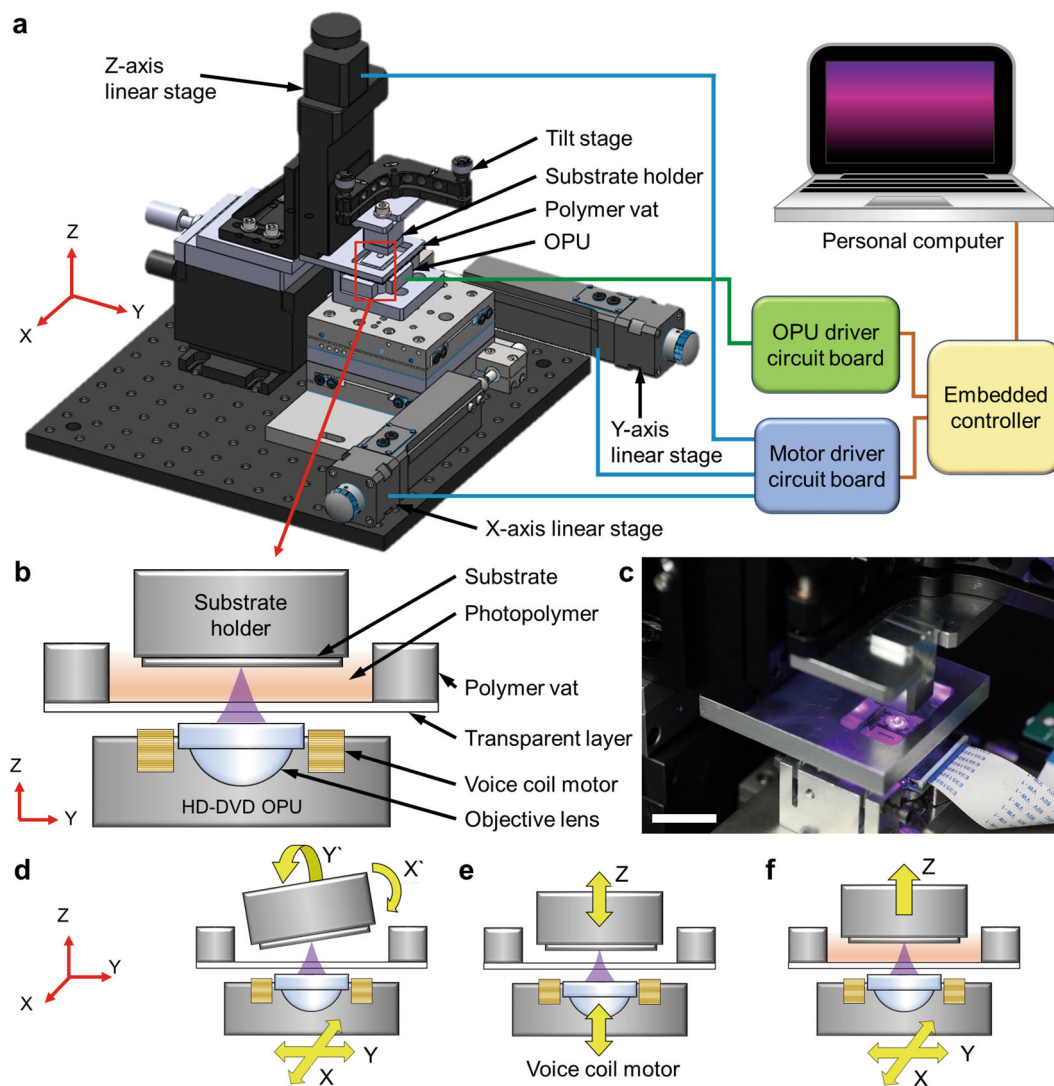


Fig. 2 Developed 3D printer using high-definition digital versatile discs (HD DVDs) optical-pickup-unit (OPU) as core optical module by focusing laser beam of 405 nm wavelength to cure photopolymer in Vat. **a** Mechanism of printer with inverted stereolithography (STL) design and control system diagram. **b** Detailed diagram of optical path. **c** Photograph of system during printing (scale bar represents 2 cm). **d** Substrate tilting diagram (X' and Y' represent tilting substrate along X-axis and Y-axis, respectively). **e** Vertical position initialisation and objective lens translation diagrams. **f** Printing solid structures layer-by-layer process diagram. These diagrams are illustrative and do not reflect the real scales.

shows a $300 \times 300 \mu\text{m}$ square printed with lines with a width of approximately $3 \mu\text{m}$ using a photopolymer of $13 \mu\text{m}$ in thickness. After further reducing the photopolymer thickness to $6 \mu\text{m}$, we achieved nanoscale linear structures along the lateral direction at different printing speeds with fixed laser power of $2.40 \mu\text{W}$, as shown in Fig. 5b–e. The nanostructures were suspended by two vertical structures with a $15 \mu\text{m}$ separation. The width of the nanostructures decreased to 992, 879, 769, and 385 nm with increasing printing speeds of 0.16, 0.18, 0.21, and 0.25 mm s^{-1} , respectively. A cross-section contour of a 385 nm wide line shows the laser energy distribution in Fig. 5f. Figure 5g shows the line width according to the printing speed, as the nanostructures can be printed repeatedly using the same parameter settings. To the best of our knowledge, this is the first system to print nanoscale structures along the lateral direction using a low-cost OPU with a continuous wave diode laser source.

3D printed structures. To verify the performance of the proposed OPU 3D printing system, we fabricated various 3D microstructures, as shown in Fig. 6. Figure 6a shows an $850\text{-}\mu\text{m}$ -

high pyramid printed with layers of $25 \mu\text{m}$ in height. Figure 6b, c show a tilted square tower and a twisted tower, respectively. These 3D microstructures were printed without stitching. Furthermore, the cylinder being $300 \mu\text{m}$ in diameter and $150 \mu\text{m}$ in height shown in Fig. 6d was printed to demonstrate printing following curved paths. Figure 6e shows a structure resembling a gate with around $800 \mu\text{m}$ in length and $400 \mu\text{m}$ in height, demonstrating the ability to print structures with overhanging features.

Discussion

Printer design and substrate adhesion. The design of the proposed OPU 3D printer can improve substrate alignment and printing layer control. Instead of moving the photopolymer vat along the horizontal direction, the XY linear stage directly drives the OPU, mitigating unstable liquid vibration by acceleration-induced and deceleration-induced forces. This printer has a maximum printing volume of $50 \times 50 \times 25 \text{ mm}^3$ that can be unlimitedly enlarged by replacing the mechanical components such as with a wider substrate, larger polymer vat, and longer

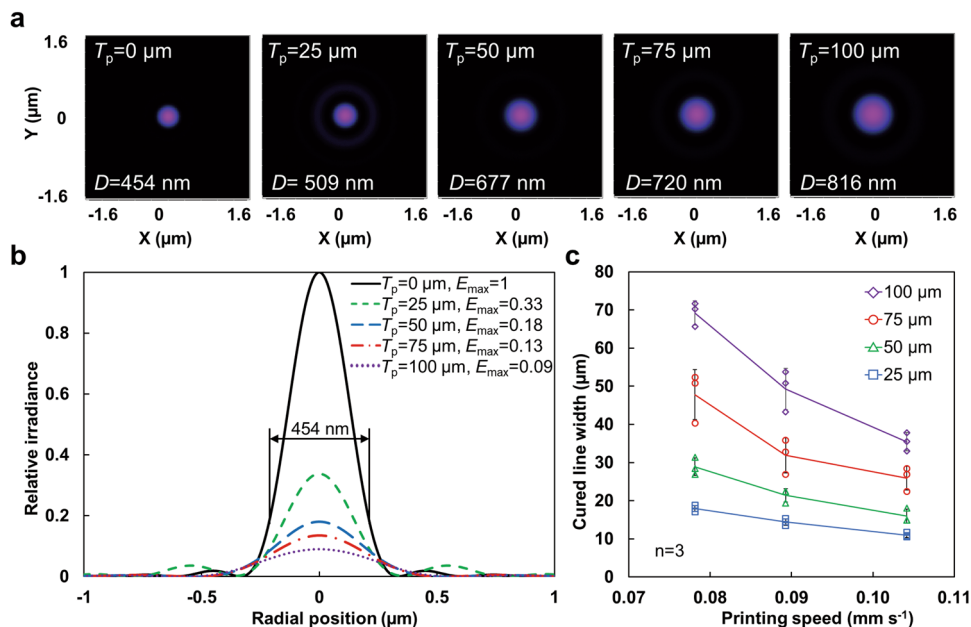


Fig. 3 Effect of photopolymer thickness on cured line width obtained from optical simulation software and experimentally validated. **a** Laser focal spot simulated in Zemax OpticStudio 20.1 at photopolymer thicknesses, T_p , of 0, 25, 50, 75, and 100 μm , with spot diameters, D , of 454, 509, 677, 720, and 816 nm, respectively. **b** Laser focal spot energy Gaussian distribution and maximum irradiance, E_{max} , at various photopolymer thicknesses. **c** Printing results illustrating the relation between the cured line width and printing speed at various photopolymer thicknesses (n represents sample size, while error bars represent one standard deviation).

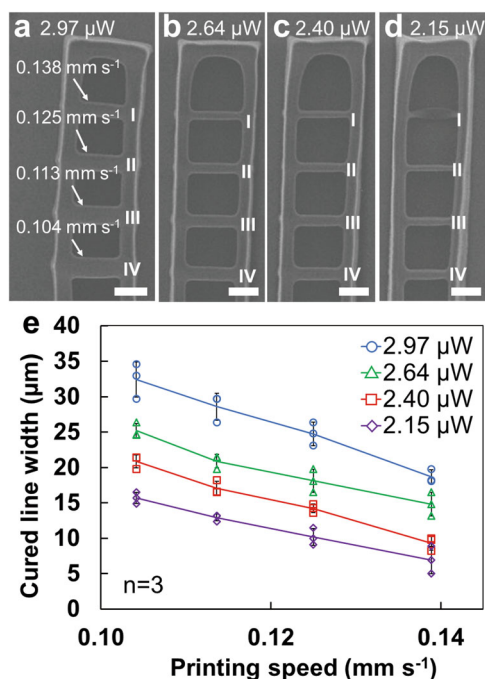


Fig. 4 Laser exposure dose verification by printing straight lines in a rectangular frame structure at varying printing speed and laser intensity. Scanning electron microscope images of cured lines at laser powers of **a** 2.97, **b** 2.64, **c** 2.40, and **d** 2.15 μW (scale bar represents 50 μm). The printing speed was set to 0.104, 0.113, 0.125, and 0.138 mm s^{-1} corresponding to labels I, II, III, and IV, respectively. **e** Cured line width according to printing speed at various laser intensities (n represents sample size, while error bars represent one standard deviation).

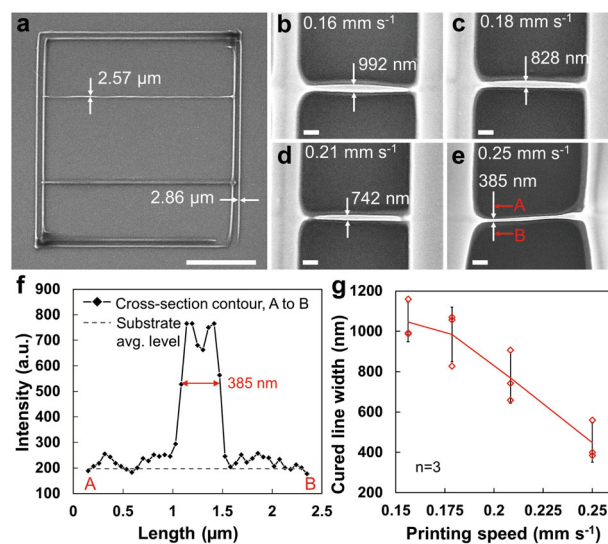


Fig. 5 Scanning electron microscope images of 3D printed nanoscale structures. **a** 300 \times 300 μm square printed with microscale lines with a width of approximately 3 μm (scale bar represents 100 μm). The nanoscale structures were cured at printing speeds of **b** 0.16, **c** 0.18, **d** 0.21, and **e** 0.25 mm s^{-1} , resulting in line widths of 992, 879, 769, and 385 nm, respectively. Two vertical lines (width approximately 5 μm) were printed with a distance of 15 μm to suspend the nanometre structures (scale bars represent 2 μm). **f** Cross-section contour of 385-nm-width structure in **e**. **g** Cured nanoscale width according to printing speed at a laser power of 2.40 μW and a photopolymer thickness of 6 μm (n represents sample size, while error bars represent one standard deviation).

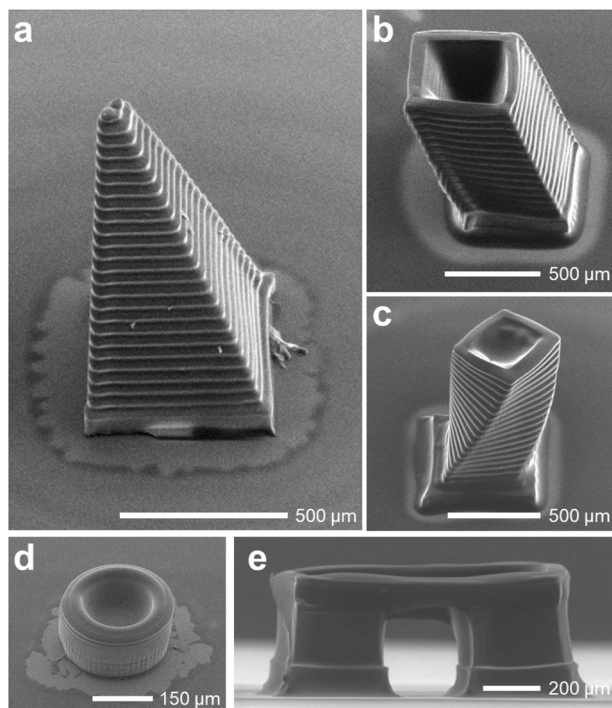


Fig. 6 Scanning electron microscope images of 3D printed structures. a Pyramid with height of approximately 850 μm and height of 25 μm per layer. **b** Tilted square tower. **c** Twisted tower. **d** Cylinder. **e** Gate-like structure.

working distance linear stages. Still, a potential drawback of our method is the possible curing of all the photopolymer between the substrate and the transparent layer, causing the printed structure to adhere to the transparent layer. Typically, continuous liquid interface production relies on oxygen inhibition to prevent the cured photopolymer from adhering to the transparent layer by applying an oxygen-penetrable film¹². For maintaining optical path completeness, we used a polymethyl methacrylate (PMMA) film to support the photopolymer and a silicon substrate to carry the cured material. Compared to PMMA, the silicon surface has higher surface energy, providing more stable adhesion of the printed structures. In addition, we printed a thicker foundation layer with higher laser exposure to support the cured structures on the substrate. The 3D structures shown in Fig. 6 show this substrate adhesion method for strong support.

Laser exposure control boundary. We were able to predict the critical exposure energy for curing the photopolymer during tests of laser intensity and printing speed through an exposure dose evaluation at laser power of 2.40 μW and printing speed of 0.104 mm s^{-1} . Although the highest laser power from the OPU is 0.2 mW, we used lower power in this study. Hence, the printing speed may be increased by applying higher laser intensity to balance the laser exposure. However, reaching the theoretical maximum speed of the stages is constrained by various factors. To raise the positioning resolution, we used a one-sixteenth step to drive the stage, thus reducing the linear speed. In addition, high current for increasing the driving motor speed caused a sudden temperature rise in the motor, changing the photopolymer temperature and destabilising the printing environment. Moreover, vibration constrained the maximum feasible speed for 3D printing, as a high speed matching the system resonant frequency caused oscillation. The printer vibration was monitored along the Z-axis using the FES. To increase the printing speed,

high-resolution linear positioning stages (e.g., piezo-driving stage, linear motor stage) should be adopted, enabling low vibration, and temperature consistency.

Photopolymer thickness and nanoscale structures. From the optical simulation, we confirmed that reducing the photopolymer thickness led to a smaller and more concentrated focal spot. Moreover, an analysis of the experimental results using multiple regression showed that the coefficient of photopolymer thickness is the most significant factor determining the cured line width. Thus, reducing the photopolymer thickness can lead to increased resolution. However, the depth of the focal laser spot and printer mechanical structure limit the minimum thickness of the printed photopolymer. Currently, the thinnest tested layer of the photopolymer is 6 μm . The cross-section contour characterised by scanning electron microscopy in Fig. 5f reflects the OPU laser energy distribution. The printer cures nanoscale linear structures with a width of 385 nm, which is below the laser spot size of 430 nm, and close to theoretical limitation of 311 nm, calculated by Fraunhofer diffraction formula of a grating³⁷. Unlike a Gaussian distribution with a single peak, the contour shows two peaks, which might reflect the optical module's laser energy distribution. The central point is approximately 18% below the two peaks. The main reason for this phenomenon might be an optical aberration. Thus, the 6 μm thick photopolymer layer setting still causes optical aberration that limits the maximum irradiance point and leads to the splitting into two peaks³⁸.

Through precisely controlling laser exposure dosage and photopolymer thickness, the printer can reach printing nanoscale structures along the lateral direction. However, the system presents some printing uncertainty, as shown in Fig. 5a, f. The high-resolution printing is sensitive to photopolymer thickness variation which locally changes the laser energy distribution. As the PMMA transparent layer (Fig. 2b) has a relatively large suspension area (30 \times 60 mm^2), an inconsistent photopolymer thickness may easily arise due to geometry deviations such as layer flatness, surface scratches, plastic deformation, and parallel misalignment to the substrate.

Polygonal structures. In 3D printing, STL is the most common file format for describing 3D structures given its efficiency and universality to transfer various kinds of structures. The STL format cuts a structure into numerous triangular facets. Then, a computer transforms the STL file into G-code commands, which are used by the printer to move along the straight lines of the triangle edges for depicting the patterns at each layer. Although, the STL format has many benefits, it compromises the smoothness of curved surfaces. In Fig. 6d, we divided the cylinder perimeter into sixty line segments for the printer to generate the rounded shape, resulting in surface discontinuity. We speculate that a curve function might prevent this problem. In G-code, clockwise and counter-clockwise curve functions (G02 and G03, respectively) can be adopted to control a two-axis motor and execute round motions to obtain smooth continuous surfaces.

Enlarged corners. By closely examining the printed structure in Fig. 6a, we observe that the corner structure is slightly larger (~120%) than the other printed features. This is due to the motor slowing down and then speeding up when printing corners. Consequently, the laser has a relatively longer exposure time in that area, causing the larger rounded features shown in the figure. This phenomenon can be eliminated by compensating the laser intensity near corners to obtain uniform structures. In addition, the large rounded corners are caused by the photopolymer

accumulating more energy when two laser exposure points are close¹⁰, being another aspect that remains to be addressed.

Conclusion

We successfully constructed a nanometre resolution 3D printer relying on an off-the-shelf OPU to cure a photopolymer. The printer successfully produces microscale 3D structures layer-by-layer, and the OPU allows to achieve nanoscale printing resolution of 385 nm along the lateral direction, outperforming any commercially available STL printer. By leveraging the OPU operation and built-in electronics, the developed 3D printing system presents many benefits regarding aspects such as reduced cost, compactness, closed-loop control, and unconstrained printing area. Therefore, the proposed OPU 3D printer can be a high-performance alternative for photopolymerization-based 3D printing. Furthermore, the compact nature of the OPU enables the possibility of using 2×2 or 3×3 OPU arrays to parallelise 3D printing for multiplying throughput. As the proposed printer can print millimetre or micrometre scale devices with nanoscale lateral resolution, it has great potential for mass-producing or scaling up the fabrication of microdevices with intricate designs, such as microscale vessels for drug delivery, microactuators, microscale medical devices, and micro-optical components.

Methods

Developed 3D printer components and mechanism. The core optical component of the gaming console HD-DVD drive OPU was the PRH-803T model (Toshiba, Tokyo, Japan) that integrates a laser diode modulation integrated circuit (ATR0885; Atmel, San Jose, CA, USA). The tilt stage (KM200V; Thorlabs, Newton, NJ, USA) was used to align the substrates with $\pm 4^\circ$ of precision tilt adjustment. The vertical linear stage (LM60-25; OWIS, Staufen, Germany) was used to move the substrate along the Z axis with 25 mm travel distance. The two-axis horizontal positioning linear stage (LNR50S, Thorlabs), including the platform and linear stepper motor, has a travel distance of 50 mm along each direction. To drive the three linear stages, we used a motor driver (A4988; Allegro MicroSystems, Manchester, NH, USA) supporting at most 16 divisions per step. The controller (myRIO-1900; National Instruments, Austin, TX, USA) was operated at clock frequency of 667 MHz considering its digital and analogue inputs/outputs for control. The software was developed by the authors, and the system programme was implemented on the LabVIEW 2016 software (National Instruments). The main structure of the printer was made of aluminium. The substrate, photopolymer vat, and OPU holder were manufactured using a milling process via computer numerical control.

Material preparation for 3D printing. We selected a commercially available white photopolymer (FLPGWH02; Formlabs, Somerville, MA, USA) as printing material with curing process activated by 405 nm wavelength light, which corresponds to the operation wavelength of the HD-DVD OPU reading laser. The solvent for washing the residual photopolymer after printing was 95% ethanol. To prepare the silicon surface for carrying the cured structure, a chemical mechanical polishing silicon wafer was sliced into a 12×12 mm² square by a grinding saw machine. The silicon surface flatness was below 1 μ m. The PMMA layer for loading the photopolymer was a clear plate with thickness of 0.5 mm. A CO₂ laser was used to cut the PMMA into a 30×60 mm² rectangle. The PMMA refractive index was 1.5051 when 405-nm wavelength light penetrated the polymer.

Measurement of laser power and dimension of cured solid structure. To characterise the laser strength, a laser power metre (PM100D; Thorlabs) was used to measure the laser intensity directly from the objective lens. After printing, a tabletop scanning electron microscope (TM3030 Plus; Hitachi, Tokyo, Japan) was used to characterise the microscale structures. A 45° tilted sample holder carried the specimen for accurate and detailed spatial feature observation.

Optical path simulation. We used Zemax OpticStudio 20.1 to simulate the laser divergence as the objective lens focused the laser beam into the photopolymer. Given that the OPU geometry parameter of the objective lens was not provided by the manufacturer, we first tried to obtain the geometry structure by optimising an aspherical objective lens which concentrated a 405 nm wavelength parallel laser beam to pass through 0.75 mm thick air layer and focused on a 0.5 mm thick PMMA layer. The objective lens was simulated with glass BK7 of 1.7 mm in thickness. The backside geometry parameters included radius of 6.913 mm, clear semi-diameter of 1.5 mm, mechanical semi-diameter of 1.5 mm, 2nd-order term of 0.317, 4th-order term of 0.019, 6th-order term of $-2.663E-03$, 8th-order term of $-8.701E-04$, and 10th-order term of $-1.421E-03$. The facade geometry

parameters included radius of 5.16 mm, clear semi-diameter of 1.288 mm, mechanical semi-diameter of 1.5 mm, 2nd-order term of -0.054 , 4th-order term of 0.011, 6th-order term of $-6.168E-03$, 8th-order term of $-5.320E-04$, and 10th-order term of $-2.466E-04$. After obtaining the objective lens with diffraction-limited performance, its position was shifted toward the PMMA layer to simulate focusing the laser inside the photopolymer layer (refractive index of 1.50). When the laser travelled through the photopolymer layer, the laser focal spot expanded, and the focal distance increased. By shifting the objective lens 25, 50, 75 and 100 μ m toward the PMMA layer, we obtained distances (inside the photopolymer) between the PMMA and focal spot of 41, 78, 117 and 155 μ m, respectively. In addition, the simulated focal laser spot diameters, D , inside the photopolymer were 509, 677, 720 and 816 nm, as shown in Fig. 3a, b, and the maximum irradiance values were 0.33, 0.18, 0.13 and 0.09, respectively.

Reporting summary. Further information on research design is available in the Nature Research Reporting Summary linked to this article.

Data availability

The data that support the findings of this study are available from the corresponding author on reasonable request.

Code availability

All code and software generated during this study are available from the corresponding author on request.

Received: 14 September 2020; Accepted: 15 January 2021;

Published online: 11 February 2021

References

- Ligon, S. C., Liska, R., Stampfl, J., Gurr, M. & Mülhaupt, R. Polymers for 3D printing and customized additive manufacturing. *Chem. Rev.* **117**, 10212–10290 (2017).
- Kodama, H. Automatic method for fabricating a three-dimensional plastic model with photo-hardening polymer. *Rev. Sci. Instrum.* **52**, 1770–1773 (1981).
- Bártolo, P. J. & Gibson, I. in *Stereolithography: Materials, Processes and Applications* (ed. Bártolo, P. J.) Ch. 2 (Springer, 2011).
- Vaezi, M., Seitz, H. & Yang, S. A review on 3D micro-additive manufacturing technologies. *Int. J. Adv. Manuf. Technol.* **67**, 1721–1754 (2013).
- Mohamed, O. A., Masood, S. H. & Bhowmik, J. L. Optimization of fused deposition modeling process parameters: a review of current research and future prospects. *Adv. Manuf.* **3**, 42–53 (2015).
- Tan, K. H. et al. Scaffold development using selective laser sintering of polyetheretherketone–hydroxyapatite biocomposite blends. *Biomaterials* **24**, 3115–3123 (2003).
- Gibson, I. & Shi, D. Material properties and fabrication parameters in selective laser sintering process. *Rapid Prototyp. J.* **3**, 129–136 (1997).
- Gaynor, A. T., Meisel, N. A., Williams, C. B. & Guest, J. K. Multiple-material topology optimization of compliant mechanisms created via PolyJet three-dimensional printing. *J. Manuf. Sci. Eng.* **136**, 061015 (2014).
- Hoey, J. M., Lutfurakhmanov, A., Schulz, D. L. & Akhatov, I. S. A review on aerosol-based direct-write and its applications for microelectronics. *J. Nanotechnol.* **2012**, 1–22 (2012).
- Sun, C., Fang, N., Wu, D. M. & Zhang, X. Projection micro-stereolithography using digital micro-mirror dynamic mask. *Sens. Actuators A Phys.* **121**, 113–120 (2005).
- Kowsari, K. et al. Photopolymer formulation to minimize feature size, surface roughness, and stair-stepping in digital light processing-based three-dimensional printing. *Addit. Manuf.* **24**, 627–638 (2018).
- Tumbleston, J. R. et al. Continuous liquid interface production of 3D objects. *Science* **347**, 1349–1352 (2015).
- Januszewicz, R., Tumbleston, J. R., Quintanilla, A. L., Mecham, S. J. & DeSimone, J. M. Layerless fabrication with continuous liquid interface production. *Proc. Natl Acad. Sci.* **113**, 11703–11708 (2016).
- Maruo, S. & Ikuta, K. Submicron stereolithography for the production of freely movable mechanisms by using single-photon polymerization. *Sens. Actuators A Phys.* **100**, 70–76 (2002).
- Misra, A. K., Grady, J. E. & Carter, R. Additive manufacturing of aerospace propulsion components. 1–21 <http://ntrs.nasa.gov/archive/nasa/casi.ntrs.nasa.gov/20150023067.pdf> (2015).
- Goole, J. & Amighi, K. 3D printing in pharmaceuticals: a new tool for designing customized drug delivery systems. *Int. J. Pharm.* **499**, 376–394 (2016).

17. Jacobs, P. F. In *Rapid Prototyping & Manufacturing: Fundamentals of Stereolithography* (ed. Reid, D. T.) Ch. 3–4 (Society of Manufacturing Engineers, 1992).
18. Lee, J. H., Prud'Homme, R. K. & Aksay, I. A. Cure depth in photopolymerization: experiments and theory. *J. Mater. Res.* **16**, 3536–3544 (2001).
19. Zhang, X., Jiang, X. N. & Sun, C. Micro-stereolithography of polymeric and ceramic microstructures. *Sens. Actuators A Phys.* **77**, 149–156 (1999).
20. Reiner, R. R., Tanguy, Y. & Hoffmann, J. Process for producing a three-dimensional structure (2016).
21. Maruo, S., Nakamura, O. & Kawata, S. Three-dimensional microfabrication with two-photon-absorbed photopolymerization. *Opt. Lett.* **22**, 132–134 (1997).
22. Xiong, W., Jiang, L. J., Baldacchini, T. & Lu, Y. F. In *Laser Additive Manufacturing: Materials, Design, Technologies, and Applications* (ed. Brandt, M.) Ch. 9 (Elsevier, 2017).
23. Wen, S. B., Bhaskar, A. & Zhang, H. Scanning digital lithography providing high speed large area patterning with diffraction limited sub-micron resolution. *J. Micromech. Microeng.* **28**, 075011 (2018).
24. Mueller, P., Thiel, M. & Wegener, M. 3D direct laser writing using a 405 nm diode laser. *Opt. Lett.* **39**, 6847–6850 (2014).
25. Hwu, E. T. & Boisen, A. Hacking CD/DVD/Blu-ray for biosensing. *ACS Sens.* **3**, 1222–1232 (2018).
26. Hwu, E. T., Illers, H., Jusko, L. & Danzebrink, H. U. A hybrid scanning probe microscope (SPM) module based on a DVD optical head. *Meas. Sci. Technol.* **20**, 084005 (2009).
27. Hwu, E. T. et al. Anti-drift and auto-alignment mechanism for an astigmatic atomic force microscope system based on a digital versatile disk optical head. *Rev. Sci. Instrum.* **83**, 013703 (2012).
28. Liao, H. S. et al. Operation of astigmatic-detection atomic force microscopy in liquid environments. *Rev. Sci. Instrum.* **84**, 103709 (2013).
29. Segerink, L. I., Koster, M. J., Sprenkels, A. J. & van den Berg, A. A low-cost 2D fluorescence detection system for μm sized beads on-chip. *Lab Chip* **12**, 1780–1783 (2012).
30. Barathur, R. et al. New disc-based technologies for diagnostic and research applications. *Psychiatr. Genet.* **12**, 193–206 (2002).
31. Rothenbach, C. A. & Gupta, M. C. High resolution, low cost laser lithography using a Blu-ray optical head assembly. *Opt. Lasers Eng.* **50**, 900–904 (2012).
32. Blu-ray Disc Association. White Paper Blu-Ray Disc™ Format. 1–48 http://www.blu-raydisc.com/Assets/Downloadablefile/White_Paper_General_4th_20150817_clean.pdf (2010).
33. Choi, J. W., Kim, H. C. & Wicker, R. Multi-material stereolithography. *J. Mater. Process. Technol.* **211**, 318–328 (2011).
34. Han, D., Yang, C., Fang, N. X. & Lee, H. Rapid multi-material 3D printing with projection micro-stereolithography using dynamic fluidic control. *Addit. Manuf.* **27**, 606–615 (2019).
35. Zhang, X., Xi, W., Huang, S., Long, K. & Bowman, C. N. Wavelength-selective sequential polymer network formation controlled with a two-color responsive initiation system. *Macromolecules* **50**, 5652–5660 (2017).
36. Taormina, G., Sciancalepore, C., Messori, M. & Bondioli, F. 3D printing processes for photocurable polymeric materials: technologies, materials, and future trends. *J. Appl. Biomater. Funct. Mater.* **16**, 151–160 (2018).
37. Fischer, J. & Wegener, M. Three-dimensional optical laser lithography beyond the diffraction limit. *Laser Photonics* **7**, 22–44 (2013).

38. Alkelly, A. A. Spot size and radial intensity distribution of focused Gaussian beams in spherical and non-spherical aberration lenses. *Opt. Commun.* **277**, 397–405 (2007).

Acknowledgements

The authors would like to acknowledge the financial support from the Villum Experiment (Grant No. 00023116), the Danish National Research Foundation (DNRF122), and Villum Foundation (Grant No. 9301) for Intelligent Drug Delivery and Sensing Using Microcontainers and Nanomechanics (IDUN) and the Novo Nordisk Foundation (NNF17OC0026910)—Microstructures, microbiota and oral delivery (MIMIO). The authors would also like to thank Lasse Højlund Eklund Thamdrup from the Department of Health Technology, Technical University of Denmark, for his help with the preparation of the printer component.

Author contributions

T.J.C. and L.V. designed and built the mechanism and electronic control system of the 3D printer. T.J.C. developed the LabVIEW programme for the 3D printer. T.J.C. and M.V. optimised the printing parameters and conducted the printing process. E.T.H. initiated the OPU 3D printing concept and provided technical consultancy for implementing the HD-DVD pickup unit. T.J.C. and O.I. built the optical model and simulated the optimisation. E.T.H., L.H.N., and A.B. supervised the experiments. T.J.C., E.T.H., and L.H.N. wrote the manuscript with the assistance of all authors.

Competing interests

The authors declare no competing interests.

Additional information

Supplementary information The online version contains supplementary material available at <https://doi.org/10.1038/s42005-021-00532-4>.

Correspondence and requests for materials should be addressed to T.-J.C.

Reprints and permission information is available at <http://www.nature.com/reprints>

Publisher's note Springer Nature remains neutral with regard to jurisdictional claims in published maps and institutional affiliations.



Open Access This article is licensed under a Creative Commons Attribution 4.0 International License, which permits use, sharing, adaptation, distribution and reproduction in any medium or format, as long as you give appropriate credit to the original author(s) and the source, provide a link to the Creative Commons license, and indicate if changes were made. The images or other third party material in this article are included in the article's Creative Commons license, unless indicated otherwise in a credit line to the material. If material is not included in the article's Creative Commons license and your intended use is not permitted by statutory regulation or exceeds the permitted use, you will need to obtain permission directly from the copyright holder. To view a copy of this license, visit <http://creativecommons.org/licenses/by/4.0/>.

© The Author(s) 2021

Appendix II

Paper II

Microscale mucoadhesion force analyzer using DVD optical pickup unit (temporary)

Tien-Jen Chang, Line Hagner Nielsen, Anja Boisen, En-Te Hwu

In preparation

Microscale mucoadhesion force analyzer using DVD optical pickup unit

Authors: Tien-Jen Chang*, Line Hagner Nielsen, Anja Boisen, En-Te Hwu

Affiliations:

The Danish National Research Foundation and Villum Foundation's Center for Intelligent Drug Delivery and Sensing Using Microcontainers and Nanomechanics (IDUN), Department of Health Technology, Technical University of Denmark, 2800 Kgs. Lyngby, Denmark

Contact email: tiech@dtu.dk

Abstract:

In the pharmaceutical field, oral drug delivery devices continue to shrink now down to micrometer scale size, driving a trending demand to investigate *in vitro* and *ex vivo* mucoadhesion force down to micro-newton scale. However, due to the limitation of measuring sensitivity, conventional methods, e.g., a texture analyzer lack reliability while measuring force in this range. Here, we report on an open-source force analyzer that utilizes an optical-pickup unit (from a DVD player) to detect cantilever-based force transducers and achieves a wide force-sensing range from 1.1 N to 0.99 nN. The cantilever force transducers can easily be adjusted to fit different force ranges by adjusting steel shim, magnets, and 3D printed components. Further, this force analyzer equips a linear stepper motor with a positioning resolution of 40 nm moving a sample stably. The force transducers were calibrated from newton to nano-newton forces, which also demonstrates the system measurement reliability. This analyzer fulfills the need for microscale mucoadhesion force measurement. To validate this analyzer, we implemented a preliminary study to investigate the effect of time and humidity on mucoadhesion of porcine intestinal tissue, and was applied to measure the mucoadhesion force of a micrometer-sized oral drug delivery device.

Keywords: Microscale, Nanoscale, Mucoadhesion, Cantilever, Force transducer, Oral drug delivery, microdevices, microcontainers

Specifications table

Hardware name	OPU force analyzer
Subject area	<ul style="list-style-type: none">• Medical (e.g. Pharmaceutical Science)• Engineering and Material Science• Educational Tools and Open Source Alternatives to Existing Infrastructure• General
Hardware type	<ul style="list-style-type: none">• Measuring physical properties and in-lab sensors• Mechanical engineering and materials science
Open Source License	<i>CC BY 4.0</i>
Cost of Hardware	<i>3000 – 3500 EUR</i>
Source File Repository	doi:10.17632/cnkd95kp65.1

1. Hardware in context

In the past decades, different micrometer-scale devices were suggested to improve oral drug delivery efficiency. These devices include microcontainers (MCs) for higher oral bioavailability of poorly water-soluble drugs [1, 2] and shape-changing microdevices for increasing the retention time in the GI tract as well as the extension of drug release [3]. The trend of shrinking the device size from the millimeter to micrometer scale leads to an unmet need to evaluate the mucoadhesive properties of microdevices.

The ability for oral drug delivery devices to be mucoadhesive in the gastrointestinal tract (GI tract) is crucial, as it influences retention time of the devices as well as absorption and bioavailability of the drugs [4-6]. In general for characterizing mucoadhesion, a flow-through [7] and a tensile strength method [8] have been used for the investigation of the interaction between a mucus layer and devices. The tensile strength method directly measures the mucoadhesion force of a single device, illustrating the mucoadhesion by a force to displacement curve [9]. The most widely used instrument for detecting mucoadhesion force is a texture analyzer, which provides force measurements in the range from newton to millinewton [4, 9, 10]. However, the mucoadhesive forces of most microdevices are in micro-newton range. As the result, the texture analyzer cannot provide a reliable measurement for the microdevices.

The texture analyzer can switch to a more sensitive loadcell for achieving a higher force measurement resolution. However, the mechanical framework design of the texture analyzer and positioning mechanism introduce internal vibrations that interferes with force sensing in the micro-newton range [10]. Atomic force microscopy can achieve high force measurement sensitivity in the nano-newton range. Thus, an atomic force microscope was modified to detect mucoadhesion of nanoparticles [11]. Nevertheless, limited by the fragile microscale cantilever, atomic force microscopy can only carry a maximum sample size in the range of tens of micrometers. The current force measurement methods cannot provide reliable characterizations of mucoadhesion force in the micro-newton scale for micrometer-sized

particles and devices. Other commercial microscale tensile force instruments might potentially be repurposed for this measurement task. However, most of these costly instruments are not available as open source, making it challenging to modify them according to customized applications [12].

An optical-pickup-unit (OPU) is an electronic component for recording and retrieving digital data on optical discs such as C.D.s, DVDs, H.D. DVDs, and Blu-rays [13]. An OPU integrates a laser source, sensors, actuators, and delicate optics in a compact size, similar to a matchbox. Benefited by mass production for the optical data storage market, an OPU unit is priced at around five US\$. Furthermore, the low-cost OPU can achieve nano-meter displacement sensitivity from 0.1 Hz to MHz frequency range. The OPU has been successfully utilized for various applications, such as atomic force microscopy [14-16], stereolithography 3D printing [17], photolithography [18], and biosensing [19].

In this manuscript, we custom-built an OPU force analyzer by repurposing the use of a DVD OPU to achieve a force-sensing range from newton to nano-newton (**Figure 1**). In addition, we implement different cantilever-based force transducers to fit target force-sensing ranges easily. This proposed OPU force analyzer provides an open-source design and fulfills the force sensing gap between the currently available mucoadhesion force measuring methods.

2. Hardware description

This OPU force analyzer mainly contains a force detection module, a sample positioning module, and a control system (**Figures 1a and b**). While the sample positioning module approaches or withdraws a sample to a microprobe, the force detection module senses the applied force (**Figures 1c and d**). Simultaneously, the control system controls the sample positioning module movement and receives the measuring signal from the force detection module.

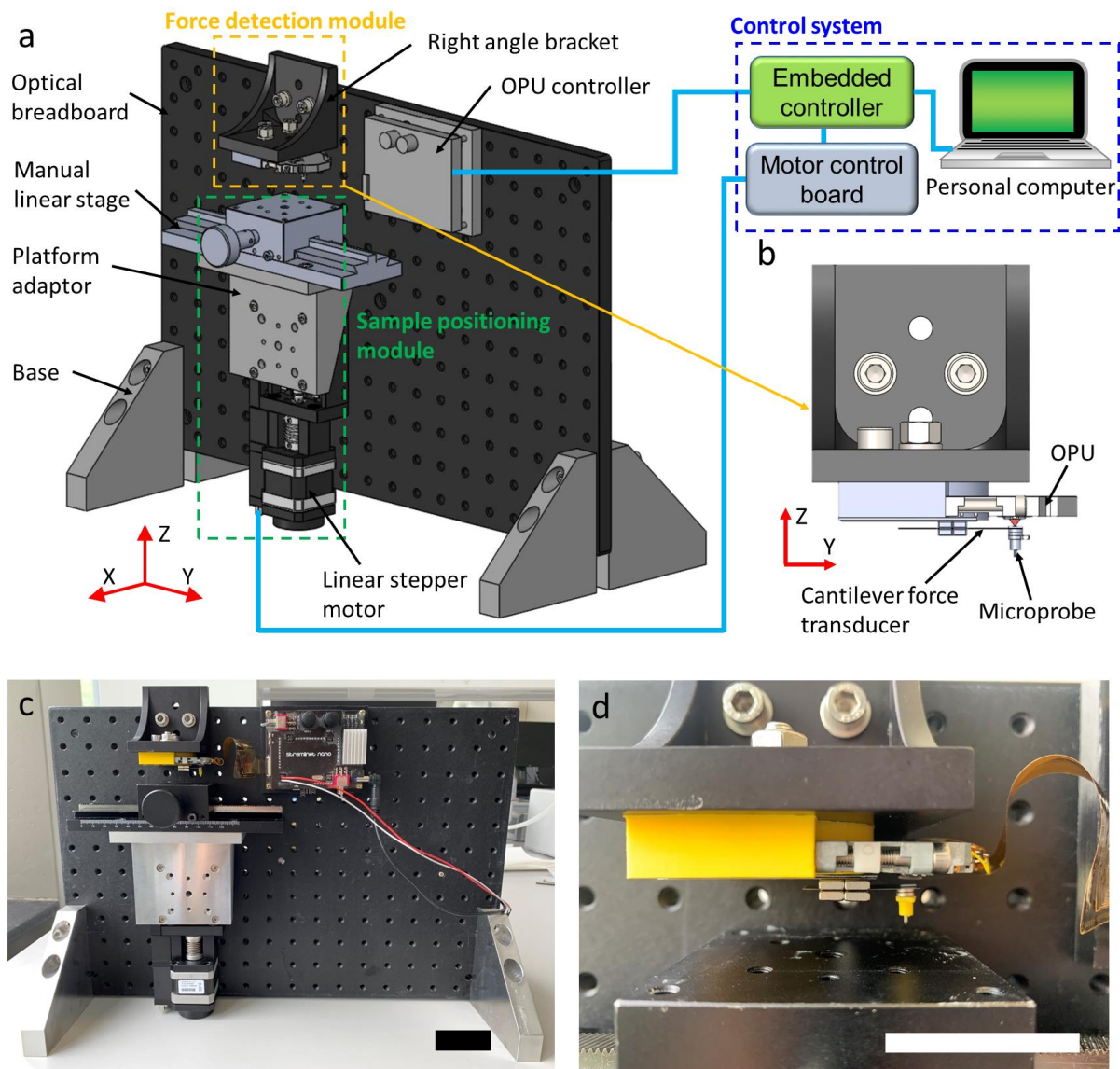


Figure 1. Development of force analyzer using a DVD optical-pickup-unit (OPU) to detect the cantilever force transducer with applied force from newton to nano-newton. **a)** Diagram of the force analyzer, including force detection and sample positioning modules and control system. **b)** Detailed diagram of force detection module assembled by OPU, cantilever force transducer, and microprobe. **c)** Photograph of the OPU force analyzer (scale bar represents 5 cm). **d)** Detailed photograph of force detection module (scale bar represents 5 cm).

2.1 Force detection module

Figure 2a shows the force detection module consisting of the OPU and the cantilever-based force transducer. The OPU emits a laser with a wavelength of 650 nm, and a built-in voice coil motor actuates an objective lens in the Z direction to precisely focus the laser on the mirror. Furthermore, the OPU integrates an astigmatic optical path and a sensor to generate a focus error signal (FES) [13]. While the mirror approaches along the Z-axis to a laser focal point, the FES appears an S shape curve (S-curve) (**Figure 2b**). The middle part of the S-curve represents a highly sensitive linear signal, which monitors the cantilever deflection with a

nanometer-scale resolution. Thus, the FES can detect the cantilever deflection caused by an applied force. The DVD OPU has a FES linear range of around a few microns.

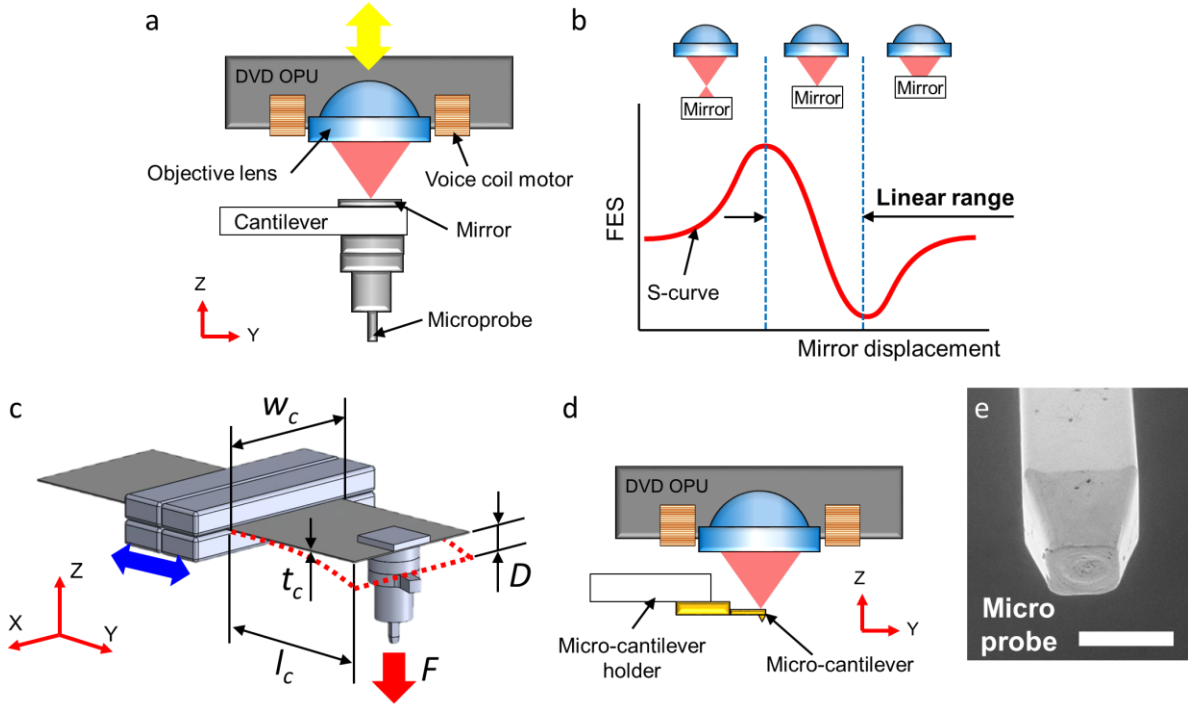


Figure 2. Illustration of the force detection module. **a)** The DVD OPU focuses a 650-nm-wavelength laser beam on a mirror to sense the deflection of the cantilever force transducer. **b)** Focus error signal (FES) presents an S-curve, while displacing the mirror along the Z direction. The S-curve presents a highly sensitive linear range. **c)** The cantilever deflection D caused by the applied force F . The force detecting range of the cantilever force transducer is defined by the thickness (t_c) and length (l_c) of cantilever. The thickness of cantilever is modified by shifting four rectangle magnets along the Y direction. **d)** Installation of micro-cantilevers for nano-newton scale force measurement. **e)** SEM image of the microprobe (scale bar represents 500 μm).

The cantilever-based force transducer converts applied force to a structure deflection during the measuring process (**Figure 2c**). The applied force F is proportional to cantilever deflection D as described in the formulation [20]:

$$F = D \frac{E_c w_c t_c^3}{4 l_c^3} \quad (1)$$

Where E_c is the Young's modulus of the cantilever, w_c , t_c , and l_c are the cantilever's width, thickness, and length, respectively.

The force detection module utilizes different cantilever-based force transducers for detecting applied forces from newton to micro-newton. Steel shim-based cantilevers can easily be adjusted to fit a suitable measuring force range by selecting the shim thickness and/or adjusting the cantilever length, according to **equation 1**. In addition, a commercial

micro-cantilever (AFM probe) can be directly attached to the edge of the steel shim for detecting force in the nano-newton scale (**Figure 2d**).

The force detection module utilizes a microprobe within the microscale contact area to increase the reproducibility of micro-newton mucoadhesion force measurements. This microprobe is a straight pin, an off-the-shelf standardized electronic component (**Figure 2e**). Compared to the centimeter-scale probe on a commercial texture analyzer, this microprobe is suitable for carrying a single micrometer-scale device.

2.2 Sample positioning module

A manual linear stage carries the sample, allowing adjustment of the sample position along the Y-axis (**Figure 1a**). To approach and withdraw the sample to the microprobe, we use a linear stepper motor (LTM 60-25, OWIS GmbH, Staufen, Germany) that provides a total travel distance of 25 mm along the Z-axis. The stepper motor moves 5 μm per step. By a maximum of 128 divided stepper motor drivers, the stage reaches the highest positioning resolution of 40 nm for a single sub-step. Within the highest positioning resolution setting, the motor has a maximum positioning speed of 1.56 mm/s.

2.3 Control system

An embedded controller (myRIO-1900; National Instruments, Austin, TX, USA) connects to an OPU controller and a motor control board (**Figure 1a**). The OPU controller calculates the FES and drives the voice coil motor. The motor control board controls the stepper motor for the sample positioning movement. The embedded controller communicates with a computer through a graphical user interface program to control the force measurement process.

In summary, the presented OPU force analyzer offers:

- Nanometer-scale sensitivity and a broad force measuring range from newton to nano-newton.
- Increased reproducibility for mucoadhesion force characterization of microscale devices by the microprobe.
- Cost-effective components and an open-source design providing users easy customization for various force measurement tasks, such as indentation test and compress test.

3. Design files

The design files were drawn by a computer-aided design (CAD) software Solidworks 2014 (Dassault Systèmes SolidWorks Corporation, Massachusetts, USA). All the design files can be download from the linked Mendeley data repository.

3.1 CAD files

Design file name	File type	Open source license	Location of the file
Base.SLDPRT	CAD	CC BY 4.0	doi:10.17632/cnkd95kp65.1
Measuring head.SLDPRT	CAD	CC BY 4.0	doi:10.17632/cnkd95kp65.1
Platform.SLDPRT	CAD	CC BY 4.0	doi:10.17632/cnkd95kp65.1
Platform adaptor.SLDPRT	CAD	CC BY 4.0	doi:10.17632/cnkd95kp65.1
Probe base.SLDPRT	CAD	CC BY 4.0	doi:10.17632/cnkd95kp65.1
Force corrector A.SLDPRT	CAD	CC BY 4.0	doi:10.17632/cnkd95kp65.1
Force corrector B.SLDPRT	CAD	CC BY 4.0	doi:10.17632/cnkd95kp65.1
OPU controller base.SLDPRT	CAD	CC BY 4.0	doi:10.17632/cnkd95kp65.1
Microprobe	CAD	CC BY 4.0	doi:10.17632/cnkd95kp65.1
Cantilever.SLDPRT	CAD	CC BY 4.0	doi:10.17632/cnkd95kp65.1
Magnet track.SLDPRT	CAD	CC BY 4.0	doi:10.17632/cnkd95kp65.1
Micro-cantilever holder.SLDPRT	CAD	CC BY 4.0	doi:10.17632/cnkd95kp65.1

3.2 3D printing files

All 3D printing files are available in the STL (STereoLithography) format on the Mendeley data repository. All parts were printed by a fused deposition 3D printer, Prusa i3 MK2.5S printer (Prusa Research, Prague, Czech Republic) with a 0.4 mm nozzle and PLA filament, with a layer height of 0.1 mm and 30 % infill rate.

Design file name	Number of required prints	Open source license	Location of the file
Measuring head.stl	1	CC BY 4.0	doi:10.17632/cnkd95kp65.1
Probe base.stl	1	CC BY 4.0	doi:10.17632/cnkd95kp65.1
Force corrector A.stl	1	CC BY 4.0	doi:10.17632/cnkd95kp65.1
Force corrector B.stl	1	CC BY 4.0	doi:10.17632/cnkd95kp65.1
OPU controller base.stl	1	CC BY 4.0	doi:10.17632/cnkd95kp65.1

3.3 Software and firmware

The firmware and the operation program were edited and compiled by LabVIEW 2016 software (National Instruments, Austin, TX, USA). A compressed file containing all the programs is available on Mendeley data repository listed in the following table. All unzipped program files are located in the same folder to maintain the original data path.

Design file name	File type	Open source license	Location of the file
OPU force analyzer	Zip	CC BY 4.0	doi:10.17632/cnkd95kp65.1

4. Bill of Materials

The bill of materials includes mechanical mechanisms, electronic components, controllers, and other needed components. As the prices vary from different suppliers or source channels, the displayed costs in the table match the price at the moment of purchase. The current prices can be found at the listed source.

Designator	Component	Number	Cost per unit [EUR]	Total cost [EUR]	Source of materials	Material type
Base	Base	4	50	200	CNC workshop	Metal
Platform	Platform	1	50	50	CNC workshop	Metal
Platform adaptor	Platform adaptor	1	67.75	67.75	CNC workshop	Metal
OPU	DVD OPU Top1300s	1	6.26	6.26	Amazon	Electronics
OPU controller	OPU controller	1	460.69	460.69	Stromlinet Nano	Electronics
Steel shim 0.1	Steel shim tape T0.1W12.7L1000	1	6.51	6.51	Misumi	Metal
Steel shim 0.3	Steel shim tape T0.3W12.7L1000	1	6.51	6.51	Misumi	Metal
Mirror	Polished Si wafer	1	18.7	18.7	Amazon	Silicon
Rectangle magnet	Rectangle magnet L20W4T2	4	0.2	0.8	Amazon or Supermagnete	Metal
Cylinder magnet	Cylinder magnet D4L1 (NO118)	10	1.635	16.35	Misumi	Metal
Linear stepper motor	Linear stepper motor (LTM 60-25)	1	1029	1029	Owis	Metal
Manual linear stage	Manual linear stage (One Knob Stage & 125mm Track Combination Stock #59-263)	1	194	194	Edmund	Metal
Optical breadboard	Optical Breadboard (MB3045_M)	1	181.3	181.3	Thorlabs	Metal
Right angle bracket	Right-Angle Bracket (MT402)	1	49.68	49.68	Thorlabs	Metal
Power supplier	Power supplier 15V	1	21.43	21.43	RS Components	Electronics

Designator	Component	Number	Cost per unit [EUR]	Total cost [EUR]	Source of materials	Material type
myRIO-1900	Embedded controller (myRIO-1900)	1	640	640	National instrument	Electronics
Stepper motor driver	Stepper motor driver (RAPS 128 Stepper Driver)	1	17.69	17.69	Reprap.me	Electronics
Motor control board	Motor control board (RADDS v1.6 board)	1	57.49	57.49	Reprap.me	Electronics
Straight pin	Straight Pin (HARWIN M20, 2.54mm Pitch, 36 Way, 1 Row, Straight Pin Header, Through Hole)	1	1.22	0.83	RS Components	Electronics
M6x20mm screw	M6x20 mm Hex head cap screws (SH6MS20)	2	0.342	0.684	Thorlabs	Metal
M6x16mm screw	M6x16 mm Hex head cap screws (SH6MS16)	15	0.322	4.836	Thorlabs	Metal
M6x10mm screw	M6x10 mm Hex head cap screws (SH6MS10)	4	0.300	1.203	Thorlabs	Metal
M4x25mm screw	M4x25 mm Hex head cap screws (SH4MS25)	4	0.150	0.601	Thorlabs	Metal
M4x8mm screw	M4x8 mm Hex head cap screws (SH4MS8)	10	0.123	1.23	Thorlabs	Metal
M3x25mm screw	M3X25 mm Hex head cap screws	1	0.20	0.20	Amazon or hardware store	Metal
M3x6mm screw	M3x6 mm Hex head cap screws (SH3M06)	5	0.145	0.725	Thorlabs	Metal
M6 nut	M6 nut	2	0.15	0.3	Amazon or hardware store	Metal

Designator	Component	Number	Cost per unit [EUR]	Total cost [EUR]	Source of materials	Material type
M4 nut	M4 nut	4	0.10	0.40	Amazon or hardware store	Metal
M6 washer	M6 washer (W25S050)	12	0.045	0.541	Thorlabs	Metal
M4 washer	M4 washer (W8S038)	4	0.0325	0.13	Thorlabs	Metal
PLA	PLA polymer	1	17.15	17.15	Reprap.me	Polymer
Micro-cantilever	Micro-cantilever (PPP-CONT)	1	27.6	27.6	Nanoandmore Gmbh	Silicon

5. Build Instructions

The assembly process of the OPU force analyzer needs instant glue and double-sided tape to bond the components firmly. The screw holes of the 3D printed parts are designed for a direct screw-in fixture, so no hole thread tapping is required. Be aware of 3D printing all the required parts before the assembly process.

5.1 Force detection module assembly (Figure 3a)

1. Components needed: 1x Steel shim 0.3, 1x OPU, 1x Measuring head, 1x M3x35mm screw, 1x M3x6mm screw, 1x Right angle bracket, 1x M6x16 mm screw, 2x M6x20mm screws, 2x M6 nuts, and 2x M6 washers.
2. Cut 38 mm of the steel shim 0.3 as a magnet track.
3. Glue the magnet track on the measuring head.
4. Fix the OPU on the measuring head with a M3x35mm screw and a M3x6mm screw.
5. Fix the measuring head on the right angle bracket with a M6X16mm screw, two M6X20mm screws, two M6 nuts, and two M6 washers.

5.2 Cantilever force transducer assembly (Figure 3b)

1. Components needed: 1x Steel shim 0.1, 4x Rectangle magnets, 2x Cylinder magnet, 1x Straight pin, 1x Probe base, 1x Mirror.
2. Cut 35 mm of the steel shim 0.1 as a cantilever force transducer.
3. Glue a mirror on the edge of the cantilever.
4. Below the mirror, glue a cylinder magnet on the bottom side of the cantilever.
5. Fix the cantilever to a target length (l_c) with four rectangle magnets.
6. Cut 10 mm of the straight pin as a microprobe.

7. Glue the microprobe in the cavity of the probe base, avoiding the microprobe protrude from the backside.
8. Glue a cylinder magnet on top of the probe base.
9. Place the cantilever forcer transducer on the magnet track and align the mirror to the OPU laser focal spot area.
10. To prepare different thickness cantilevers, repeat the assembly process 2-5.
11. The cantilever length and thickness influence the force measuring range. The force calibration for reference is shown in Section 7.2.

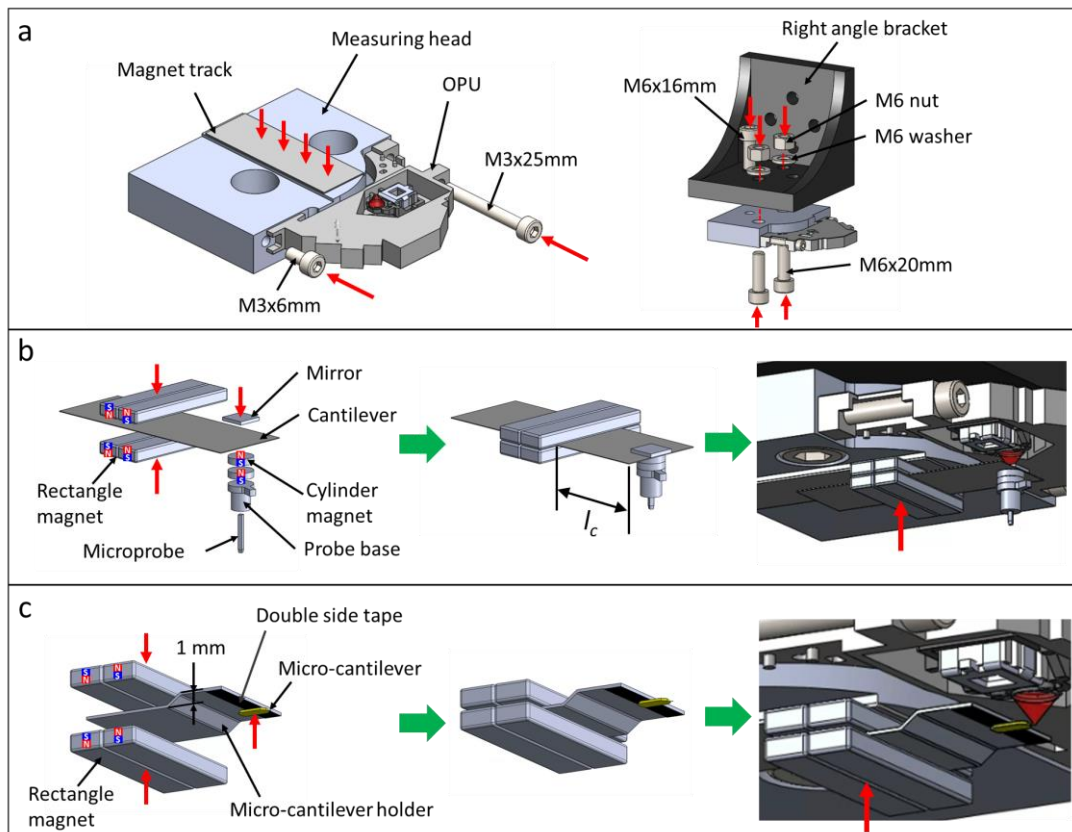


Figure 3. Assembly of **a)** force detection module, **b)** cantilever force transducer **c)** force transducer equipped with micro-cantilever.

5.3 Micro-cantilever force transducer assembly (Figure 3c)

1. Components needed: 1x Steel shim 0.3, 4x Rectangle magnets, 1x micro-cantilever.
2. Cut 20 mm of the steel shim 0.3.
3. Bend it as a micro-cantilever holder (**Figure 3c**).
4. Fix a micro-cantilever on the edge of the micro-cantilever holder with double-sided tape.
5. Fix the cantilever with four rectangle magnets.
6. Place the micro-cantilever holder on the magnet track and align the micro-cantilever to the laser focal spot area.

5.4 Whole system assembly (Figure 4)

1. Components needed: 1x Optical breadboard, 4x Bases, 1x OPU controller base, 1x Linear stepper motor, 1x Platform, 1x Platform adaptor, 1x Manual linear stage, 1x Force detection module, 1x OPU controller, 14x M6x16mm screws, 4x M6x12mm screws, 4x M4x25mm screws, 10x M4x8mm screws, 4x M3x6mm screws, 10x M6 washers, 4x M4 washers, 4x M4 Nuts.
2. Fix four bases on the four corners of the optical breadboard with eight M6x16mm screws (**Figure 4a**). Slightly adjust each base's vertical position to let the system stand on a flat surface stably.
3. Fix the OPU controller base on the optical breadboard with four M6x16mm screws.
4. Fix the linear stepper motor on the optical breadboard with four M4x25mm screws, four M4 nuts, and four M4 washers (**Figures 4a and b**).
5. Fix the platform adaptor on the platform of the linear stepper motor with four M4x8mm screws.
6. Fix the platform on the platform adaptor with six M6x8mm screws.
7. Fix the manual linear stage on the platform with four M6x8mm screws.
8. Fix the force detection module on the optical breadboard with two M6x16mm screws and two M6 washers (**Figures 4a and c**).
9. Fix the OPU controller on the OPU controller base with four M3x5mm screws (**Figure 4d**).

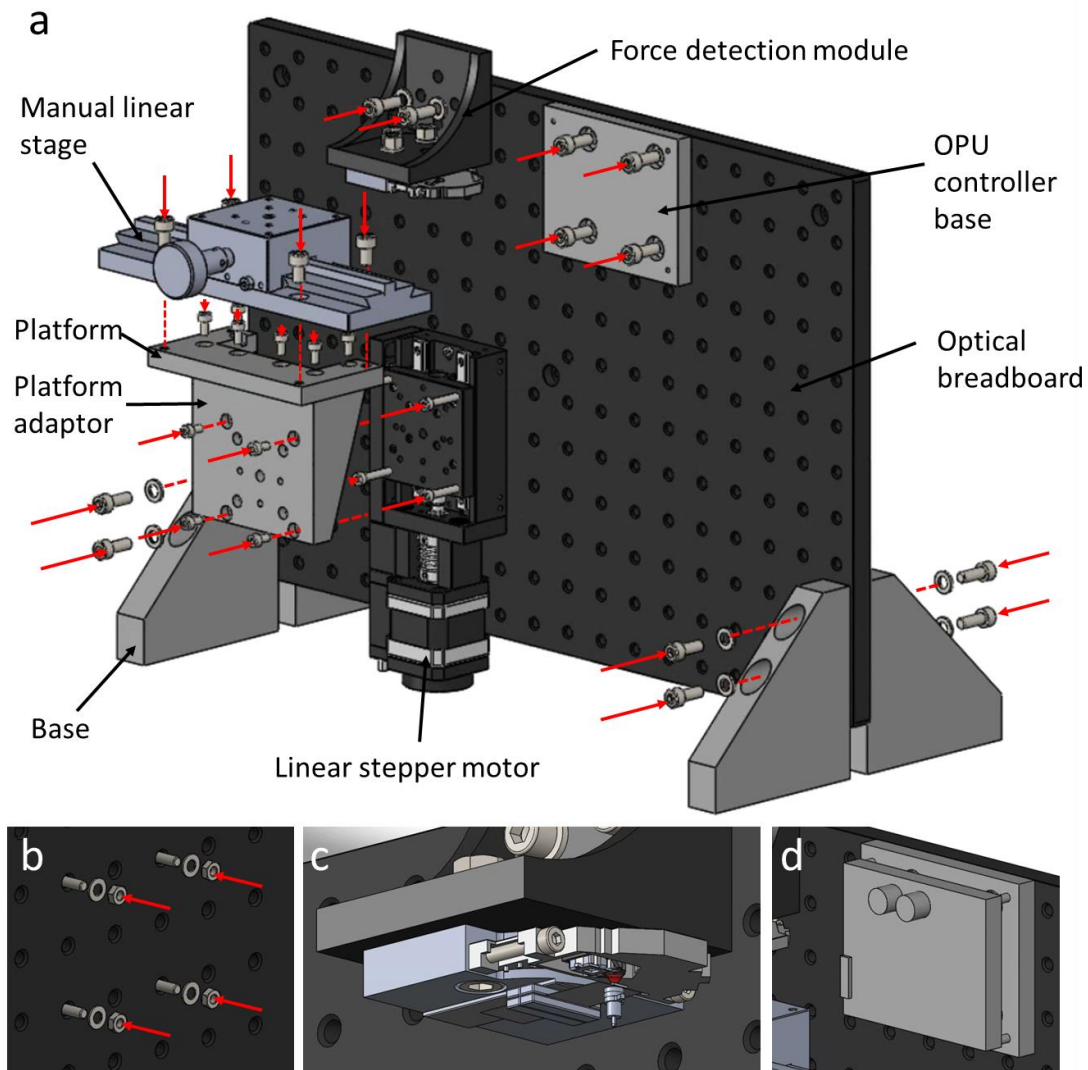


Figure 4. Assembly diagram of **a)** the whole system, **b)** fixing the linear stepper motor (view from the backside of optical breadboard), **c)** fixing the force detection module with cantilever force transducer, and **d)** fixing the OPU controller.

5.5 Wiring the control system (Figure 5)

1. Components needed: 1x myRIO-1900, 1x OPU controller, 1x OPU, 1x Stepper motor driver, 1x Motor control board, 1x Linear stepper motor, 1x Power supply
2. Connect the OPU controller's FES output pins to the myRIO-1900's ports A1+ and AGND (connector C). Then connect myRIO-1900's ports A1- and AGND. (**Figure 5a**)
3. Connect the OPU flat cable to the OPU controller (**Figure 5b**).
4. Mount the stepper motor driver on the motor control board (**Figures 5a** and **c**).
5. Connect the stepper motor driver's pins DIR, STP, MS_3, MS_2, MS_1, EN, and GND to port DIO0, DIO1, DIO12, DIO11, DIO10, DIO2, and GND (myRIO-1900 connector A), respectively.
6. Connect the stepper motor driver's pins 1A, 2A, 1B, and 2B to the linear stepper motor's pins 1, 2, 3, and 4, respectively.

7. Connect the power supply to the OPU controller.
8. Connect the power supply to 110 – 220 V power, and connect the OPU controller to the power adaptor.
9. Connect myRIO-1900 to a computer.

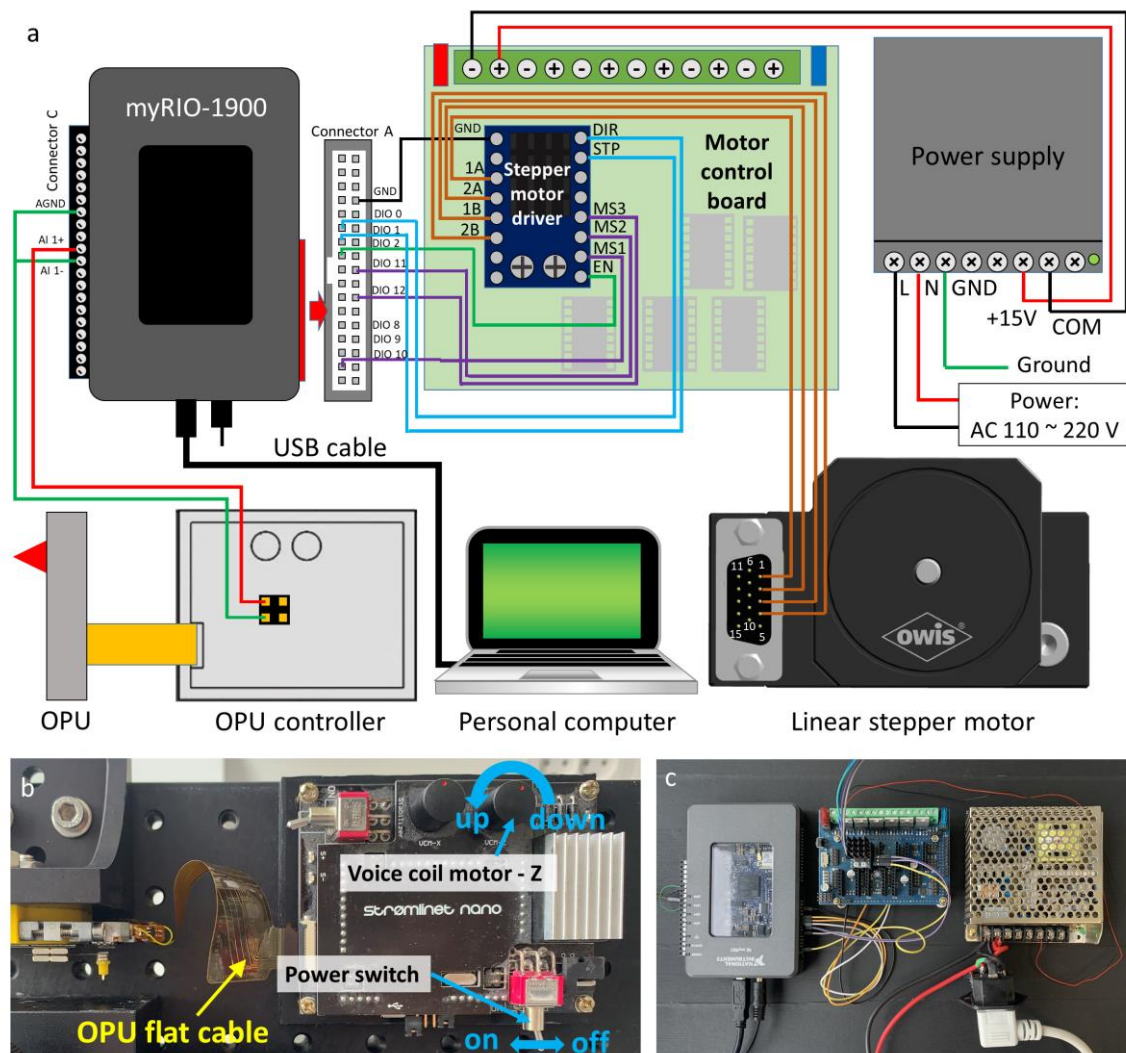


Figure 5. Illustration of the controlling system of OPU force analyzer. **a)** Wiring diagram. **b)** Photograph of the OPU connection and OPU the controller operation **c)** Photograph of the controlling system.

6. Operation Instructions (Figure 6)

1. Switch on the myRIO-1900, the power supply, and the OPU controller power (**Figure 5b**).
2. Open a LabVIEW project named "OPU force analyzer" and a Vi named "OPU force analyzer." Then press the "run" button to start the program. The FES appears in the signal chart.

3. Adjust a voice coil motor-z knob (on the OPU controller, **Figure 5b**) clockwise/counterclockwise to shift the objective lens upward/downward. Utilize the knob to adjust the vertical position of the laser spot.
4. Focus the laser spot on the mirror on the top side of the cantilever force transducer (**Figure 2**) or a micro-cantilever directly.
5. Adjust the knob and shift the FES to the center of the linear range (**Figure 2**).
6. Place a sample on the manual linear stage.
7. Activate the linear stepper motor by clicking the "Enable" button, and move the sample to a suitable position by "move up" and "move down" buttons.
8. Set the measurement parameters, "contact force," "contact time," "retreat point," and "Speed." The retreat point represents the stop position while withdrawing the sample from the microprobe.
9. Set the "Force sensitivity (S_F)" to convert the FES voltage to force reading value. The S_F could be referred to in Section 7.2 calibration process.
10. Click the "start" button to enable the measurement procedure. The signal chart plots and records the measured force curve.
11. After the measuring process, press the "Save" button to save the recorded signal chart.

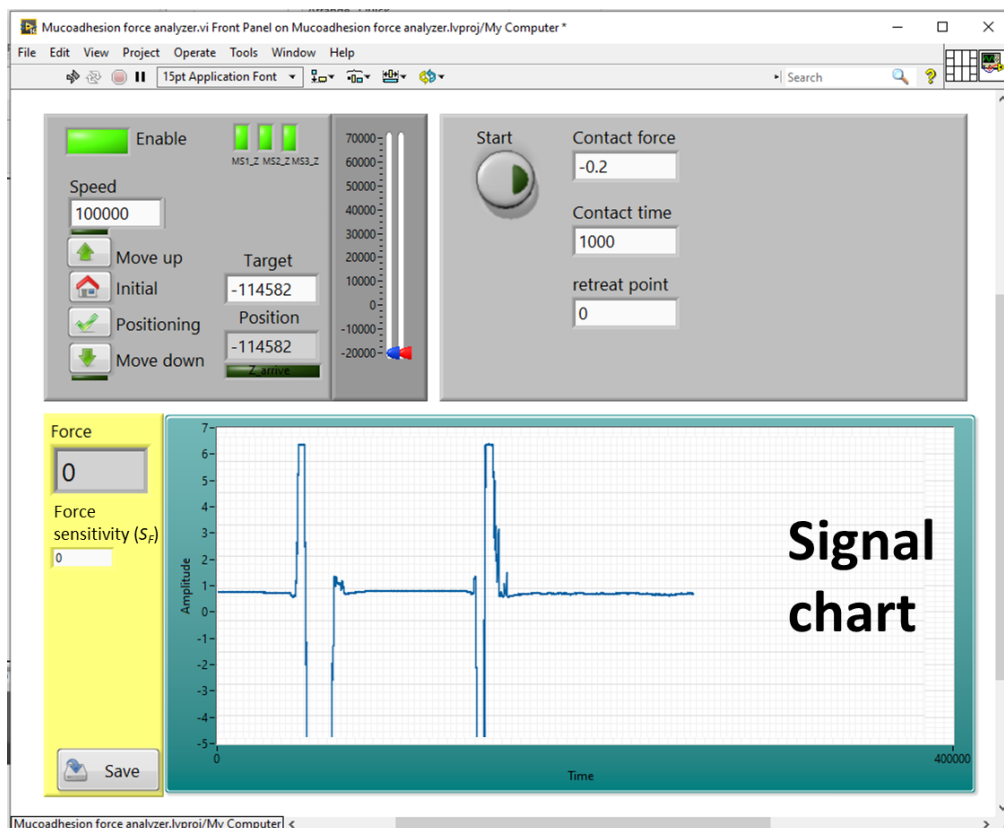


Figure 6. The interface of the operation program for implementing force measurement, while setting parameters of contact force, contact time, retreat point, speed, and force sensitivity.

7. Validation and Characterization

7.1 Linear range and noise analysis (Figure 7)

It is crucial to characterize the linear range of the S-curve and the FES noise level before sensing the cantilever-based force transducer. **Figure 7a** shows the S-curve with upper and lower signal cutoff (due to the signal saturation). The S-curve linear range was further analyzed in **Figure 7b**. The full range inner S-curve (blue line, 8.68 V to -9.98 V) has an R-square value of 0.982, which is unsuitable for accurate displacement measurement. When reducing the sensing range to 3.76 and -9.98V, the R-square value is 0.999, showing much better signal linearity. Thus, the OPU force analyzer is working at this linear range (red line) with an effective displacement sensing range of 1.07 μm and a sensing sensitivity of 0.077 nm/mV.

The FES from the OPU controller has a root mean squared (RMS) noise level of 28 mV, which corresponds to a displacement sensing noise of 2.2 nm. Further, we investigate the combined system noise level by focusing the focal spot onto the mirror on the top side of the cantilever. At this condition, the FES signal containing environmental vibration noise and electrical noise from the OPU controller, was processed by a 100 Hz low pass filter (**Figure 7c**). Hence, the FES used for detection has a RMS noise of 64 mV, corresponding to a displacement sensing noise of 4.9 nm. A Gaussian distribution statistical analysis (**Figure 7d**) shows that the FES signal noise has a mean value and standard deviation of 0.972 V and 0.032 V, respectively. The combined system noise can be reduced if the OPU force analyzer is placed on an optical table.

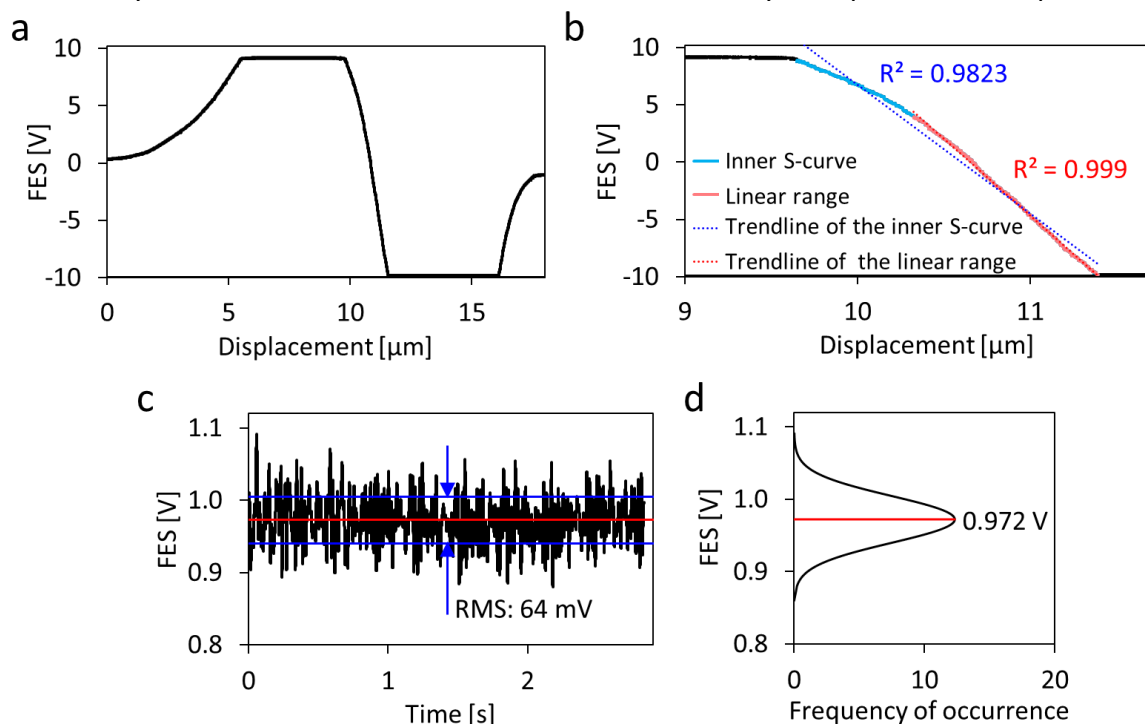


Figure 7. S-curve linear range and noise analysis. **a)** The whole S-curve detected from 8.68 to -9.98. V **b)** Analysis of inner S-curve presenting that the signal between 3.76 and -9.98V appears a linear region, as R-square value is 0.999. **c)** Signal noise of FES in the linear region of S-curve shows a RMS noise of 64 mV, after processed by 100 Hz low pass filter. **d)** The signal noise shows a Gaussian distribution.

7.2 Force transducers calibration

After the signal sensitivity characterization, the OPU force analyzer can monitor different cantilever-based force transducers to reach different target force measurement ranges.

7.2.1 Newton to milli-newton force transducer calibration (Figure 8)

To achieve a force-sensing range from newton to milli-newton scale, five 0.3 mm steel shims were stacked and glued into a 1.5 mm thick cantilever transducer. The length of the cantilever was adjusted to 8.26 mm. The microprobe was attached to the free end of the thick cantilever. A digital scale (JoeFrex corp., Huston, United States) on the sample stage was driven upward to contact the microprobe. Three contact force (translated from the weight) values from the digital scale were used to calibrate the FES, with a force sensitivity (S_F) of 0.086 N/V. The thick cantilever transducer enables the OPU force analyzer to measure a force ranging from 1.1 N to 5.50 mN.

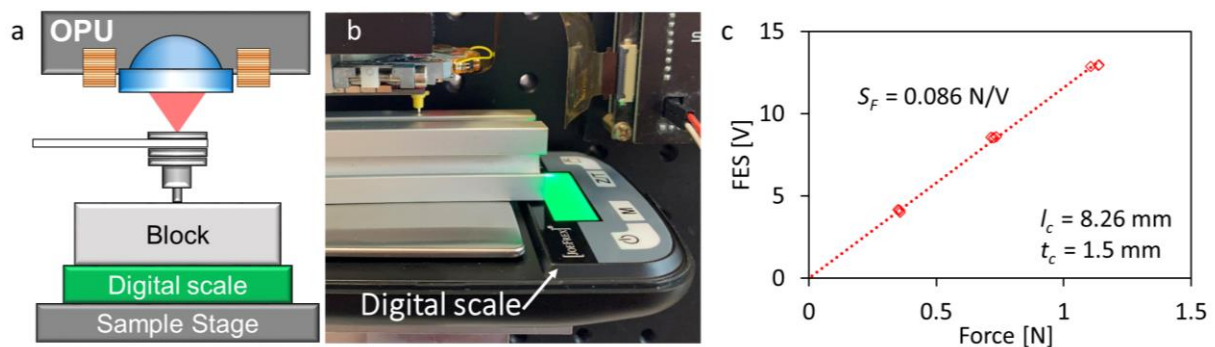


Figure 8. Force calibration of cantilever force transducer in the range from newton to milli-newton **a)** Diagram of the calibration process presenting OPU monitors the cantilever deflection while the sample stage position the digital scale upward to contact the microprobe. **b)** Photograph of the force calibration process. **c)** Calibration curve of using 1.5 mm-thick cantilever present force sensitivity (S_F) of 0.086 N/V, while applying force from 1.1 N to 5.50 mN, $n=3$.

7.2.2 Milli-newton to micro-newton force transducers calibration (Figure 9)

A different method was used to calibrate the cantilever force transducers for milli-newton and micro-newton ranges. A standard steel shim ($t_c = 0.3 \text{ mm}$) was used as a milli-newton cantilever transducer. **Figure 9a** shows a force corrector A attached to the bottom of the cantilever. Different known weights from 2.74 to 60.98 mg (weighted by precision balance XPE26, Mettler Toledo, Greifensee, Switzerland) were loaded on the force corrector A (**Figure 9b**). The force corrector B on the sample stage was driven upward and unloaded the weight. The weight loading and unloading process were monitored by the FES (**Figure 9c**), which was then calibrated with multiple cantilever length ($l_c = 8.26, 13.3, \text{ and } 18.4 \text{ mm}$) settings (**Figure 9d**). A micro-newton cantilever transducer is a thin steel shim ($t_c = 0.1 \text{ mm}$) that was calibrated with the same process (**Figure 9e**). Both the milli-newton and micro-newton cantilever

transducers have linear correspondences between the FES and weight at different l_c length settings.

Since the milli- and micro-newton cantilever transducers are primarily used for single microdevice mucoadhesion force measurements, we further analyzed the force sensing ranges and sensitivities of both transducers with different cantilever length settings. **Figure 9f** shows the force sensing range, sensitivity, and resolution of the milli-newton transducer, which can sense a maximum force of 111.56 mN and the highest resolution of 0.05 mN. The micro-newton transducer can reach a maximum force limit of 3,271.3 μ N and the highest resolution of 3.5 μ N (**Figure 9g**). Users can reference the above-mentioned l_c and t_c parameters to find a suitable force-sensing range for their experiments easily.

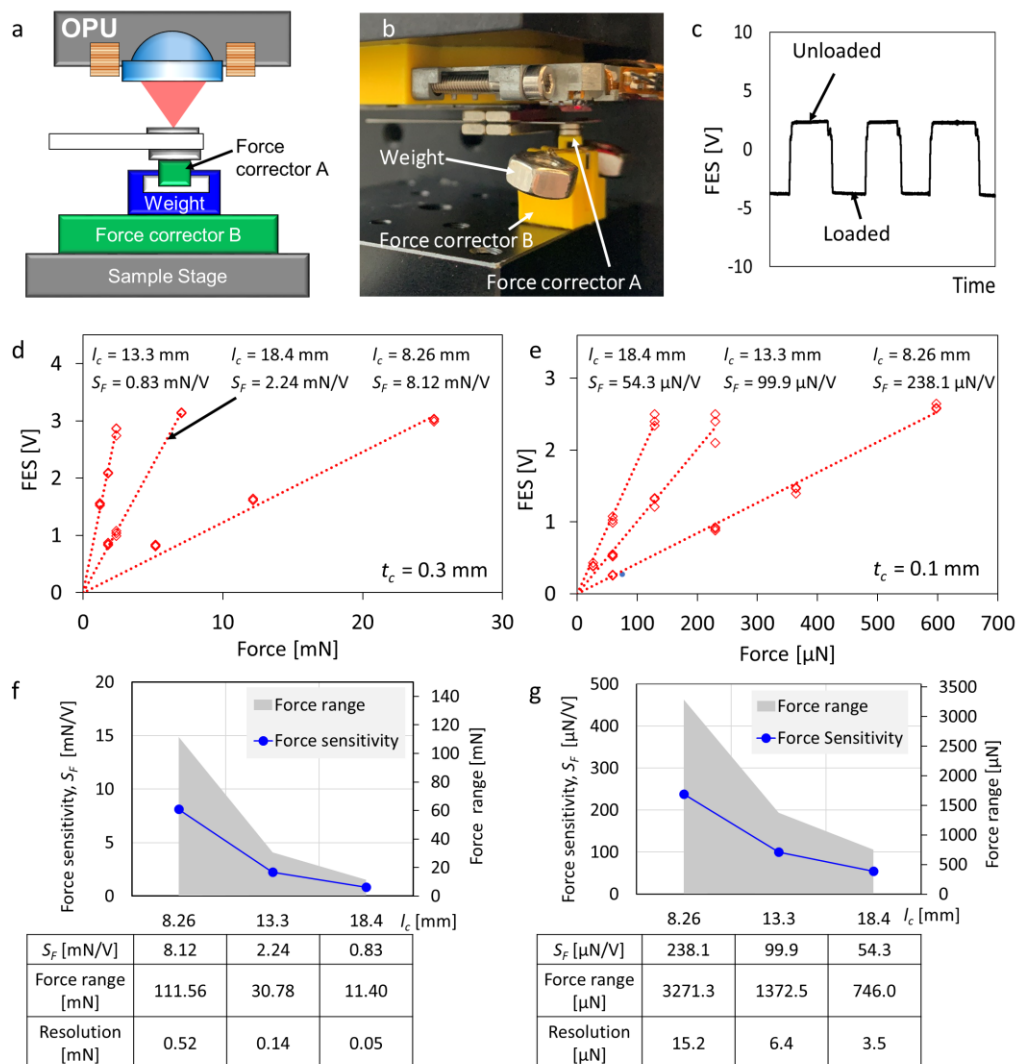


Figure 9. Force calibration of cantilever force transducer in the range from milli-newton to micro-newton **a)** Diagram of the calibration process by loading a known weight (from 2.74 to 60.98 mg) on the cantilever force transducer and unloading cantilever by lifting the sample stage. **b)** Photograph of the force calibration process. **c)** Focus error signal (FES) step signal while loading unloading the cantilever force transducer. **d)** Calibration curves of milli-newton scale force using 0.3 mm-thick cantilever present force sensitivity (S_F) of 0.83, 2.24, 8.12

mN/V, with adjusted cantilever length of 18.4, 13.3, and 8.26 mm, respectively, $n=3$. **e)** Calibration curves of milli-newton scale force using 0.1 mm-thick cantilever present force sensitivity (S_F) of 54.3, 99.9, 238.1 $\mu\text{N}/\text{V}$, with adjusted cantilever length of 18.4, 13.3, and 8.26 mm, respectively, $n=3$. Force sensitivity (S_F), force range, and resolution of each cantilever parameter setting of **f)** milli-newton range **g)** micro-newton range.

7.2.3 Nano-newton force transducer calibration (Figure 10)

For nano-newton range force sensing, we utilized an AFM probe (PPP-CONT, NanosensorsTM, Neuchatel, Switzerland) containing a micro-cantilever with an $l_c = 450 \mu\text{m}$, $w_c = 50 \mu\text{m}$, and $t_c = 2 \mu\text{m}$, and a tip (height = 15 μm) at the bottom side of the micro-cantilever. The nanoscale laser spot of the OPU is beneficial to monitor the micro-cantilever, which can work as a nano-newton force transducer. The AFM probe was attached to the micro-cantilever holder by a double-sided tape (**Figure 10a** and **b**). The OPU laser can directly focus on the micro-cantilever (through 6. "Operation Instructions" step 4 to align the laser focal spot). A silicon substrate on the sample stage was positioned upward and touched the tip during the calibration process. The stage further moved 200, 400, and 800 nm while the FES monitored the micro-cantilever deflection simultaneously. Since the micro-cantilever has a typical force constant of 0.2 nN/nm, the OPU force analyzer can reach a force sensitivity of 15.5 nN/V and a resolution of 0.99 nN (**Figure 10c**).

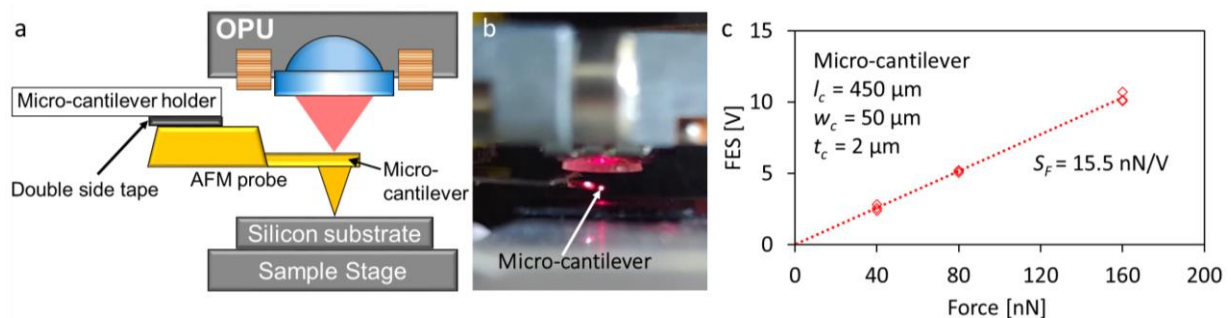


Figure 10. Force calibration of nano-newton force transducer. **a)** Diagram of the calibration process presenting OPU monitors the micro-cantilever deflection induced by the movement of sample stage. The force constant of micro-cantilever is 0.2 nN/nm. **b)** Photograph of the force calibration process. **c)** Calibration curve of nano-newton scale force using micro-cantilever presents force sensitivity (S_F) of 15.5 nN/V, while sample stage move 200, 400 and 800 nm upward, corresponding to applied force of 40, 80 and 160 nN, respectively.

7.3 Preliminary study of mucoadhesion force alteration while time and moisture escape

While characterizing the mucoadhesive force of microdevices using the intestinal mucus layer, the dehydrating effect caused the mucus layer to be more adhesive and increased the measured mucoadhesion force. The dehydrating effect usually becomes severe as time passes by. Two experimental groups were set with a dry and a wet sample to realize how time affected the adhesive behavior of the mucus layer. A slice of porcine small intestinal tissue was measured the mucoadhesive force using the microprobe for every 10 min of the interval.

For the wet sample group, phosphate-buffered saline (PBS buffer) with a pH of 6.5 was constantly sprayed on the tissue to moisten the mucus layer for every 20 min of the interval. On the contrary, the tissue for the dry sample group was without any treatment. The tissue sample was approached and withdrawn the microprobe to directly investigate mucoadhesive properties with a contact force of 80 μN , a contact time of 1 s, and an approach/withdraw speed of 0.156 mm/s. The measurements were performed at room temperature and 45 ± 5 % relative humidity.

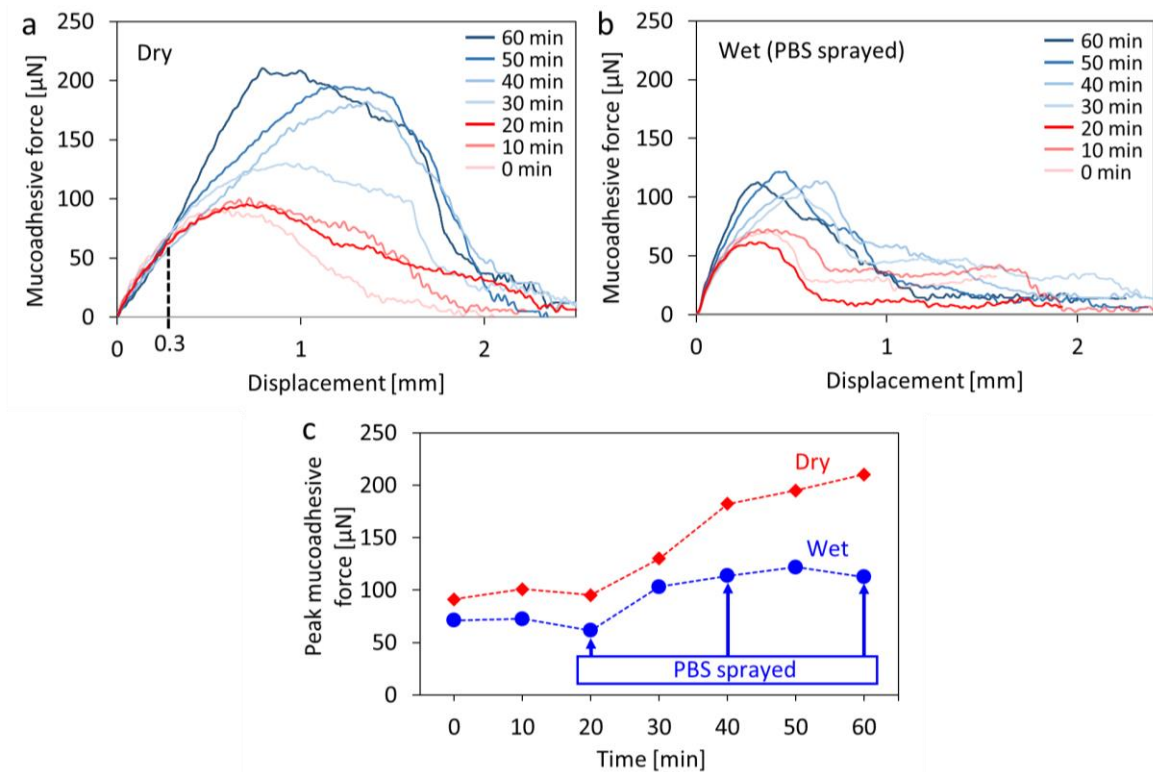


Figure 23. Investigation of mucoadhesive force alteration while time and moisture escapes. Mucoadhesive force to displacement curves were measured while withdrawing a microprobe from the porcine small intestinal mucosa of **a)** dry group (no treatment), and **b)** wet group (phosphate-buffered saline (PBS) sprayed on the tissue for every 20 min), for every 10 min of the interval. **c)** Peak mucoadhesive force of the dry and wet groups every 10 min in 1 h. The mucoadhesive force of the dry group increases 130 % after 1 h, as the wet group increases 57 %.

The mucoadhesion measurements for the dry and wet groups are shown in **Figure 11a** and **b**, respectively. The result indicates that the mucoadhesive force of groups increased as time passed. In the first 20 min, both groups had relatively stable mucoadhesive force (**Figure 11c**). The mucoadhesive force of the dry group increased continuously for 60 min. In the end, the mucoadhesive force peaked at approximately 130 % compared to the initial level. The mucoadhesion force of the wet group increased approximately 57 % within 60 min.

Furthermore, the slope of the force growing curve of the dry group (in the displacement of 0.3 mm) fluctuated at various time points (**Figure 11a**). The wet group kept the same slope

(**Figure 11b**). This preliminary study indicated that the PBS treatment maintained mucus layer stability during the mucoadhesive force measurements. Furthermore, the mucus layer behaves stable within 20 min.

7.4 Mucoadhesive force measurement of microcontainers

MCs are polymeric cylindrical microdevices for oral drug delivery [1, 2]. On the top side, MCs have a cavity for drug loading and as there is only one side open, the MCs can provide unidirectional drug release through the GI tract to increase drug absorption effectivity. The transit mechanism has been investigated by an *ex vivo* intestinal perfusion model and animal studies [7, 21]. However, the mucoadhesion force of a single MC is still not thoroughly studied due to a limited resolution of the conventional texture analyzer.

In this study, the OPU force analyzer was utilized to measure the mucoadhesive force of a single SU-8 MC using a porcine small intestinal tissue. The adhesion of PBS buffer to MC was also investigated for comparison. The MC was glued on the tip of the microprobe for the contact of the sample (mucus and PBS) with top and bottom sides, respectively (**Figures 12a** and **b**). The fresh tissue was opened using scissors and placed on the sample stage with mucosa side upward (**Figure 12c**). In addition, a PMMA plate was placed on the sample stage to carry the PBS buffer. The PBS buffer appeared an approximately 30-mm-diameter round, leading to a flat top surface to contact the MC. The parameters were set to a constant speed of 0.078 mm/s and a contact time of 1 s. Four measurements of each sample of both the top and bottom sides of the MC were implemented.

The result shows that the adhesive force curve of PBS to MC presents a right triangle (**Figure 12d**). In the sample withdrawal process, the adhesive force proportionally increased to an average peak force of 93.7 μN (top) and 91.6 μN (bottom). As the PBS separated from the MC, the force curve jumped back to the original level. The mucus presented a symmetrical hill profile with an average peak force of 75.5 μN (top) and 75.1 μN (bottom) in the middle (**Figure 12e**). Instead of a sudden detachment, the mucus gradually separated from the MC. In **Figure 12f**, the comparison indicates that MC is more adhesive to the PBS buffer than the mucus. The measurements of the PBS buffer show relatively low variation due to the material uniformity of the PBS buffer. The measurements of mucoadhesive force show high deviation. Both sides of the MC present the same adhesion level, as the MC possesses a symmetrical structure of both sides. The fact that the adhesive force of the top side shows a higher degree of variation, probably due to that the edge of cavity on the top side easily cause uncertain contact with mucus.

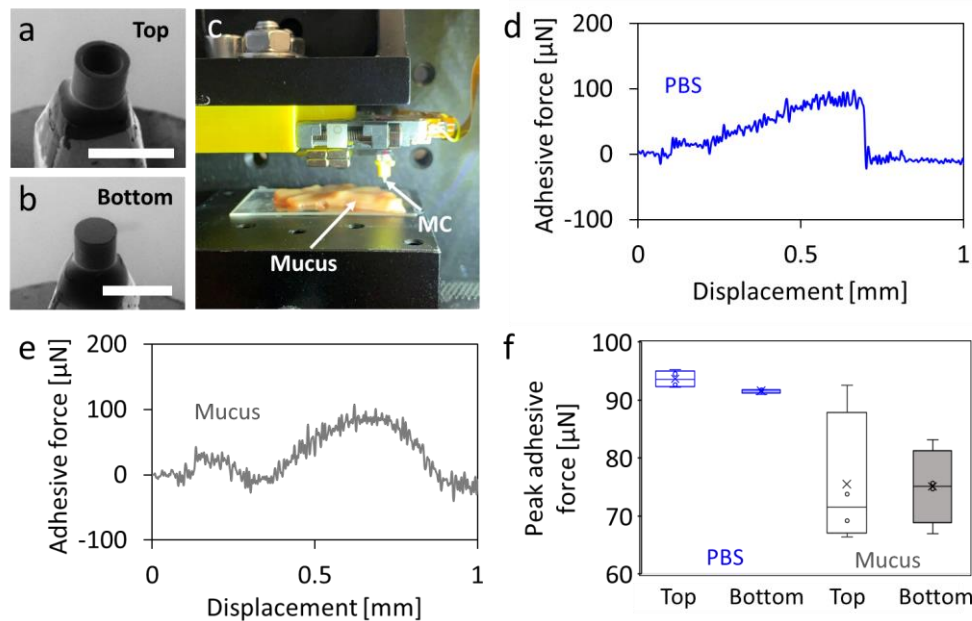


Figure 12. Investigation of adhesive force of PBS buffer and porcine small intestinal mucus to microcontainers (MCs). SEM image of mounting MC on the microprobe with **a)** top and **b)** bottom side for measurement (scale bar represents 500 μm). **c)** Photograph of approaching and withdrawing MC to intestinal mucus with a constant speed of 0.078 mm/s and contact time of 1 s. While withdrawing the MC from the sample, the force detection module obtained the adhesive force to displacement curves of **d)** PBS buffer to MC, and **e)** porcine small intestinal mucus to MC, respectively. **f)** The peak adhesive force of PBS and mucus to both sides of MC, respectively. Mean \pm SD, $n = 4$.

Conclusion

- The OPU force analyzer utilizes different cantilever force transducers that provide a broad range of force measurements ranging from 1.1 N to 0.99 nN.
- The positioning module provides a 25 mm travel distance and 40 nm resolution, which have high flexibility for a wide variety of sample measurements.
- The OPU force analyzer can successfully measure micro-newton scale interaction force curves between a single MC and intestinal mucus layer at different conditions.
- The simple, cost-effective, and open-source OPU force analyzer has a high potential to perform various force measurement applications in different fields.

Acknowledgments

The authors would like to acknowledge the financial support from the Villum Experiment (Grant No. 00023116), the Danish National Research Foundation (DNRF122), the BioInnovation Institute Foundation (Grant No. NNF20SA0063552), Villum Foundation (Grant No. 9301) for Intelligent Drug Delivery and Sensing Using Microcontainers and Nanomechanics (IDUN) and the Novo Nordisk Foundation (NNF17OC0026910)—Microstructures, microbiota and oral delivery (MIMIO).

Declaration of interest

The authors declare no conflict of interest.

References:

- [1] L.H. Nielsen, A. Melero, S.S. Keller, J. Jacobsen, T. Garrigues, T. Rades, A. Müllertz, A. Boisen, Polymeric microcontainers improve oral bioavailability of furosemide, *Int. J. Pharm.* 504 (2016) 98–109. doi: 10.1016/j.ijpharm.2016.03.050.
- [2] C. Mazzoni, F. Tentor, S.A. Strindberg, L.H. Nielsen, S.S. Keller, T.S. Alstrøm, C. Gundlach, A. Müllertz, P. Marizza, A. Boisen, From concept to in vivo testing: Microcontainers for oral drug delivery, *J. Control. Release.* 268 (2017) 343–351. doi: 10.1016/j.jconrel.2017.10.013.
- [3] A. Ghosh, L. Li, L. Xu, R.P. Dash, N. Gupta, J. Lam, Q. Jin, V. Akshintala, G. Pahapale, W. Liu, A. Sarkar, R. Rais, D.H. Gracias, F.M. Selaru, Gastrointestinal-resident, shape-changing microdevices extend drug release in vivo, *Sci. Adv.*, 6 (2020), doi: 10.1126/sciadv.abb4133.
- [4] P.O. Okeyo, S.T. Rajendran, K. Zór, A. Boisen, Sensing technologies and experimental platforms for the characterization of advanced oral drug delivery systems, *Advanced Drug Delivery Reviews* (2021). doi: 10.1016/j.addr.2021.113850.
- [5] V.V. Khutoryanskiy, *Advances in Mucoadhesion and Mucoadhesive Polymers*, *Macromol. Biosci.* 11 (2011) 748–764, doi: 10.1002/mabi.201000388.
- [6] L. Vaut, J.J. Juszczak, K. Kamguyan, K.E. Jensen, G. Tosello, A. Boisen, 3D Printing of Reservoir Devices for Oral Drug Delivery: From Concept to Functionality through Design Improvement for Enhanced Mucoadhesion, *ACS Biomater. Sci. Eng.* 6 (2020) 2478–2486. doi: 10.1021/acsbiomaterials.9b01760.
- [7] M.D. Mosgaard, S. Strindberg, Z. Abid, R.S. Petersen, L.H.E. Thamdrup, A.J. Andersen, S.S. Keller, A. Müllertz, L.H. Nielsen, A. Boisen, Ex vivo intestinal perfusion model for investigating mucoadhesion of microcontainers, *Int. J. Pharm.* 570 (2019) 118658. doi: 10.1016/j.ijpharm.2019.118658.
- [8] N. Thirawong, J. Nunthanid, S. Puttipipatkachorn, P. Siamornsak, Mucoadhesive properties of various pectins on gastrointestinal mucosa: an in vitro evaluation using texture analyzer. *Eur. J. Pharm. Biopharm.* 67 (2007) 132–40. doi: 10.1016/j.ejpb.2007.01.010
- [9] T.A. Sonia, C.P. Sharma, 4 - Experimental techniques involved in the development of oral insulin carriers, *Oral Delivery of Insulin*, Woodhead Publishing, Sawston, 2014, 169–217. doi: 10.1016/C2013-0-18177-9
- [10] TA.XTplusC Texture Analyser, <https://www.stablemicrosystems.com/TAXTplus.html>, 2020 (accessed 17.07.21)
- [11] J. Sotres, S. Jankovskaja, K. Wannerberger, T. Arnebrant, Ex-Vivo Force Spectroscopy of Intestinal Mucosa Reveals the Mechanical Properties of Mucus Blankets, *Sci. Rep.* 7 (2017). doi: 10.1038/s41598-017-07552-7

- [12] MicroTester,
https://www.cellscale.com/products/microtester/?gclid=Cj0KCQjw_8mHBhCIARIsABfFggpSOLSDS1Kgz_I fjosaM22S3SA0vDp4JQQncxxwWOyj2VZ3eH5qCrwaAiR6EALw_wcB, (accessed 17.07.21)
- [13] E.T. Hwu, A. Boisen, Hacking CD/DVD/Blu-ray for biosensing, *ACS Sens.* 3 (2018) 1222–1232. doi: 10.1021/acssensors.8b00340
- [14] E.T. Hwu, H. Illers, L. Jusko, H.U. Danzebrink, A hybrid scanning probe microscope (SPM) module based on a DVD optical head. *Meas. Sci. Technol.* 20 (2009) 084005. doi: 10.1088/0957-0233/20/8/084005
- [15] E.T. Hwu, H. Illers, W.M. Wang, I.S. Hwang, L. Jusko, H.U. Danzebrink, Anti-drift and auto-alignment mechanism for an astigmatic atomic force microscope system based on a digital versatile disk optical head. *Rev. Sci. Instrum.* 83 (2012) 013703. doi: 10.1063/1.3673001
- [16] H.S. Liao, K.Y. Huang, I.S. Hwang, T.J. Chang, W.W. Hsiao, H.H. Lin, E.T. Hwu, C.S. Chang, Operation of astigmatic-detection atomic force microscopy in liquid environments. *Rev. Sci. Instrum.* 84 (2013) 103709. doi: 10.1063/1.4826494
- [17] T.J. Chang, L. Vaut, M. Voss, O. Ilchenko, L.H. Nielsen, A. Boisen, E.T. Hwu, Micro and nanoscale 3D printing using optical pickup unit from a gaming console, *Communications Phys.* 4 (2021) 23. doi: 10.1038/s42005-021-00532-4
- [18] C.A. Rothenbach, M.C. Gupta, High resolution, low cost laser lithography using a Blu-ray optical head assembly. *Opt. Lasers Eng.* 50 (2012) 900–904. doi: 10.1016/j.optlaseng.2011.12.004
- [19] L.I. Segerink, M.J. Koster, A.J. Sprenkels, A. van den Berg, A low-cost 2D fluorescence detection system for μm sized beads on-chip. *Lab Chip* 12 (2012) 1780–1783. doi: 10.1039/c2lc21187d
- [20] J.M. Gere, B.J. Goodno, *Mechanics of Materials* (Eighth ed.), Cengage Learning, Boston, 2012
- [21] J.F. Christfort, A.J. Guillot, A. Melero, L.H.E. Thamdrup, T.M. Garrigues, A. Boisen, K. Zór, L.H. Nielsen, Cubic microcontainers improve in situ colonic mucoadhesion and absorption of amoxicillin in rats, *Pharmaceutics.* 12 (2020) 1–16. doi: 10.3390/pharmaceutics12040355.

Appendix III

Paper III

3D printed radiopaque microdevices with enhanced mucoadhesion geometry for oral drug delivery (preliminary)

Tien-Jen Chang, Rolf Bech Kjeldsen, Juliane Fjelrad Christfort, Eduard Marzo I Vila, Tommy Sonne Alstrøm, Kinga Zòr, En-Te Hwu, Line Hagner Nielsen, Anja Boisen (temporary order)

In preparation

Title

3D Printed Radiopaque Microdevices with Enhanced Mucoadhesion Geometry for Oral Drug Delivery

Authors

Tien-Jen Chang^{a,*}, Rolf B. Kjeldsen^a, Juliane F. Christfort^a, Eduard M. Vila^a, Tommy S. Alstrøm^b, Kinga, Zór^{a,c}, En-Te Hwu^{a,c}, Line H. Nielsen^a, Anja Boisen^{a,c}

*Corresponding author. Email: tiech@dtu.dk

Affiliations

^aThe Danish National Research Foundation and Villum Foundation's Center for Intelligent Drug Delivery and Sensing Using Microcontainers and Nanomechanics (IDUN), Department of Health Technology, Technical University of Denmark, 2800 Kgs. Lyngby, Denmark.

^bDepartment of Applied Mathematics and Computer Science, Technical University of Denmark, Richard Petersens Plads 321, 2800 Kgs. Lyngby, Denmark

^cBioInnovation Institute Foundation, 2200 Copenhagen, Denmark

Abstract

In the last decades, several microdevices have been designed, fabricated, and evaluated for oral drug delivery, and most of them indicate sustained and extended drug release. However, fabrication of such microdevices using conventional methods is often limited to planar or simple 3D designs. To allow for more flexibility and potentially increase gastrointestinal (GI) retention, this work explores how microscale 3D printing can be used to fabricate microdevices for oral drug delivery, such as microcontainers, with enhanced mucoadhesive geometries. Furthermore, an x-ray contrast agent is incorporated into the microcontainer shell to make them traceable with x-rays. *Ex vivo* force measurements suggest increased mucoadhesion for microcontainers with adhering features, such as pillars and arrows, compared to a neutral design as a control. *In vivo* studies utilizing subsequent planar x-ray imaging determines the GI location of the microcontainers over time, whereas computed tomography scanning, and cryogenic scanning electron microscopy reveal detailed information about spatial dynamics and mucosal interactions, respectively.

Teaser

3D printing of radiopaque and mucoadhesive microcontainers may solve the current challenges found within oral drug delivery.

39 Introduction

40 Most patients prefer the oral administration route, which, therefore, often results in high
41 patient compliance. Additionally, oral dosage forms do not require sterile production or
42 trained personnel for administration, which all together lowers their production cost
43 compared to for example injectables (1). However, several gastrointestinal (GI) tract
44 related challenges must be addressed before the delivered drug can be successfully
45 absorbed from the intestine. These include a steep pH gradient and several digestive
46 agents, such as bile, enzymes, and pancreatic secretions. Furthermore, the inner surface
47 of the GI tract is covered by a mucus layer of varying thicknesses (2), which is the body's
48 last line of defense to avoid absorption of unwanted compounds.

49 During the past decades, several microfabricated drug delivery devices have been
50 developed to address challenges in oral drug delivery. Despite significant design
51 differences, most of them are based on the same overall structure; a central reservoir for
52 drug loading, which offers protection until a unidirectional release occurs after
53 dissolution of a polymeric lid. However, it was shown that specific changes in the design
54 could improve oral drug delivery. For example, Chirra *et al.* (3) found that planar poly-
55 methylmethacrylate (PMMA) microdevices significantly improved retention in the
56 small intestine and, which led to a better bioavailability of acyclovir after dosing to mice.
57 Recently, Ghosh *et al.* (4) developed therapeutical grippers, theragrippers, with sharp
58 microtips, which spontaneously fold at the temperature of the GI tract with force
59 sufficient to penetrate the mucus layer, resulting in retention in the colon of living rats
60 for 24 h after rectal delivery.

61 While planar microdevices have been highlighted for their resistance to shear stress,
62 microdevices with a larger aspect ratio, for example microcontainers, are beneficial
63 considering their large loading capacity and embedment in mucus (5). Microcontainers
64 are polymeric devices (typically 200-300 μm in size) with an inner cavity for drug
65 loading and an open topside providing a unidirectional release. They have shown to be
66 advantageous for oral delivery of multiple compounds, including small-molecule drugs
67 (6-8), peptides (9, 10), probiotics (11) and vaccines (12). In an *in situ* perfusion model
68 in rats, microcontainers have been also shown to possess inert mucoadhesive properties (7).
69 The mucoadhesive polymers chitosan and PEG have been studied for functionalization
70 of the open topside to increase mucoadhesion (9). However, the improved mucoadhesion
71 observed *ex vivo*, has not translated into significant alterations in drug absorption *in vivo*
72 (13). Recently, cubic microcontainers were found to adhere significantly better to the
73 mucosa than cylindrical microcontainers after *in situ* perfusion in the rat colon (14).

74 As a revolutionary manufacturing technique, 3D printing allows more geometry
75 design and fabrication flexibility than conventional methods (15, 16). Thus, 3D printing
76 has a substantial advantage when creating innovative geometries and functions (*e.g.*
77 controlled release or co-delivery) for drug delivery devices (17-19). Furthermore, the
78 simplicity of the 3D printing process reduces the dosage form development time (20).
79 Earlier, through a digital light processing 3D printer, a drug carrier was printed with
80 delicate anchor-like features to expand the contact area with intestinal mucus (21). These
81 anchor-like features showed extended retention time in an *ex vivo* model. Nevertheless,
82 limited by printing resolution, most 3D-printed oral drug devices are fabricated in the
83 centimeter scale. The two-photon technique possesses nanoscale printing resolution,
84 which can achieve complex structures on the surface of microdevices (15). However, the
85 two-photon technique has several limitations, such as microscale printing volume and
86 slow printing speed, resulting in low throughput (22-24). In addition, its high cost leads
87 to no economic benefit for the pharma industry. Recently, a custom-built HD-DVDs-
88 based 3D printer was developed to achieve micro- and nanoscale printing resolution (25).
89 At the same time, this printer is cost-effective and without limitations in volume size.
90 Thereby, it can scale-up the fabrication of microdevices, such as microcontainers with
91 innovative microscale structures for enhancing mucoadhesion. However, it is
92 challenging to locate the microdevices when mucoadhesion is studied *in vivo*, and,

93 therefore, different imaging techniques have been investigated for their application in
94 GI tracking of microdevices.

95 For many decades, x-ray imaging, composed of planar x-ray imaging and computed
96 tomography (CT) scanning, has been used for medical applications. These involve
97 aspects within conventional procedures (*i.e.* mammography, interventional radiography,
98 GI and musculoskeletal radiology)) to more advanced and recent (pre-)clinical studies
99 on passive and active targeted diagnosis of tumors (26) and 3D bioprinting of artificial
100 organs and tissues for surgical purposes (27). GI tracking of orally dosed capsular devices
101 at millimeter scale has also previously been carried to better understand their GI
102 behavior in rats (28, 29), dogs (30) and humans (31). In fact, x-ray imaging has also been
103 utilized for quantitative GI tracking of microscale oral drug delivery devices in rats (32).
104 However, the loading of a contrast agent, such as barium sulfate (BaSO₄), was needed
105 to make them traceable with the x-rays in the GI tract. In a recent study with
106 microcontainers, BaSO₄ occupied all the void space, thereby leaving no room for a
107 potential drug. It would be of great interest to enable both tracking of the devices and
108 delivery of drugs. Previously, Bettini *et al.* (33) and Du *et al.* (34) used a similar approach
109 to prepare radiopaque microspheres by utilizing thermally induced phase separation and
110 a one-step electrospaying method, respectively.

111 For the first time, this paper presents a novel approach for 3D printing and evaluation
112 of radiopaque microdevices with enhanced mucoadhesion geometry (**Fig. 1**). The
113 mucoadhesive properties are evaluated *ex vivo* by high-precision cantilever force
114 measurements and *in vivo* in rats using x-ray imaging. Except for quantifying GI
115 retention and transit time using planar x-ray imaging, further investigation of spatial
116 dynamics and mucosal interactions in the small intestine is made using CT scanning and
117 cryogenic (cryo) scanning electron microscopy (SEM), respectively.

118 **Results and Discussion**

119 **Fabrication of 3D printed microcontainers**

120 Three designs were created and fabricated aiming to enhance mucoadhesion of
121 microcontainers to control the orientation of the unidirectional release and extend the GI
122 retention time. Considering promising data from adhesion of cubic microcontainers *in*
123 *situ* (14), we designed all the microcontainers to be square shaped. First, we created
124 microcontainers with a large contact area of the top side (with cavity), and a small
125 contact area of the bottom side (neutral design, **Fig. 2A**). This design appeared as an
126 inverted trapezoid from the view of the lateral direction. This asymmetrical structure
127 might increase the probability for the top side to face towards the mucosa and facilitate
128 unidirectional release towards the intestinal wall. The dimension of these neutral
129 microcontainers were 400 × 300 × 240 μm³ (length × width × height), while the length
130 of the bottom side is 240 μm. As the second design, sixteen 10-μm-diameter and 50-
131 μm-high micro-pillars were printed on the top side of neutral microcontainers (pillar
132 design). The micro-pillars are hypothesized to penetrate the mucin network structure for
133 enhancing mucoadhesion. Finally, we designed microcontainers with four 300-μm-long
134 arrow structures on the side to drastically increase the surface area and extend retention
135 time. The arrows could hook the mucus layer for deeper entanglement.

136 These design concepts were realized by utilizing a custom-built micro and nanoscale
137 3D printer (25). The 3D printer cured the biocompatible photopolymer to produce 100
138 microcontainers in a 10 × 10 matrix on a silicon chip (**Fig. 2B and 2C**). The
139 microcontainers were fabricated with a cavity space for carrying drugs (**Fig. 2D and**
140 **2G**). After a washing process, the feature could be observed clearly without residual
141 photopolymer in the cavity. As shown in **Fig. 2E and 2H**, the sixteen micro-pillars were
142 successfully printed on the wall of microcontainers. Additionally, the arrows were
143 printed on the side of the microcontainers (**Fig. 2F and 2I**).

144 The 3D printer enabled the mass fabrication of microcontainers with microscale
145 structure on a large area (10 × 10 mm²), challenging for other 3D printing methods (25).
146

147 The result of the neutral design shows a clear overhang asymmetrical structure. Within
148 the small contact area of the bottom side, the microcontainers still well adhered to the
149 substrate. Thus, the following drug loading and lid coating processes can be
150 implemented while the devices are still on the substrate. The 3D-printed micro-pillars
151 (dimension: $11.5 \times 47.4 \mu\text{m}^2$, diameter \times height) are small enough to penetrate the mucin
152 network structure, which comprises numerous tens-of-microns holes (35). Although one
153 printing batch took approximately 12 h, the manufacturing capacity was suitable for
154 producing microcontainers for the *in vivo* study. The printing time can be further
155 optimized by tuning printing speed and laser intensity.

156 Nevertheless, it is challenging to reach a sharp tip of the arrow structure, due to the
157 accumulation of relatively more laser energy in the area close to the tip while the printer's
158 motor slowed down. Besides, limited by the phenomenon of light diffusion, the
159 dimension of each microcontainers were slightly variant. The printing parameter was
160 tuned for each microcontainer to compensate for the laser dosage and overcome this
161 inconsistency.

162 The arrow structure was slightly bent upward after the washing process. Inner stress
163 accumulation during the printing process might contribute to the deformation. This
164 slight deformation did not affect the designed functionality. From another aspect, the
165 microcontainers might be easier to detach from the substrate for collection.

166 **A microdevice for controlled oral drug delivery – *in vitro* proof-of-concept**

167 To evaluate if the microcontainers are suitable as a drug carrier for oral drug delivery,
168 the 3D printed microcontainers were loaded with furosemide and coated with the pH-
169 sensitive polymer Eudragit[®] L100 (Fig. 3A). The release of furosemide was measured
170 in media simulating gastric and intestinal pH conditions (Fig. 3B). Each chip holding
171 100 microcontainers was loaded with 1.0 ± 0.2 mg furosemide, corresponding to
172 approximately $10 \mu\text{g}/\text{microcontainer}$. This is a substantially larger loading capacity
173 than what has been reported for similarly sized microdevices, $1.5 \mu\text{g}/\text{microdevice}$ (3) and
174 $3\text{-}5 \mu\text{g}/\text{microdevice}$ (36).

175 The *in vitro* release profile from the furosemide-loaded microcontainers was obtained
176 using a $\mu\text{DISS Profiler}^{\text{TM}}$. This is a common method applied for *in vitro* evaluation of
177 drug release also from microcontainers before proceeding to animal studies (6–8). The
178 release was studied in a two-step model simulating the pH in the GI tract of fasted rats,
179 where a 30 min gastric step (4mM hydrochloric acid pH 2.4) was followed by an
180 intestinal step (phosphate buffered saline (PBS), pH 7.5) until a complete release was
181 achieved (Fig. 3C). During the gastric step, only 4.4 ± 1.0 % (mean \pm SD, $n = 4$) of the
182 loaded furosemide was released, but after changing to intestinal media, furosemide was
183 gradually released until 90 min after initiating the study. This release profile is consistent
184 with the release observed from microcontainers fabricated by other methods (6, 8). Thus,
185 the 3D printed microcontainers are promising as an oral drug delivery device for targeted
186 delivery to the small intestine, when combined with a pH-sensitive polymeric coating.

187 ***Ex vivo* mucoadhesion force measurements**

188 A broad range force analyzer was used to measure the mucoadhesive forces of
189 microcontainers to characterize potential interactions with the mucus layer (37). Two *ex*
190 *vivo* studies were implemented to investigate the orientation of microcontainers and
191 mucoadhesion of additive features, respectively. In both studies, porcine small intestinal
192 tissue was utilized.

193 In the study investigating orientation, the dynamic orientation of microcontainers was
194 predicted by comparing the mucoadhesion of both sides of the devices and
195 symmetrically square MCs (dimension: $300 \times 200 \mu\text{m}^2$, width \times height) were 3D printed
196 as control to compare with the asymmetrical neutral and arrow designs. The
197 microcontainers were glued on a microprobe to contact mucus with the top and bottom
198 sides, respectively (Fig. 4A). The force analyzer recorded the mucoadhesive force while
199
200

201 approaching and withdrawing the microcontainers during the measurement (**Fig. 4C**).
202 To eliminate the tissue variation, we used the microprobe as a standard sample
203 normalized to the mucoadhesive force measured from different tissues.

204 The results indicate that the square microcontainers have the same level of
205 mucoadhesion on both sides (**Fig. 4D**). The top side of neutral microcontainers show a
206 larger mucoadhesion than the bottom side, due to the asymmetrical structure design.
207 The arrow microcontainers show the significant enhancement of mucoadhesive forces
208 on both sides. The result validates that the mucoadhesion has a positive relationship to
209 the contact area at the microscale dimension. However, the bottom side of both the
210 neutral and square microcontainers present a similar level of mucoadhesive force, even
211 if the neutral design has a smaller area of the bottom side. The reason might be that the
212 lateral slope of the bottom side of neutral microcontainers is still in contact with mucus
213 for adhering.

214 In the study of additive features, we measured the mucoadhesive forces of
215 microcontainers' top side compared to the mucoadhesion of different additive features.
216 The neutral design was used as a control, since it does not have any additive features.
217 **Fig. 4E** shows the normalized mucoadhesive force result, where the micro-pillars
218 showed a slight enhancement of mucoadhesion compared to the other two types.
219 However, none of these features present a significant enhancement of mucoadhesion.

220 **Incorporation of BaSO₄ into 3D printed microcontainers**

221 To trace the microdevices in the GI tract, the contrast agent BaSO₄ was embedded into
222 the microcontainers (**Fig. 5A, 5B and 5C**). The printer cured the photopolymer mixed
223 with BaSO₄ nanoparticles, fabricating microcontainers in a 10 × 10 matrix on the
224 substrate. Neutral, pillar and arrow designs were produced, 400 units in total, for a proof-
225 of-concept animal study. While printing with BaSO₄, the three designs maintained the
226 same scale and structure as microcontainers printed without contrast agent. SEM
227 analysis showed clear contrast of BaSO₄ nanoparticles embedded in the microcontainer
228 shell (**Fig. 5D**).

229 An energy dispersive x-ray analysis (EDX) method showed the surface distribution of
230 the photopolymer and BaSO₄ by analyzing elements. Carbon, oxygen, barium, and
231 sulfur were detected and mapped (**Fig. 6A**) and the SEM image revealed a rough surface
232 with numerous protruded microparticles. Although BaSO₄ nanoparticles were used, the
233 aggregation effect led to microscale particle size. Besides this, the homogeneity of the
234 BaSO₄ particles seemed weak (**Fig. 6B**). The reason is the insolubility of BaSO₄ to the
235 photopolymer. In the printing process, BaSO₄ was temporarily suspended in the
236 photopolymer and gradually sedimented. The suspension effect of this material recipe is
237 kept for over one day, allowing a complete 3D printing cycle.

238 **Quantitative gastrointestinal tracking for retention and transit time**

239 To confirm the differences or similarities in mucoadhesive properties observed for the
240 three microcontainer designs *ex vivo*, a quantitative transit time analysis was made
241 through an *in vivo* rat study using planar x-ray imaging for quantitative GI tracking.
242 After oral administration of microcontainers and subsequent euthanasia, planar x-ray
243 images of removed GI tracts were obtained (**Fig. S2**) and the amount of retained
244 microcontainers was counted (**Fig. 7**). From the results presented, it can be observed that
245 microcontainers in all three designs appeared in the stomach 0.5 h after dosing. For the
246 neutral and pillar design, an average of approximately 60 % of the microcontainers were
247 found in the stomach after 0.5 h (**Fig. 7A and 7B**). After 1 h, 0-10 % of the
248 microcontainers were found in caecum, which increased to an average of 50-70 % after
249 3 h, while the amount in the previous GI sections decreased. On the contrary, only 20 %
250 of the arrow design microcontainers were observed in the stomach after 0.5 h (**Fig. 7C**),
251 but most of them (60 %) had already moved on to the proximal small intestine.

254 For the distal part of the small intestine, the microcontainers are clearly seen to enter
255 this region and increase in number with time, before moving to the large intestine. The
256 majority of the neutral, pillar and arrow microcontainers were found in the distal small
257 intestine after 2, 2 and 1 h (50 %, 60 % and 78 %), respectively. After 3 h, the majority
258 of all three designs were located in the cecum, and for the neutral and arrow design no
259 considerable amount of microcontainers could be detected in any other region at this
260 time. However, the pillar design resulted in a 50:50 distribution between the distal small
261 intestine and the caecum after 3 h (**Fig. 7B**), indicating trends towards improved
262 adhesion of the pillar design in the distal small intestine.

263 Despite some trends indicating an improved retention of the microcontainers with
264 pillars in the small intestine, no significant retention could be observed in rats *in vivo*.
265 Additionally, the enhanced mucoadhesion observed for the arrow design *ex vivo* (**Fig.**
266 **4D**), did not translate into increased retention in the GI tract *in vivo*. A similar
267 discrepancy between *ex vivo* and *in vivo* adhesion has previously been observed for SU-
268 8 microcontainers coated with PEG and chitosan (9, 13). Here, microcontainers coated
269 with PEG significantly improved the adhesion *ex vivo* when compared to uncoated
270 microcontainers (9). However, when this was evaluated *in vivo* after oral dosing to rats,
271 no difference could be observed in the pharmacokinetic profile for paracetamol, which
272 was loaded into the microcontainers (13). This indicates that the PEG and chitosan
273 coatings did not have a pronounced mucoadhesive effect *in vivo*. Furthermore, the
274 impact of morphology and geometry on mucoadhesion has been investigated extensively
275 for micro- and millimeter-sized devices *in vitro*, *ex vivo* and *in situ* (14, 21, 38–40). The
276 addition of nano and micro-sized surface structures was found to improve mucoadhesion
277 *in vitro* and *ex vivo*, respectively, while shape has been shown to affect retention in
278 perfusion models *ex vivo* and *in situ* (14, 39). Although these design modifications remain
279 to be investigated *in vivo*, the results from the present study indicate that more drastic
280 design changes will be required in order to see a considerable effect *in vivo*.

281 In a living animal, peristaltic forces and the flow of foods and liquids represent a
282 challenge that is not simulated *in vitro* and *ex vivo*. Since *in situ* studies are performed
283 in live anesthetized animals, they can be utilized to study mucoadhesion in the presence
284 of peristaltic forces. However, the gastrointestinal transit time has been shown to be
285 reduced by approximately 50 % in anesthetized rats (41).

286 Recently, active microdevices, such as theragrippers, have shown promising
287 mucoadhesion *in vivo* (4). Theragrippers spontaneously fold at body temperature with a
288 force sufficient to penetrate the colonic mucus layer with their microtips and the
289 microdevices resided inside the colon of live animals for up to 24 hours after rectal
290 administration. In addition, micromotors, capable of propelling themselves into the GI
291 mucus layer, have resulted in improved intestinal retention 6 hours after oral dosing,
292 compared to static microparticles (42).

293 **Spatial dynamics and mucosal interactions**

294 Mucoadhesive properties of drug delivery devices *in vivo* are not always easily
295 predictable and, as in this case with 3D printed microcontainers, they might not be
296 straightforward to investigate (43, 44). Trying to get a level further down than quantitative
297 GI tracking, spatial dynamics and mucosal interactions of the microcontainers in the
298 small intestine were investigated by CT scanning and CryoSEM (**Fig. S3**). Here, spatial
299 dynamics cover specific location and overall orientation of the microcontainers, whereas
300 mucosal interactions describe the embedment of microcontainers in the mucosa and their
301 specific orientation in that regard.

302 The CT scanned intestinal pieces (**Fig. 8A**) revealed details about the spatial dynamics.
303 For example, it showed the exact location and distribution of the microcontainers but
304 also that they had no preferred orientation towards the intestinal wall. The CryoSEM
305 provided a close observation of the interaction between the microcontainer and mucosa.
306 Two pillar-design microcontainers were found on the mucus layer with side-way posture
307

(Fig. 8B), and a pillar microcontainer faced down with the top side contact the mucus layer (Fig. 8C). The microcontainers were covered by the mucus; therefore, only the shape of microcontainers can be recognized. The microcontainers' surface topography and micro-pillars feature are difficult to observe.

Conclusively, the presented 3D printing method enabled, for the first time, microscale fabrication of versatile microdevices with contrast embedded in the device itself. This allows for precise tracking of GI retention using x-ray imaging, while the absorption of a drug can be assessed at the same time. Three different microcontainer designs were fabricated and tested, but in the future, more designs with other exceptional adhesive features like hooks or branched spikes can easily be adopted and 3D printed. Based on the *in vivo* results, some sort of active or shape changing mechanism seems to be necessary in order to significantly improve mucoadhesion of microdevices in the presence of peristaltic forces and food contents *in vivo*.

Materials and Methods

Materials

Silicon wafers (4in, b100N, n-type) were acquired from Okmetic (Vantaa, Finland). The biocompatible photopolymer (Biomed Clear) for 3D printing was obtained from Formlabs (Sommerville, MA, USA) and the BaSO₄ nanopowder (100nm, purity 99%) was ordered from Nanoshel (Dera Bassi, Punjab, India). Eudragit[®] L100 was bought from Evonik Röhm GmbH (Darmstadt, Germany), dibutylsebacate (DBS) was obtained from Sigma Aldrich (St. Louis, MO, USA) and 2-propanol (IPA) was purchased from VWR International (Radnor, PA, USA). Male Sprague-Dawley rats were ordered from SCANBUR A/S (Karlslunde, Denmark).

3D printing of microcontainers

All the design of microcontainers was drawn by the software, SolidWorks 2014 (Dassault Systèmes SolidWorks Corporation, Massachusetts, USA), to generate the 3D CAD format. The CAD file was converted to G-code, computer numerical control commands, for executing the printing path and parameter. The HD-DVDs-based 3D printer utilized a 405-nm-wavelength laser to cure the photopolymer and fabricate the microcontainers on a 12.5 × 12.5 mm² polished silicon substrate. The printing procedure was followed by aligning the printer, printing process, cleaning, and post-curing. For one printing batch, the printer printed 100 microcontainers by a 10 x 10 array, with an interval distance of 900 μm between the microcontainers. The following parameter settings were used: printing speed from 0.10 to 0.15 mm/s, laser intensity of 2.40 μW, and photopolymer thickness of 25 μm. Each microcontainer design was a total of ten layers, with each layer of 21 μm in height. The additive feature of pillars and forks were printed to six layers, with 9-μm-high for each layer. The printing process was operated at room temperature (20 °C) and relative humidity below 30 %. A compensation method was applied to slightly tune each microcontainer's printing speed to maintain the exact laser exposure dosage during the printing process. In the cleaning process, the microcontainers were first immersed in IPA for 5 minutes and then continuously flushed with IPA until there was no residual photopolymer. As the solvent evaporated, the microcontainers were placed in a 405 nm wavelength chamber (Formlabs, Somerville, MA, USA) for post-curing (30 minutes).

The quality of empty, loaded, and coated 3D printed biocompatible microcontainers was investigated using a tabletop SEM (TM3030Plus, Hitachi High-Technologies Europe, Krefeld, Germany). A 45° tilted metallic holder carried the specimen. The sample was observed using an electron acceleration voltage of 5 keV, and a backscatter electron detector in a standard mode.

***In vitro* proof-of-concept study**

For the *in vitro* release study, the microcontainers were loaded with furosemide as previously described (7, 45). Briefly, furosemide was manually distributed on the microcontainer chip and excess drug between the microcontainers was subsequently removed with an air gun. After loading, an ultrasonic spray coater (ExactaCoat, Sono-Tek, Milton, NY, USA) equipped with an accumist nozzle was applied to seal the furosemide-loaded microcontainers with the pH-sensitive polymer Eudragit[®] L100. A solution of the polymer (1% w/v Eudragit and 5 % w/w in relation to the polymer of DBS was dissolved in IPA) was sprayed over a chip of drug-loaded microcontainers. The specific settings applied for the spray coating process are described in detail elsewhere. In brief, the microcontainers were coated by 30 passages with a flow rate of 0.1 mL/min on a heating plate set to 40 °C. The furosemide release was measured using a μ DISS Profiler[™] (Pion Inc., Billerica, MA, USA), as previously described in literature. Briefly, a microcontainer chip was fixed on top of a cylindrical magnetic stirring bar with double-sided carbon tape, placed in a sample vial and covered with 10 mL gastric buffer (hydrochloric acid, pH 2.4). Individually calibrated UV probes were immersed into the buffer and the experiment was initiated. After 30 min, the release medium was changed to 10 mL intestinal buffer (PBS, pH 7.5). The release was measured at 37 °C with a stirring rate of 100 RPM, and UV measurements (310-350 nm) were conducted every 10 s.

Mucoadhesion force measurement

The broad range optical-pickup-unit (OPU) force analyzer was utilized for *ex vivo* mucoadhesion force measurement. The force analyzer was equipped with a precise optical module and a cantilever force transducer to detect micro-newton scale force sensitively. As the cantilever structure transferred the applied force into deflection, the optical module sensed the cantilever deflection. The dimension of the cantilever was 12 × 8.2 × 0.1 mm in width, length, and thickness, respectively. A homemade alignment instrument precisely placed the microcontainers on the tip of the micro-probe. Then, the microcontainers were mounted with UV cross-linkable glue. Fresh porcine small intestinal tissue from a slaughterhouse was stored in a freezer below -17 °C. The tissue was thawed at room temperature for 30 minutes and sliced into a small piece, approximately 20 mm in length. During the measurement process, the OPU force analyzer lifted the sample stage with tissue to approach the microcontainers with a constant speed of 0.078 mm/s. While the microcontainer contacted the mucus layer, the platform lifted 80 μ m to ensure complete contact between the microcontainer surface and the mucus. After 0.5 s contact time, the platform was withdrawn with the same constant speed of 0.078 mm/s, detaching the mucus layer from the microcontainers. Simultaneously, the force analyzer recorded the cantilever deflection induced by the mucoadhesion force, plotting it into a force-displacement chart. The maximum point of the curve was defined as the peak mucoadhesion force. To compare the mucoadhesion force, the micro-probe was utilized as a blank sample to normalize the mucoadhesion between each test group.

For investigation of the orientation, force measurements of each microcontainers design was implemented with the order of blank, top side, bottom side, and blank, at the exact location on small intestinal tissue. This measurement repeated triplicate test rounds with a new tissue for each round. Then other triplicate test rounds were operated with a swapped order of the top side and bottom side.

For the additive feature comparison study, the test started and ended with the blank sample measurement. In between, a design of experiment method was implemented to arrange all order combinations of three microcontainers designs, neutral, pillar, and fork. In total six test groups were measured, as shown in the supplementary material.

3D printing of radiopaque microcontainers

To make the 3D printed microcontainers traceable with x-ray imaging, BaSO₄ nanoparticles (37.9 w/v%) were mechanically mixed into to 3D print resin. The shape, chemical composition and homogeneity of the 3D printed radiopaque microcontainers were investigated using SEM, EDX and μ CT scanning. The SEM investigation was conducted as previously described, but EDX (80 mm² X-Max silicon drift detector, Oxford Instruments, Abingdon, Oxfordshire, United Kingdom) analysis was included. For μ CT scanning (ZEISS XRadia 410 Versa, ZEISS, Pleasanton, CA, USA) of the 3D printed radiopaque microcontainers, the distance between the x-ray probe and the sample was set to obtain a voxel size, which corresponds to the spatial scan resolution, of 4.468 μ m. X-rays were generated using a voltage of 60 kV and a power of 10 W (current of 0.17 mA). The respective 3D visualizations for all samples were created from single planar scans using 3201 projections with 1 frame per projection and an exposure time of 2 s. The final scan time was 3 h and 3 min. The following tomographic reconstructions were made in the software provided with the μ CT scanner system (Scout-and-Scan Control System Reconstructor, ZEISS, Pleasanton, CA, USA) using a Feldkamp, Davis and Kress algorithm (46), which is a filtered back-projection algorithm. The reconstructed data were processed and investigated using a 3D visualization and analysis software (Avizo, Thermo Fisher Scientific Inc., Waltham, MA, USA).

In vivo rat study

All animal care, housing and procedures were performed at the Bio Facility at the Technical University of Denmark. The study was approved by The Danish Animal Experiments Inspectorate under the license 2020-15-0201-00610 and conducted in compliance with the Danish laws regulating experiments on animals and the EC Directive 2010/63/EU. For this study, male Sprague-Dawley rats with a weight of 288-320 g were used. The rats were acclimatized for one week prior to the study at a room temperature and humidity of 22 °C and 55%, respectively, and with an alternating 12/12 h light/dark cycle. During the entire acclimatization period, the rats had free access to standard food pellets and water. In total, 24 rats were used, and a detailed experimental design of the *in vivo* rat study is shown in Table S1. The rats were fasted 16-18 h before gelatin capsules, each filled with 50 microcontainers having either neutral, pillar or arrow design, were administered by oral gavage. This was done using a device with a stick dosing mechanism, which ensured the gelatin capsules to be expelled from the device without introducing air or water into the stomach of the rats. After dosing, the rats were given free access to water throughout the study. The rats were euthanized in groups 0.5 h to 3 h post-administration by gassing for 2-3 min with a 60% carbon dioxide in 40% oxygen mixture directly followed by decapitation. After euthanasia, all rat GI tracts from the stomach to the terminal end of rectum were removed. The stomachs and small intestines were placed in large Petri dishes whereas the ceca and colons were placed in small Petri dishes. The GI tracts were frozen and stored at -18 °C until later planar x-ray imaging was performed. Subsequently to planar x-ray imaging of the entire GI tracts, small intestinal pieces containing microcontainers were cut from one of the two 0.5 samples in each group of microcontainer design. These three small intestinal pieces were first placed hanging inside Falcon using needles for CT scanning and then, they were opened using a scissor prior to investigation with CryoSEM.

Planar x-ray imaging and quantification of microcontainers

Planar x-ray imaging of the entire removed frozen GI tracts for quantitative tracking of the microcontainers was carried out using a CT scanner (Nikon XT H 225, Nikon Metrology, Tokyo, Japan). The distance between the x-ray probe and the samples was set to get at a magnification of 2.5 and x-rays were generated using a voltage of 70 kV and a power of 30 W (current of 0.43 mA). Acquisition of planar x-ray images, including a background signal for shading correction, was done using 8 frames with an exposure

470 time of 1 s for each. Shading corrections and subsequent manually quantification, by
471 two independent persons, of microcontainers found throughout the entire GI tracts were
472 made using an image processing software (ImageJ, freeware).
473

474 **CT scanning and CryoSEM of small intestinal pieces**

475 To visualize the microcontainers in 3D inside the small intestine, the three frozen small
476 intestinal pieces were CT scanned. The distance between the x-ray probe and the sample
477 was fixed to get a magnification of 20 for all scans in order to keep the voxel size, which
478 corresponds to the spatial resolution, constant at 19.962 μm , and x-rays were generated
479 using a voltage of 70 kV and a power of 25 W (current of 0.36 mA). Each of the 3D
480 visualizations were created from single planar scans using 1572 projections with 2
481 frames per projection and an exposure time of 1 s, which gave a final scan time of
482 approximately 53 min. The following tomographic reconstructions were made using a
483 Feldkamp, Davis and Kress algorithm (46) in the software provided with the CT scanner
484 system (CT Pro 3D, Nikon Metrology, Tokyo, Japan). Finally, to process and investigate
485 the CT scan data, a 3D visualization and analysis software (Avizo, Thermo Fisher
486 Scientific Inc., Waltham, MA, USA) was used.
487

488 **References**

- 489 1. S. Maher, D. J. Brayden, Overcoming poor permeability: Translating permeation enhancers for oral
490 peptide delivery. *Drug Discovery Today: Technologies*. **9**, e113–e119 (2012).
- 491 2. C. Atuma, V. Strugala, A. Allen, L. Holm, The adherent gastrointestinal mucus gel layer: thickness and
492 physical state in vivo. **280**, G922–G929 (2001).
- 493 3. H. D. Chirra, L. Shao, N. Ciaccio, C. B. Fox, J. M. Wade, A. Ma, T. A. Desai, Planar Microdevices for
494 Enhanced In Vivo Retention and Oral Bioavailability of Poorly Permeable Drugs. *Advanced Healthcare*
495 *Materials*. **3**, 1648–1654 (2014).
- 496 4. A. Ghosh, L. Li, L. Xu, R. P. Dash, N. Gupta, J. Lam, Q. Jin, V. Akshintala, G. Pahapale, W. Liu, A.
497 Sarkar, R. Rais, D. H. Gracias, F. M. Selaru, Gastrointestinal-resident, shape-changing microdevices
498 extend drug release in vivo. *Sci. Adv.* **6**, 4133–4144 (2020).
- 499 5. L. H. Nielsen, S. S. Keller, A. Boisen, Microfabricated devices for oral drug delivery. *Lab on a Chip*. **18**,
500 2315–2478 (2018).
- 501 6. C. Mazzoni, F. Tentor, S. A. Strindberg, L. H. Nielsen, S. S. Keller, T. S. Alstrøm, C. Gundlach, A.
502 Müllertz, P. Marizza, A. Boisen, From concept to in vivo testing: Microcontainers for oral drug delivery.
503 *Journal of Controlled Release*. **268**, 343–351 (2017).
- 504 7. L. H. Nielsen, A. Melero, S. S. Keller, J. Jacobsen, T. Garrigues, T. Rades, A. Müllertz, A. Boisen,
505 Polymeric microcontainers improve oral bioavailability of furosemide. *International Journal of*
506 *Pharmaceutics*. **504**, 98–109 (2016).
- 507 8. Z. Abid, S. Strindberg, M. M. Javed, C. Mazzoni, L. Vaut, L. H. Nielsen, C. Gundlach, R. S. Petersen, A.
508 Müllertz, A. Boisen, S. S. Keller, Biodegradable microcontainers-towards real life applications of
509 microfabricated systems for oral drug delivery. *Lab on a Chip*. **19**, 2905–2914 (2019).
- 510 9. C. Mazzoni, R. D. Jacobsen, J. Mortensen, J. R. Jørgensen, L. Vaut, J. Jacobsen, C. Gundlach, A.
511 Müllertz, L. H. Nielsen, A. Boisen, Polymeric Lids for Microcontainers for Oral Protein Delivery.
512 *Macromolecular Bioscience*. **19** (2019), doi:10.1002/mabi.201900004.
- 513 10. J. R. Jørgensen, M. L. Jepsen, L. H. Nielsen, M. Dufva, H. M. Nielsen, T. Rades, A. Boisen, A. Müllertz,
514 Microcontainers for oral insulin delivery – In vitro studies of permeation enhancement. *European*
515 *Journal of Pharmaceutics and Biopharmaceutics*. **143**, 98–105 (2019).
- 516 11. K. Kamguyan, A. M. Torp, J. F. Christfort, P. R. Guerra, T. R. Licht, L. Hagner Nielsen, K. Zor, A.
517 Boisen, Colon-Specific Delivery of Bioactive Agents Using Genipin-Cross-Linked Chitosan Coated
518 Microcontainers. *ACS Applied Bio Materials*. **4**, 752–762 (2021).
- 519 12. C. von Halling Laier, B. Gibson, J. A. S. Moreno, T. Rades, S. Hook, L. H. Nielsen, A. Boisen,
520 Microcontainers for protection of oral vaccines, in vitro and in vivo evaluation. *Journal of Controlled*
521 *Release*. **294**, 81–101 (2019).
- 522 13. J. F. Christfort, S. Strindberg, S. Al-khalili, D. Bar-Shalom, A. Boisen, L. H. Nielsen, A. Müllertz, In
523 vitro and in vivo comparison of microcontainers and microspheres for oral drug delivery. *International*
524 *Journal of Pharmaceutics*. **600** (2021), doi:10.1016/j.ijpharm.2021.120516.
- 525 14. J. F. Christfort, A. J. Guillot, A. Melero, L. H. E. Thamdrup, T. M. Garrigues, A. Boisen, K. Zór, L. H.
526 Nielsen, Cubic microcontainers improve in situ colonic mucoadhesion and absorption of amoxicillin in
527 rats. *Pharmaceutics*. **12** (2020), doi:10.3390/pharmaceutics12040355.
- 528 15. S. C. Ligon, R. Liska, J. Stampfl, M. Gurr, R. Mülhaupt, Polymers for 3D Printing and Customized
529 Additive Manufacturing. *Chemical Reviews*. **117**, 10212–10290 (2017).

- 530 16. M. Vaezi, H. Seitz, S. Yang, A review on 3D micro-additive manufacturing technologies. *International*
531 *Journal of Advanced Manufacturing Technology*. **67**, 1721–1754 (2013).
- 532 17. J. Goole, K. Amighi, 3D printing in pharmaceuticals: A new tool for designing customized drug delivery
533 systems. *International Journal of Pharmaceutics*. **499**, 376–394 (2016).
- 534 18. X. Xu, A. Awad, P. Robles-Martinez, S. Gaisford, A. Goyanes, A. W. Basit, Vat photopolymerization 3D
535 printing for advanced drug delivery and medical device applications. *Journal of Controlled Release*. **329**,
536 743–757 (2021).
- 537 19. P. Robles-Martinez, X. Xu, S. J. Trenfield, A. Awad, A. Goyanes, R. Telford, A. W. Basit, S. Gaisford,
538 3D printing of a multi-layered polypill containing six drugs using a novel stereolithographic method.
539 *Pharmaceutics*. **11** (2019), doi:10.3390/pharmaceutics11060274.
- 540 20. S. J. Trenfield, A. Awad, A. Goyanes, S. Gaisford, A. W. Basit, 3D Printing Pharmaceuticals: Drug
541 Development to Frontline Care. *Trends in Pharmacological Sciences*. **39**, 440–451 (2018).
- 542 21. L. Vaut, J. J. Juszczyk, K. Kamguyan, K. E. Jensen, G. Tosello, A. Boisen, 3D Printing of Reservoir
543 Devices for Oral Drug Delivery: From Concept to Functionality through Design Improvement for
544 Enhanced Mucoadhesion. *ACS Biomaterials Science and Engineering*. **6**, 2478–2486 (2020).
- 545 22. W. Xiong, L. J. Jiang, T. Baldacchini, Y. F. Lu, in *Laser Additive Manufacturing: Materials, Design,*
546 *Technologies, and Applications* (Elsevier Inc., 2017), pp. 237–256.
- 547 23. S. Maruo, O. Nakamura, S. Kawata, Three-dimensional microfabrication with two-photon-absorbed
548 photopolymerization. *Optics Letters*. **22**, 132–134 (1997).
- 549 24. R. Reinhard Reiner, Y. Tanguy, J. Hoffmann, Process for producing a three-dimensional structure
550 (2016).
- 551 25. T. J. Chang, L. Vaut, M. Voss, O. Ilchenko, L. H. Nielsen, A. Boisen, E. te Hwu, Micro and nanoscale
552 3D printing using optical pickup unit from a gaming console. *Communications Physics*. **4** (2021),
553 doi:10.1038/s42005-021-00532-4.
- 554 26. X. Li, N. Anton, G. Zuber, T. Vandamme, Contrast agents for preclinical targeted X-ray imaging.
555 *Advanced Drug Delivery Reviews*. **76**, 116–133 (2014).
- 556 27. T. H. Jovic, E. J. Combella, Z. M. Jessop, I. S. Whitaker, 3D Bioprinting and the Future of Surgery.
557 *Frontiers in Surgery*. **7** (2020), doi:10.3389/fsurg.2020.609836.
- 558 28. N. Gómez-Lado, I. Seoane-Viaño, S. Matiz, C. M. Madla, V. Yadav, P. Aguiar, A. W. Basit, A. Goyanes,
559 Gastrointestinal tracking and gastric emptying of coated capsules in rats with or without sedation using
560 CT imaging. *Pharmaceutics*. **12** (2020), doi:10.3390/pharmaceutics12010081.
- 561 29. S. Saphier, A. Rosner, R. Brandeis, Y. Karton, Gastro intestinal tracking and gastric emptying of solid
562 dosage forms in rats using X-ray imaging. *International Journal of Pharmaceutics*. **388**, 190–195
563 (2010).
- 564 30. M. Marvola', A.-M. Hannula ', E. Westermarck, I. Happonen, T. Kopra, Disintegration of hard gelatin
565 capsule formulations in the dog stomach-a radiological study. *International Journal of Pharmaceutics*.
566 **44**, 159–167 (1988).
- 567 31. M. Marvola, A. Kannikoski, H. Aito, S. Nyk~inen, The effect of food on gastrointestinal transit and drug
568 absorption of a multiparticulate sustained-release verapamil formulation. *International*
569 *Journal of Pharmaceutics*. **53**, 145–155 (1989).
- 570 32. R. B. Kjeldsen, M. N. Kristensen, C. Gundlach, L. H. E. Thamdrup, A. Müllertz, T. Rades, L. H. Nielsen,
571 K. Zór, A. Boisen, X-ray Imaging for Gastrointestinal Tracking of Microscale Oral Drug Delivery
572 Devices. *ACS Biomaterials Science and Engineering*. **7**, 2538–2547 (2021).
- 573 33. A. Bettini, P. S. Patrick, R. Day, D. Stuckey, (BMJ, 2021), pp. A138–A139.
- 574 34. Q. Du, L. Li, Y. Liu, J. Zeng, J. Li, C. Zheng, G. Zhou, X. Yang, Fabrication of inherently radiopaque
575 BaSO₄@BaAlg microspheres by a one-step electrospraying method for embolization. *Journal of*
576 *Materials Chemistry B*. **6**, 3522–3530 (2018).
- 577 35. J. Sotres, S. Jankovskaja, K. Wannerberger, T. Arnebrant, Ex-Vivo Force Spectroscopy of Intestinal
578 Mucosa Reveals the Mechanical Properties of Mucus Blankets. *Scientific Reports*. **7** (2017),
579 doi:10.1038/s41598-017-07552-7.
- 580 36. S. E. Birk, C. Mazzoni, M. Mobasharah Javed, M. Borre Hansen, H. Krogh Johansen, J. Anders Juul
581 Haagensen, S. Molin, L. Hagner Nielsen, A. Boisen, Co-delivery of ciprofloxacin and colistin using
582 microcontainers for bacterial biofilm treatment. *International Journal of Pharmaceutics*. **599** (2021),
583 doi:10.1016/j.ijpharm.2021.120420.
- 584 37. Tien-Jen Chang, Line Hagner Nielsen, Anja Boisen, En Te Hwu, Open source force analyzer with broad
585 sensing range based on an optical-pickup-unit. *HardwareX (unpublished work)* (2021).
- 586 38. C. B. Fox, Y. Cao, C. L. Nemeth, H. D. Chirra, R. W. Chevalier, A. M. Xu, N. A. Melosh, T. A. Desai,
587 Fabrication of Sealed Nanostraw Microdevices for Oral Drug Delivery. *ACS Nano*. **10**, 5873–5881
588 (2016).
- 589 39. M. Dalskov Mosgaard, S. Strindberg, Z. Abid, R. Singh Petersen, L. Højlund Eklund Thamdrup, A.
590 Joukainen Andersen, S. Sylvest Keller, A. Müllertz, L. Hagner Nielsen, A. Boisen, Ex vivo intestinal
591 perfusion model for investigating mucoadhesion of microcontainers. *International Journal of*
592 *Pharmaceutics*. **570** (2019), doi:10.1016/j.ijpharm.2019.118658.

- 593 40. W. R. Lykins, M. E. Hansen, X. Sun, R. Advincula, J. A. Finbloom, A. K. Jain, Y. Zala, A. Ma, T. A.
594 Desai, Impact of Microdevice Geometry on Transit and Retention in the Murine Gastrointestinal Tract.
595 *ACS Biomaterials Science and Engineering* (2021), doi:10.1021/acsbomaterials.0c01606.
- 596 41. M. C. Torjman, J. I. Joseph, C. Munsick, M. Morishita, Z. Grunwald, Effects of Isoflurane on
597 gastrointestinal motility after brief exposure in rats. *International Journal of Pharmaceutics*. **294**, 65–71
598 (2005).
- 599 42. X. Wei, M. Beltrán-Gastélum, E. Karshalev, B. Esteban-Fernández De Ávila, J. Zhou, D. Ran, P.
600 Angsantikul, R. H. Fang, J. Wang, L. Zhang, Biomimetic Micromotor Enables Active Delivery of
601 Antigens for Oral Vaccination. *Nano Letters*. **19**, 1914–1921 (2019).
- 602 43. C. Woertz, M. Preis, J. Breitreutz, P. Kleinebudde, Assessment of test methods evaluating
603 mucoadhesive polymers and dosage forms: An overview. *European Journal of Pharmaceutics and*
604 *Biopharmaceutics*. **85**, 843–853 (2013).
- 605 44. J. das Neves, B. Sarmiento, in *Mucosal Delivery of Biopharmaceuticals: Biology, Challenges and*
606 *Strategies* (Springer US, 2014), vol. 9781461495246, pp. 35–58.
- 607 45. L. H. Nielsen, T. Rades, B. Boyd, A. Boisen, Microcontainers as an oral delivery system for spray dried
608 cubosomes containing ovalbumin. *European Journal of Pharmaceutics and Biopharmaceutics*. **118**, 13–
609 20 (2017).
- 610 46. L. A. Feldkamp, L. C. Davis, J. W. Kress, Practical cone-beam algorithm. *J. Opt. Soc. Am. A*. **1** (1984),
611 doi:10.1364/JOSAA.1.000612.

612

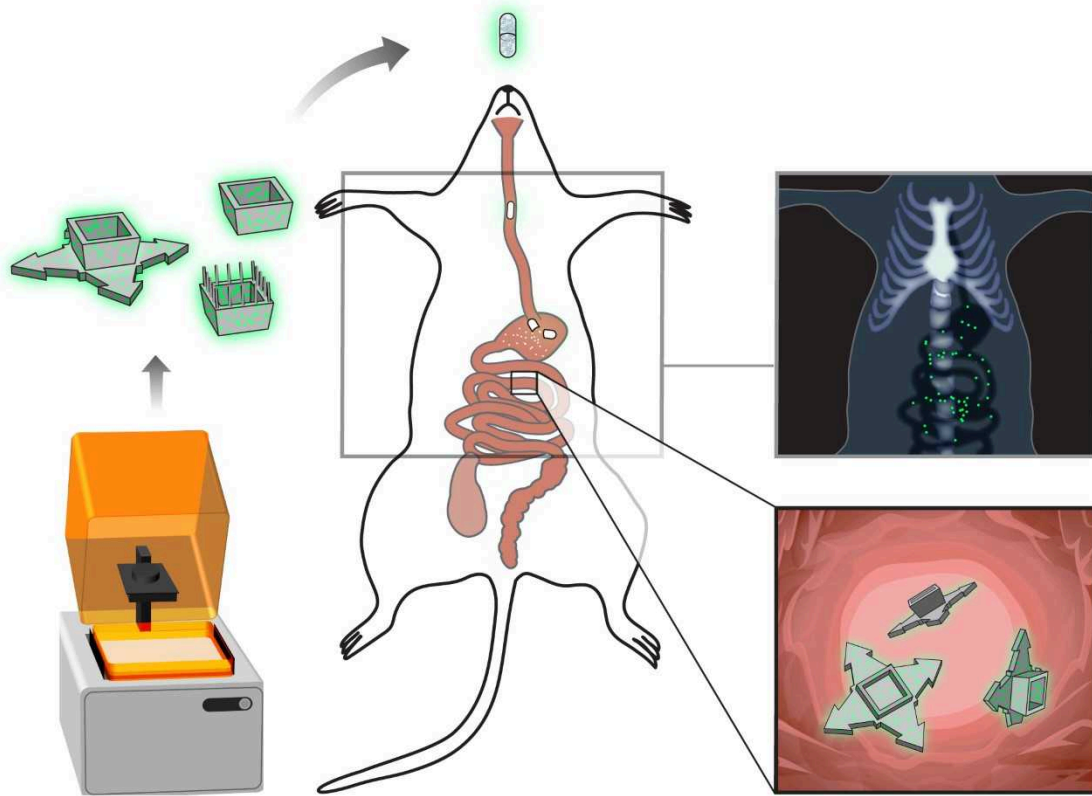
613 Acknowledgments

614 Thanks to the Bio Facility and the 3D Imaging Center, both at the Technical University
615 of Denmark, for support regarding the *in vivo* rat study and for accessibility to x-ray
616 imaging equipment, respectively.

617

618 **Funding:** The authors would like to acknowledge the Danish National Research
619 Foundation (DNRF122) and Villum Fonden (Grant No. 9301) for Intelligent Drug
620 Delivery and Sensing Using microcontainers and Nanomechanics (IDUN). Furthermore,
621 the study was supported by the Novo Nordisk Foundation (NNF17OC0026910) as a part
622 of the project Microstructures, Microbiota and Oral Delivery (MIMIO). KZ, ETH and
623 AB acknowledge the financial support from BioInnovation Institute Foundation for
624 Therapeutic drug monitoring (grant number NNF20SA0063552).

625



628

629

630

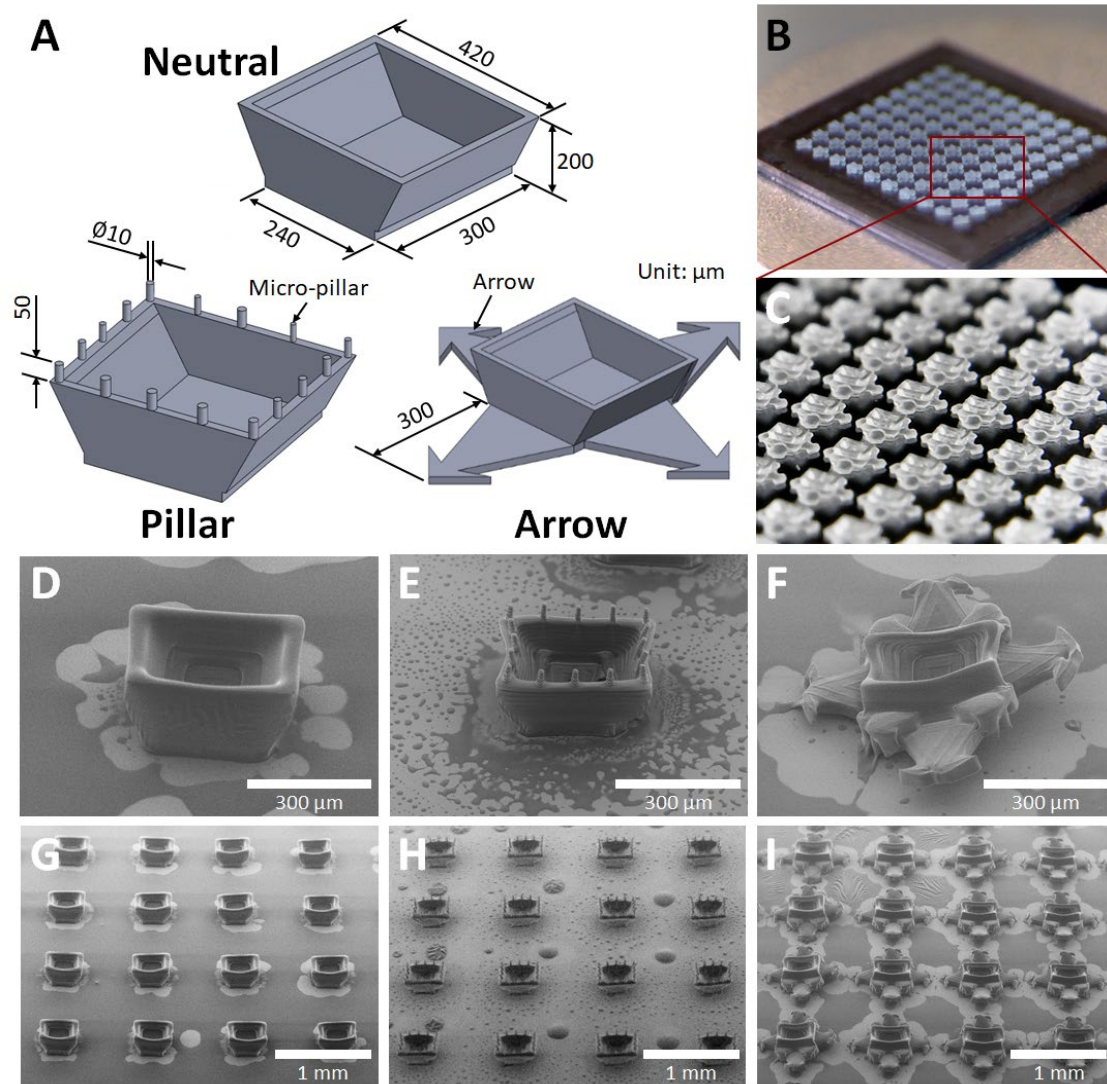
631

632

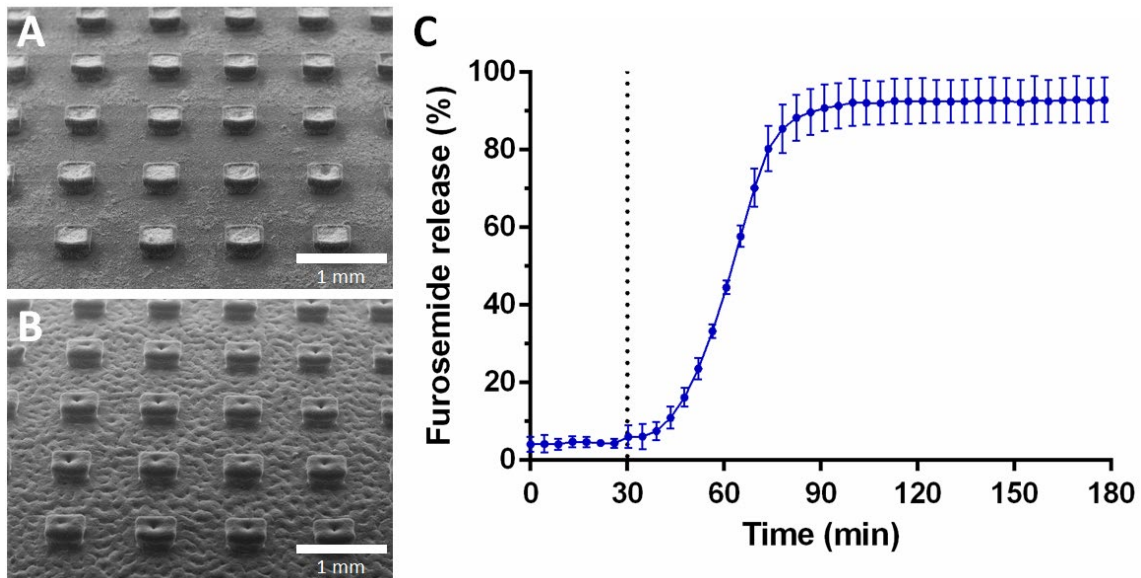
633

634

Fig. 1. Schematic illustration of the experimental setup. Radiopaque microcontainers were 3D printed in three different designs and dosed to rats in gelatin capsules using oral gavage. Their location in the GI tract was determined by planar x-ray imaging 0.5 to 3 h after dosing. Further investigation of spatial dynamics and mucosal interactions in the small intestine was carried out using CT scanning and CryoSEM, respectively.

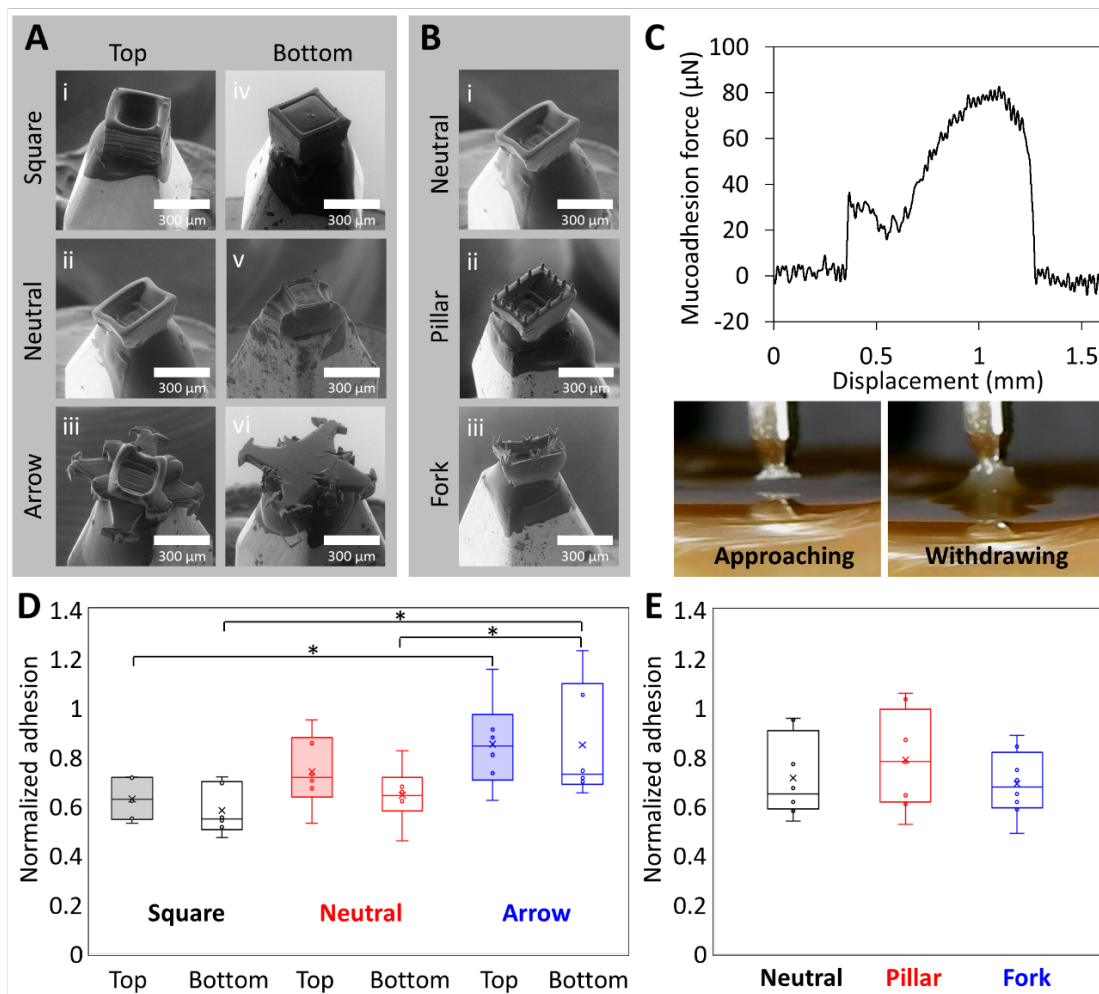


635
 636
 637 **Fig. 2. 3D printed biocompatible microcontainers with three geometry designs for**
 638 **enhancing mucoadhesion.** (A) Schematic of neutral, pillars, and arrows design. (B)
 639 Photograph of 3D printed 100 MCs in a 10×10 array on a silicon chip. (C) Microscope
 640 image of detailed 3D printed microcontainers result. SEM image of (D) neutral, (E)
 641 pillar, and (F) arrow design. (G-I) SEM images of mass-produced microcontainers.



642
643
644
645
646
647
648
649

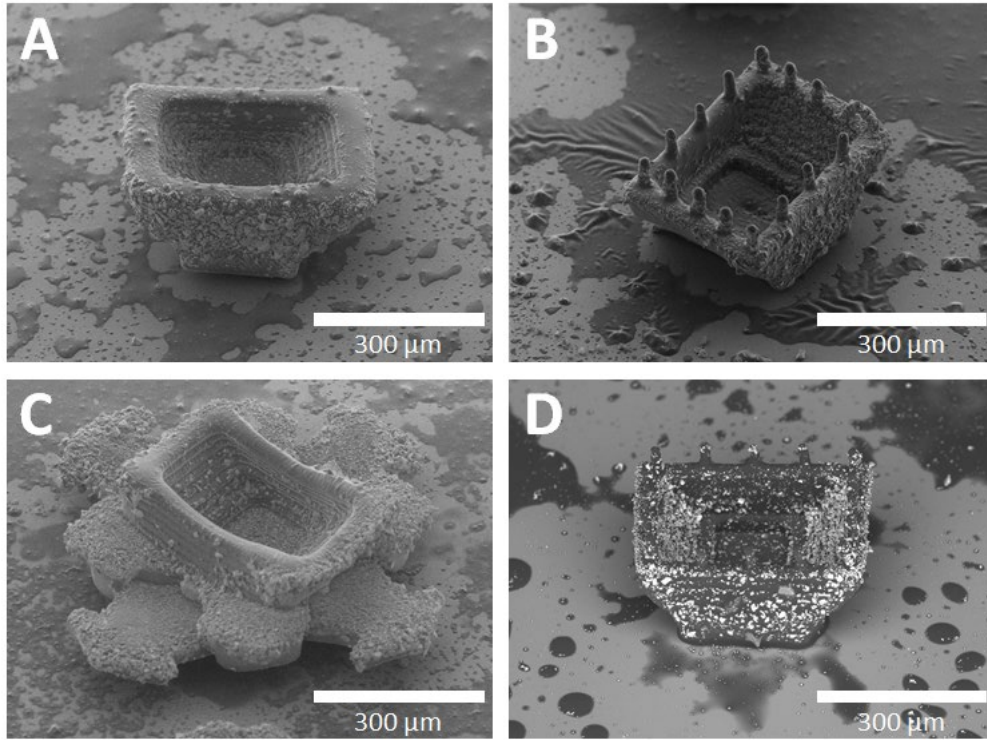
Fig. 3. Proof-of-concept that the 3D printed microcontainers can be used for targeted drug delivery to the small intestine. (A) SEM images of 3D printed microcontainers loaded with furosemide (top) and coated with Eudragit[®] L100 (bottom). (B) Percentage release of furosemide from microcontainers. During the first 30 min, the release (C) was measured in gastric pH (pH 2.4), followed by an intestinal step (pH 7.5). Mean \pm SD, n = 4.



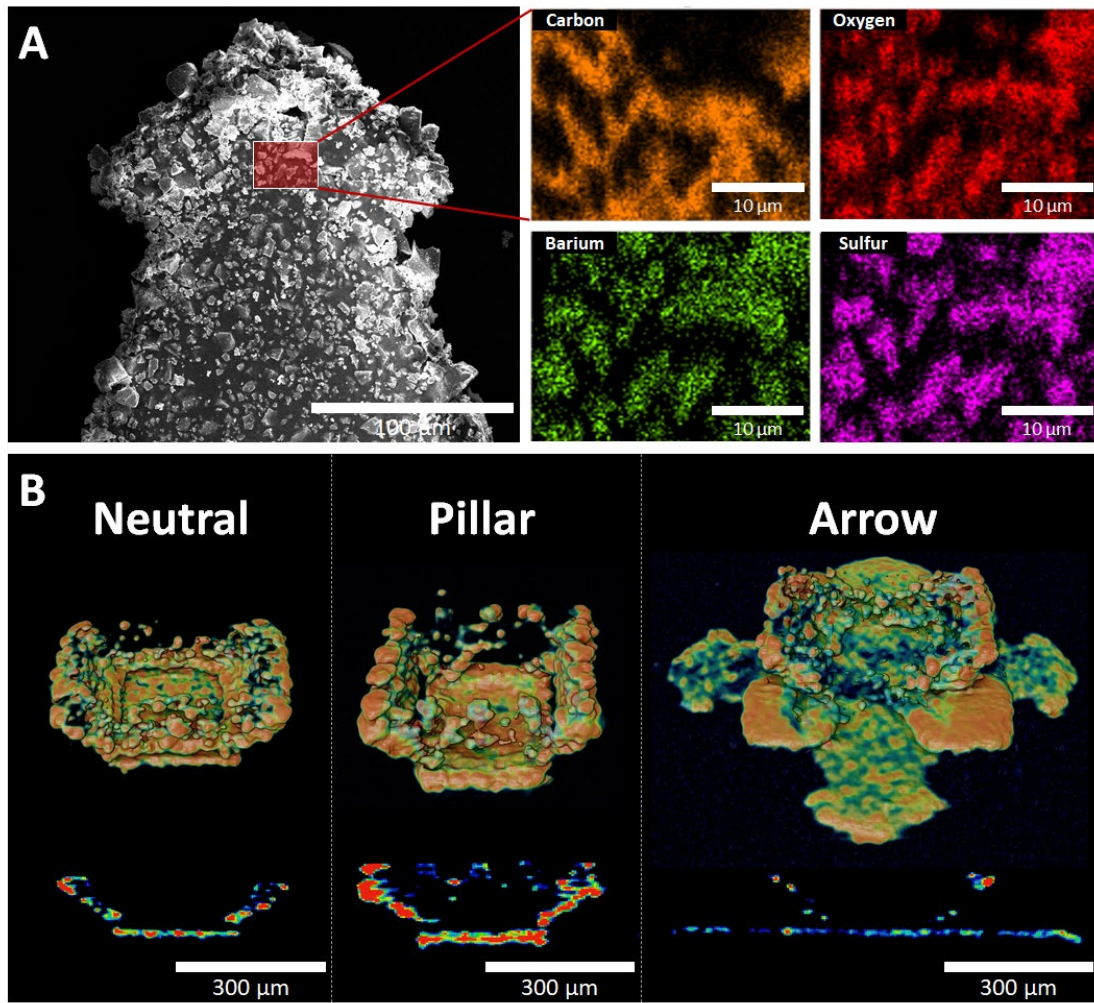
650
651
652
653

Fig. 4. Ex vivo mucoadhesion characterization of 3D printed microcontainer. (A) SEM image of the top side of (i) square, (ii) neutral, and (iii) arrow microcontainer on microprobe; and the bottom side of (iv) square, (v) neutral, and (vi) arrow

654 microcontainer on the microprobe. (B) SEM image of the top side of (i) neutral, (ii)
655 pillar, and (iii) fork microcontainer on the microprobe. (C) Mucoadhesion force versus
656 displacement curve while approaching and withdrawing bottom side of arrow
657 microcontainer to porcine small intestinal tissue. (D) Orientation study with normalized
658 mucoadhesion of square, neutral, and arrow microcontainer's both top and bottom sides.
659 Mean \pm SD, n = 6, t-Test with two-sample variances. (E) Additive feature study shows
660 normalized mucoadhesion of neutral, pillar, and fork microcontainer's top side. Mean \pm
661 SD, n = 6.
662



663 **Fig. 5. Incorporation of BaSO₄ into 3D printed microcontainers.** SEM images of (A)
664 neutral, (B) pillar, and (C) arrow design. (D) High contrast SEM image clearly indicating
665 the BaSO₄ particles.
666
667



668
 669 **Fig. 6. EDX analysis and μ CT scanning.** (A) SEM image of radiopaque
 670 microcontainers surface and EDX analysis mapping of detected elements, including
 671 carbon, oxygen, barium and sulfur. (B) μ CT scanning showing the homogeneity of
 672 BaSO_4 nanoparticles in the 3D printed radiopaque microcontainers (see Fig. S1 for
 673 multiple microcontainers).
 674
 675

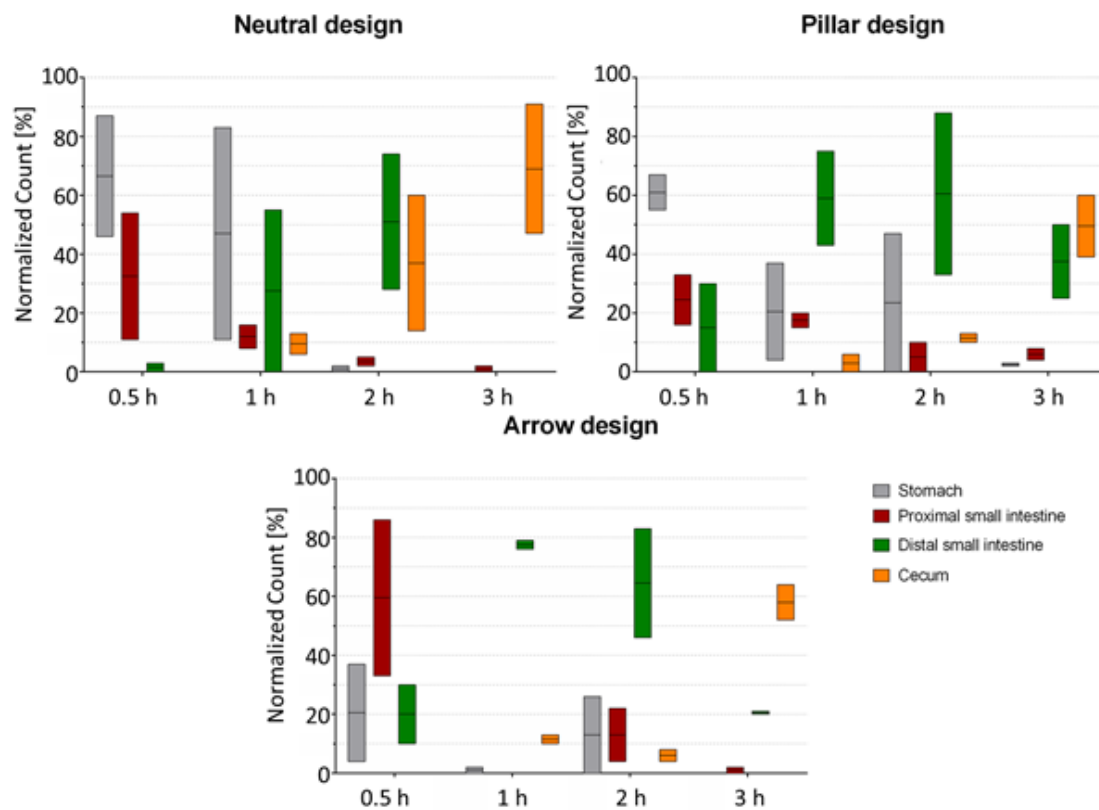


Fig. 7. GI retention and transit time of microcontainers. Graphs showing the normalized count of microcontainers at specific locations over time for the neutral, pillar and arrow design.

676
677
678
679
680

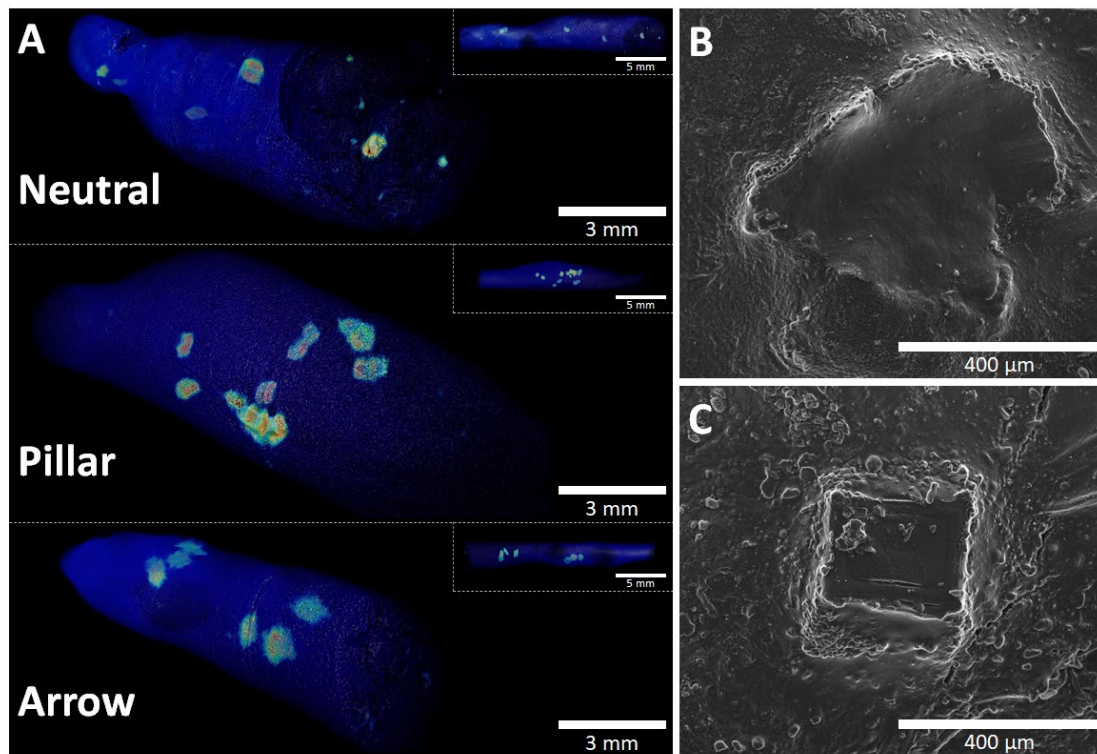


Fig. 8. Spatial dynamics and mucosal interactions of microcontainers. (A) CT scan images of neutral, pillar and arrow designed microcontainers inside small intestinal pieces revealing their spatial dynamics. (B-C) CryoSEM images of pillar microcontainers showing their mucosal interactions such as embedment into the intestinal tissue and the microcontainer orientation.

681
682
683
684
685
686
687

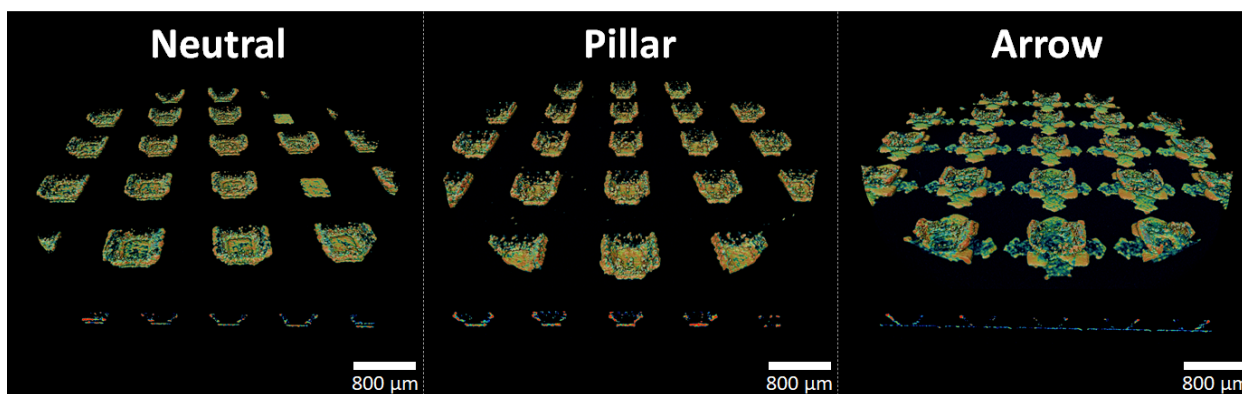


Fig. S1. μ CT scanning of microcontainers. μ CT scanning showing the homogeneity of BaSO_4 nanoparticles in the 3D printed radiopaque microcontainers (supplement to Fig. 6B).

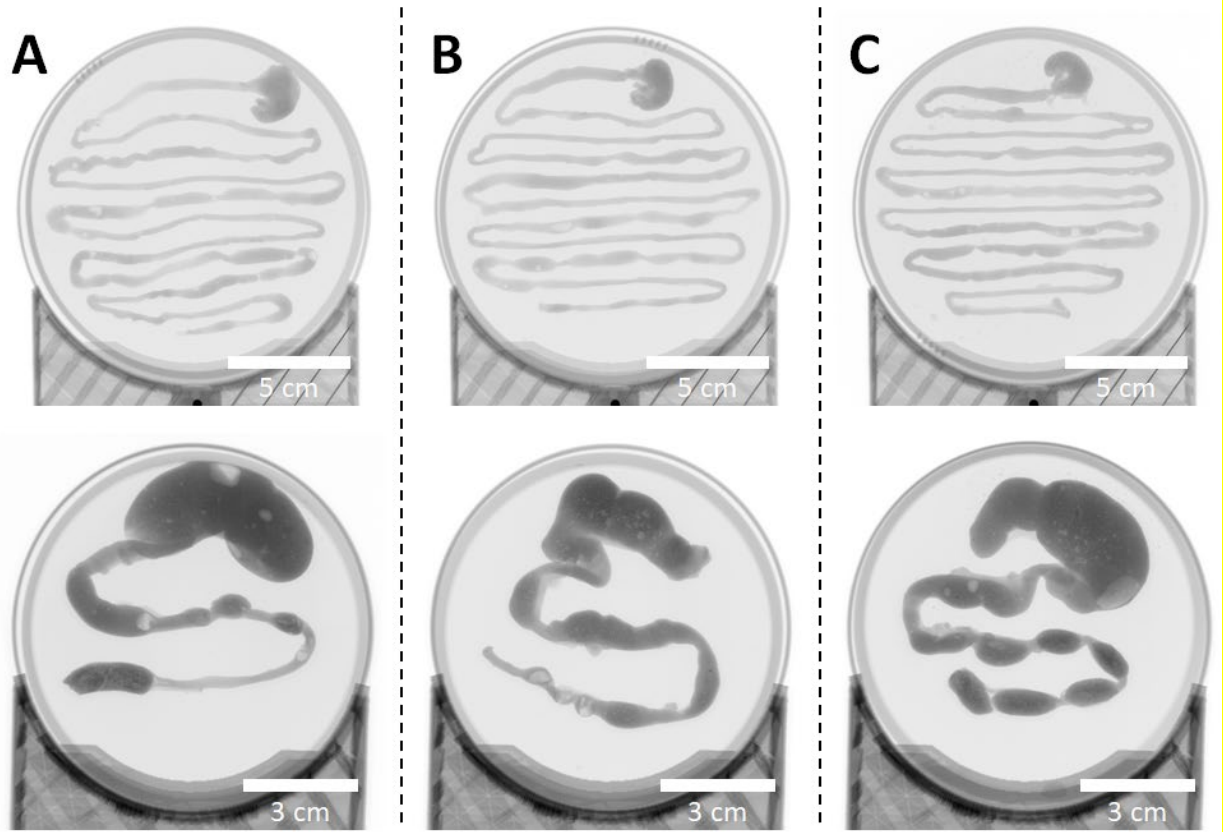


Fig. S2. Representative GI tracts. Planar x-ray images of three representative removed GI tracts at 0.5 h. (A) neutral design, (B) pillar design and (C) arrow design.

696
697
698
699

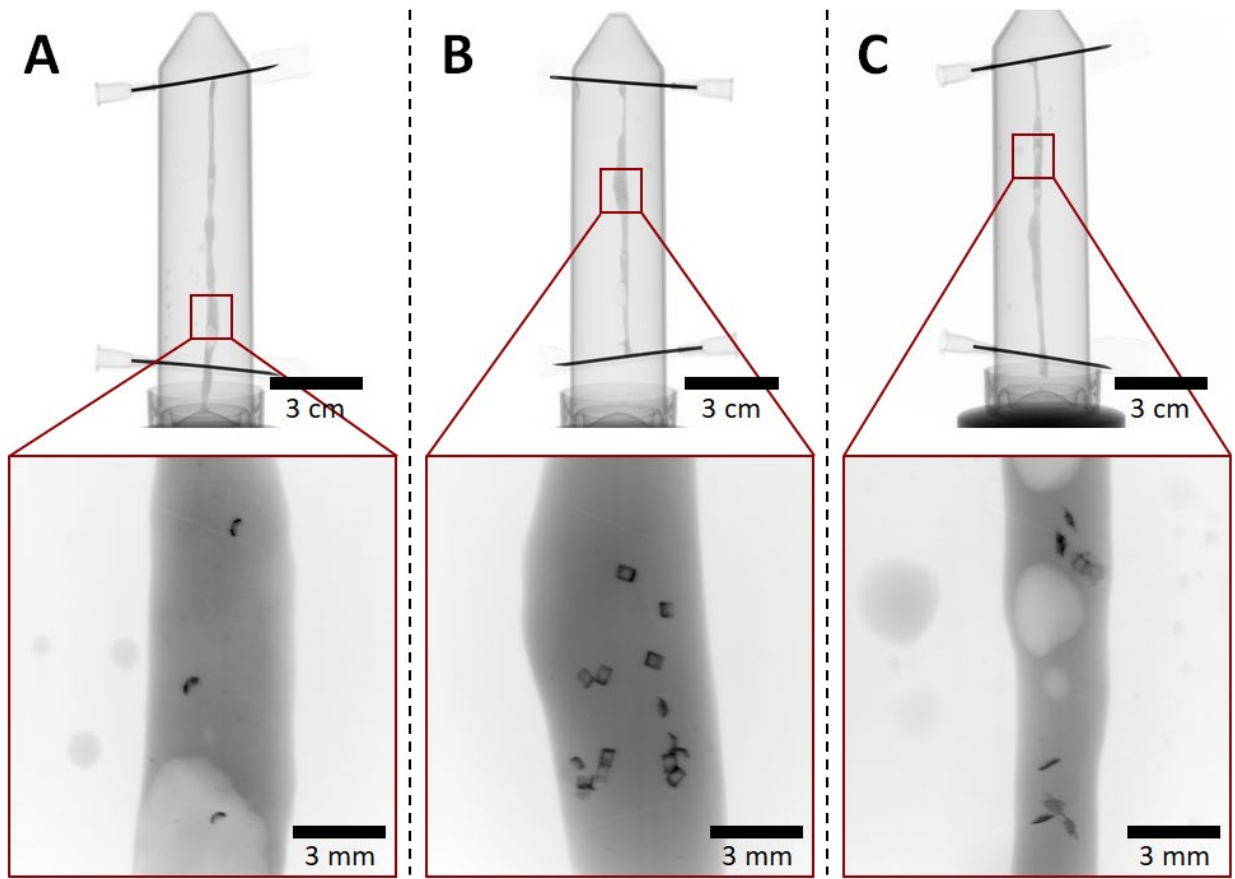


Fig. S3. Samples for CT scanning and CryoSEM. Planar x-ray images of the three samples used for CT scanning and CryoSEM. (A) neutral design, (B) pillar design and (C) arrow design.

701
702
703
704
705

Table S1. Experimental design of *in vivo* rat study and following examination. 24 rats in three different groups were totally used for the *in vivo* rat study and indications “+” and “-” means yes and no, respectively, in relation to the following examination.

Group	Neutral				Pillar				Arrow			
Euthanasia [h]	0.5	1	2	3	0.5	1	2	3	0.5	1	2	3
Number of rats	2	2	2	2	2	2	2	2	2	2	2	2
Removal of GI tract	+	+	+	+	+	+	+	+	+	+	+	+
Planar x-ray imaging of GI tract and manual counting	+	+	+	+	+	+	+	+	+	+	+	+
CT scanning and CryoSEM of small intestinal piece	+	-	-	-	+	-	-	-	+	-	-	-

706
707
708
709

710